Measurements of the Electric Form Factor of the Neutron at Q^2=0.45 and 1.13 (GeV/c)^2

by

Shigeyuki Tajima

Department of Physics
Duke University

Date

Approved:

Calvin R. Howell, Supervisor

Richard Madey, Co-Supervisor

Ashutosh V. Kotwal

Roxanne P. Springer

Stephen W. Teitsworth

Richard L. Walter

Dissertation submitted in partial fulfillment of
the requirements for the degree of
Doctor of Philosophy in the Department of
Physics in the Graduate School
of Duke University

2003

Abstract

(Physics – TUNL)

Measurements of the Electric Form Factor of the Neutron at Q^2=0.45 and 1.13 $(GeV/c)^2$

by

Shigeyuki Tajima

Department of Physics
Duke University

Date

Approved:

Calvin R. Howell, Supervisor

Richard Madey, Co-Supervisor

Ashutosh V. Kotwal

Roxanne P. Springer

Stephen W. Teitsworth

Richard L. Walter

An abstract of a dissertation submitted in partial
fulfillment of the requirements for the degree
of Doctor of Philosophy in the Department
of Physics in the Graduate School
of Duke University

2003

Abstract

Precise measurements of the electric form factor of the neutron, G_E^n, over a wide range of the square of the four-momentum transfer, Q^2, are important for understanding nucleon and nuclear electromagnetic structure. In the non-relativistic limit, the electric and magnetic form factors are related to the charge and magnetization distribution inside a nucleon, respectively. The measured values of the form factors also serve as an important test for nucleon models. Among the four nucleon form factors, the electric form factor of the neutron, G_E^n, is the most difficult one to measure and therefore has been very poorly known especially in the region $Q^2 > 1$ $(\mathrm{GeV/c})^2$ due to the lack of a free neutron target and the small value of G_E^n.

The Jefferson Laboratory E93-038 collaboration measured the ratio of the electric to magnetic form factor of the neutron, $g = G_E^n/G_M^n$, at three acceptance-averaged Q^2 values of 0.45, 1.13 and 1.45 $(\mathrm{GeV/c})^2$ using the quasi-elastic $^2\mathrm{H}(\vec{e}, e'\vec{n})^1\mathrm{H}$ reaction. In our experiment, an electron was scattered quasielastically from a neutron in a liquid-deuterium target, and the electron was detected in an electron spectrometer in coincidence with the neutron which was detected in a neutron polarimeter. The polarimeter was used to analyze the polarization of the recoil neutrons by measuring the *np* elastic scattering asymmetry. The experiment was performed in Hall-C at

Thomas Jefferson National Accelerator Facility during the period from September 2000 to April 2001. The value of g was determined from the measured ratio of the sideways and longitudinal components of the neutron polarization vector. The values for G_E^n were computed from our measured values of $g = G_E^n/G_M^n$ using the G_M^n values obtained from a fit to the world data. The E93-038 collaboration reported the first measurements of G_E^n using polarization techniques at Q^2 greater than 1 $(GeV/c)^2$. Furthermore, our measurements of G_E^n at the two higher Q^2 values of 1.13 and 1.45 $(GeV/c)^2$ are more precise than prior measurements at lower Q^2.

In this dissertation, the data analyses and our results for g and G_E^n at Q^2=0.45 $(GeV/c)^2$ and Q^2=1.13 $(GeV/c)^2$ are given. Our high-accuracy data are included with the "world" data for G_E^n to form an improved data set that was fit with an empirical function to give a simple parameterization of G_E^n as a function of Q^2. In addition, the data for the ratio G_E^n/G_M^n are compared to theoretical models of the nucleon. We found that no theoretical model predicts both proton and neutron form factor data.

Acknowledgements

Since I joined the NTOF group at TUNL in August 1999, I have met and worked with so many excellent people.

First and foremost, I would like to thank my advisor, Dr. Calvin Howell. I have been quite fortunate to work with him because he always gave me a quite appropriate suggestion whenever I did not know what to do. He is always enthusiastic about physics, and he never refused to answer my questions no matter how tired or busy he was. I greatly appreciate his help during my research at Duke. I always enjoyed working with him.

Secondly, I would like to thank Dr. Richard Madey, the spokesperson for the experiment. We are quite lucky because our spokesperson is such a pioneer in recoil polarization measurements in nuclear physics. I thank Dick for giving me an opportunity to work in such an excellent experiment. I also received a lot of help and suggestions from Dick.

Special thanks also go to Dr. Steve Churchwell. My analysis would have never been completed without his unlimited support and help, because he developed many key algorithms and subroutines for the analysis. He is also the first person for me to talk with whenever an issue came up. Every suggestion he gave me was quite useful.

I would also like to thank the members of the analysis team for our collaboration. I thank Dr. Andrei Semenov for a number of helps and suggestions that he gave me. It would have been very difficult for me to do the analysis without his help. I also thank Drs. James Kelly, Simon Taylor, Mark Jones, Allena Opper and Mike Finn. I enjoyed discussing physics with them during the data analysis.

The graduate students in the E93-038 collaboration (Aram Aghalaryan, Erick Crouse, Glen MacLachlan, William Tireman, Brad Plaster, and Chenyu Yan) deserve a special recognition. We worked together very hard every day at the Lab to take shifts and to perform on- and off-line data analysis. I really enjoyed working with them. I especially thank Brad for many helpful discussions. I always enjoyed discussing physics with him. One of my primary jobs for the collaboration was to develop an analyzing software, known as the E93038 Engine. Although this job was not easy, I was able to accomplish this task because the experts such as Drs. Wei-Ming Zhang, Ken Garrow, and Steve Wood helped me all the time. I am extremely thankful for this.

Back at TUNL, I offer thanks to Drs. Haiyan Gao and Dipangkar Dutta for useful discussions. I thank my best friends, Konstantin Sabourov and Rob Macri for helping me all the time. Konstantin introduced me to a world of Mac, and he has been my Mac Mentor. I ended up buying the same computer and the same accessories as he owns! I enjoyed using my Mac whenever I worked on this thesis. It was Rob who suggested that I work with Calvin when I was looking for an advisor in the summer of 1999. He stressed that Calvin was a nice professor to work with, and that was one of the reasons why I decided to join the group. I would also like to thank TUNL staff for their support. After I returned to TUNL from JLab, Dr. Alex Crowell, a TUNL computer staff, installed a huge disk ($\sim$200 GB) on a Linux machine. That allowed me to download all data for this experiment from JLab. Without this disk space, my data analysis would have been much more difficult and time consuming. **Finally, I would like to thank my parents for their support and encouragement through my entire education.**

Contents

List of Figures

List of Tables

Chapter 1

Introduction

1.1 Magnetic Moments and Structure of Nucleons

Sir James Chadwick discovery of the neutron in 1932 [Cha32] solved the problem of the missing mass of the nucleus. Chadwick, who was a student of Lord Rutherford, was awarded the Nobel Prize in Physics in 1935 for this work. Because of the closeness of the masses of the proton and neutron and because both particles have a spin of $1/2$, Heisenberg speculated that they are different states of the same fundamental particle, which he called the *nucleon*. Heisenberg invented the new quantum number of isospin to distinguish the two states of the nucleon, assigning the z component (projection onto the isospin quantization axis) of $+1/2$ to the proton and $-1/2$ to the neutron. However, it became evident that the nucleons probably were not fundamental point particles. The first pieces of evidence were their measured magnetic moments, which were not as expected for spin $1/2$ point particles. The magnetic moment μ of a

spin-$\frac{1}{2}$ particle is given by

$$\mu = g \left(\frac{\mathcal{Q}}{2m} \right) \frac{\hbar}{2}, \tag{1.1}$$

where g is known as the gyromagnetic ratio (also known as the g-factor), $\mathcal{Q}$ is the charge of the particle, m is the mass of the particle and $\hbar$ is the Planck constant h divided by 2π. The value for g for a spin 1/2 particle which *does not possess any internal structure* (a Dirac particle) is 2, which is obtained from the Dirac equation. The measured value of $g = 2.0023$ for an electron agrees quite well with the theoretical value, which indicates that the electron has no internal structure [1].

If the proton and neutron are point particles like an electron, it is expected that they have the magnetic moments of 1 and 0, respectively, in units of the *nuclear magneton*, $\mu_N = \frac{e\hbar}{2M_p}$, where M_p is the mass of the proton. Table 1.1 gives the measured

	Values if they *were* point particles	Measured values	Anomalous values
Proton	1.0	2.79	1.79
Neutron	0.0	-1.91	-1.91

Table 1.1: Magnetic moments of the proton and neutron in units of nuclear magneton, μ_N. The measured values of the magnetic moments of the nucleons are significantly different from the expected values. See text for detail.

values of magnetic moments. The first reliable measurements of the magnetic moments of the nucleons were performed in 1930's. These early measurements were the origin of what would become the long-standing puzzle of why the measured values of the magnetic moments of the nucleons differed significantly from the expected values for Dirac particles. The amount unaccounted for by point-particle considerations is

[1] The deviation of the measured value from $g = 2$ can be explained by considering the higher-order Feynman diagram which shows the emission/absorption of a virtual photon. See for example [Hal84].

historically known as the anomalous values of the magnetic moments of the nucleons. The anomalous values were the first indicators that the proton and neutron were not point particles but have internal structure. This realization led to the speculation that there might be particles inside the nucleons that are more fundamental.

The second pieces of evidence for the internal structure of the nucleons were discovered in proton cross-section measurements. It was demonstrated in the 1950's by Hofstadter and his colleagues at the Stanford Linear Accelerator (SLAC) that the cross section for elastic electron scattering from the proton as a function of the scattering angle in the lab frame did not follow the form of electron scattering from a Dirac particle [Hof53, Hof55, Cha56]. These observations implied that the proton must have internal structure, which was a conclusion that was consistent with the implication of the anomalous magnetic moment. Because of his work in using electrons to probe the internal structure of the proton, Hofstadter won the Nobel Prize in Physics in 1961. But if the nucleons were not the most fundamental strongly interacting particles, what were? Now, after only two decades of completing the picture of the building blocks of nuclei, physics were starting to look inside these building blocks, i.e., to take a closer look at nucleons. It was the information revealed in the deep inelastic scattering experiments of electrons from protons performed by Friedman, Kendall, and Taylor in 1968 at SLAC [Blo69, Bre69] that would eventually win them the 1990 Nobel Prize in Physics, and would with certainty identify the strongly interacting point particles that make up the nucleons. The newly discovered particles were called quarks. After these pioneering works, it would take at least a few more decades to make precise measurements of the electromagnetic structure of the proton. The most accurate measurements of the proton elastic electromagnetic structure functions have been made only recently, because it is only

in the last two decades that high-energy high-current polarized electron beams have become available [Jon00, Gay02]. The progress made on probing the electromagnetic structure of the neutron has not been as fast as that made on the proton mainly because of the technical difficulties in electron-neutron scattering experiments. The aim of the work in this thesis is to make a substantial improvement to the existing data for the electric form factor of the neutron.

Throughout this thesis, with the exception of Section 1.1, we employ the unit conventions, $\hbar = c = 1$, where c is the speed of light.

1.2 Four-Momentum Transfer

High-energy electron beams can be used to directly probe the internal electromagnetic structure of nucleons and nuclei (hadrons). In the field theory picture , the interaction of an electron with a hadron is due to the exchange of virtual photons. In the single-photon exchange picture, the wavelength of the virtual photon is inversely proportional to the momentum transfered to the struck hadron by the scattered electron; that is, the larger the momentum transfer, the shorter is the wavelength of the exchanged photons. In essence, the momentum transfered is a kinematic parameter that sets the spatial size to which the scattering process is sensitive.

Because the mass of the electron is much smaller than that of hadrons, about 2000 times less massive than a nucleon, electron scattering has the very useful kinetic feature that the momentum transfered to the struck particle can be varied independently of the energy absorbed by that particle. It is this feature that enables the measurement of the ground state properties of hadrons separate from the state transition properties. For instance, the electromagnetic structure function for the

transition from the ground state of ^{12}C to the first excited state at 4.414 MeV above the ground state can be made by adjusting the kinematics so that the ^{12}C nucleus absorbs 4.414 MeV of energy from the scattered electrons for all values of the momentum transfered to the nucleus in the scattering process. Similarly, the ground state structure functions can be measured by adjusting the kinematics so that none of the energy lost by the electron goes into exciting internal degrees of freedom of the hadron.

For elastic electron-nucleon scattering, the following energy and momentum conservation relations hold.

$$k^{\mu} + p^{\mu} = k^{'\mu} + p^{'\mu}, \tag{1.2}$$

where k^{μ} and $k^{'\mu}$ (p^{μ} and $p^{'\mu}$) are the initial and final electron (nucleon) four-momenta and $\mu = 0, 1, 2, 3$. The 0th component of a four-momentum represents energy, and the 1st, 2nd, and 3rd components represent x,y, and z components of the three momentum vector, respectively. Figure 1.1 shows a Feynman diagram for the lowest order electron-nucleon elastic scattering. The four momenta in Equation 1.2 in the lab frame can be given as

$$k^{\mu} = (E_e, \vec{p_e}), \tag{1.3}$$

$$p^{\mu} = (M, \vec{0}), \tag{1.4}$$

$$k^{'\mu} = (E'_e, \vec{p'_e}), \tag{1.5}$$

$$p^{'\mu} = (E', \vec{p'}), \tag{1.6}$$

where E_e (E'_e) is the energy of the incident (scattered) electron in the lab frame and $\vec{p_e}$ ($\vec{p'_e}$) is the incident (scattered) electron momentum vector. In this coordinate system, $\vec{p_e}$ points to the Z-direction. The square of each four momentum is equal to

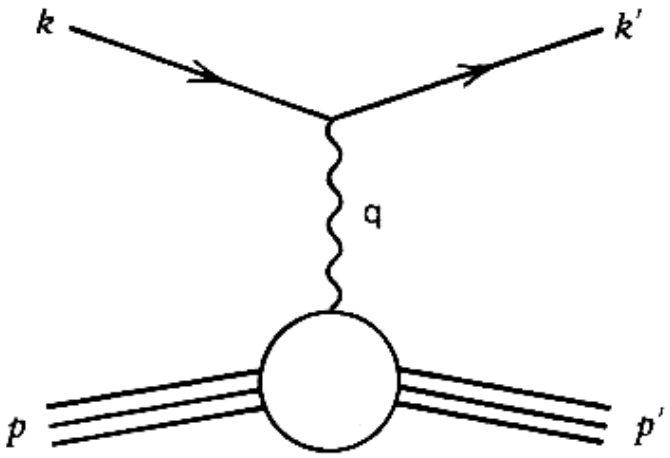

Figure 1.1: Lowest order electron-nucleon elastic scattering.

the square of its particle mass, so

$$k^\mu k_\mu = k'^\mu k'_\mu = m_e^2 \qquad \text{and} \tag{1.7}$$

$$p^\mu p_\mu = p'^\mu p'_\mu = M^2, \tag{1.8}$$

where M is the mass of the target nucleon, which is at rest in lab frame. The four-momentum transfer, q^μ, for this elastic scattering is then defined as

$$q^\mu \equiv k^\mu - k'^\mu \tag{1.9}$$

$$= p'^\mu - p^\mu \tag{1.10}$$

Therefore, we have $q^\mu = (E_e - E'_e, \vec{p_e} - \vec{p'_e})$. The four-momentum-transfer squared, q^2, which is a Lorentz scaler, can be calculated from the above definition. To obtain the expression for the four-momentum squared $q^2 \equiv q^\mu q_\mu$, we square both sides of $q^\mu + p^\mu = p'^\mu$. We then obtain $q^2 + 2q^\mu p_\mu + p^\mu p_\mu = p'^\mu p'_\mu$. Noting that $q^\mu p_\mu =$

$M(E_e - E'_e)$ and using Equation 1.8, we have

$$q^2 \;=\; -2q^\mu p_\mu = -2M(E_e - E'_e). \tag{1.11}$$

Therefore, Equation 1.11, obtained for *elastic* electron-nucleon scattering, suggests that q^2 is proportional to the amount of energy transfered from the incident electron to the nucleon. Similarly, by squaring both sides of Equation 1.9 and neglecting the electron mass ($m_e \approx 0$), q^2 is also given as

$$q^2 \;\simeq\; -2k^\mu k'_\mu \tag{1.12}$$

$$\;=\; -2(E_e E'_e - \vec{p_e} \cdot \vec{p'_e}) \tag{1.13}$$

$$\;=\; -4\, E_e\, E_e^{'} \sin^2(\theta_e/2), \tag{1.14}$$

where θ_e is the scattering angle of the electron in the lab frame. The E'_e is obtained easily from Equations 1.11 and 1.14, and it is

$$E_e^{'} \;\simeq\; \frac{E_e}{1 + 2\frac{E_e}{M}\sin^2(\theta_e/2)}, \tag{1.15}$$

where the electron mass is once again neglected.

The formulas given in this section are valid for elastic electron-nucleon scattering. For *inelastic* electron-nucleon scattering, the energy lost by the electron is equal to the sum of the recoil nucleon energy and the nuclear excitation energy. Therefore, Equations 1.11, 1.14, and 1.15 are no longer valid. The expressions for q^2 (E'_e) for *quasielastic* scattering of an electron from a nucleon inside a *composite target* is reasonably well approximated by Equations 1.11 and 1.14 (Equation 1.15) provided that the binding energy of the target is much smaller than the nucleon mass.

Because the value of q^2 is negative, we define the absolute value of q^2 to be

$$Q^2 \;=\; -q^2 > 0. \tag{1.16}$$

1.3 Electromagnetic Interaction and Form Factors

Spin-$\frac{1}{2}$ particles are described by the Dirac equation, which is Lorentz covariant. A free electron in the presence of electromagnetic field A^μ satisfies

$$(\gamma^\mu p_\mu - m_e)\psi \;=\; -e\gamma_\mu A^\mu \psi, \tag{1.17}$$

where ψ is the four-component spinor, γ^μ's are the Dirac gamma matrices, and m_e and $-e$ are the mass and charge of the electron. The RHS in Equation 1.17 represents the electromagnetic interaction. The scattering amplitude, T_{fi}, for an electron making the transition from an initial state i to a final state f, can be calculated using the first-order perturbation theory. It is given by

$$T_{fi} \;=\; -i \int j_\mu A^\mu d^4x, \tag{1.18}$$

where the electromagnetic current j_μ for an electron is given by

$$j_\mu \;=\; -e\,\bar{\psi}(k')\gamma_\mu\psi(k) \tag{1.19}$$

$$\;=\; -e\,\bar{u}(k')\,\gamma^\mu\,u(k)\,e^{i(k'-k)\cdot x}, \tag{1.20}$$

where we took the form of $\psi(k)$ to be $\psi(k) = u(k)e^{-ik\cdot x}$, where $u(k)$ is the four-component spinor independent of x [2]. Similarly, $\psi(k') = u(k')e^{-ik'\cdot x}$. Here, we assumed that the electromagnetic interaction is sufficiently weak that the outgoing plane wave for the electron is not distorted after the interaction. The gamma matrix γ^μ takes the initial state $u(k)$ to the final state $u(k')$. The current j_μ can be given in terms of k, k', and the antisymmetric tensor $\sigma_{\mu\nu} \equiv \frac{i}{2}[\gamma_\mu, \gamma_\nu]$ using the following identity known as the Gordon decomposition [Sak67].

$$\bar{u}(k')\,\gamma^\mu\,u(k) = \frac{1}{2m_e}\bar{u}(k')\left[(k'^\mu + k^\mu) + i\sigma_{\mu\nu}(k'^\mu - k^\mu)\right]u(k). \tag{1.21}$$

[2] k, and k' are four momenta given in Equations 1.3 and 1.5, and x is a four vector, $x = (t, \vec{x})$.

From Equations 1.20 and 1.21, Equation 1.18 is written as

$$T_{fi} = -i \int \left(\frac{-e}{2m_e}\right) \bar{u}(k') \left[(k'^{\mu} + k^{\mu}) + i\sigma_{\mu\nu}(k'^{\mu} - k^{\mu})\right] u(k) e^{i(k'-k)\cdot x} A^{\mu} d^4x. \quad (1.22)$$

To understand Equation 1.22, let us consider T_{fi} in the nonrelativistic limit. Assuming the electromagnetic field A^{μ} is time-independent, the time integration in Equation 1.22 can be performed. Because $e^{i(k'-k)x} = e^{i(E'_e - E_e)t} e^{-i(\vec{p_e}' - \vec{p_e})\cdot\vec{x}}$, Equation 1.22 becomes

$$\begin{aligned} T_{fi} &= -2\pi i \delta(E'_e - E_e) \left(\frac{-e}{2m_e}\right) \\ &\quad \int \bar{u}(k') \left[(k'^{\mu} + k^{\mu}) + i\sigma_{\mu\nu}(k'^{\mu} - k^{\mu})\right] u(k) e^{i(\vec{p_e}' - \vec{p_e})\cdot\vec{x}} A^{\mu} d^3x. \quad (1.23) \end{aligned}$$

In the nonrelativistic limit, we have $(k'+k)_0 = E'_e + E_e \sim 2m_e$ and $(k'+k)_l = 0$ $(l = 1, 2, 3)$. Therefore, $(k'+k)_{\mu} A^{\mu} \sim 2m_e A^0 = 2m_e \phi$, where ϕ is the scaler potential. Plugging this result into Equation 1.23, we see the first term becomes the electric interaction. To interpret the second term in Equation 1.23, more algebra is needed. Making use of the nonrelativistic result, $(k'-k)_0 = E'_e - E_e = 0$, it can be shown that the second term represents the magnetic interaction. Thus, in the the nonrelativistic limit with time-independent A^{μ}, we have [Hal84]

$$\begin{aligned} T_{fi}^{NR} &= -2\pi i \, \delta(E'_e - E_e) \cdot \\ &\quad \left(\int \psi_A^{\dagger}(k')(-e\,\phi)\psi_A(k) \, d^3x + \int \psi_A^{\dagger}(k') \left(-\vec{\mu}\cdot\vec{B}\right) \psi_A(k) \, d^3x \right), \quad (1.24) \end{aligned}$$

where ψ_A contains the two *large* components of the wave function ψ. The first term in Equation 1.24 is the term which arises from the electric potential, $-e\phi$. The second term is due to the potential energy of the magnetic moment $\vec{\mu}$ interacting with the magnetic field, $\vec{B}$, created by the electron current. The $\vec{\mu}$ is given by $\vec{\mu} = -(e/2m_e)\,\vec{\sigma}$, where the components of $\vec{\sigma}$ are the Pauli spin matrices.

Now, let us return to the discussion of the relativistic electromagnetic interaction between an electron and a nucleon. The lowest-order transition amplitude for elastic electron-nucleon scattering with one-photon exchange can be expressed using the electromagnetic currents at the electron and nucleon vertex. The electron transition current j^μ is given in Equation 1.20. As we already mentioned in Section 1.1, the proton and neutron are not point particles. Therefore, the matrix for the electromagnetic current at the nucleon vertex is not just γ^μ as it is for the electron which has no internal structure. Thus, we need to construct the electromagnetic current of a nucleon J^μ to maintain the Lorentz covariance. Using the spinor of the form similar to $\psi(k)$, J^μ can be written as

$$J^\mu \;=\; +e\,\bar{u}(p')\,\lambda^\mu\,u(p)\,e^{i(p'-p)\cdot x}, \tag{1.25}$$

where the form of the matrix λ^μ will be determined later. To calculate the amplitude T_{fi}, let us rewrite Equation 1.18. At the nucleon vertex, we note that the electromagnetic transition current, J^μ, satisfies Maxwell's equations,

$$\Box^2 A^\mu = J^\mu. \tag{1.26}$$

The solution of this equation is given by

$$A^\mu = -\frac{1}{q^2} J^\mu, \tag{1.27}$$

where we used Equations 1.25 and 1.10. Therefore, T_{fi} in Equation 1.18 is given as

$$T_{fi} \;=\; -i \int j_\mu \left(\frac{-1}{q^2}\right) J^\mu d^4x, \tag{1.28}$$

where $(-1/q^2)$ corresponds to the photon propagator.

To determine the form of the matrix λ^μ, we consider the following things. The matrix λ^μ takes the most general form that can be constructed from the gamma

matrices. It can be written as

$$\begin{aligned}\lambda^{\mu} &= A(q^2)\,\gamma^{\mu} + B(q^2)\,(p^{\mu} + p^{'\mu}) + C(q^2)\,(p^{\mu} - p^{'\mu}) \\ &\quad + D(q^2)\,i\,\sigma^{\mu\nu}(p_{\nu} - p^{'}_{\nu}) + E(q^2)\,i\,\sigma^{\mu\nu}(p_{\nu} + p^{'}_{\nu}). \end{aligned} \tag{1.29}$$

The factors A, B, C, D, and E in the above equation are functions of q^2 as it is the only independent Lorentz scaler at the nucleon vertex. Terms involving γ^5 are excluded from λ^{μ} because they would violate conservation of parity. Equation 1.29 can be simplified in the following way. The second term in the RHS of Equation 1.29 can be expressed as a linear combination of γ^{μ} and $i\,\sigma^{\mu\nu}(p^{'\nu} - p^{\nu})$ using the Gordon decomposition (here, m_e, k, and k' in Equation 1.21 need to be replaced with M, p, and p', respectively). So, the structure information that would be contained in $B(q^2)$ is distributed to $A(q^2)$ and $D(q^2)$. Similarly, the last term can be written in terms of $p^{\nu} - p^{'\nu}$, which is parameterized in the third and fourth terms in Equation 1.29. Therefore, we can simplify Equation 1.29 by distributing the second term into the first and third terms and similarly by absorbing the fifth term in the third and fourth terms and then setting $B = E = 0$. In addition, because the term that depends on $p^{\nu} - p^{'\nu}$ would violate current conservation, which requires that $\partial_{\mu} J^{\mu} = 0$, we impose the condition that $C = 0$. Considering all of the above simplifications, symmetry constraints, and conservation constraints, the final form of λ^{μ} has only two terms

$$\lambda^{\mu} = F_1(q^2)\,\gamma^{\mu} + \frac{\kappa}{2M} F_2(q^2)\,i\,\sigma^{\mu\nu} q_{\nu}, \tag{1.30}$$

where the factors $F_1(q^2)$ and $F_2(q^2)$ are called, respectively, the Dirac and Pauli form factors and the κ is the anomalous magnetic moment of a nucleon. The first term in Equation 1.30 conserves the electron helicity because of the structure of the γ^{μ} matrix, while the second term can cause spin flip. The functions $F_1(q^2)$ and $F_2(q^2)$ contain the crucial information about the internal structure of the nucleon. Plugging

Equations 1.19, 1.25, and 1.30 into Equation 1.18, the scattering amplitude T_{fi} is given by

$$T_{fi} = -i \int (-e)\,\bar{u}(k')\,\gamma^{\mu}\,u(k)\left(\frac{-1}{q^2}\right) e\,\bar{u}(p')\,\{F_1(q^2)\,\gamma^{\mu} + \frac{\kappa}{2M}F_2(q^2)\,i\,\sigma^{\mu\nu}q_{\nu}\}\,u(p)e^{i(k'+p'-k-p)\cdot x}\,d^4x. \quad (1.31)$$

Using the Gordon decomposition at the *nucleon* vertex,

$$\bar{u}(p')\,\gamma^{\mu}\,u(p) = \frac{1}{2M}\bar{u}(p')\left((p^{'\mu}+p^{\mu}) + i\sigma^{\mu\nu}(p^{'\mu}-p^{\mu})\right)u(p), \quad (1.32)$$

the λ^{μ} becomes

$$\lambda^{\mu} = F_1(q^2)\,\frac{(p^{'\mu}+p^{\mu})}{2M} + F_2(q^2)\frac{1+\kappa}{2M}\,i\,\sigma^{\mu\nu}q_{\nu}. \quad (1.33)$$

Following the discussion of the electromagnetic current at the electron vertex, it can also be shown in the nonrelativistic limit($q^2 \to 0$) that the first and second term in Equation 1.33, respectively, gives us the electric interaction with charge ($e\,F_1$) and the magnetic interaction with $\mu = (1+\kappa)\,F_2$. Note that the photon with long wavelength cannot see the structure of a nucleon in the nonrelativistic limit. Therefore, we must have charge e and magnetic moments $1+\kappa$ at $q^2 = 0$. Consequently, the values of F_1 and F_2 for proton and neutron at $q^2 = 0$ are given by

$$F_1^p(0) = 1 \quad (1.34)$$

$$F_2^p(0) = 1 \quad (1.35)$$

$$F_1^n(0) = 0 \quad (1.36)$$

$$F_2^n(0) = 1, \quad (1.37)$$

where the superscripts p and n denote proton and neutron, respectively. Equation 1.36 is due to the fact that neutron has no net charge.

The cross section for this reaction in the lab frame is obtained by evaluating

$$d\sigma = \frac{|\mathcal{M}|^2}{F} dQ, \tag{1.38}$$

where $\mathcal{M}$ is the invariant amplitude which is related to T_{fi} (see for example [Hal84]), F is the incident electron flux in the lab frame, and dQ is the Lorentz invariant phase space factor. The cross section is given by

$$\left(\frac{d\sigma}{d\Omega}\right)_{\text{Lab}} = \frac{\alpha^2}{4E_e^2 \sin^4(\theta_e/2)} \frac{E_e^{'}}{E_e} \left[\left(F_1^2 + \tau\kappa^2 F_2^2\right) \cos^2 \frac{\theta_e}{2} + 2\tau(F_1 + \kappa F_2)^2 \sin^2 \frac{\theta_e}{2} \right], \tag{1.39}$$

where the recoiling factor, $E_e^{'}/E_e$, is given by $E_e^{'}/E_e = \frac{1}{1+2\frac{E_e}{M}\sin^2(\theta_e/2)}$ (from Equation 1.15), and the fine structure constant α and the kinematic factor τ are given by

$$\alpha = \frac{e^2}{4\pi} \qquad \text{and} \tag{1.40}$$

$$\tau = \frac{-q^2}{4M^2} = \frac{+Q^2}{4M^2}. \tag{1.41}$$

Equation 1.39 is known as the Rosenbluth formula [Ros50]. Because Equation 1.39 contains terms that are both linear combinations and products of F_1 and F_2, it is more convenient to use the Sachs form factors [Sac62], which are the linear combinations of F_1 and F_2.

$$G_E(Q^2) = F_1(Q^2) - \tau\,\kappa\,F_2(Q^2) \tag{1.42}$$

$$G_M(Q^2) = F_1(Q^2) + \kappa\,F_2(Q^2), \tag{1.43}$$

where $G_E(Q^2)$ and $G_M(Q^2)$ are called the electric and magnetic form factors, respectively. Using the Equations 1.34 through 1.37, the values of the Sachs form factors

at $Q^2 = 0$ are evaluated.

$$G_E^p(0) = 1 \tag{1.44}$$

$$G_M^p(0) = 1 + \kappa_p = \mu_p \tag{1.45}$$

$$G_E^n(0) = 0 \tag{1.46}$$

$$G_M^n(0) = 0 + \kappa_n = \mu_n, \tag{1.47}$$

where κ_p and μ_p (κ_n and μ_n) are the *anomalous* magnetic moment and the *measured* magnetic moment of proton (neutron), respectively. The values of these magnetic moments are given in Table 1.1.

Using G_E and G_M, Equation 1.39 is expressed as

$$\left(\frac{d\sigma}{d\Omega}\right)_{\text{Lab}} = \frac{\alpha^2}{4E_e^2 \sin^4(\theta_e/2)} \frac{E_e'}{E_e} \left[\frac{G_E^2 + \tau G_M^2}{1+\tau} \cos^2\frac{\theta_e}{2} + 2\tau G_M^2 \sin^2\frac{\theta_e}{2}\right], \tag{1.48}$$

In the nonrelativistic limit ($Q^2 \to 0$) in which the target nucleus has no recoil energy, we have $\tau \to 0$ and $E_e'/E_e \to 1$. Therefore, the above equation becomes

$$\left(\frac{d\sigma}{d\Omega}\right)_{\text{Lab}} = \left(\frac{d\sigma}{d\Omega}\right)_{\text{Mott}} \left(G_E(Q^2)\right)^2, \tag{1.49}$$

where the Mott cross section is given by

$$\left(\frac{d\sigma}{d\Omega}\right)_{\text{Mott}} = \frac{\alpha^2}{4E_e^2 \sin^4(\theta_e/2)} \cos^2\frac{\theta_e}{2}, \tag{1.50}$$

assuming that the velocity of the electron is still close to c even at this low energy limit. It can be shown from Equation 1.49 that within the nonrelativistic limit the electric form factor, $G_E(Q^2)$ ($= G_E(q^2)$), is the Fourier transform of the charge distribution, $\rho(\vec{x})$, within the nucleus [Hal84]. So,

$$G_E(\vec{q}) = \int \rho(\vec{x}) e^{i\vec{q}\vec{x}} d^3x, \tag{1.51}$$

where we replaced q^2 with three-momentum vector $\vec{q}$ because $q^2 \sim -|\vec{q}|^2$ in this limit. The function $\rho(\vec{x})$ is normalized so that

$$\int \rho(\vec{x}) d^3x = 1. \tag{1.52}$$

If $|\vec{q}|$ is small, the exponential in Equation 1.51 can be expanded,

$$G_E(\vec{q}) = \int \rho(\vec{x})(1 + i\vec{q}\cdot\vec{x} - \frac{(\vec{q}\cdot\vec{x})^2}{2} + ...)d^3x. \tag{1.53}$$

The mean-square charge radius is defined as

$$\langle r_c^2 \rangle = \int r^2 \rho(\vec{x}) d^3x, \tag{1.54}$$

where $r \equiv |\vec{x}|$. It can be shown using Equations 1.54 and 1.52 that G_E in Equation 1.53 becomes

$$G_E(q^2) \sim 1 - \frac{1}{6}|q|^2 \langle r_c^2 \rangle + \cdots, \tag{1.55}$$

From Equation 1.55, $\langle r_c^2 \rangle$ is given by

$$\langle r_c^2 \rangle \;=\; 6\left(\frac{d\,G_E(q^2)}{d(q^2)}\right)_{q^2=0} \tag{1.56}$$

with the boundary condition for the proton that $G_E(q^2) = 1$, and for the neutron $G_E(q^2) = 0$. Note that in the non-relativistic limit, $|\vec{q}|^2 \sim -q^2$. From Equation 1.56, $\langle r_c^2 \rangle$ represents the slope of $G_E(q^2)$ at the origin. The measured value of $\langle r_c^2 \rangle$ serves as a constraint on the behavior of the electric form factor at small values of q^2. Many experiments on the measurements of the charge radius of the neutron, $\langle (r_c^n)^2 \rangle$, have been performed. For example, Kopecky *et al.* [Kop97] measured the neutron-electron scattering length, b_{ne} by scattering low-energy neutron from heavy atoms. The value of $\langle (r_c^n)^2 \rangle$ determined from the measured value of $b_{ne} = (-1.33 \pm 0.04) \times 10^{-3}$ (fm) for a ^{208}Pb target is $\langle (r_c^n)^2 \rangle = -0.112 \pm 0.003(\text{fm})^2$. The negative value of $\langle (r_c^n)^2 \rangle$ indicates that the core of the neutron is slightly positive while volume near the surface

is slightly negative. The measured value of $(r_c^n)^2$ imposes a restriction on the slope of G_E vs Q^2, as is clear in Equation 1.56.

Similarly for $\langle r_c^2 \rangle$, one can obtain in the non-relativistic limit an expression for the mean-square magnetization radius, $\langle r_m^2 \rangle$,

$$\langle r_m^2 \rangle = \frac{6}{\mu} \left(\frac{d\, G_M(q^2)}{d(q^2)} \right)_{q^2=0}, \tag{1.57}$$

where μ is the nucleon magnetic moment (values of μ are given in Table 1.1).

1.4 Previous measurements of G_E^n and G_M^n

Because targets of free neutrons are not in reach of current technology, deuteron and helium-3 targets have been used for measurements of $\mathrm{G}_E(\mathrm{Q}^2)$ and $\mathrm{G}_M(\mathrm{Q}^2)$ of the neutron, $G_E^n(\mathrm{Q}^2)$ and $G_M^n(\mathrm{Q}^2)$, respectively. We summarize below the techniques and the results of the previous measurements of G_E^n and G_M^n.

1.4.1 Elastic scattering of electrons from the deuteron

Deuteron targets were used in the early measurements of G_E^n, which was determined from measurements of the deuteron structure function $A(Q^2)$. The cross section for the unpolarized elastic electron-deuteron scattering is given by the Rosenbluth formula,

$$\left(\frac{d\sigma}{d\Omega} \right)_{\mathrm{Lab}} = \left(\frac{d\sigma}{d\Omega} \right)_{\mathrm{Mott}} \left[A(Q^2) + B(Q^2) \tan^2 \frac{\theta}{2} \right], \tag{1.58}$$

where $A(Q^2)$ and $B(Q^2)$ are deuteron structure functions. $A(Q^2)$ is given by

$$A(Q^2) \;=\; G_C^2(Q^2) + \frac{8}{9}\tau^2 G_Q^2(Q^2) + \frac{2}{3}\tau G_M^2(Q^2)(1+\tau), \tag{1.59}$$

where τ is given in Equation 1.41 with M being the deuteron mass. The functions G_C, G_Q, and G_M in Equation 1.59 are the charge, quadrupole, and magnetic form factors of the deuteron, respectively, and each contains a term involving the isoscaler electric form factor, $G_{ES} = (G_E^p + G_E^n)/2$. Therefore, G_E^n can be determined from measurements of A(Q^2). The sum of the first and second terms in Equation 1.59 is dominant at least until Q^2=1.0 (GeV/c)^2 [Pla90]. The form factors of G_C and G_Q are given by

$$G_C = (G_E^p + G_E^n)\, C_E \qquad \text{and} \tag{1.60}$$

$$G_Q = (G_E^p + G_E^n)\, C_Q, \tag{1.61}$$

where C_E and C_Q are structure integrals involving deuteron wave functions ($u(r)$ for the S-state, and $w(r)$ for the D-state). They are given by

$$C_E = \int \left(u^2(r) + w^2(r)\right)\, j_0\left(\frac{qr}{2}\right)\, dr \tag{1.62}$$

$$C_Q = \frac{3}{\tau\sqrt{2}} \int \left(u(r)w(r) - \frac{w^2(r)}{\sqrt{8}}\right)\, j_2\left(\frac{qr}{2}\right)\, dr, \tag{1.63}$$

where $j_0(qr/2)$ and $j_2(qr/2)$ are spherical Bessel functions. To determine G_E^n using this technique, contributions to the electron-deuteron elastic scattering cross section from $B(Q^2)$ and the proton electric form factor must be taken into account. In addition, $A(Q^2)$ must be corrected for relativistic and MEC effects. The G_E^n was measured up to 0.8 (GeV/c)^2 by Platchkov*et al.* [Pla90] using this technique and the dipole parameterization for the proton form factor.

This technique has a large theoretical uncertainty because the value for G_E^n strongly depends on the choice of the model of the deuteron wave functions that are in Equations 1.62 and 1.63. Furthermore, this method cannot be used at higher Q^2 values ($Q^2 > 1$ (GeV/c)^2) because theoretical calculations of relativistic and MEC effects become less reliable.

Galster *et al.* [Gal71] also determined G_E^n up to Q^2=0.51 (GeV/c)^2 using this technique and obtained a fit of the G_E^n world data including their results for G_E^n. The best fit for the range 0.0 < (GeV/c)^2< Q^2< 1.0 (GeV/c)^2 gives the following parameterization for G_E^n [Gal71],

$$G_E^n = -\mu_n \left(\frac{\tau}{1 + p\tau} \right) G_D, \tag{1.64}$$

where $G_D = (1 + Q^2/0.71)^{-2}$ is the dipole parameterization for G_E^p which will be discussed in detail in Section 2.1.1, and the parameter p obtained is $p = 5.6$ with a nucleon-nucleon potential of Feshbach-Lomon [Lom67]. Although the data were fitted up to $Q^2 \sim$ 1.0 (GeV/c)^2, this parameterization is often used to estimate the G_E^n values at higher Q^2.

1.4.2 Inclusive electron-deuteron quasielastic scattering

Values for $(G_E^n)^2$ have been determined from inclusive quasielastic electron-nucleon *(e-N)* scattering from a deuteron target [Bar73, Lun93]. Because only the scattered electrons were detected in these experiments, the measured cross sections were due to the collective effects of electron-proton *(e-p)* and electron-neutron *(e-n)* quasielastic scattering. To obtain cross sections solely due to *(e-n)* quasi-elastic scattering, the contribution to the cross section from the *(e-p)* scattering had to be subtracted. The Rosenbluth separation technique was applied in these studies. Rosenbluth [Ros50] calculated the cross section for the elastic electron scattering from the proton at high energy, as given in Equation 1.48. The proton contribution was subtracted from the measured cross section and the Rosenbluth separation was done to determine $(G_E^n)^2$ at different Q^2 values. Let us consider Equation 1.48 once again. One can perform several measurements of the cross section at a fixed Q^2 value

by changing the scattering angle θ_e and the beam energy while keeping the relation of Q^2 in Equation 1.14 constant. From Equations 1.48 and 1.50, we have

$$\frac{\left(\frac{d\sigma}{d\Omega}\right)_{\rm Lab}}{\left(\frac{d\sigma}{d\Omega}\right)_{\rm Mott}} = AX + B, \tag{1.65}$$

where the variable X is $X = \tan^2(\theta_e/2)$, and the constants A (slope) and B (intercept) are $A = 2\,\tau G_M^2$ and $B = (G_E^2 + \tau G_M^2)/(1+\tau)$, respectively. Lung *et al.* [Lun93] measured $(G_E^n/G_D)^2$ from Q^2=1.75 to 4.00 (GeV/c)^2 using the following form for the reduced cross section,

$$\sigma_R \equiv \frac{\left(\frac{d\sigma}{d\Omega}\right)_{\rm Lab}}{\left(\frac{d\sigma}{d\Omega}\right)_{\rm Mott}} (1+\tau)\,\epsilon = R_T + \epsilon\, R_L, \tag{1.66}$$

where the variable ϵ is the longitudinal polarization of the virtual photon, which is given by $\epsilon = [1+2(1+\tau)\tan^2(\theta_e)]^{-1}$. The R_T (R_L) in Equation 1.66 is the transverse (longitudinal) response function; it is proportional to the sum of electric (magnetic) form factors of the proton and neutron,

$$R_T = \tau\left[(G_E^p)^2 + (G_E^n)^2\right]\, I(W^2, Q^2) \tag{1.67}$$

$$R_L = \left[(G_M^p)^2 + (G_M^n)^2\right]\, I(W^2, Q^2), \tag{1.68}$$

where $I(W^2, Q^2)$ is an integral over the deuteron $S-$ and $D-$state wave functions, and W^2 is the invariant mass squared. Because ϵ is the only variable in Equation 1.66, the Rosenbluth separation using a linear fit function gives R_T and R_L for each value of ϵ. To determine the value for $(G_E^n/G_D)^2$, the proton contribution was determined from their proton form factor measurements, and was subtracted from R_T. The data were fitted with model calculations to give the results of $(G_E^n/G_D)^2$. Because this technique gives results which have strong model dependence, the results of $(G_E^n/G_D)^2$ have large systematic uncertainties. In addition, the accuracy of $(G_E^n/G_D)^2$ determined using the Rosenbluth technique is limited because the relation $(G_E^n)^2 \ll \tau(G_M^n)^2$ holds especially at large Q^2. The values for $(G_E^n/G_D)^2$

determined in these experiments are consistent with zero, and also with the Galster parameterization.

1.4.3 Double polarization technique I – Recoil polarimetry

It was suggested [Akh74, Arn81] that the G_E^n can be determined from the measurement of the polarization components of the recoil neutron in elastic scattering of longitudinally polarized electrons from a *free* neutron target. In reality, the neutron is always bound inside a nucleus. Therefore, the use of nuclear targets such as ^{2}H and ^{3}He, where the application of the plane wave impulse approximation (PWIA) is reasonably accurate, was important for the development and eventual use of this technique. In the PWIA, the recoil neutron has sideways and longitudinal polarization components in the scattering plane, which is defined as the plane containing both the incident and scattered electron momentum vectors. The components of the neutron polarization vector are defined relative to the neutron momentum vector. The longitudinal component of the polarization vector is along the momentum vector, and the sideways component is perpendicular to the momentum direction and in the electron the scattering plane. The G_E^n can be determined from measurements of scattering asymmetry, ξ, of the neutron in a polarimeter. In a neutron polarimeter with the scattering plane perpendicular to the electron scattering plane, the measured asymmetry is proportional to neutron's sideways polarization component, P'_S.

$$D_{LS'} \equiv \frac{P_{S'}}{P_e} \quad = \quad \frac{\xi}{\langle A_y \rangle P_e}, \tag{1.69}$$

where P_e is the electron beam polarization, and $\langle A_y \rangle$ is the analyzing power for neutron-nucleus scattering averaged over the acceptance of the polarimeter. The $D_{LS'}$ is the longitudinal-to-sideways electron-neutron polarization transfer coefficient.

It is given by

$$D_{LS'} = \frac{(G_E^n/G_M^n)K_1(\theta_e, Q^2)}{K_2(\theta_e, Q^2) + (G_E^n/G_M^n)^2}, \quad (1.70)$$

where $K_1(\theta_e, Q^2)$ and $K_2(\theta_e, Q^2)$ are kinematic factors [Ede94] that depend on θ_e and Q^2. Therefore, a measurement of ξ with known $\langle A_y \rangle$ and P_e yields the ratio of G_E^n/G_M^n. The advantage of this technique is that the sideways polarization is insensitive to nuclear effects such as meson exchange currents (MEC), final state interactions (FSI), and isobar configurations (IC), and the choice of the deuteron wave functions [Are87]. [The following three nuclear effects are considered: (1) FSI: the nucleons (the proton and the neutron) may interact after the electrodisintegration of the deuteron, and that causes *rescattering* of the neutron. (2) MEC: the virtual photon may couple to a virtual meson that is exchanged between the nucleons. (3) IC: the virtual photon may couple to the virtual excitation of the nuclear resonances.]

This recoil polarization transfer technique became a practical alternative as polarized electron beams became available at electron-beam accelerator facilities. To perform such an experiment, a liquid-deuterium (LD_2) target is used. Longitudinally polarized electrons are scattered quasielastically from a neutron in a LD_2 target. The pioneering experiment using this technique was performed by Madey *et al.* at the Bates Linear Accelerator Center in early 90's [Ede94]. In that seminal work, G_E^n was measured at Q^2=0.255 (GeV/c)^2 using the $^2\mathrm{H}(\vec{e}, e'\vec{n})^1\mathrm{H}$ reaction. While this first experiment demonstrated the feasibility of using the recoil polarization technique to determine the ratio of G_E^n/G_M^n, there was clear room for improvements. Because of the low (0.8%) duty factor of the electron beam of Bates, the measurement had a large statistical uncertainty. In addition, the systematic uncertainty in their result is large mainly because of the relatively large systematic uncertainty (about 11%) in their measurement of the average analyzing power of the polarimeter.

Clearly, the ratio of G_E^n/G_M^n can be determined with much smaller systematic uncertainty by measuring the *ratio* of the recoil polarization components, $P_{S'}/P_{L'}$. The reduced systematic uncertainty is a result of the cancellation of the analyzing power at the polarimeter and the electron beam polarization in the ratio. To obtain information on $P_{L'}$, the neutron polarization must be precessed through some angle about an axis perpendicular to the electron scattering plane. A dipole magnet can be located in front of the neutron polarimeter to precess the neutron polarization vector through an angle χ before the neutron enters the polarimeter. If the neutron polarization vector is precessed by $\chi = +90°$, then the longitudinal component becomes the *transverse* component and is measured by the polarimeter. Therefore, the scattering asymmetry, ξ_{90}, with the spin precession through 90°is proportional to $P_{L'}$. Because the scattering asymmetry, ξ_0, with *no* spin precession is proportional to $P_{S'}$, the ratio $P_{S'}/P_{L'}$ becomes equal to ξ_0/ξ_{90}. This technique yields small systematic uncertainties because the ratio of the neutron polarization components is insensitive to the electron beam polarization and to the polarimeter analyzing power. Also, other uncertainties are minimized in the ratio.

This improved technique was employed in the Mainz experiments [Ost99, Her99] as well as in our JLab E93-038 experiment [Mad03]. The details of this technique are given later in section Section 1.7. The Mainz experiments measured G_E^n at Q^2=0.15 and 0.34 $(GeV/c)^2$.

1.4.4 Double polarization technique II – Polarized targets

Values for G_E^n have been extracted from electron-neutron quasielastic scattering experiments using a polarized ^{2}H or ^{3}He target and a longitudinally polarized electron beam, which only became available in recent years. Suppose the polarization of a

free neutron in the target has a polar angle Θ and an azimuthal angle φ, as shown in Figure 1.2, then the asymmetry for scattering, A, of longitudinally polarized

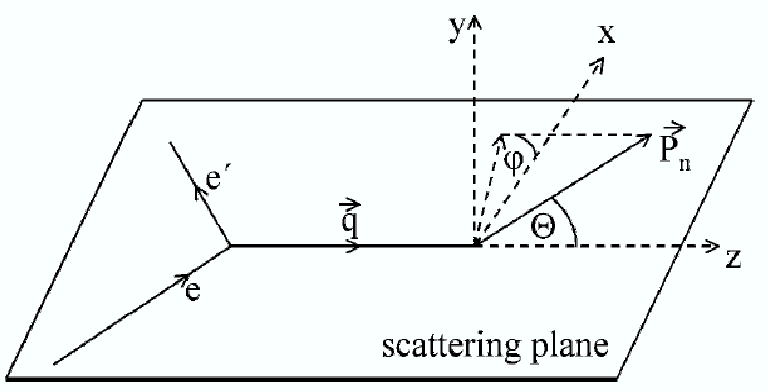

Figure 1.2: Definition of the target polarization angles. Θ is the polar angle between the target polarization P_n and $\vec{q}$. The azimuthal angle φ is the out-of-plane angle measured from the x-axis, which is in the scattering plane. The figure is from [Bec99].

electrons from a *free* polarized neutron at rest, is given by [Don86]

$$A = P_e P_n f \frac{a \sin\Theta \cos\varphi \, G_E^n G_M^n + b \cos\Theta \, (G_M^n)^2}{c \, (G_E^n)^2 + d \, (G_M^n)^2} \tag{1.71}$$

$$= A_\perp \sin\Theta \cos\varphi + A_\parallel \cos\Theta, \tag{1.72}$$

where f is the dilution factor, which is caused by the materials in the target that contain unpolarized neutrons. The kinematic factors a, b, c, and d are given by

$$a = -2\sqrt{\tau(1+\tau)} \tan(\frac{\theta_e}{2}) \tag{1.73}$$

$$b = -2\tau \sqrt{1 + \tau + (1+\tau)^2 \tan^2(\frac{\theta_e}{2})} \tan(\frac{\theta_e}{2}) \tag{1.74}$$

$$c = 1 \tag{1.75}$$

$$d = \tau + 2\tau(1+\tau)\tan^2(\theta_e/2)], \tag{1.76}$$

and $A_\perp$ is the asymmetry when the target polarization vector is in the scattering plane and is perpendicular to $\vec{q}$ ($\Theta = 90°$,$\varphi = 0°$), and $A_\parallel$ is the asymmetry when it is

parallel to $\vec{q}$ ($\Theta = 0^\circ$). The vector $\vec{q}$ is the three-component momentum transfer vector, and is the momentum vector of the recoil neutron in electron-neutron quasielastic scattering kinematics. The value of G_E^n can be extracted from the measurement of $A_\perp$, which is given by

$$A_\perp = P_e P_n f \frac{-2\sqrt{\tau(\tau+1)}\tan(\theta_e/2) G_E^n G_M^n}{(G_E^n)^2 + (G_M^n)^2 \tau[1 + 2(1+\tau)\tan^2(\theta_e/2)]} \tag{1.77}$$

Because $A_\perp$ contains the interference term, $G_E^n\, G_M^n$, the ratio G_E^n/G_M^n can be written from Equation 1.77 in terms of $A_\perp$, P_e, P_n, f and the kinematic factors. Therefore, a measurement of the asymmetry, $A_\perp$ yields the ratio G_E^n/G_M^n. However, because Equation 1.77 is valid for a *free* neutron target, corrections for nuclear effects must be made to obtain the final value of G_E^n. So far, the measurements of G_E^n using this technique have been performed at NIKHEF [Pas99] and Jefferson Lab [Zhu01, War04] using a polarized deuteron target. In these measurements, longitudinally polarized electrons interact with polarized neutrons in a polarized ^{2}H target, and e-n quasielastic scattering experiments were performed to measure the beam-target asymmetry. The NIKHEF (JLab) experiment measured G_E^n at Q^2=0.21(GeV/c)^2(Q^2=0.5 and 1.0 (GeV/c)^2).

In this technique, the dilution factor, f must be determined before a value for G_E^n/G_M^n can be obtained. The experimental asymmetry ϵ is given by [Are88, Are95]

$$\epsilon = f \frac{P_e A_e + P_e P_1^d A_{ed}^V + P_e P_2^d A_{ed}^T}{1 + P_1^d A_d^V + P_2^d A_d^T}, \tag{1.78}$$

where P_1^d (P_2^d) is the target vector (tensor) polarization, respectively. The A_e is the asymmetry due to the electron beam, A_d^V and A_d^T are the vector and tensor deuteron target asymmetries, and A_{ed}^V (A_{ed}^T) is the vector (tensor) beam-target asymmetries. For the target with the polarization vector in the scattering plane, Equation 1.78

reduces to

$$\epsilon = f \frac{P_e P_1^d A_{ed}^V}{1 + P_2^d A_d^T}. \tag{1.79}$$

In the JLab experiment, a frozen deuterated ammonia target, $^{15}ND_3$ was used. The target consisted of ammonia granules immersed in liquid helium. The target temperature was maintained at 1 K by a ^{4}He evaporation refrigerator. A 5 T magnetic field provided by a superconducting coil was used to polarize the target. The direction of the magnetic field lied in the horizontal plane, and was perpendicular to the the mean $\vec{q}$. The average target polarization during the measurements was $P_1^d = 0.21 \pm 0.01$. In this experiment, the experimental asymmetry was diluted because the electrons did not always scatter from the polarized neutrons, but from materials such as the nitrogen in $^{15}ND_3$, the liquid helium, the NMR coils and target windows. A Monte Carlo simulation program was used to determine the dilution factor, f, and to correct for the detector acceptance averaging of the theoretical asymmetries.

The ratio of G_E^n/G_M^n can be measured from the ratio of the $A_\perp$ to $A_\parallel$. From Equation 1.71, it is given by

$$\frac{A_\perp}{A_\parallel} = \frac{1}{\sqrt{\tau + \tau(1+\tau)^2 \tan^2(\frac{\theta_e}{2})}} \frac{G_E^n}{G_M^n}. \tag{1.80}$$

Therefore, after $A_\perp$ and $A_\parallel$ are measured independently by selecting the target polarization angles Θ and φ, the ratio of the form factors, G_E^n/G_M^n, is obtained from Equation 1.80, assuming a *free* neutron target. The advantage of this ratio technique is that the result is insensitive to the uncertainty in the measurement of the beam polarization and target polarization as well as the uncertainty in the dilution factor which is caused by the electrons scattering from neutrons in the target materials other than the polarized compound.

So far, all the measurements of G_E^n using this ratio technique with polarized targets were performed with polarized ^{3}He targets at Mainz using the Mainz Microtron (MAMI) accelerator. When ^{3}He is polarized, the spins of the two protons in ^3He cancel out as they point in opposite directions. Thus, the polarization of the ^{3}He nucleus is effectively due to the neutron spin direction. Using this technique and polarized ^{3}He targets, G_E^n for Q^2 up to 0.67 $(GeV/c)^2$ have been extracted [Mey94, Bec99, Roh99, Ber03, Gol01]. There have been two determinations of G_E^n made by measuring $A_\perp$ only using a polarized deuterium target. These measurements were made at NIKHEF with a polarized gas target at Q^2=0.21$(GeV/c)^2$ [Pas99], and at JLab with a polarized deuterated ammonia target at Q^2=0.5 and 1.0$(GeV/c)^2$ [Zhu01, War04].

1.4.5 Theoretical analysis of *ed* elastic scattering data

Schiavilla and Sick [Sch01] recently analyzed existing e-d elastic scattering data for the purpose of determining G_E^n over a wide range of Q^2 values from the measured deuteron quadrupole form factor, $F_{C2}(Q^2)$. The $F_{C2}(Q^2)$ was chosen because it is mostly due to the long-range π-exchange operator up to $Q^2 \sim 1.7(GeV/c)^2$, and the calculation of the $F_{C2}(Q^2)$ is less sensitive to the short-range two-body currents which are not well under control. Thereby, calculated value of $F_{C2}(Q^2)$ is only slightly model dependent. The theoretical values of $F_{C2}(Q^2)$ assuming G_E^n=0 are significantly different from the data for $F_{C2}(Q^2)$ for the Q^2 up to 1.7 $(GeV/c)^2$. Thus, non-zero values for G_E^n contribute to the $F_{C2}(Q^2)$. They determined the values for G_E^n from Q^2=0.01$(GeV/c)^2$ to Q^2=1.7$(GeV/c)^2$.

1.4.6 Previous measurements of G_M^n

Because we measured the ratio of G_E^n/G_M^n, the value of G_M^n is needed to determine G_E^n. We summarize the previous measurements of G_M^n in this subsection. Until recently, G_M^n was measured by the inclusive quasielastic electron-deuteron scattering [Roc82, Lun93]. However, similar to the determination of G_E^n from this reaction, contributions from the electron interaction with the proton to the cross section must be subtracted. Therefore, the uncertainty in these results is large because the values depend on the choice of the theoretical model of the deuteron wave function. The G_M^n was also determined from the exclusive cross section measurement of electron-neutron coincidence from the $^2\mathrm{H}(\vec{e}, e'\vec{n})$ reaction [Bar69, Bar72, Mar93]. The main difficulty with this type of measurement is the determination of the absolute efficiency of the neutron detectors. To reduce the sensitivity to the nuclear structure function, the cross-section ratio of $^2\mathrm{H}(\vec{e}, e'\vec{n})$ to $^2\mathrm{H}(\vec{e}, e'\vec{p})$ can be evaluated. The G_M^n determined using this technique has a small systematic uncertainty (a few percent or less) [Ank94, Bru95, Ank98, Kub02]. Recently, polarized ^3He targets were also used to measure G_M^n from inclusive quasielastic scattering of polarized electrons [Gao94, Xu00, Xu03]. In the E93-038 experiment, we used the G_M^n values obtained from the fit to the world data [Kel02] to determine G_E^n from the measured ratio of G_E^n/G_M^n. The G_M^n data points used for the fit were [Mar93, Bru95, Ank94, Ank98, Kub02, Lun93, Roc82, Xu00]. The details about the fitting and data selection are given in [Kel02]. These data points are plotted in Figure 1.3. The values for G_M^n that we used in our analysis are given in Chapter 8.

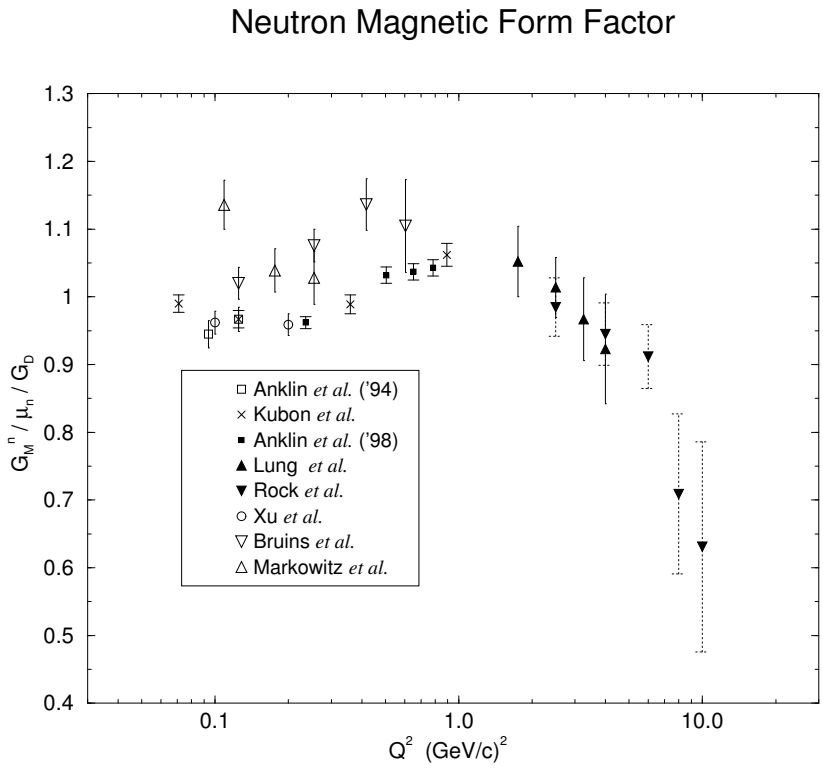

Figure 1.3: G_M^n world data points used for fitting to obtain G_M^n values for E93-038 data analysis. See text for detail.

1.5 Motivation for the Experiment

The nucleon electromagnetic (EM) form factors are fundamental quantities which contain crucial information on the internal structure of the nucleon. The electric (magnetic) form factor is related to the charge (magnetization) density inside a nucleon in the non-relativistic limit as discussed in Section 1.3. The precise values of the EM form factors serve as an important test of QCD models that describe the structure of nucleons. Furthermore, the form-factor data are used for determination of the strange content of the proton by parity violating electron-proton elastic scattering [Mus94].

The proton and neutron form factors have been measured since three decades ago at a variety of the electron beam facilities. Probing the structure of the nucleon from the electron scattering has been successful because the interaction between an electron and a nucleon is small (1/137) so that the electron does not disturb the structure of the nucleon. Proton form factors are well known compared to neutron form factors. The electric form factor of the proton, G_E^p, has been measured up to Q^2=9 (GeV/c)^2, and the magnetic form factor of the proton, G_M^p, up to 30 (GeV/c)^2. (See the article by Gao[Gao03] for a review on the nucleon EM form factors.) Neutron form factor measurements are more difficult than the proton form factor measurements because of a lack of a free neutron target. For a measurement of neutron form factors (G_E^n and G_M^n), a composite target such as a deuteron or ^{3}He target must be used. Therefore, contribution from other nucleon(s) in the target must be subtracted. In addition, the value for G_E^n is small because the neutron has no net charge. In fact, the measured quantity involving G_E^n is often dominated by the much larger G_M^n value. This situation makes the determination of G_E^n difficult. Therefore, G_E^n is the most difficult one to measure among the four nucleon form factors, and it is indeed poorly known. By the time our experiment started in September 2000, G_E^n data for Q^2>0.6 (GeV/c)^2 had very large uncertainties. Although the Rosenbluth separation technique was often used to measure G_E^n, this technique gave rather large uncertainties as described in Section 1.4. So, our collaboration proposed a measurement based on the polarization transfer technique.

As we mention in the next section, two of our three measurements of G_E^n are at Q^2 values above 1(GeV/c)^2. Such new G_E^n data with small uncertainties at relatively higher Q^2 values are important for developing QCD models of the nucleons. Furthermore, distributions of the charge and magnetization densities inside a nucleon

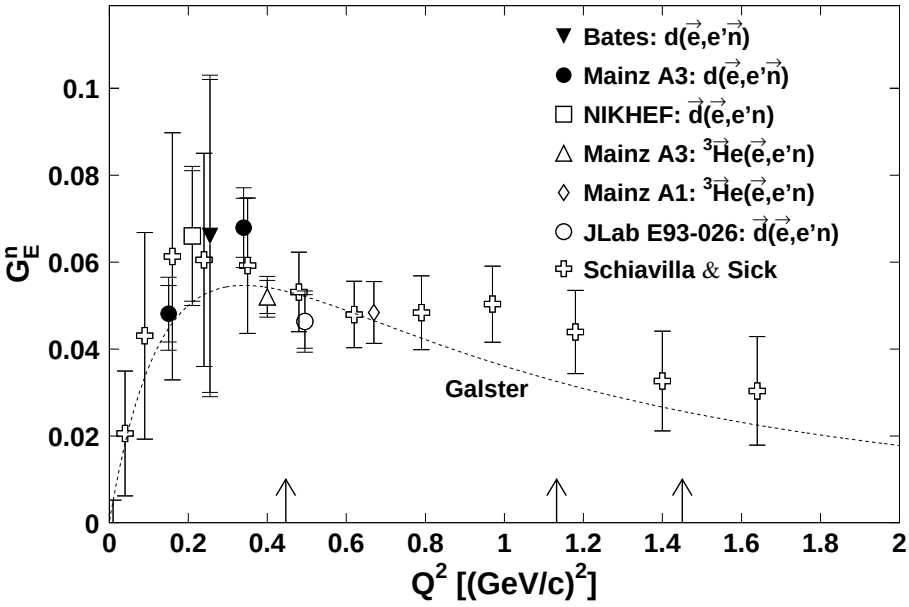

Figure 1.4: World data of G_E^n (without JLab E93-038 data points). Plotted data points are Bates [Ede94], Mainz A3 (LD_2) [Her99, Ost99], NIKHEF [Pas99], Mainz A3 ($^3\vec{He}$) [Bec99, Gol01], Mainz A1 [Ber03, Roh99], JLab E93-026 [Zhu01], and Schiavilla and Sick [Sch01]. The dashed line is the Galster parameterization [Gal71]. The arrows on the horizontal axis indicate the Q^2 values for the JLab E93-038 measurements, which are $\langle Q^2 \rangle$ =0.45, 1.13, and 1.45(GeV/c)^2.

can be determined from the form factor data [Kel02].

1.6 Experiment 93-038 at Jefferson Laboratory

The Jefferson Lab E93-038 collaboration [Mad99] measured the ratio of the electric form factor to magnetic form factor of the neutron via recoil polarimetry [Mad95] from the quasi-elastic $^2\mathrm{H}(\vec{e}, e'\vec{n})^1\mathrm{H}$ reaction. By measuring the ratio of G_E^n to G_M^n by employing the recoil polarization technique, we were able to measure G_E^n with small uncertainties. Details of the experimental technique will be discussed in Chapter 4.

The experiment was performed in Hall-C of the Continuous Electron Beam Accelerator Facility (CEBAF) at the Thomas Jefferson National Accelerator Facility (TJNAF). The experiment ran from September 2000 to April 2001. The data were taken at nominal central Q^2 values of 0.447, 1.140, 1.169 and 1.474 $(GeV/c)^2$. The values of key kinematics quantities for our measurements at Q^2= 0.447 and 1.14 $(GeV/c)^2$ are listed in Table 1.2. Because the beam energy for the measurements at Q^2=1.14 $(GeV/c)^2$ data was changed slightly at one point during the data accumulation, two sets of kinematics values are listed in the table for this Q^2. We call the kinematics sets kin1, kin2a, kin2b, kin2c and kin3, respectively. The data at Q^2=1.14

	Q^2 $(GeV/c)^2$	E_0 (GeV)	θ_e (degrees)	P_e (MeV/c)	P_n (MeV/c)	T_n (MeV)
(kin1)	0.447	0.884	52.65	643.	711.	239.
(kin2a)	1.136	2.326	30.930	1718.	1227.	606.
(kin2b)	1.140	2.335	30.849	1725.	1230.	608.
(kin2c)	1.169	2.415	30.148	1789.	1249.	624.
(kin3)	1.474	3.395	23.55	2606.	1448.	786.

Table 1.2: Kinematics values for E93-038 data points. E_0 is the energy of the electron beam, θ_e is the scattering angle of the electron, P_e is the momentum of the scattered electron, P_n is the momentum of the recoil neutron and T_n is the kinetic energy of the recoil neutron.

$(GeV/c)^2$ (average of kin2a and kin2b) and 1.169 $(GeV/c)^2$ (kin2c) are statistically weighted averaged to give the results at Q^2=1.15 $(GeV/c)^2$. In addition, the values of Q^2 are averaged over the detector acceptance as will be discussed in Chapter 6. Therefore, Jlab E93-038 collaboration reports the values for G_E^n/G_M^n and G_E^n at

the *acceptance-averaged* Q^2 values of $\langle Q^2 \rangle$= 0.45,1.13 and 1.45 (GeV/c)^2. [3] Our measurements at $\langle Q^2 \rangle$=1.13 and 1.45 (GeV/c)^2 will provide a new insight on the internal structure of the neutron. Our measurement at $\langle Q^2 \rangle$=0.45 (GeV/c)^2 serves as a consistency check with the world data. For this dissertation, the data analyses at $\langle Q^2 \rangle$=0.45 (GeV/c)^2 (kin1) and 1.13 (GeV/c)^2 (kin2a and kin2b) have been performed, and they are discussed in this thesis.

1.7 Recoil Polarization Technique

In this section, we present basic equations for G_E^n/G_M^n and G_E^n based on the plane-wave-impulse-approximation (PWIA) with a *free* neutron target. Because a LD_2 target was used to perform this experiment, the formulas for G_E^n/G_M^n and G_E^n given in this section *cannot be used* to determine our final results. Nonetheless, those formula can give an insight on how values of G_E^n/G_M^n and G_E^n are related with other physics quantities in this approximation. Because a deuteron is a composite nucleus, the neutron in a deuteron cannot be treated as a *free* nucleon; therefore, some nuclear physics effects must be accounted for in our analysis. They are accounted for using Monte-Carlo simulations that are based on the model calculations of electro-disintegration of the deuteron by Arenhövel *et. al* [Are88, Lei91, Are95]. The final results are obtained by comparing the measured data with the simulated values. We will not discuss in this section details about this final analysis. It will be left until Chapter 6.

[3] We deal with the nominal central Q^2 values until Chapter 6 where we discuss how to obtain the values for $\langle Q^2 \rangle$. In Chapters 7 and 8, $\langle Q^2 \rangle$ is always used.

1.7.1 Advantages of the Recoil Polarization Technique

It was suggested [Akh74, Arn81] that the the ratio of the form factors, G_E^n/G_M^n, can be measured via recoil polarimetry. Consider the elastic scattering of a longitudinally polarized electron from a *free* neutron target. One of the advantages of this ratio technique is that the systematic uncertainty is small because G_E^n/G_M^n is insensitive to the beam polarization and the analyzing power. Because the neutron in our LD_2 target is inside a deuteron nucleus, the data analysis must include the nuclear physics effects such as FSI, MEC, and IC. However, for quasielastic electron-neutron scattering, both polarization components are *insensitive* to those nuclear effects [Are87, Are02]. Therefore, the ratio of the polarization components, which is measured in our double-polarization experiment, is also insensitive to them.

1.7.2 Basic Equations for the Impulse Approximation

Upon interaction in the target, the polarization of the electron is transfered to the recoil neutron. In the plane-wave-impulse-approximation (PWIA) for electron-neutron elastic scattering, the polarization vector of the recoil neutron lies in the scattering plane [Dom69]. In PWIA, it is assumed that the plane waves of the initial electron and neutron wave functions are not distorted upon interaction, and therefore their final wave functions can also be described by plane waves. In addition, each nucleon in the target nucleus has independent current and charge distributions, and exchange currents between nucleons are neglected. In our case, a single photon emitted by the incident electron couples to the neutron in a deuteron, and all the momentum transfered by the electron goes to the neutron only, i.e., the proton is merely a spectator in the collision.

The polarization vector of the recoil neutron has sideways ($P_S^{'}$) and longitudinal ($P_L^{'}$) polarization components in the scattering plane. We consider longitudinal-to-sideways ($D_{LS'}$) and longitudinal-to-longitudinal ($D_{LL'}$) polarization transfer coefficients. They are defined as

$$D_{LS'} \equiv \frac{P_S^{'}}{P_e} \tag{1.81}$$

$$D_{LL'} \equiv \frac{P_L^{'}}{P_e}, \tag{1.82}$$

where P_e is the polarization of the electron beam. These polarization coefficients and the form factors of the neutron satisfy the following equations [Arn81]:

$$I_0\, D_{LS'} = -K_S\, G_M^n\, G_E^n \tag{1.83}$$

$$I_0\, D_{LL'} = K_L\, (G_M^n)^2 \tag{1.84}$$

$$I_0 \equiv (G_E^n)^2 + K_0\, (G_M^n)^2\,, \tag{1.85}$$

where the kinematic factors K_S, K_L, and K_0, along with τ are given by:

$$K_S = 2\sqrt{\tau(1+\tau)}\tan(\theta_e/2) \tag{1.86}$$

$$K_L = 2\,\tau\sqrt{(1+\tau)(1+\tau\sin^2(\theta_e/2)\,)}\ \sec(\theta_e/2)\ \tan(\theta_e/2) \tag{1.87}$$

$$K_0 = \tau\,[\,1 + 2\,(1+\tau)\tan^2(\theta_e/2)] \tag{1.88}$$

Here, θ_e is the scattering angle of the electron, M_N is the mass of the neutron, and τ is given in Equation 1.41.

Although G_E^n appears in Equation 1.83, the RHS of this equation is dominated by G_M^n, because it is much larger than G_E^n. However, dividing Equation 1.83 by Equation 1.84 gives us the ratio of the form factors, which also becomes directly proportional to the ratio of the polarizations.

$$\frac{P_S^{'}}{P_L^{'}} \equiv \frac{D_{LS'}}{D_{LL'}} = -\left(\frac{K_S}{K_L}\right)\left(\frac{G_E^n}{G_M^n}\right), \tag{1.89}$$

where Equations 1.81 and 1.82 have also been used. Therefore, the ratio g in PWIA is given by

$$g \equiv \frac{G_E^n}{G_M^n} = -K_R \left(\frac{P_S^{'}}{P_L^{'}}\right) \quad (1.90)$$

$$= -K_R \left(\frac{D_{LS'}}{D_{LL'}}\right) \quad (1.91)$$

where

$$K_R \equiv \frac{K_L}{K_S} = \sqrt{\frac{\tau\left(1+\tau\sin^2\left(\frac{\theta_e}{2}\right)\right)}{\cos\left(\frac{\theta_e}{2}\right)}}. \quad (1.92)$$

It is clear from Equation 1.90 that the ratio of the form factors is equal to the ratio of the polarizations in PWIA. Equation 1.90 also suggests that $P_S^{'}$ and $P_L^{'}$ are proportional to G_E^n and G_M^n, respectively. Thus, that leads to much smaller $P_S^{'}$ than $P_L^{'}$. However, we stress again that Equations 1.89 and 1.90 are valid for a *free* neutron target. Therefore, these equations were not used in our analysis to determine values of G_E^n/G_M^n and G_E^n.

It is clear from Equations 1.81, 1.82, and 1.89, that the g in Equation 1.91 is not dependent on P_e, as it canceled in the ratio. In addition, as will be discussed in Chapter 4, the g in Equation 1.91 does not depend on the analyzing power of the reaction, A_y, as it cancels also in this ratio technique. This ratio technique leads to small systematic uncertainties in g, as will be discussed in Chapter 7. The detailed procedure for determining the ratio g and the advantages of this ratio technique will be discussed in detail in Chapter 4.

Chapter 2

Theoretical Models of Nucleon

2.1 Nuclear Models

Many nucleon models have been developed by theorists since several decades ago to understand the electromagnetic structure of the nucleon. A good nucleon model should be able to describe and predict the behavior of the electromagnetic form factors which are a function of Q^2. We discuss below several models for the nucleon form factors that have been developed.

2.1.1 Dipole Parameterizations

The dipole parameterization is a simple phenomelogical parameterization. The dipole parameterizations for the Sachs form factors G_E^p, G_M^p, and G_M^n are given as

follows.

$$G_E^p(Q^2) = \left(1+\frac{Q^2}{A}\right)^{-2} \equiv G_D \tag{2.1}$$

$$G_M^p(Q^2) = \mu_p G_D \qquad (\mu_p = 2.79284739) \tag{2.2}$$

$$G_M^n(Q^2) = \mu_n G_D \qquad (\mu_n = -1.9130428) \tag{2.3}$$

The parameter $A = 0.71(\mathrm{GeV/c})^2$ in Equation 2.1 is a purely empirical parameter. This parameterization describes the proton form factors rather well at low Q^2. See for example the results of G_E^p by Bosted *et al.* [Bos92], Höhler *et al.* [Hoh76], and Kirk *et al.* [Kir73]. The observed dipole parameterization for the proton corresponds to a charge distribution which decays exponentially with the radius r,

$$\rho(r) = \rho(0)e^{-ar}, \tag{2.4}$$

where the value of the parameter is $a = 4.27$ (fm^{-1}). The $\rho(0)$ is a normalization constant. From Equations 2.4 and 1.54, the mean-square radius can be calculated, and it is 0.81 (fm). Note that Equations 2.1 and 2.2 suggest that the ratio, G_E^p/G_M^p is a constant. However, the recent experiments from JLab show that this ratio decreases linearly as a function of Q^2 [Jon00, Gay02].

According to the dipole parameterization, $G_E^n(Q^2)$=0 for all values of Q^2 because the net charge of the neutron is zero. However, following an analogy with the proton, a *dipole parameterization for* G_E^n is often used.

$$G_E^n = -\tau(\mu_n G_D) = \frac{-\mu_n \tau}{\left(1+\frac{Q^2}{0.71}\right)^2} \tag{2.5}$$

This parameterization can be understood by assuming that the Dirac form factor vanishes for all Q^2, i.e., $F_1^n(Q^2) = 0$. With this assumption, we obtain $G_E^n = -\tau G_M^n$ from Equations 1.42 and 1.43, which is the same as Equation 2.5. However,

Equation 2.5 does not agree with the world data of G_E^n. Because of this problem, the Galster parameterization for G_E^n as given in Equation 1.64 has been used often to describe the measured values for G_E^n at Q^2 values below about $1(\mathrm{GeV/c})^2$.

2.1.2 Vector Meson Dominance

A model called the vector meson dominance (VMD) model [Sak69] was developed to describe the electromagnetic interaction. According to VMD, when a virtual photon interacts with a hadron, the photon transforms into one of the low-mass vector mesons (such as the ρ, ω, and ϕ mesons) that has the same quantum numbers as the photon. The virtual photon then interacts with the nucleon via *coupling with the vector mesons*. A diagram of the interaction of a nucleon with the electromagnetic field is shown in Figure 2.1. The amplitude for the interaction is the product of the

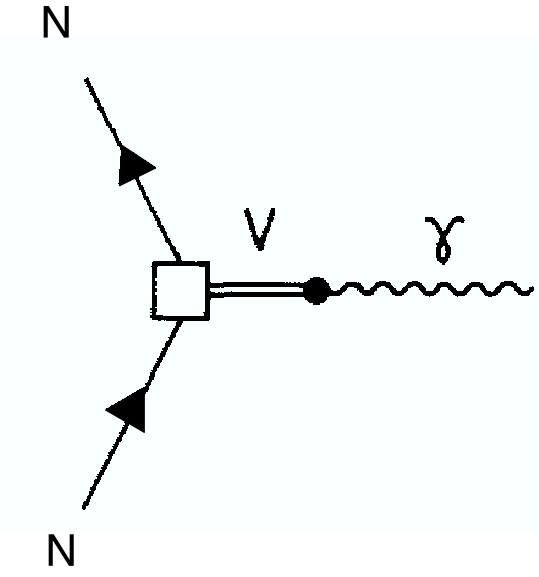

Figure 2.1: Interaction of a nucleon with the electromagnetic field.

electromagnetic coupling of the electron with the virtual photon at one vertex and

the strong nuclear coupling at the other vertex. In practice, the electromagnetic amplitudes are related to hadronic collision amplitudes.

In the model developed by Iachello *et al.* [Iac73], the contributions from the mesons, ρ, ω, and ϕ, are included. Assuming that vector mesons have zero width, the Dirac and Pauli isoscalar and isovector form factors in the low Q^2 region are written as a product of an intrinsic form factor $g(Q^2)$ and a term describing the interaction of the bare nucleon with the electromagnetic field: in the 1973 model of Iachello *et al.*, the Dirac and Pauli form factors are parameterized as follows, [Iac73],

$$F_1^S(Q^2) = \frac{e}{2} g(Q^2) \left[(1 - \beta_\omega - \beta_\phi) + \beta_\omega \frac{\mu_\omega^2}{\mu_\omega^2 + Q^2} + \beta_\phi \frac{\mu_\phi^2}{\mu_\phi^2 + Q^2} \right], \quad (2.6)$$

$$F_1^V(Q^2) = \frac{e}{2} g(Q^2) \left[(1 - \beta_\rho) + \beta_\rho \frac{\mu_\rho^2}{\mu_\rho^2 + Q^2} \right], \quad (2.7)$$

$$F_2^S(Q^2) = \frac{e}{2} g(Q^2) \left[(-0.120 - \alpha_\phi) \frac{\mu_\omega^2}{\mu_\omega^2 + Q^2} + \alpha_\phi \frac{\mu_\phi^2}{\mu_\phi^2 + Q^2} \right], \quad (2.8)$$

$$F_2^V(Q^2) = \frac{e}{2} g(Q^2) \left[3.706 \frac{\mu_\rho^2}{\mu_\rho^2 + Q^2} \right], \quad (2.9)$$

where the parameters $\beta_\rho, \beta_\omega, \beta_\phi, \alpha_\phi$ are the coupling constant for interaction between the meson and the photon, and μ_ρ, μ_ω, and μ_ϕ denote the mass of the ρ, ω, and ϕ meson, respectively. These coupling constants can be obtained from the experimental data for the e^+e^- decays of the vector mesons. The electromagnetic Sachs form factors can be expressed in terms of F_1^V, F_1^S, F_2^V, and F_2^S,

$$G_M^p(Q^2) = (F_1^V + F_1^S) + (F_2^V + F_2^S), \quad (2.10)$$

$$G_E^p(Q^2) = (F_1^V + F_1^S) + \frac{-Q^2}{4M^2}(F_2^V + F_2^S), \quad (2.11)$$

$$G_M^n(Q^2) = (F_1^S - F_1^V) + (F_2^S - F_2^V), \quad \text{and} \quad (2.12)$$

$$G_E^n(Q^2) = (F_1^S - F_1^V) + \frac{-Q^2}{4M^2}(F_2^S - F_2^V). \quad (2.13)$$

2.1.3 Gari-Krümpelmann Model

Gari and Krümpelmann developed a model which took into account VMD at low Q^2 and the scaling laws from perturbative QCD (pQCD) at high Q^2 [Gar85, Gar86]. The model is consistent with VMD at low Q^2 by including the contributions from the dominating ρ and ω mesons. Furthermore, the model is constrained by the scaling behavior of perturbative QCD at high Q^2, such that $F_1^p \sim Q^{-4}$ and $F_2^p \sim Q^{-6}$ are satisfied. They also included the ϕ meson in their model for the purpose of studying the effect of the strange quark on the form factors. The strange quarks do not contribute to the Dirac form factor at low Q^2 because they are not coupled to the nucleon because of the Zweig rule (conservation of strangeness) as shown in Figure 2.2 [Hal84]. However, it turns out that they can have a large contribution to

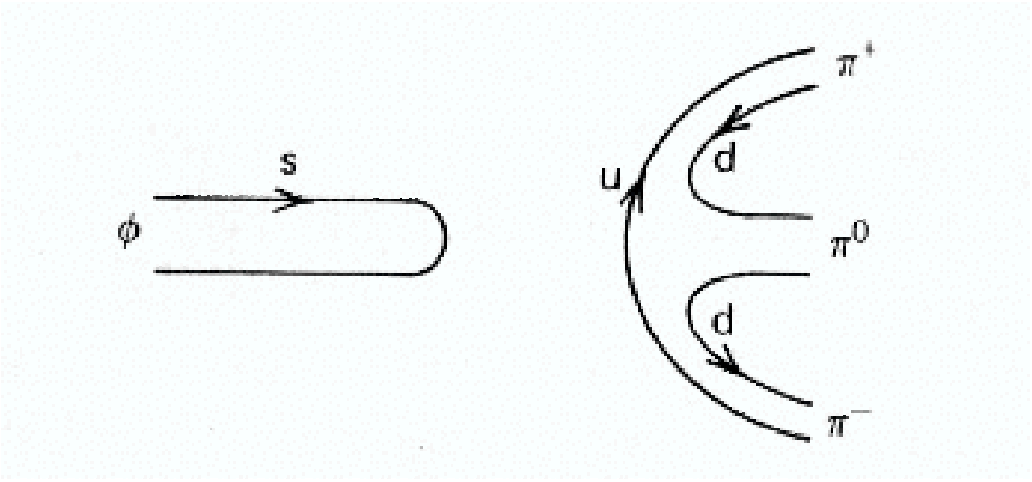

Figure 2.2: Zweig rule. The ϕ meson is not coupled to the nucleon at low Q^2.

G_E^n at the intermediate energy region (less than $2(\mathrm{GeV/c})^2$) by reducing the value for G_E^n significantly although no strong effects were observed for the the other form factors [Gar92].

Extended Gari-Krümpelmann Model

The model by Gari-Krümpelmann which included VMD and pQCD was further extended by Lomon [Lom01, Lom02]. His model includes contributions from the width of the ρ meson. The contribution from the $\rho'(1450)$ and $\omega(1420)$ poles were also added to the model. The world data of the form factors were fitted with 12 parameters. This model agrees well with the existing proton form factor data, but falls below the neutron data above Q^2 $\sim$1.2 $(GeV/c)^2$.

2.1.4 Soliton Model

Topological soliton models for the structure and dynamics of baryons are based on effective nonlinear Lagrangians for selected mesonic degrees of freedom. Holzwarth created a model called the chiral soliton model [Hol96, Hol02], which was developed from the model by Skyrme [Sky61]. The concept of the chiral soliton is based on the observation that there exists an energetically favored configuration of chiral fields which binds valence quarks in a well localized object, a *soliton* [Tho01]. The soliton model requires three basic features: an extended object, partial coupling to vector mesons, and relativistic recoil corrections. In one of the models used by Holzwarth called Model B, the Lagrangian is the sum of the terms representing the vector mesons (π, ρ, and ω)

$$\mathcal{L} = \mathcal{L}^{(\pi)} + \mathcal{L}^{(\rho)} + \mathcal{L}^{(\omega)}. \tag{2.14}$$

A soliton model of the nucleon was created from this Lagrangian using the Skyrme model [Sky61]. It is interesting to note that the ratio of G_E^p/G_M^p falls off linearly at high Q^2 in this model. Although this trend is consistent with the recent results from the JLab experiments [Jon00, Gay02], those results were not available when

this soliton model was developed in 1996. One of the fit results, called Model 2B, shows that G_E^n from this model differs slightly from the Galster parameterization. However, because the location of the maximum value of G_E^n is shifted slightly to lower Q^2, the mean-square radius of the neutron predicted by this model is larger by about a factor two than the experimental value by Kopecky *et al.* [Kop97]. Furthermore, the ratio of the neutron form factors, G_E^n/G_M^n, from this model strongly disagrees with the data as we will see in Chapter 8.

2.1.5 Constituent Quark Models

Although a nucleon is, in reality, a system of many quarks and gluons interacting with each other, the constituent quark model (CQM) treats a nucleon as a three-quark system. Those three quarks inside a nucleon play a key role on the nucleon form factors. In this model, each constituent quark is assumed to be an extended object with the mass of ∼300 MeV, and it presumably has a form factor associated with its internal structure. A relativistic constituent quark model was developed using the light-front dynamics for the constituent quarks. This model has two free parameters; the quark confinement scale $1/\alpha$, and the mass of the constituent quark, m_q. Chung and Coester [Chu91] calculated nucleon form factors using a relativistic constituent quark model for $0 < Q^2 < 6.0$ $(\mathrm{GeV/c})^2$, for several sets of α and m_q. Reasonably good results for the proton form factors were obtained for $m_q = 0.24\mathrm{GeV}$, which is significantly smaller than the conventional choice of one-third of the nucleon mass (∼0.3 GeV). Results for the neutron form factor $F_{2n}(Q^2)$ agree with the data while results for $F_{2n}(Q^2)$ are quite sensitive to the parameters chosen. Consequently, G_E^n from this model deviates from the data.

CQM with the Goldstone Boson Exchange Interaction

QCD cannot be solved perturbatively in the low and intermediate energy regimes, and identification of proper degrees of freedom in these energy regions is difficult. One could consider the spontaneous breaking of chiral symmetry as an essential low-energy property of QCD; Goldstone bosons appear as a result of this broken symmetry, and they couple directly to the constituent quarks. Glozman *et al.* [Glo98] included the Goldstone boson exchange (GBE) hyperfine interaction, and showed that this nucleon model using the constituent quarks with GBE interaction basically reproduces the energy level of the lowest light- and strange-baryon states, thus providing a unified description of the ground state and excitation spectra of the light and strange baryons. Recently, Wagenbrunn *et al.* [Wag01] and Boffi *et al.* [Bof02] calculated nucleon form factors using this model. The calculation was performed in a covariant framework using the point form approach. The Hamiltonian of the three-quark system has a relativistic kinetic energy operator as well as the linear confinement potential (V_{conf}) and the GBE hyperfine potential (V_{hf}),

$$H = \sum_{i=1}^{3} \sqrt{\vec{k}_i^2 + m_i^2} + \sum_{i<j=1}^{3} [V_{conf}(i,j) + V_{hf}(i,j)], \tag{2.15}$$

They used a single-particle current operator for point-like constituent quarks that corresponds to a relativistic impulse approximation in point form, which is referred to as the point-form spectator approximation (PFSA). Note that the impulse delivered to the nucleon is different from that delivered to the struck constituent quark.

The results of the calculated nucleon form factors using PFSA are qualitatively consistent with the existing data. In addition, their model with PFSA gives the values for the square of the charge radius and the magnetic moments of the proton and neutron. Their calculated values for the proton are in good agreement with

the measured values while their results for the neutron qualitatively agree with the measured values. It was found that predictions of their model without relativistic effects included, disagree substantially with the experimental values. Therefore, the relativistic effects play an important role in this model.

Light Front Cloudy Bag Model

Miller made a model of the nucleon using light-front dynamics. In this model, called the light front cloudy bag model (LFCBM) [Mil02], the nucleon is treated as a relativistic system of three bound constituent quarks. They are confined in a bag of radius r, and the bag is surrounded by a *cloud of pions*. A virtual photon can have an electromagnetic interaction with a bare nucleon, or with a nucleon while a pion is present, or with a charged pion in flight. The cloud of pions plays a key role in describing the neutron charge radius that is related to G_E^n at low Q^2. Because the square of the neutron charge radius, $(r_c^n)^2$, is negative, as we saw in Section 1.3, this model assumes that this effect is caused by the distribution of a negative pion cloud that extends to the surface. At large Q^2, the effects of the pion cloud must be calculated relativistically. For this reason, the Feynman diagrams for the electromagnetic interaction must be evaluated with a nucleon in the presence of a pion. The nucleon form factors in this model can be written as

$$F_{i\alpha}(Q^2) \;=\; Z\left[F_{i\alpha}^{(0)}(Q^2) + F_{ib\alpha}(Q^2) + F_{ic\alpha}(Q^2)\right], \tag{2.16}$$

where Z is the renormalization constant, $i = 1, 2$ denotes the Dirac and Pauli form factors, respectively, and $\alpha = n, p$. The first and second terms inside the brackets are the form factor of a bare nucleon and a nucleon in the presence of the pionic field, respectively. The third term represents the form factor calculated when the virtual

photon interacts with the pion in flight. The calculated value for $G_E^n(\mathrm{Q}^2)$ shows that the contribution from the relativistic quarks is small in the low Q^2 regime (Q^2<0.5 (GeV/c)^2), and it is large in the high Q^2 regime (Q^2>1.0 (GeV/c)^2). The values for $(r_c^n)^2$ determined in this model ranges from -0.103 to -0.111 (fm)^2 and are in good agreement with the measured value of -0.112 (fm)^2 by Kopecky *et al.* [Kop97]. The prediction for G_E^n in this model is in good agreement with the measured values, but the prediction for $\mu_p G_E^p/G_M^p$ falls below the proton data at high Q^2.

Model Based on SU(6) Breaking Effects

Assuming the spin-flavor SU(6) symmetry, the relations $G_E^n(Q^2) = 0$ and $G_M^p(Q^2)/G_M^n(Q^2) = -3/2$ hold for all Q^2 values [Car99]. However, non-zero value of G_E^n that have been measured suggests that the SU(6) asymmetry is broken. Recently, Cardarelli and Simula [Car00] studied the effects of both kinematical and dynamical SU(6) breaking on the nucleon form factors within the constituent quark model on the light-front with the quark potential model based on the one gluon exchange model (OGE) [Cap86]. They considered a dynamical breaking of the SU(6) symmetry due to the mixed symmetry component in the nucleon wave function by the spin-dependent terms of the effective quark-quark potential. In addition, they took into account a kinematical SU(6) breaking due to the Melosh rotation which produces a recoupling of the angular momentum and spin of the constituent quarks; therefore, the nucleon wave function is no longer written as a product of a spatial part and a spin-isospin function. Their prediction for $\mu_n G_E^n/G_M^n$ is in good agreement with the measured values. Their results for the ratio $\mu_p G_E^p/G_M^p$ is qualitatively consistent with the data but deviates from the proton data above $\mathrm{Q}^2\sim$ 3.0 (GeV/c)^2.

2.1.6 Comparison of the Theoretical Predictions

Figure 2.3 shows the theoretical predictions of the ratio of the form factors for selected models. In this figure, "VMD+pQCD" denotes the extended Gari-Krümpelmann model by Lomon [Lom01, Lom02]; "Chiral Soliton" denotes the chiral soliton model by Holzwarth [Hol96, Hol02] (results for model B2 are plotted); "OGE CQM" denotes the CQM on the light-front with one-gluon exchange interaction by Cardarelli and Simula [Car00] and Simula [Sim01]; "LFCBM" denotes light-front cloudy bag model by Miller [Mil02]; and "GBE CQM" denotes the CQM with Goldstone boson exchange interaction by Wagenbrunn *et al.* [Wag01] and Boffi *et al.* [Bof02]. The top panel in Figure 2.3 shows the predictions for $\mu_p G_E^p/G_M^p$ along with the measured data points from Milbrath *et al.* [Mil98], Jones *et al.* [Jon00], Gayou *et al.* [Gay02], and Pospischil *et al.* [Pos01]. The bottom panel shows the predictions for $\mu_n G_E^n/G_M^n$ along with the measured data points from Eden *et al.* [Ede94], Zhu *et al.* [Zhu01], Herberg *et al.* [Her99], Ostrick *et al.* [Ost99], Becker *et al.* [Bec99], Golak *et al.* [Gol01], Bermuth *et al.* [Ber03], Rohe *et al.* [Roh99], and Passchier *et al.* [Pas99]. However, recent results for G_E^n/G_M^n from Madey *et al.* [Mad03] by E93-038 collaboration, and by Warren *et al.* [War04] are not plotted [1].

Note that the predictions of the "VMD+pQCD" and the "Chiral Soliton" models for $\mu_p G_E^p/G_M^p$ qualitatively agree with the world data over a relatively broad Q^2 range. The quality of the agreement of predictions from the other models with the data for $\mu_p G_E^p/G_M^p$ is much worse. Over the narrow Q^2 range, $Q^2<0.5$ $(\mathrm{GeV/c})^2$, where data for $\mu_n G_E^n/G_M^n$ exist, most model predictions qualitatively agree with the data. To clearly distinguish between the different models, accurate data for

[1] In Chapter 8, we will present a figure similar to Figure 2.3 with those recent data points of G_E^n/G_M^n included.

$\mu_n G_E^n/G_M^n$ at high Q^2 values above $0.5(\mathrm{GeV/c})^2$ are needed. The E93-038 experiment was designed to provide such data.

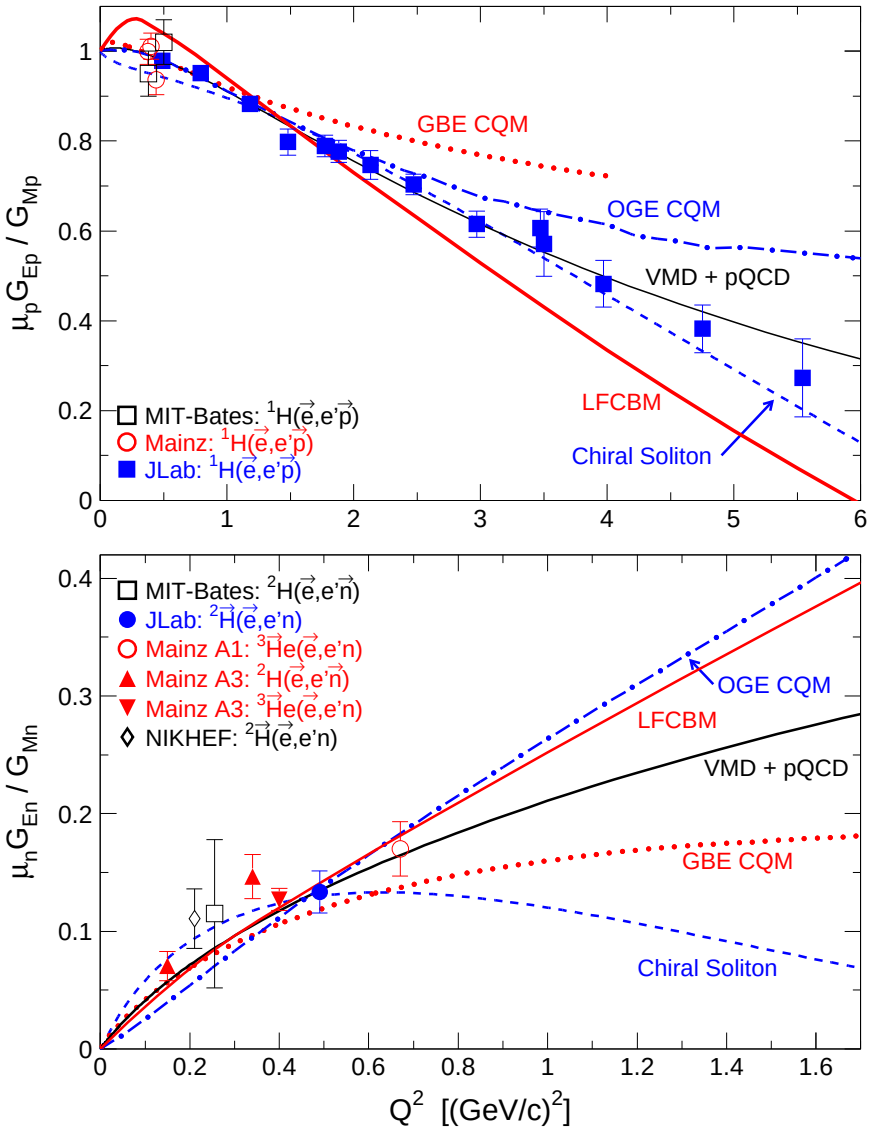

Figure 2.3: Theoretical predictions of selected models of the ratio of the nucleon electromagnetic form factors in comparison with experimental data. Plots are made from the selective models. Measured data points are also plotted. See text for detail.

Chapter 3

Experiment

3.1 Overview of the Experiment 93-038

In the JLab E93-038, we measured the ratio of the electric form factor to magnetic form factor of the neutron $g = G_E^n/G_M^n$ via recoil polarimetry from the quasi-elastic $^2\mathrm{H}(\vec{e}, e'\vec{n})^1\mathrm{H}$ reaction at three $\langle \mathrm{Q}^2 \rangle$ values, 0.45, 1.13, and 1.45$(\mathrm{GeV/c})^2$. Figure 3.1 is a schematic diagram of the neutron polarimeter, and Figure 3.2 a side view of the neutron detector arm of the experimental setup. A longitudinally polarized electron beam with polarization of about 70-80 % was incident on a 15-cm-long cylindrical liquid deuterium target ($\mathrm{LD_2}$). The electrons that quasi-elastically scatter from the neutron or proton in the deuterium target are detected in the High Momentum Spectrometer (HMS) in coincidence with the recoil nucleon that is detected in the Neutron Polarimeter (NPOL). Our technique of measuring the ratio of G_E^n/G_M^n is based on the feature that the amount of polarization transfered from the electron to the struck nucleon is strongly dependent on the ratio of electromagnetic

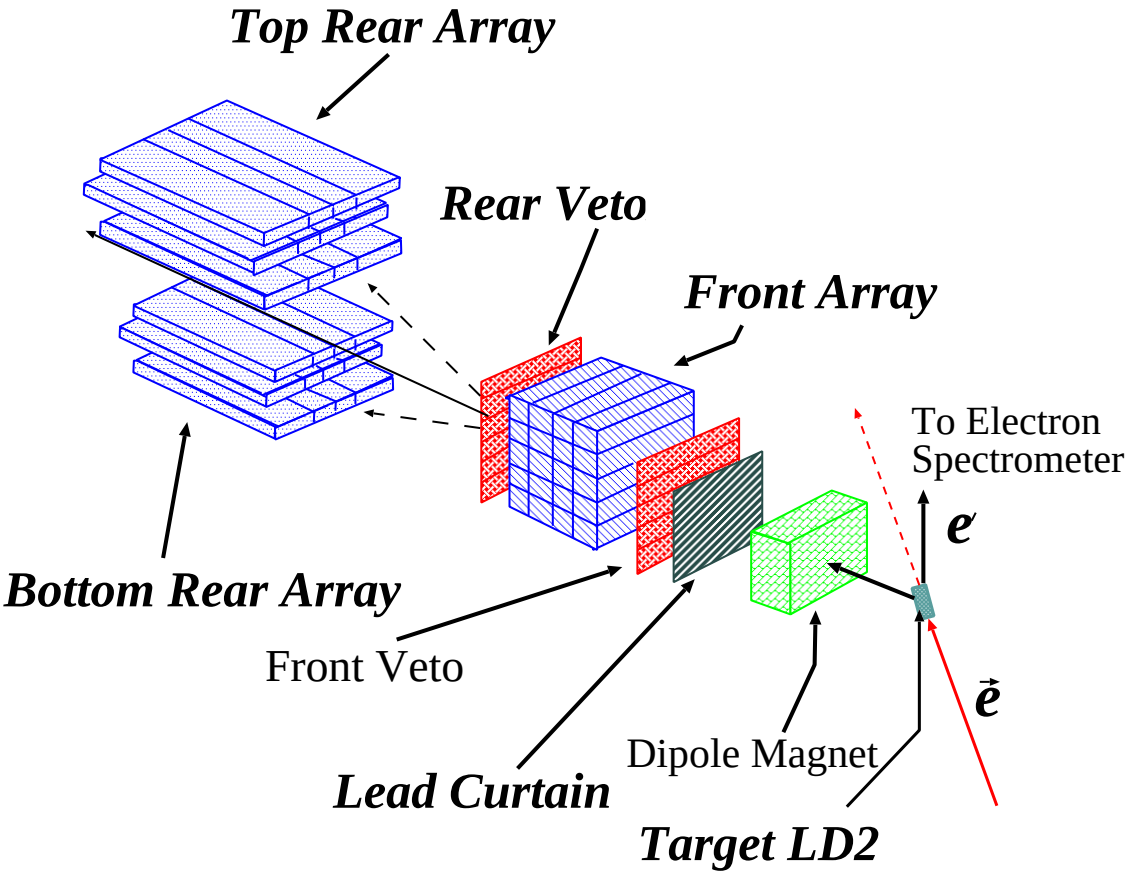

Figure 3.1: A schematic diagram of the neutron polarimeter

form factors.

In the plane-wave approximation, the neutron polarization that is transfered from the electron lies in the electron scattering plane, which was defined by the axis of the incident electron beam and the axis of the scattered electron detected in the HMS. Thus, the neutron polarization can have two components, a longitudinal component($P_L^{'}$) and a sideways component ($P_S^{'}$), which are parallel and transverse to the momentum of the neutron, respectively. A dipole magnet called *Charybdis* with the magnetic field perpendicular to the horizontal plane was located at the entrance of the NPOL. By adjusting the current of the Charybdis magnet, the neutron

polarization vector can be precessed Using this spin-precession technique, the ratio of the longitudinal to transverse component of the neutron polarization vector can be extracted from the values of the scattering asymmetries measured in the NPOL. This technique will be explained in detail in Chapter 4. The lead curtain located between the Charybdis magnet and the NPOL attenuated the electromagnetic radiation and the low-energy charged particles that came from the target. Each major piece of instrumentation used in our experiment will be discussed in the following sections of this chapter. About 1300 tons of concrete was used to shield the NPOL

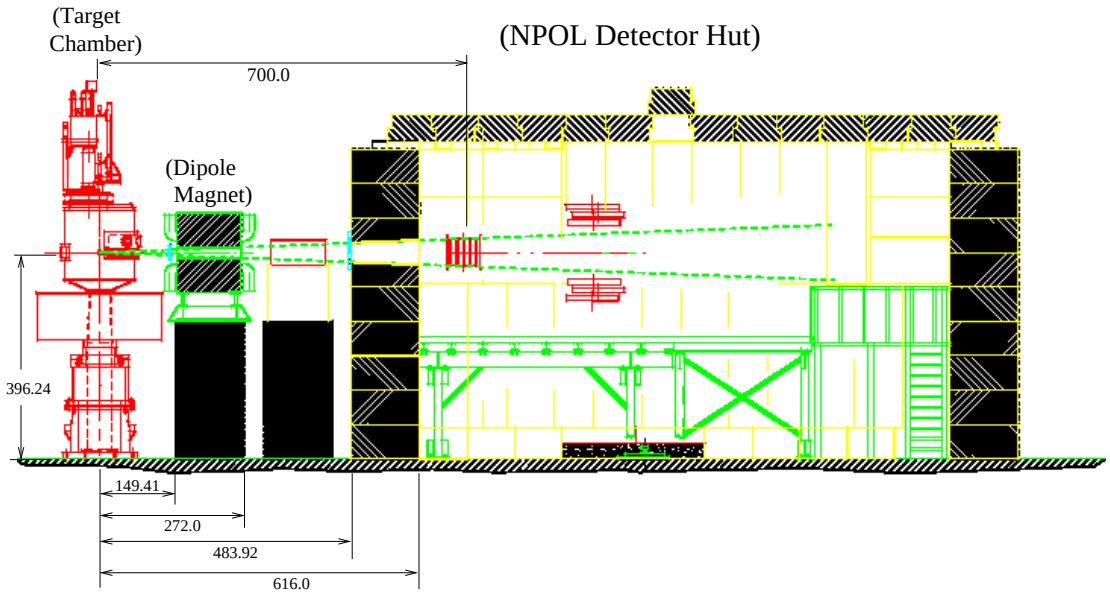

Figure 3.2: A side view of the target, Charybdis magnet, collimator and neutron detector hut. The numbers given in the figure have units of cm, and they indicate either the distance from the center of the target chamber or the height from the floor level.

to reduce the event rate due to the background particles caused by interactions of the high-energy electron beam with the target chamber entrance and exit windows, the beam dump, and the beamline. The horizontal angle of the polarimeter from

the beamline was fixed at 46.0° during the experiment. This angle was optimized by how the figure-of-merit (FOM) changes with the electron scattering angles at our Q^2 points for a given angle for the polarimeter [1]. The FOM is inversely-proportional to the amount of beam time to obtain the required number of events. Therefore, one wants to choose the kinematics setting with the maximum FOM. The FOM for this experiment, which is a function of the *electron* scattering angle, is given by

$$FOM = \left(\frac{D_{LS'}}{f_1}\right)^2 \langle\sigma_3\rangle, \tag{3.1}$$

where f_1 is a kinematic function which depends on $D_{LS'}$ and θ_e [Mad93], and $\langle\sigma_3\rangle$ is the triple-coincidence cross section for this experiment. The angle for the neutron polarimeter relative to the z-axis, which we eventually chose to be 46°, was determined such that the value for the FOM at every Q^2 point of our experiment is reasonably large.

3.2 Accelerator at Jefferson Lab

A schematic diagram of the CEBAF Accelerator is shown in Figure 3.3. The electron beam is accelerated in the injector to achieve 45 MeV in energy. At this energy, the velocity of the electron is already very close to c (it is in fact $0.994c$). Thus, the electron velocity is treated as *constant* when it is being accelerated in the accelerator. The accelerator is a race-track shaped accelerator with two straight accelerating sections that are connected at each end with arc magnets. The electron beam from the injector enters and passes through the north linear accelerator (linac) where it gains 400 MeV in energy from a series of superconducting radio-frequency

[1] Since the NPOL is heavily shielded, the NPOL angle was not changed during the experiment. At each Q^2 point, the quasielastic kinematics at a given beam energy was achieved by changing the HMS angle.

cavities. After exiting the north linac, the beam is bent in the east arc magnets and then passes through the south linac to gain another 400 MeV in energy. Therefore, electrons gain a total of 800 MeV in energy in each pass. At the end of the south

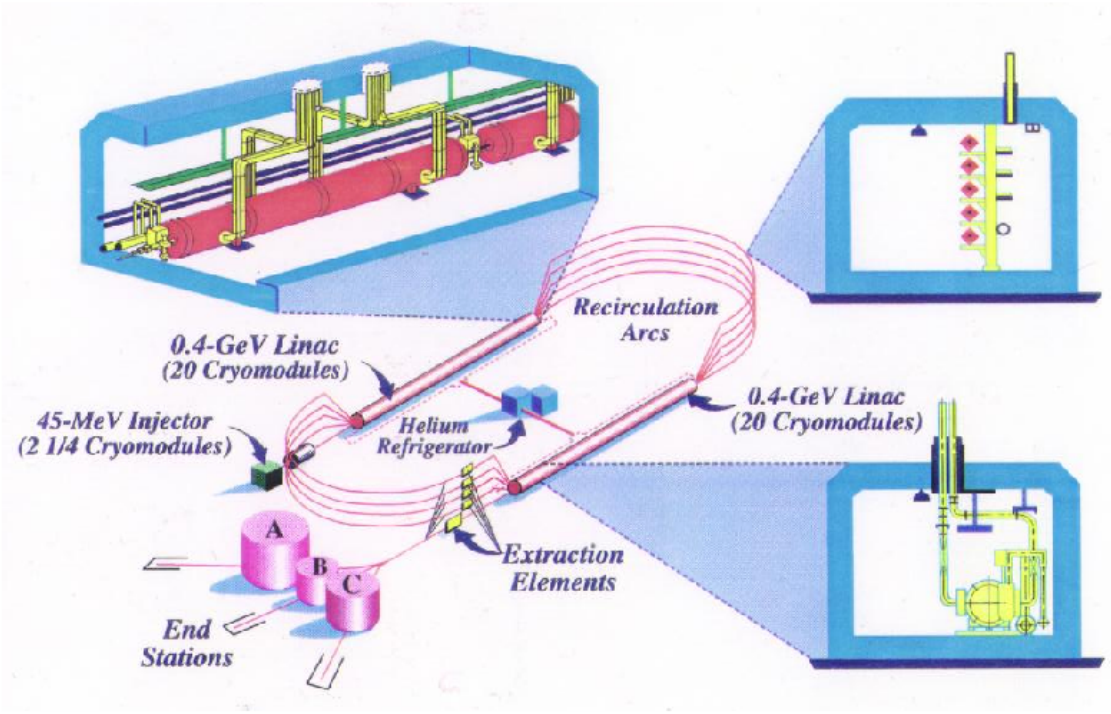

Figure 3.3: Schematic diagram of the CEBAF Accelerator

linac, the beam can be sent to the west arc to gain more energy by passing through the linac sections again. It can go through the accelerator loop up to five passes. Because the energy gain in linac can be adjusted, the net energy is given by a multiple of the energy gained in each pass through the accelerator loop plus the initial energy of the injection.

Because the strength of the magnetic field in the arc depends on the electron energy, there exist five (four) separate arcs in the east (west). These arcs are placed on top of each other and each arc is designed to bend a beam of a particular energy. At the beginning of each arc, the beams from different passes split, and they are recombined at the end of the arc.

After the beam has reached the desired energy at the end of the south linac, the beam is sent to the the Beam Switch Yard (BSY) where it can be selectively sent to any of the three experimental halls (A,B, and C), thus enabling the simultaneous running of experiments in all three halls. The feature that three beams with different energies can co-exist in the accelerator enables the simultaneous running of experiments in three halls at different energies and beam currents.

3.3 Hall C Arc and Beamline

After passing through the BSY, the beam is sent to the Hall C arc magnet which bends the beam into the hall. Beam diagnostics instrumentation is located in the Hall C arc and along the beamline. These instruments provide measurements of the beam position, current and energy. The Hall C arc and beamline are shown in Figures 3.4 and 3.5, respectively.

3.3.1 Beam Position Monitors

During data taking, it is important to monitor the beam position in the Hall C arc to make sure the beam passes nearly through the center of the target. Each Beam Position Monitor (BPM) consists of a cavity with four antennas that lie in a plane perpendicular to the electron beam axis. The axis of each antenna makes an angle

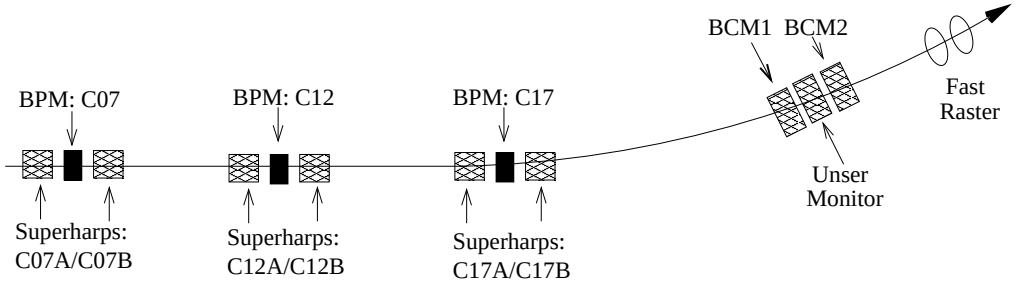

Figure 3.4: Schematic diagram of the Hall C Arc

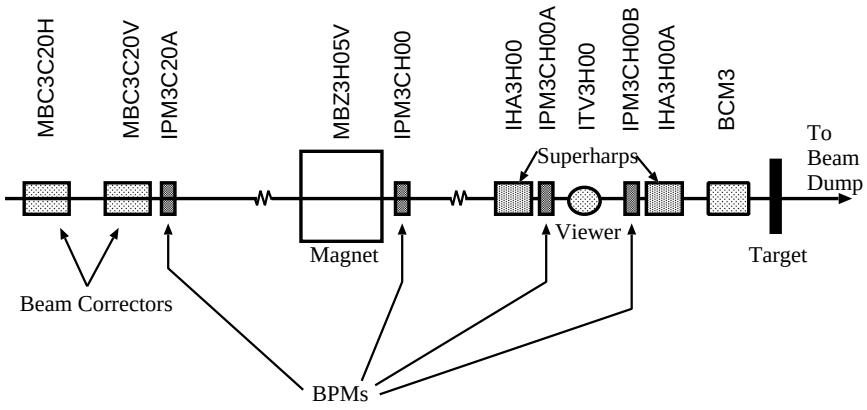

Figure 3.5: Schematic diagram of the Hall C Beamline

of 45°with the horizontal axis in the plane of the antennas. The signal from each antenna is proportional to the distance from the beam to the antenna. Therefore, the position of the beam can be determined by taking the ratio of the signals from the opposing antennas [Guea]. The accuracy of the measurement is about ±1.0 mm. Several BPMs are located on the Hall C arc and beamline (Figures 3.4 and 3.5). As will be explained later, a different position measurement using a device called a superharp is performed for the beam energy measurement.

3.3.2 Beam Current Monitors

The system for measuring the Hall C beam current consists of three components. They are a parametric DC current transformer (Unser monitor) and two resonant cavities known as Beam Current Monitors (BCMs). The BCMs are labeled BCM1 and BCM2 and both of them are used to monitor the beam current during data-taking. The BCMs and Unser monitor are located on the Hall C beamline (Figure 3.4), and they are about 26 meters upstream of the target chamber. The BCM is a cylindrical wave guide made out of stainless steal and is placed coaxially along the beamline. The resonant frequency of the cavity can be adjusted to 1497 MHz, and the electron beam with an RF frequency of 499 MHz excites the TM_{010} mode of the cavities. A wire loop antenna placed inside the cavity detects the stored power. The antenna then sends the AC signal, which is proportional to the power, to the electronics.

An absolute current measurement was performed with the Unser monitor [Boc99]. The Unser monitor consists of two toroids and the absolute gain of the cavity can be calibrated. Although the gain of the Unser monitor is quite stable in time, its zero-offset is not. Therefore, the Unser gain was used to calibrate the BCMs. The details of beam current measurement is given in [Boc99]. For the E93-038, the BCM calibration was performed before our first data for G_E^n were taken.

3.3.3 Beam Energy Measurement

The beam energy can be measured after the beam positions and a map of magnetic field in the Hall C arc are obtained. Let B be a magnetic field, which is perpendicular to the plane of the electron's motion. The momentum of the electron,

P_e, is given in terms of the integral of B over the electron path in the arc,

$$P_e = \frac{e}{\Theta} \int B\, dl, \tag{3.2}$$

where e is the electron charge and Θ is the net bending angle of the electron, which is $\Theta = 34.3°$.

However, a more precise measurement of the beam positions than can be achieved by the BPMs is needed for the beam energy measurement. For this purpose, a device called a superharp is used.

A superharp consists of three tungsten wires which are fixed inside a wooden fork: two wires are placed vertically and the other placed horizontally (Figure 3.6). This fork can be inserted in and out of the beam pipe using the stepper motor

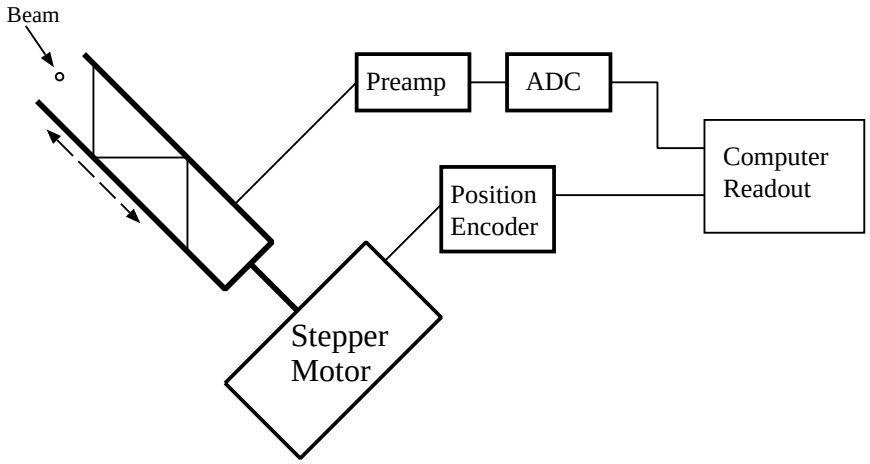

Figure 3.6: Schematic diagram of the Hall C Harp

attached to the fork. When it is inserted, charges are liberated from the wires due to the interaction between a wire and the electron beam. The amount of charge collected from each wire depends on the wire position in the beam pipe. Therefore, one can determine the beam position by continuously changing the position of the

wires in the beampipe. The vertical wires measure the horizontal position of the beam, while the horizontal wire measures the vertical position of the beam. The accuracy of the measurement is about ±0.2 mm [Gueb]. The signal from each wire is sent to an ADC (LeCroy 1881-ADC) which digitizes the data. The ADC registers the number of electrons collected as the wire crosses the beam. Several superharps are located on the Hall C arc and beamline (Figures 3.4 and 3.5). Because the beam can be disturbed by the superharp wires, this measurement is done when data for G_E^n were not taken.

3.3.4 Beam Rastering System

Because the CEBAF beam is a high current beam and has a very small transverse size ($< 200\mu m$ FWHM [2]), the beam would cause local boiling in the cryogenic target and a damage on the beam dump if the beam position at the target were completely fixed. To prevent these problems, the beam position is rastered horizontally and vertically before it enters the target chamber.

There are two rastering systems in Hall C: the fast raster and slow raster. The fast raster system is located about 20 meters upstream of the target chamber and is designed to prevent local boiling in the cryogenic target. The fast raster system consists of two sets of magnet. The first set rasters the beam vertically and the second set rasters it horizontally. The current in the magnet is changed sinusoidally at 17.0 kHz in the vertical direction and 24.2 KHz in the horizontal direction. As a result of this, the beam spot on the plane perpendicular to the beam direction always lies inside a fixed rectangular region. as it forms a Lissajous pattern In this experiment, the vertical and horizontal size of the raster were set to 2.0 x 2.0 mm.

[2] It stands for Full Width Half Maximum

The slow raster system is located about 2 meters upstream of the target chamber and is designed to prevent damage on the beam dump. However, the slow raster was not used during this experiment. Because our beam currents were not too high ($< 70\mu A$), only the fast raster is needed to prevent such damage in our case.

3.3.5 Møller Polarimeter

As discussed in Section 1.7, the extracted value of g does *not* depend on the absolute value of the beam polarization, P_e. Nonetheless, P_e still needed to be measured during our experiment to allow us to account for fractional changes in the value of P_e during the steps of our measuring sequence. Because the measured value of P_e and its uncertainty ΔP_e changed from one set of measurements to another, we have to do the following things to calculate the average value of key quantities determined in our measurements.

1. Because ΔP_e contributes to the systematic uncertainty in g, ΔP_e for each set of runs has to be scaled according to the value of the P_e to calculate the average of the uncertainties.

2. As we will see in Chapter 5, the measured asymmetry ξ for each run is proportional to P_e. Therefore, both ξ and the uncertainty $\Delta\xi$ need to be scaled according to the P_e for the run. This needs to be done when the average of the asymmetries is calculated.

The items listed above will be explained in detail in Chapters 5 and 8, respectively.

The Møller polarimeter [Hau01] was used to measure P_e of the CEBAF beam delivered to Hall C. It is designed to measure the scattering asymmetry from the

$\vec{e} + \vec{e} \rightarrow e + e$ reaction. The main components of the Møller polarimeter are the Møller target, the super-conducting solenoid for the target, two quadrupoles, the collimator system, and detector package for detection of the Møller electrons. Those components are shown in Figure 3.7. The Møller target consists of four foils made of

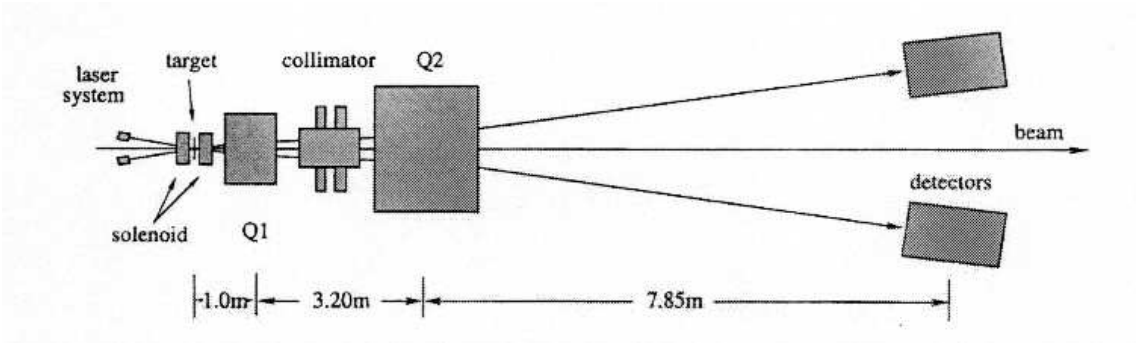

Figure 3.7: The Hall C Møller polarimeter. This Figure is taken from [Hau01].

pure iron and the plane of the foils are placed perpendicular to the beam direction. The outer shell electrons in the iron are polarized parallel to the beam direction by an external magnetic field of 4 (T), which is provided by the super-conducting solenoid. The longitudinally-polarized electron beam scatters from the polarized target electrons. Because the cross section of the reaction $\vec{e} + \vec{e} \rightarrow e + e$ depends on the relative orientation of the beam polarization and the target electron polarization, the P_e can be determined by measuring the scattering asymmetry of the reaction. Because this reaction is described by QED, its cross section can be calculable to high precision. Let us define P_{targ} as the degree of the target polarization and $A_{zz}(\theta)$ as the analyzing power, which is a function of the scattering angle (θ) in the center-of-mass (c.m.) frame. From the lowest-order diagram for this reaction with one-photon

exchange, the cross section is given by

$$\frac{d\sigma}{d\Omega} = \frac{d\sigma_0}{d\Omega}\left[1 + P_{targ}P_e A_{zz}(\theta)\right], \tag{3.3}$$

where the cross section $d\sigma_0/d\Omega$ and $A_{zz}(\theta)$ are given, respectively, by

$$\frac{d\sigma_0}{d\Omega} = \left(\frac{\alpha(4-\sin^2\theta)}{2m_e\gamma\sin^2\theta}\right)^2 \tag{3.4}$$

$$A_{zz}(\theta) = -\left(\frac{\sin^2\theta(8-\sin^2\theta)}{(4-\sin^2\theta)^2}\right)^2, \tag{3.5}$$

where m_e is the electron mass, α is the fine structure constant given in Equation 1.40, γ is given by $\gamma = (1-\beta^2)^{-\frac{1}{2}}$ and β is the electron velocity divided by c.

The scattering asymmetry is obtained by measuring the cross sections with the beam helicity being parallel and anti-parallel to the target polarization.

$$\varepsilon = \frac{\left(\frac{d\sigma}{d\Omega}\right)^{\uparrow\uparrow} - \left(\frac{d\sigma}{d\Omega}\right)^{\uparrow\downarrow}}{\left(\frac{d\sigma}{d\Omega}\right)^{\uparrow\uparrow} + \left(\frac{d\sigma}{d\Omega}\right)^{\uparrow\downarrow}} = P_{targ}P_e A_{zz}(\theta) \tag{3.6}$$

At $\theta = 90^\circ$, $A_{zz}(\theta)$ has the largest negative value of $-7/9$, which is very large. The degree of the iron polarization is well known, and it is about 8 %. Therefore, by detecting the electrons scattered at 90° in the c.m. frame, the beam polarization P_e can be determined from the measured asymmetry and the known values of A_{zz} and P_{targ}.

Because the angle deviation of the electrons that scatter in the the Møller target is very small ($\sim 1^\circ$), they need to be deflected for an asymmetry measurement in the detector package. The Hall C Møller polarimeter has two quadrupoles, which are referred as Q1 and Q2 (Figure 3.7), The Q1 is placed 1.0 m down stream of the Møller target. It serves to deflect Møller electrons very slightly so that they are focused to the acceptance of the Q2. This is especially important for the low energy electron beam whose laboratory scattering angle (1.8° at $E_{beam} = 1.0$ GeV) is larger.

The Q2, located at 3.20 (m) downstream of the Q1, defocuses the Møller electrons and they are detected in the left and right detector packages.

The collimator system, placed between Q1 and Q2, consists of seven collimators and it is designed to select a range of scattering angles. The layout of the collimator system is shown in Figure 3.8. The collimators are made of densimet, which has a high density of $\sim$18 g/cm^3, and have a thickness of about 8 cm. The desired scattering angles are selected by six movable collimator jaws whose horizontal or vertical positions can be adjusted remotely. The range of collimator positions corresponds to the range of beam energy from 1 to 6 GeV, and therefore the Møller polarimeter was (usually) operational in this energy range. In addition, one central collimator with a fixed circular hole is placed at the beamline. When the Møller polarimeter is not in use, all the collimators are removed by remote control.

Because the electrons from the Mott scattering (electrons that scatter from the nucleus) cause a large scattered flux, the collimator system is designed to prevent those electrons from entering the detectors. Note that the electrons from the Mott scattering have energy close to the incident beam energy while the Møller electrons with 90° in c.m. have half of the beam energy. Therefore, the Mott electrons have even smaller scattering angle than the Møller electrons, and most of those background Mott electrons are removed by the collimators. As mentioned earlier, $A_{zz}(\theta)$ has the largest negative value at $\theta = 90°$ in c.m. and therefore the asymmetry is measured at this angle. In the laboratory frame, this situation happens when the electron scattering angle and recoil angle are the same. Therefore, two detector systems are placed at the equal angle from the beam direction in order to detect both electrons in coincidence. This allows us to identify the Møller electrons quite easily because there is virtually no background in this detection system.

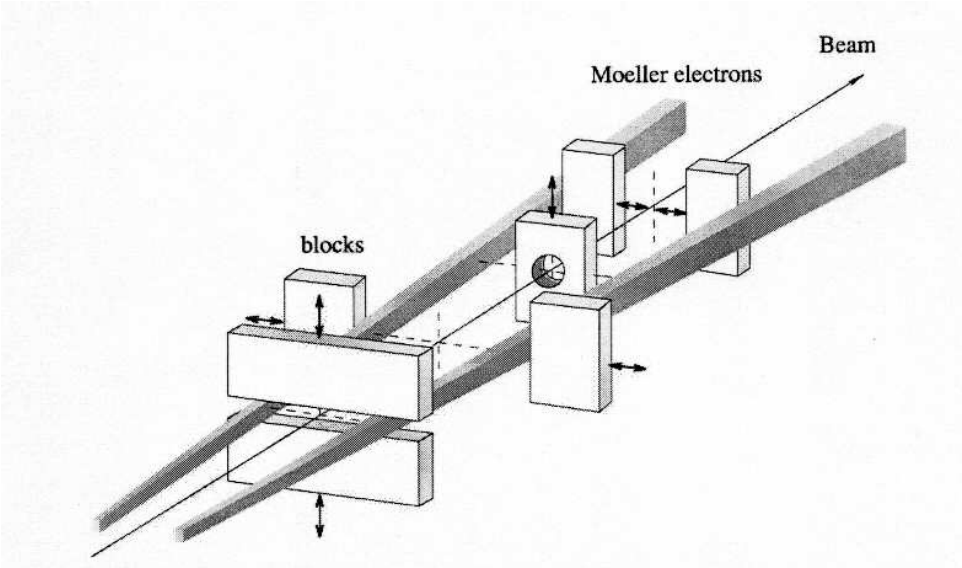

Figure 3.8: Collimators for the Møller polarimeter. This Figure is taken from [Hau01].

A Møller Detector package consists of hodoscopes, a collimator, and a lead-glass counter with a photo-multiplier tube (PMT). The package is shown in Figure 3.9. The hodoscopes consist of 14 plastic scintillator bars which are placed vertically. Each bar has the dimensions of 8 x 12 x 80 mm and is equipped with a PMT. The light signal from a bar is read out only when both lead-glass counters detected a pair of Møller electrons in coincidence. In front of the hodoscopes, there is a 1-cm thick lead shielding which removes the low-energy background particles. This shielding helps us reduce not only the counting rates in the hodoscope but also the amount of shower energy in the lead-glass which would otherwise be deposited by those particles. The collimator placed between the hodoscopes and the shower counter defines the actual acceptance of the detector. The Møller electrons are detected in the lead-glass counter which has the dimensions of 20 x 14 x 23 cm^3. The electrons cause shower in the lead-glass until they stop completely in this counter. The amplitude of the

light signal is measured with one 5-inch phototube. For the Q^2=1.14 $(GeV/c)^2$ data,

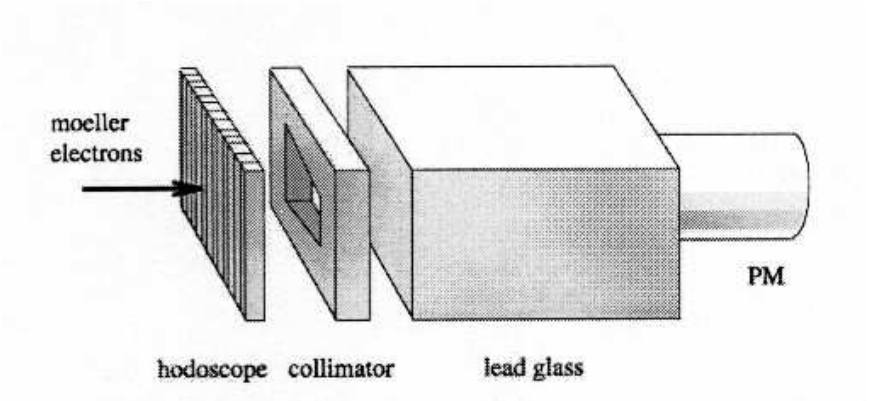

Figure 3.9: Detector package of the Møller polarimeter. This Figure is taken from [Hau01].

the measurements of P_e were performed once every few days while for the Q^2=0.45 $(GeV/c)^2$ data they were performed at the beginning of each run cycle. In addition, the measurements were performed whenever beam delivery condition changed. Low current ($< 3\mu$A) beam was always used for the measurements as beam currents higher than 10 μA would damage some of the components. The statistical uncertainty in the measurement of P_e is usually better than 0.5 %.

For the measurements of P_e for the Q^2=0.45 $(GeV/c)^2$ data, some special changes were made to the Møller polarimeter. The changes were necessary because the beam energy for this Q^2 point was lower than the minimum operational energy of 1.0 GeV of the Møller polarimeter. In March 2001, just before we started taking those G_E^n data, the Q1 was moved upstream by 6 inches so that P_e could be measured at the lower beam energy. After the Q1 was moved, the polarimeter was re-tuned for the new geometry to make sure that the scattered and recoil electrons from the Møller target were within the acceptances of Q1 and Q2. The tuned quadrupole currents no longer matched the original currents, and therefore new 'standard' tunes

for the new geometry were obtained. In addition, the calibration of the polarimeter analyzing power $A_{zz}(\theta)$ had to be recalculated.

3.4 Targets

A liquid deuterium target was used to perform the measurements of G_E^n. During this experiment, most of the data were taken with a 15-cm long cryogenic liquid deuterium (LD_2) target. In addition, data were taken with a 15-cm long liquid hydrogen (LH_2) target so that the measurements of the false-asymmetry, which is caused by the charge-exchange reaction in the lead, could be evaluated. Such a process will contribute to the systematic uncertainty in the measured value of the ratio g. Solid targets such as aluminum, carbon, and a BeO viewer were available. They were used during the commissioning period and whenever some experimental devices seem to be malfunctioning. Data with the carbon target were taken to check the HMS optics and electron track reconstruction. The BeO viewer was used for checking the beam position on target. The target called 'dummy' consisted of two aluminum plates. Each plate is nearly 10 times thicker than the aluminum endcap for a cryogenic target. Both plates were placed at the same positions as the endcaps of the cryogenic cells.

All targets were located inside the scattering chamber. The chamber has an inner radius 123.2 cm, is 136.5 cm high, and it has a wall thickness of 6.35 cm. Inside the scattering chamber, the cryogenic targets were mounted on the target ladder. Each target cell was connected to one of three cryogenic loops (loop 1, 2, and 3). In this experiment, loop 1 and loop 2 were used for the LD_2 and LH_2 targets, respectively, and no targets existed for loop 3. Each loop had two target cells. Figure 3.10 shows

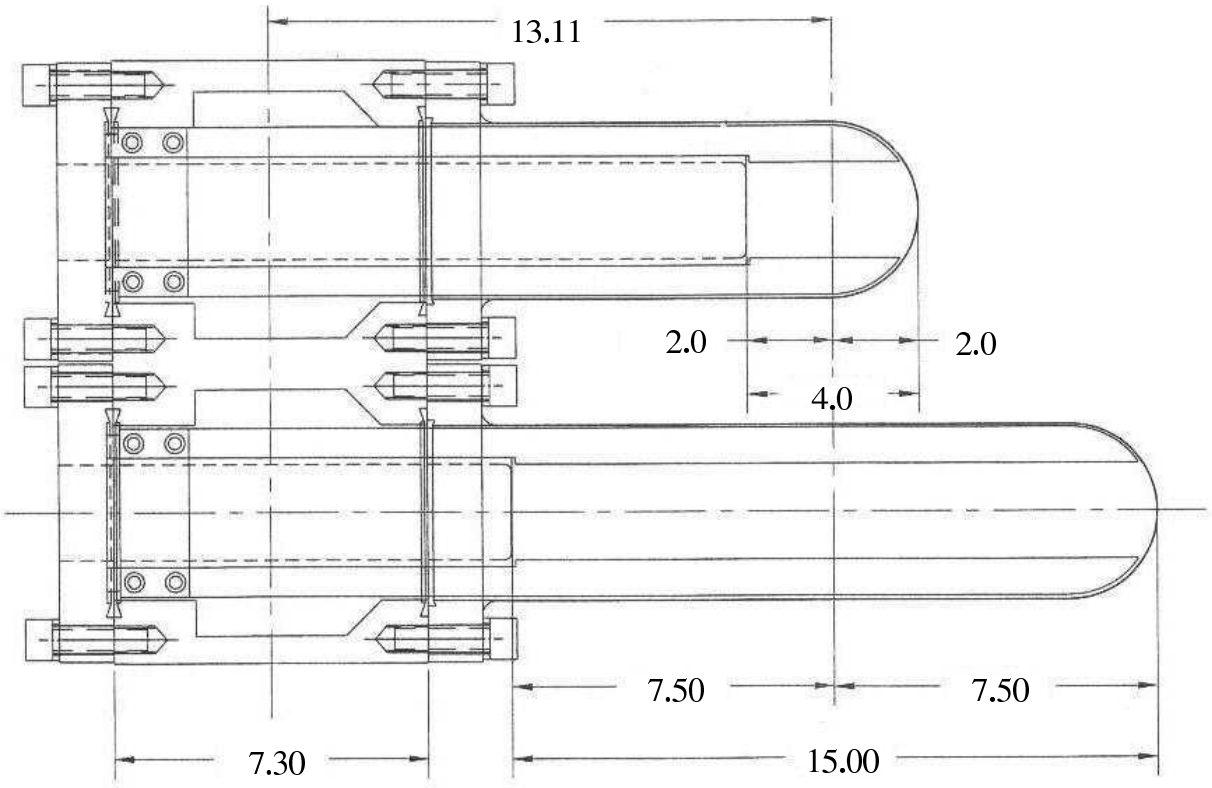

Figure 3.10: Target cells for one of the cryogenic loops. Units are cm. Each cell is a cylindrical object with inner radius of 2.0 cm. The top (bottom) cell is for 4-cm (15-cm) long target. The beam enters from left and exits the cell on right in this figure.

the two different-sized target cells that were operated on one loop: a 15-cm long and the other 4-cm long target. The identical set of cells were connected to the second loop in our experiment. However, data were not taken with the 4-cm long targets in this experiment. The density of the LD_2 target with no beam current on target was 0.174 g/cm^3. The solid targets were mounted at the bottom of the cryotarget ladder. Although there existed inside the chamber a separate and independent ladder for solid targets, it was not used in this experiment.

During data taking, the temperature for loop 1 was kept at 22.0 K, and 19.0 K for loop 2. If the target temperature becomes too high, the liquid target will boil.

On the other hand, if the temperature becomes too low, the target will freeze and the cryogenic system will be seriously damaged. Therefore, the target temperatures needed to be constantly monitored during experiment. The targets were cooled by the helium coolant provided by the End Station Refrigerator (ESR) at CEBAF. The beam raster with 2 x 2 mm size was always used to avoid local boiling inside the target, as mentioned in Section 3.3.4. Hall C cryogenic targets are described in detail in [Dun97].

3.5 High Momentum Spectrometer

The High Momentum Spectrometer (HMS) in Hall C has a large momentum acceptance of $\pm 10\%$ about the central momentum, and electrons with central momentum up to 7.4 GeV/c can be analyzed. The momentum resolution of the HMS is less than 0.1%. The horizontal angle resolution of the HMS on the scattering plane is 0.8 mrad, and the vertical (out-of-plane) angle resolution is 1.2 mrad. Furthermore, the electron time-of-flight (TOF) can be also measured with the HMS. In E93-038, the scattered electron and the recoil neutron (detected in the neutron polarimeter) are measured in coincidence. For the neutron TOF measurement, the HMS timing signal is sent to the polarimeter electronics rack. The electron information obtained from the HMS was used extensively to identify the quasielastic events.

The HMS consists of three quadrupole magnets (Q1, Q2, and Q3), one dipole magnet and a detector package which sits inside a highly-shielded detector hut. These HMS components are on a common carriage that can rotate to a desired angle around a rigidly mounted central bearing. Figure 3.11 shows a side view of the HMS. The quadrupoles determined the focusing properties of the spectrometer, and to a large

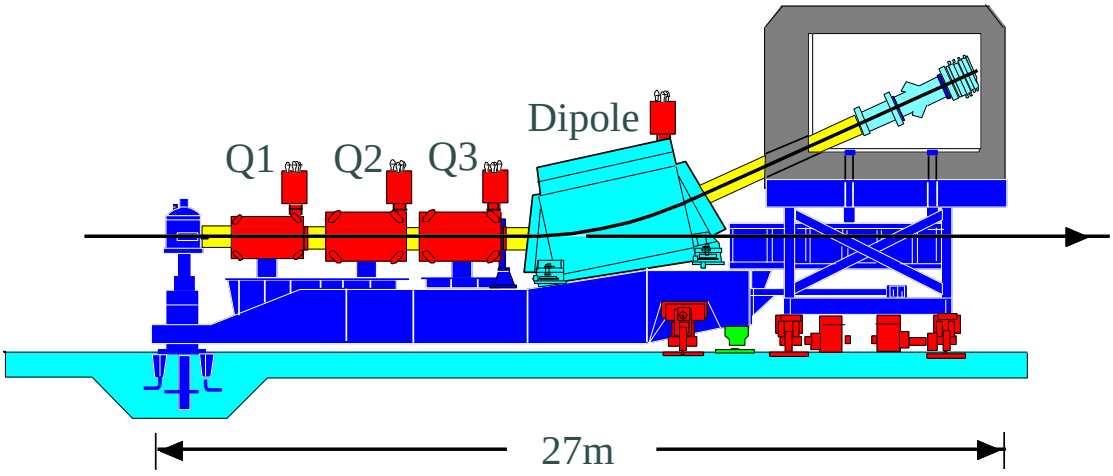

Figure 3.11: Side view of the HMS. Three quadrupoles, a dipole and the detector hut are shown. Note that the dispersive direction is perpendicular to the electron trajectory and it lies in the plane of this paper.

extent, its acceptance. Q1 and Q3 focus the scattered electrons in the dispersive direction while Q2 focuses them in the transverse direction. The quadrupoles are powered by three Danfysik System 8000 power supplies which provide up to 1250 amps at 5 volts.

The HMS dipole is the dispersive element in the system and determined the central momentum of the system. The dipole is a superconducting, cryo-stable magnet with a vertical bending angle of 25° for the electrons with the central momentum. Electrons passing through the dipole are deflected upward and the amount of deflection depends on the electron momentum. The dipole is powered by three Danfysik System 8000 power supplies which provide up to 3000 amps at 10 volts. All four magnets are cooled with 4K liquid helium provided by the CEBAF End Station Refrigerator (ESR).

3.5.1 HMS Detector Package

The HMS detector package is shown in Figure 3.12. The package sits inside the highly-shielded detector hut The detector package consists of two multi-wire drift chambers (DC1 and DC2) for particle track reconstruction, two planes of XY scintillator hodoscopes (S1X, S1Y, S2X, and S2Y) for triggering and measuring the particle TOF, a gas Čerenkov detector for particle identification (electron or pion), and a lead glass calorimeter for particle energy measurement and particle identification (electron or pion). Each detector component is described in detail in the following sections.

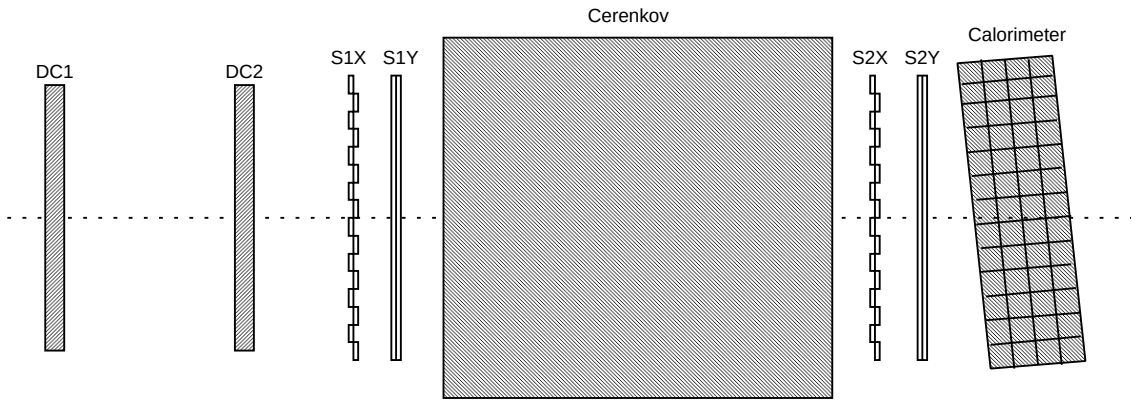

Figure 3.12: Schematic diagram of the HMS detector package. Particles are incident from left in this figure.

3.5.2 Drift Chambers

HMS drift chambers (DCs) measure the position of a particle when it passes through them; the particle track is reconstructed from the position information. There are two DCs in the HMS detector package. The Chambers are separated by 81.2 cm. Each chamber consists of six planes of wires. Each drift chamber plane

measures the electron position in a particular direction: two planes (referred as X,X′) measure the x position, another two planes (Y,Y′) measure the y, and the remaining two planes (U,V) measure the u and v positions. The u and v axes are rotated by $\pm 15^\circ$ from the x axis. Figure 3.13 shows a front view of the HMS drift chamber. The order of these six planes as seen from the direction of the incident electrons is X,Y,U,V,Y′,X′ and the planes are separated by 1.8 cm. Note that the x axis (y axis) is vertical (horizontal) in this figure. The Y and Y' wires, which are placed vertically, measure the horizontal position (y position). Similarly for the X and X' wires which are placed horizontally.

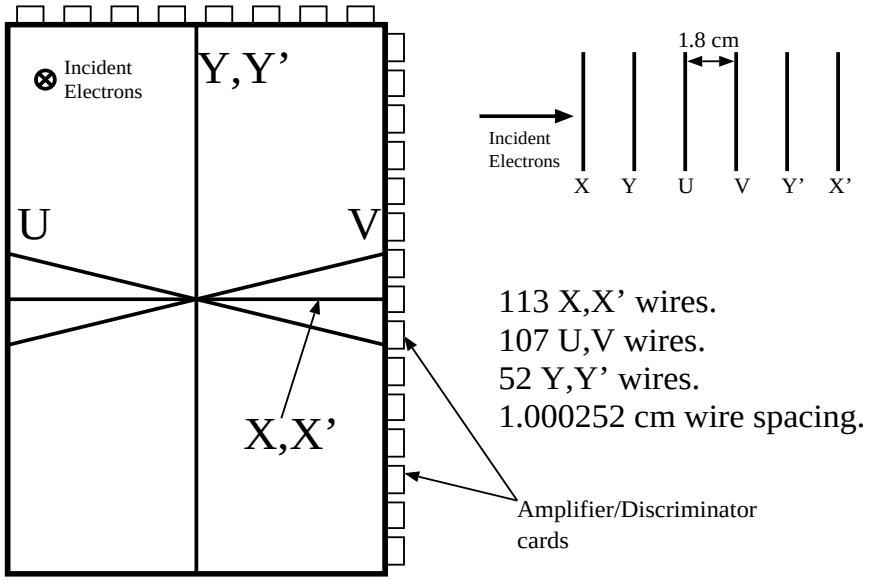

Figure 3.13: Front view of the HMS drift chamber. The dispersion direction ,x axis, is vertical (down) in this figure. Also shown on the upper right corner is a schematic side view of the drift chamber planes.

Each chamber, which has an active area of 113 cm (x) by 52 cm (y), is filled with a mixture of gas (argon/ethane) along with 1% Isopropyl alcohol to clean the wires. Each plane is composed of many wires placed parallel to each other. The

sense wires (anodes) are 25 μm diameter gold-plated tungsten wires, and the field wires (cathodes) are 150 μm diameter gold-plated copper-beryllium tungsten wires. The field wires are biased to a negative potential, creating an electric field between cathode and anode wires that points toward the cathode wires. As the charged particle passes through the drift chamber, the gas inside it becomes ionized and many pairs of an electron and a positive ion are created. The electrons are attracted to the sense wires while the positively charged particles are attracted to the cathode wires. This behavior is called *drift*. The drift time is given by the time interval between the creation of the electron and positive ion pairs and their arrival at the wires. The distance that the electron passes from the sense wire can be calculated from the drift time and the velocity of the particle drift. With our chambers, using the wire location and the drift time measurements, the position of the particle trajectory through each wire plane could be determined to an accuracy of $\pm 60 \mu m$ [Bak95]. From the very precise position measurement in the six wire planes, the particle trajectory was reconstructed.

A virtual plane called the detection plane is located halfway between the two chambers and is parallel to the chamber planes. Because the detection plane is located close to the focal plane of the magnetic spectrometer, the position on the focal plane is considered to be that on the detection plane. This will be explained in more detail in Section 5.4.7.

3.5.3 HMS Scintillator Hodoscopes

The HMS scintillator hodoscopes provide the fast signal which is used to measure the accurate time of a particle interaction. There are four HMS Scintillator planes. Each plane consists of several scintillator bars, which are made of polyvinyltolulene.

Two of the planes are segmented in the X direction (S1X and S2X in Figure 3.12), while the other two planes are segmented in the Y direction (S1Y and S2Y in Figure 3.12). Each detector bar is 1.0 cm thick and 8.0 cm wide. The X elements are 75.5 cm long, and the Y elements are 120.5 cm long. The S1X and S2X consists of 16 bars, and the S1Y and S2Y consists of 10 bars.

When an incident charged particle interacts with the material in a bar, the atoms in the material become ionized, and the atoms are excited. A flash of light called scintillation light is then emitted when they decay. The scintillation light in each bar is converted to an electrical signal by PMTs, which are attached on each end of the bar. The signals are sent to the counting house through a splitter. A signal with one-third of the PMT anode signal is sent to a Fastbus Analog-to-Digital Converters (ADCs). The other signal from the splitter, which has the remaining two-third amplitude of the PMT anode signal is sent to a discriminator. The discriminator output signals are sent to a Fastbus Time-to-Digital Converters (TDCs), a VME scaler, and the HMS trigger supervisor. A diagram of the HMS hodoscope trigger circuit is shown Figure 3.14. During E93-038, the HMS trigger signal was generated whenever 3 out of 4 HMS scintillator planes fired. The HMS trigger signal was also used to form the coincidence trigger between the neutron polarimeter and the HMS.

3.5.4 Gas Čerenkov Detector

A gas Čerenkov detector is used to identify the particle (electron or pion) which caused the trigger in the HMS. The Čerenkov detector detects the Čerenkov radiation which is emitted when a charged particle travels through a medium with a velocity greater than the speed of light in that medium, c/n, where c is the speed of light in

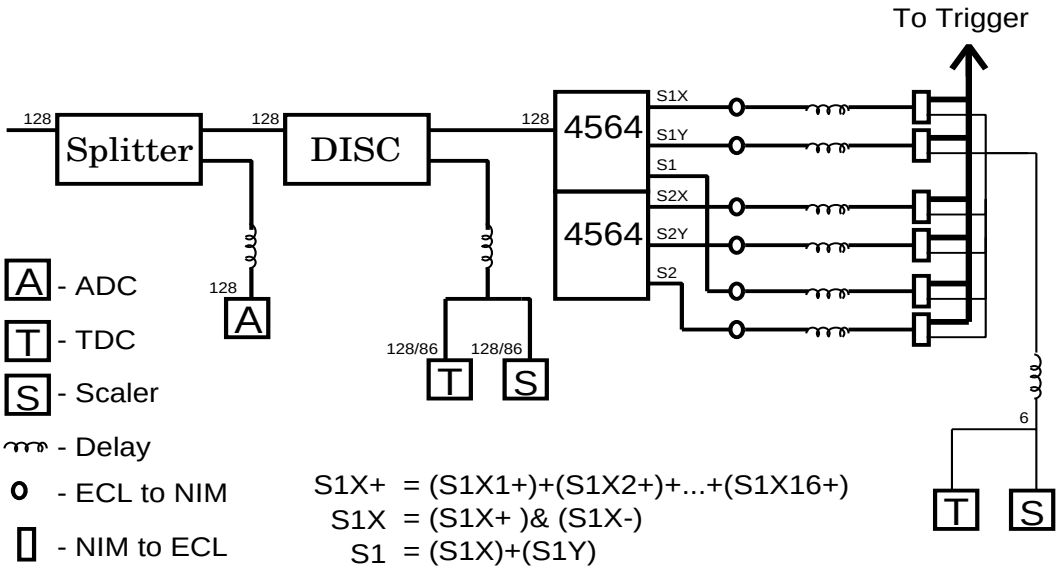

Figure 3.14: Electronics diagram of the HMS hodoscopes. The numbers next to each module shows the number of channels used in the HMS.

vacuum and n is the index of refraction of the medium. The angle of the radiation emission, θ_c, is given by

$$\cos\theta_c \;=\; \frac{1}{\beta\, n}, \tag{3.7}$$

where β is the particle velocity divided by c. Therefore, the medium for the detector is carefully selected so that the electrons in the momentum range of 0.5 to 4 GeV/c can cause the Čerenkov radiation while the pions cannot. It turns out the range of the index of refraction n that satisfied this condition is very small, $10^{-4} \leq (n-1) \leq 10^{-3}$. Thus, a gas was used as the medium for the Čerenkov detector. The Čerenkov detector consists of a large cylindrical tank which has a diameter of 150 cm and a length of 150 cm. The tank is made out of 0.5-inch thick aluminum walls. The entrance window to the tank was made as thin as possible because the pions can hit the window and produce many knock-on electrons (δ rays), which can cause Čerenkov radiation, even though the pion momentum is always below threshold. The density

of the gas has a very small effect on the rate of δ-ray production.

The Čerenkov light is reflected onto two 5-inch Burle 8854 PMTs by two mirrors. The anode signal from each PMT was sent to the counting house where each was split, and one set of outputs was sent to LeCroy 1881 ADCs. The other set of outputs was summed in an Phillips 740 linear fan-in module and sent through a discriminator to provide trigger signals and signals to TDCs and scalers. The signals from the Čerenkov detector were not part of the HMS trigger for this experiment. Figure Figure 3.15 is a diagram of the readout electronics for the Gas Čerenkov detectors. The ADC channel number obtained corresponds to the number of photoelectrons collected through the PMTs.

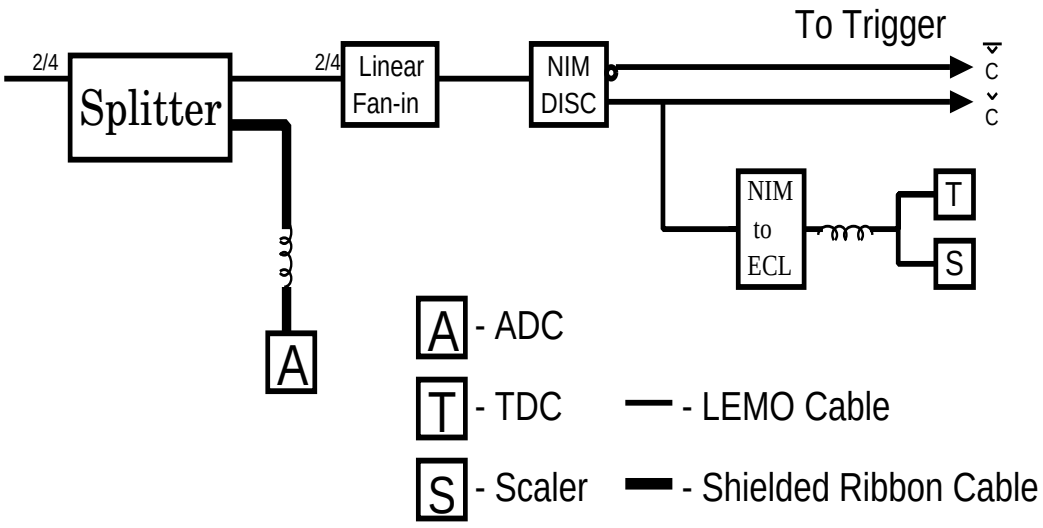

Figure 3.15: Electronics diagram of the Čerenkov detector. The numbers next to each module indicate the number of channels for the HMS.

3.5.5 Lead Glass Calorimeter

A lead glass calorimeter (shower counter) is an electromagnetic calorimeter. It is used in conjunction with the Čerenkov detector to perform electron/pion identifi-

cation. In addition, the calorimeter measures the energy of the particle incident on the HMS. A high energy electron radiates photons through Bremsstrahlung in the calorimeter, and these photons then create positron-electron pairs. Those pairs in turn radiate photons which again create positron-electron pairs. Therefore, repeating this process produces a shower of secondary particles (photons, electrons, and positrons) in the calorimeter. These particles deposit all of their kinetic energy by radiation and stop in the calorimeter. On the other hand, pions interact strongly with nuclei and create a hadronic shower. A pion usually deposits $\sim$ 300 MeV in the calorimeter. Therefore, the particle ID (electron/pion) can be determined from the energy spectrum of particles in the calorimeter.

The HMS calorimeter is made out of TF-1 lead glass blocks. The blocks are arranged in 4 layers along the direction of the electrons, and there are 13 blocks high in each layer for a total of 52 blocks. Each block has a dimension of 10 cm $\times$ 10 cm $\times$ 70 cm with a PMT on one end. TF-1 lead glass has a density of 3.86 g/cm^3 and a radiation length of 2.54 cm. Thus, the total thickness of the calorimeter (40 cm) corresponds to about 16 radiation lengths. The signals are sent from the PMTs to the counting house. The signals then split and one set of outputs is sent to LeCroy 1881M ADC. The other set of outputs is sent to Philips 740 linear fan-in modules and sent through a discriminator to provide trigger signals, TDC stop signals, and scalers signals. However, the signals from the shower counter were not part of the HMS trigger for this experiment. Figure 3.16 is a diagram of the readout electronics for the calorimeter.

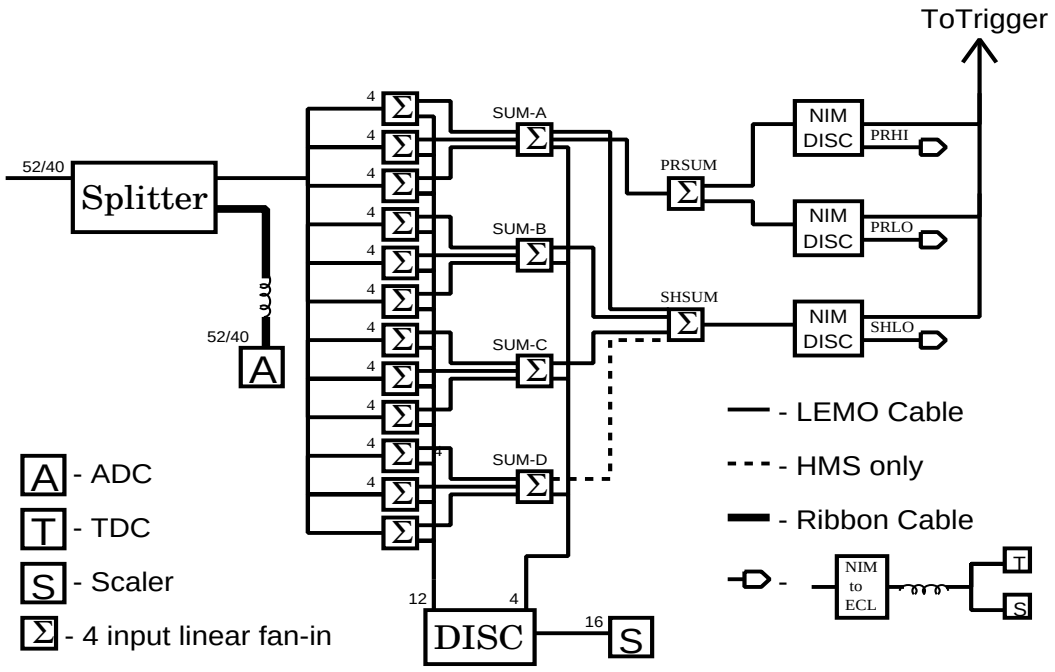

Figure 3.16: Electronics diagram of the calorimeter. The numbers next to each module indicate the number of channels used in the HMS.

3.6 Charybdis Dipole Magnet

A dipole magnet called *Charybdis* was used to precess the spin of the neutron. It was located between the target chamber and the collimator for the polarimeter. The size of the Charybdis magnet along the Z_{pol} axis is 122.59 cm, and the distance from the center of the target to the front of the Charybdis is 149.41 cm (see Figure 3.2). The magnet has an 8.25" vertical gap and the magnetic field points nearly vertically (up or down) so that the spin is precessed horizontally. In order to minimize field gradients, the magnet is equipped with 2-inch field clamps. For the Q^2=0.45 $(GeV/c)^2$ data with the $\pm 40^\circ$ precession method, the current in the magnet was $\pm$170.5 A. For the Q^2=1.14 $(GeV/c)^2$ data with the 0° and $\pm 90^\circ$ precession method, it was 0.0 and $\pm$540.3 A.

3.7 Lead Shield for NPOL

A lead curtain with 10-cm thickness (total 40 lead sheets) was installed in front of NPOL to attenuate the electromagnetic radiation from the target. Without the shielding, the event rates became so high due to too many background events that it was not possible to perform the data taking.

Before the official data taking was started at each Q^2 point, the singles event rates with various lead thicknesses were examined to determine the optimal thickness of the lead. We found that the event rates became tolerable with the 10-cm thick lead shield (40 lead sheets). For data taken at Q^2=1.14 $(GeV/c)^2$, 28 and 12 lead sheets were placed upstream and downstream of the Charybdis magnet respectively (Figure 3.2). However, for data taken at Q^2=0.45 $(GeV/c)^2$, all 40 lead sheets were placed downstream of the Charybdis magnet (Figure 3.1).

Because charged particles lose energy due to the electromagnetic interaction as they go through the lead, low-energy particles can lose all of the energy in the 10-cm lead. At Q^2=0.45 $(GeV/c)^2$, most charged particles lost all the energies and stopped in the lead while at Q^2=1.14 $(GeV/c)^2$ most charged particles penetrated the shielding. Although background rates were reduced due to the lead shield, it was possible that the two-step process $^2H(\vec{e}, e'\vec{p})$+Pb$(\vec{p}, \vec{n})$ happened to create a neutron from an incoming proton. Because such neutrons might contribute to a false scattering asymmetry, data with hydrogen target were taken at each Q^2 point to investigate this issue.

3.8 Neutron Polarimeter

The Neutron Polarimeter (NPOL) based on *np* scattering [Mad95] was designed to measure the physical scattering asymmetry of recoil neutrons generated from the quasi-elastic ^{2}H$(\vec{e}, e'\vec{n})^1$H reaction. The NPOL consisted of a total of 62 (70) plastic scintillators for the measurements at Q^2=1.14 (GeV/c)^2 (Q^2=0.45 (GeV/c)^2). Each scintillator detector was assigned a *detector ID number*, which runs from 1 through 70. Figure 3.17 shows a side view (seen from $-x$ direction) and top view (seen from $+y$ direction) of the NPOL detectors. The NPOL consisted of front (IDs 1-20), rear (IDs 21-44), and veto (IDs 45-70) detector arrays. The rear array consisted of bottom (IDs 21-32) and top (IDs 33-44) arrays. The veto array consisted of front veto (FRVT) (IDs 45-54) and rear veto (REVT) (IDs 55-70) arrays.

The NPOL sits inside the NPOL detector hut which shielded the polarimeter from background particles. To limit the flux of the particles entering the NPOL, a collimator was installed at the entrance of the detector hut (Figure 3.2). The acceptances of the collimator matched those of the front array. Therefore, nearly all the particles passing through the collimator go through the front array. Each of the 70 detectors which comprised the NPOL is a NE-102 plastic scintillator. It is made of polyvinyltolulene and its density is 1.032 (g/cm^3) [Gro00]. The minimum ionizing energy (dE/dx$|_{min}$) of the material is 1.956 (MeV cm^2/g) [Gro00].

Every NPOL detector was equipped with two photo-multiplier tubes (PMTs), one on each end. Because the detector material is composed of an organic material which contains hydrogen and carbon most of the neutrons scattered from the *protons* in hydrogen and carbon in the front and rear detectors. Therefore, the scattering of the neutron is treated as an *np* scattering.

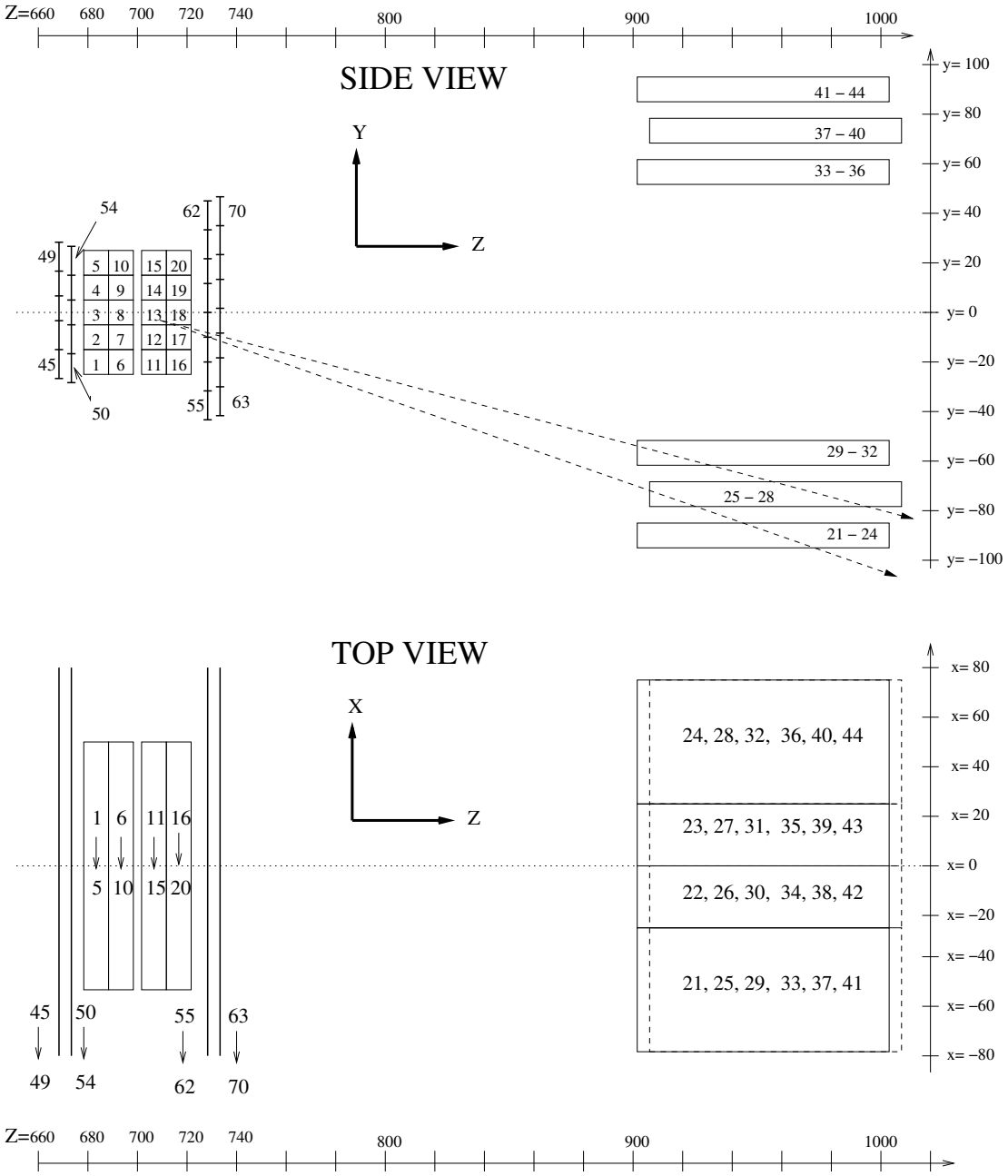

Figure 3.17: A side view (top figure) and top view (bottom figure) of the neutron polarimeter. Both figures are drawn to scale and the unit is cm. The numbers (1-70) marked in the figures are detector ID numbers. The fourth veto plane with detector IDs 63 through 70 did not exist when the data at Q^2=1.14 (GeV/c)^2 were taken. See text for detail.

3.8.1 NPOL Detector Arrays

Front Array

The front array served as the analyzer for the scattering asymmetry measurements. The center of the front array was located at 7.0 m from the target. It consisted of 4 vertical layers with 5 detectors in each layer. There was a 2-mm gap between the first and second layers, and the third and fourth layers. There was a 3-cm gap between the second and third layers (see Figure 3.17). A scintillator for the front array has the dimensions of 100.0 cm x 10.0 cm x 10.0 cm (in POL X,Y,Z coordinates, respectively). Scintillators in the front array are placed parallel to x-axis.

Rear Arrays

The rear arrays detect the particles scattered (or recoiled) from the material in the front array. They were located about 3 m from the front array. Top and bottom rear arrays were placed symmetrically with respect to the POL Y-axis (see Table B.2). Each rear array had 3 horizontal layers with 4 detectors on each layer. Scintillators in the rear arrays are placed parallel to z-axis. Two types of plastic scintillator were used: the *outer* two detectors in each rear layer were twice as wide as the *inner* two detectors. The dimensions of the outer (inner) detectors in POL coordinates are 50.8 cm x 10.2 cm x 101.6 cm (25.4 cm x 10.2 cm x 101.6 cm).

In order to optimize the rear detector positions, the following things were considered. First, the rear detectors were placed away from the direct particle flux, which was limited by the collimator for NPOL. Therefore, no particles can reach the rear arrays without interacting with the front detectors (see Figure 3.2). In other words,

the particles must be scattered in the front array to reach the rear arrays. Second, by taking into account the kinematics of the *np* scattering in the incident neutron energy range from 0.711 to 1.450 GeV/c, the rear arrays were placed so that both the neutron and proton from the same *np* reaction cannot be detected in the rear arrays. For example, if a scattered neutron is detected in a bottom rear detector, the recoil proton from *np* scattering *always* misses the upper rear detectors. This feature made it easy for us to determine whether the neutron scattered up or down. Third, the analyzing power for *np* scattering, A_y, depends on the scattering angle. Because the measured asymmetry value is proportional to A_y (as will be given in Equation 4.15), positions of the rear arrays were optimized to achieve larger A_y, thus larger asymmetry value. Finally, the positions were further optimized to maximize the neutron detector efficiency for the rear arrays. To do this, the second and fourth layers in the rear arrays (IDs 25-38 and 37-40) were placed 5-cm backward in the Z-direction. With this arrangement, the incoming neutrons were most likely to pass through *two* rear detector layers. The dashed lines in Figure 3.17 show the particles which pass through two rear detector layers. The efficiency of detecting neutrons in the front array was about 10%. However, because on average neutrons travel longer distances in the rear array than in the front, the efficiency for the top or bottom rear array is estimated to be about 30% [Sem00].

The rear detector positions were determined by taking into account those things discussed above. The position of each detector in the POL coordinate system is given in Appendix B.

Front Veto Array

The front veto (FRVT) array, located just in front of and parallel to the front array, consisted of 2 vertical layers with 5 detectors on each layer. The dimensions of each veto detector in POL coordinates are 160.0 cm × 11.0 cm × 0.635 cm. The FRVT served to identify the charge status of the particle which entered the front array. The FRVT covers a larger area than the acceptances of the collimator and front array (see Figure 3.17). Because each FRVT detector has a thickness of only 0.6 cm along the z direction, the probability that neutral particles interact with the FRVT detectors is quite small. When charged particles enter the NPOL, both FRVT and front detectors most likely have hits, and those hits must be closely correlated in time. Therefore, by examining the hit information from the FRVT and front detectors, one can tell the charge status of the particle which entered the front array. Thus, allowing us to select events involving neutral particles in the front array. During E93-038, veto signals are not part of the G_E^n event trigger (see Table 3.1) Therefore, the particle identification was left for the data analysis. The details of this particle identification for the front array will be discussed in Chapter 5.

Rear Veto Array

There was another veto array 5-cm behind the front 4th plane, and was parallel to the front array. We refer to these detector planes as the rear veto (REVT) array. Identical plastic scintillators as in FRVT were used in the REVT. When the Q^2=1.14 $(GeV/c)^2$ data were taken in year 2000, there existed only 1 vertical layer with 8 detectors on it. However, the second REVT layer with 8 detectors on it was installed in January of 2001. Each REVT plane covers the area larger than the acceptances

of the Rear detector arrays seen from the Front array.

Similarly with the FRVT array, neutral particles rarely interact with the REVT array. The REVT detectors were placed at *staggered* positions along the y-direction with respect to the front detectors (Figure 3.17). Because of this arrangement, the trajectory of a charged particle passed through both front and REVT detectors could be reconstructed from the position information from each detector. From the tracking information and the hit position(s) in the rear array, the charge status of a particle detected in the rear arrays could be determined. This feature will be discussed in detail in Chapter 5.

3.9 NPOL Electronics

3.9.1 NPOL Electronics (Detector Hut)

The detector hut electronics were located under the detector platform in the detector shielding enclosure. Figure 3.18 shows a schematic diagram of the NPOL front and rear detector electronics in the shielding hut. A PMT was coupled to each end of the plastic scintillator bar through a Lucite light pipe. A light-emitting diode (LED) was embedded in each light pipe and used for PMT gain stabilization. The high voltage supply were powered remotely by a 64 channel high-voltage CAEN crate which was located in the counting house. The anode signal from each PMT, also called as the pulse-height signal, was used. The anode signals from the front detectors were amplified by a factor of eight. The front pulse-height signals had to be amplified because of the reduced operational high-voltage of the PMTs. The lower high voltage was required to reduce the in the front PMTs and thereby to extend

the operational lifetime of the PMTs under the high-counting rate conditions of the front detector array The anode signal from the rear PMT was not amplified. The

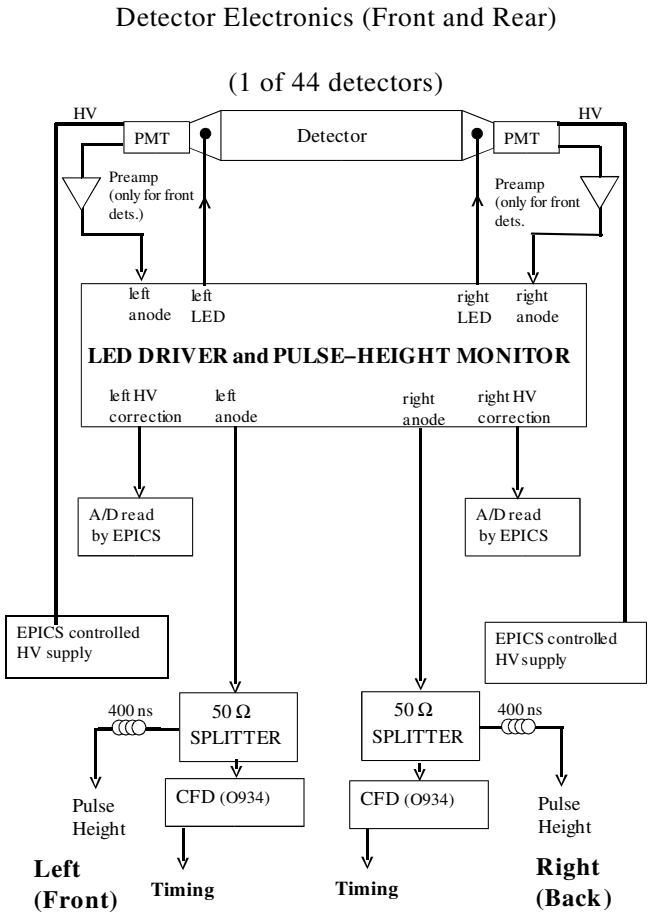

Figure 3.18: Detector electronics for front and rear detectors.

PMT anode signal was sent to the LED driver and pulse height monitor (PHM) module. The "LED driver and PHM" was a self-contained system that was built by the group from the Kent State University. For each PMT, the LED driver outputted a highly regulated pulse to the LED. The PMT anode signal from the LED flash was integrated with a 10-bit digitizer. A high-voltage correction value was generated

by comparing the new value of the integrated anode pulse to the rolling average of the previous 5 measurements This system was used to monitor any pulse-height drift of a detector. Because the response of the LED was Gaussian, a Gaussian fit was performed and the channel number that corresponds to the peak position was recorded.

After the PHM, each PMT anode signal was sent an Ortec 934 constant fraction discriminator (CFD) to form the timing signal for that PMT and to the counting house for pulse height measurements. The 50-Ω splitter was passive, so each output branch had half of the amplitude as the input. The 400-ns delay was made of RG58 cable and was needed to align the analog signals at the ADCs in the counting house with the ADC gates.

Figure 3.19 shows a schematic diagram of the NPOL veto detector electronics in the shielding hut. The electronics for the veto detectors is is similar to that for the front/rear detectors. However, as can be seen in Figure 3.19, the veto detector electronics does not have a PHM. In addition, leading-edge discriminators (LeCroy P710) were used instead of CFDs. The time resolution obtained from the leading-edge discriminator is not accurate compared to that of CFD. However, the ultra-precise time resolution of the veto detectors is not critical in our analysis, because we only need to identify the charged particles entering/existing the NPOL by looking at the time-correlation between the front and veto hits. A time resolution of a few ns was sufficient for this purpose. On the other hand, excellent time resolution was required for the front and rear arrays because the accuracy of the measured particle velocities and the position of hits in the detector arrays were directly related to the PMT time resolution.

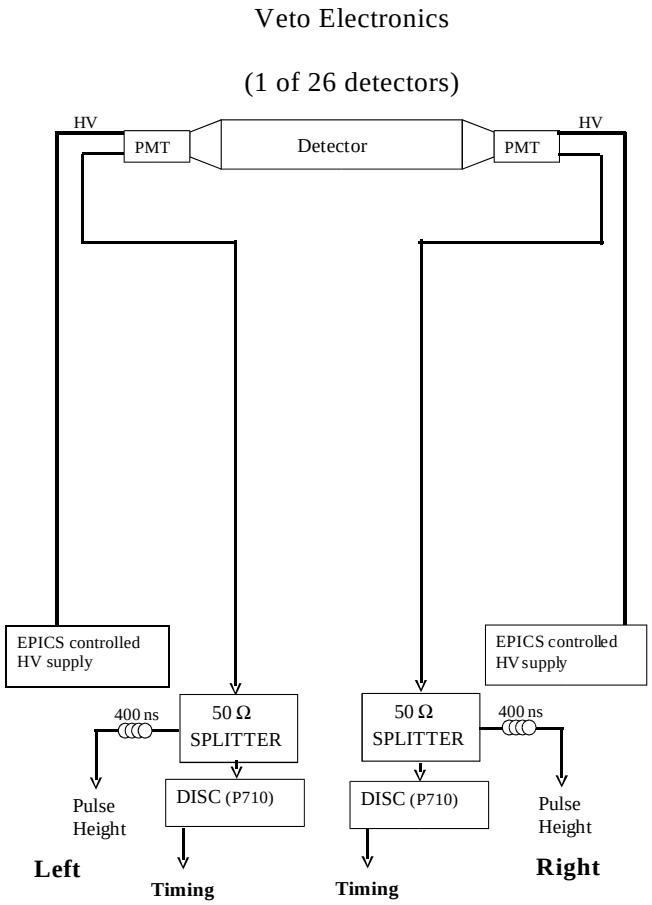

Figure 3.19: Detector electronics for veto detectors.

3.9.2 NPOL Electronics (Counting House)

Figure 3.20 shows a schematic diagram of the trigger electronics for front detectors in the counting house. Both analog and timing signals were passed through a filter transformer to reduce low-frequency noise. The timing signal from each PMT was sent to a LeCroy 3412 discriminator, to regenerate the signal and to convert it from NIM to ECL (emitter-coupled logic). One output from the LeCroy 3412 was sent to a level translator and another discriminator to form the TDC stop signal

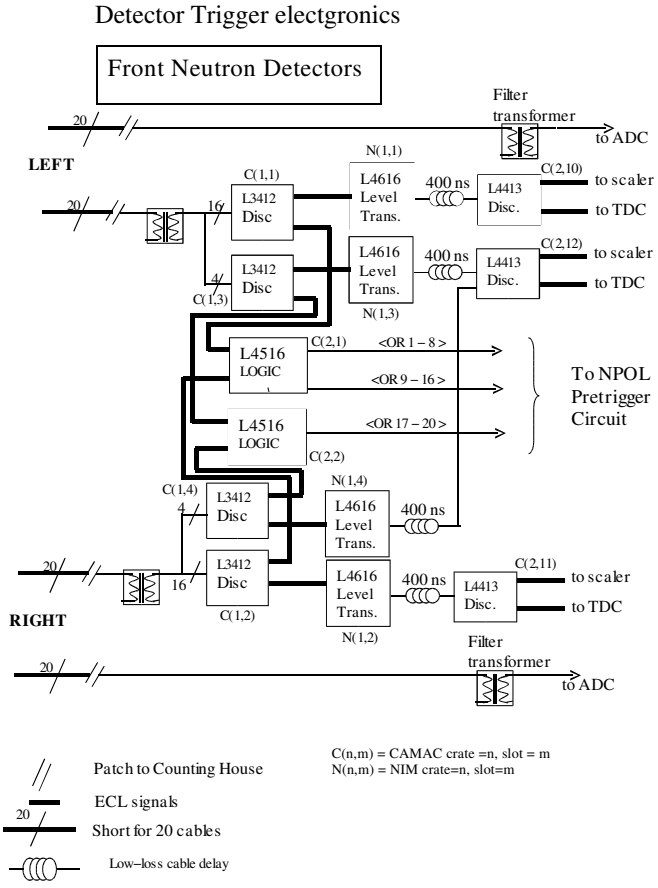

Figure 3.20: Detector trigger electronics for front detectors.

for that PMT and the scaler input for measuring the counting rate of that PMT. The other output from the LeCroy 3412 discriminator was sent to the LeCroy 4516 logic module. Here, an overlap coincidence of the left and right PMT timing signals was required. That is, a valid hit in a scintillator bar required timing signals from both PMTs to be present within a resolving time of about 50 ns. The output of this module is the logical OR of groups of eight detector bars, so the logical OR of detectors 1-8, 9-16, and 17-20 were sent to the circuit for generating the common signals for the digitizers Figure 3.21 is a schematic diagram of the trigger electronics

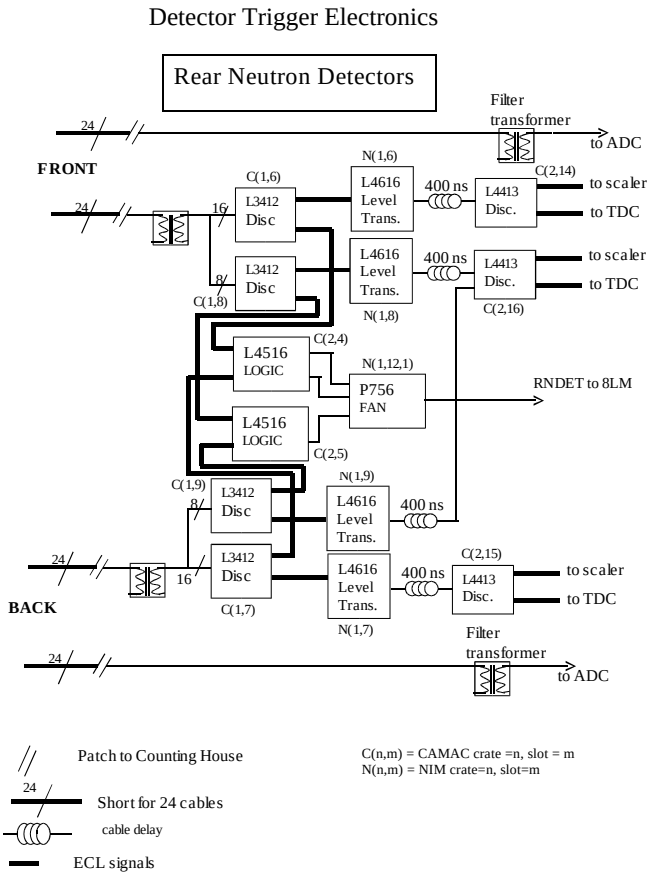

Figure 3.21: Detector trigger electronics for rear detectors.

for rear detectors. This diagram is quite similar to Figure 3.20. One major difference is that after the LeCroy 4516 logic module, the signal was sent to a Phillips 756 fan-in module where the detector signals were ORed before being sent to form common signals for the digitizers. Figures 3.22 and 3.23 are schematic diagrams of

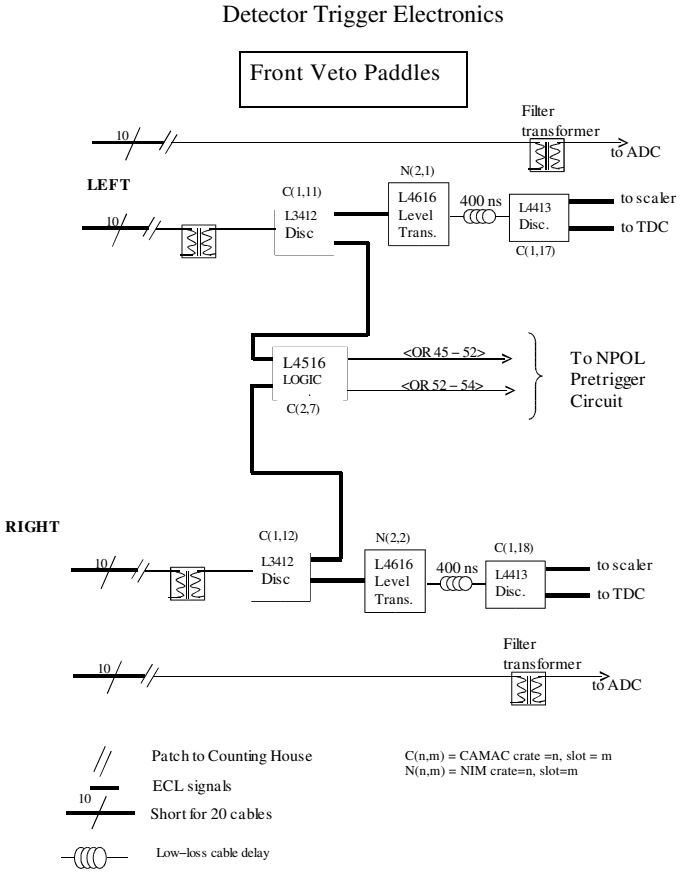

Figure 3.22: Detector trigger electronics for front Veto detectors.

the trigger electronics for veto detectors. Both diagrams are similar to Figure 3.20.

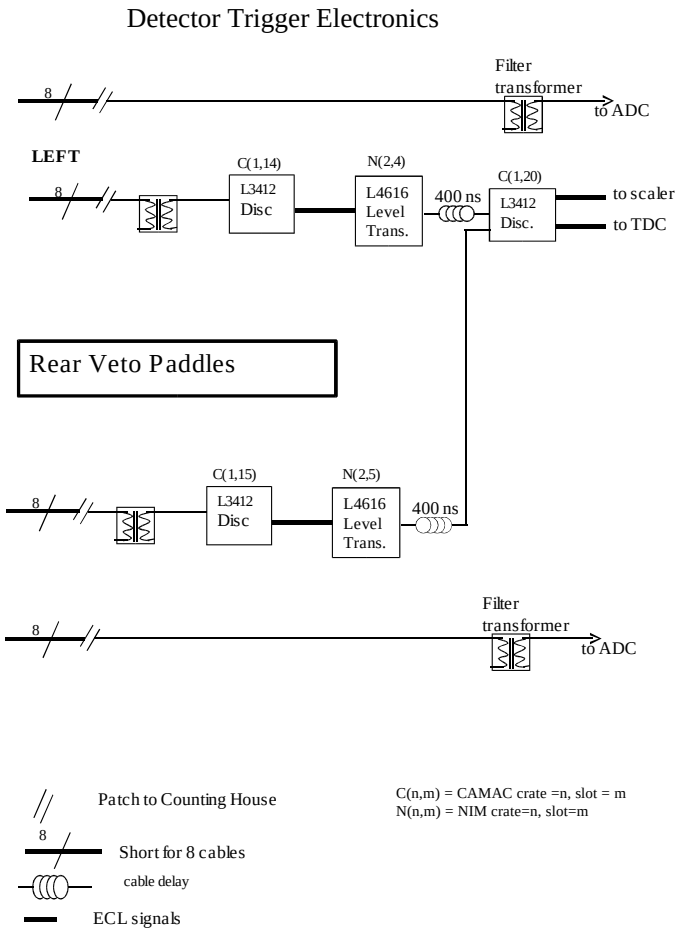

Figure 3.23: Detector trigger electronics for rear veto detectors.

3.9.3 NPOL Electronics for Digitizer Common Signals

Figure 3.24 is a schematic diagram of the TDC and ADC common signal circuit. This diagram shows how the the TDC common signals and ADC gate signals for each trigger were generated. The status of the trigger was controlled by the Trigger Supervisor (TS). The TS generated a L1 accept signal when the DAQ was not busy, that is, the system is not processing an event. TDC common signals and ADC gates were generated only when a level-one accept signal was logically true.

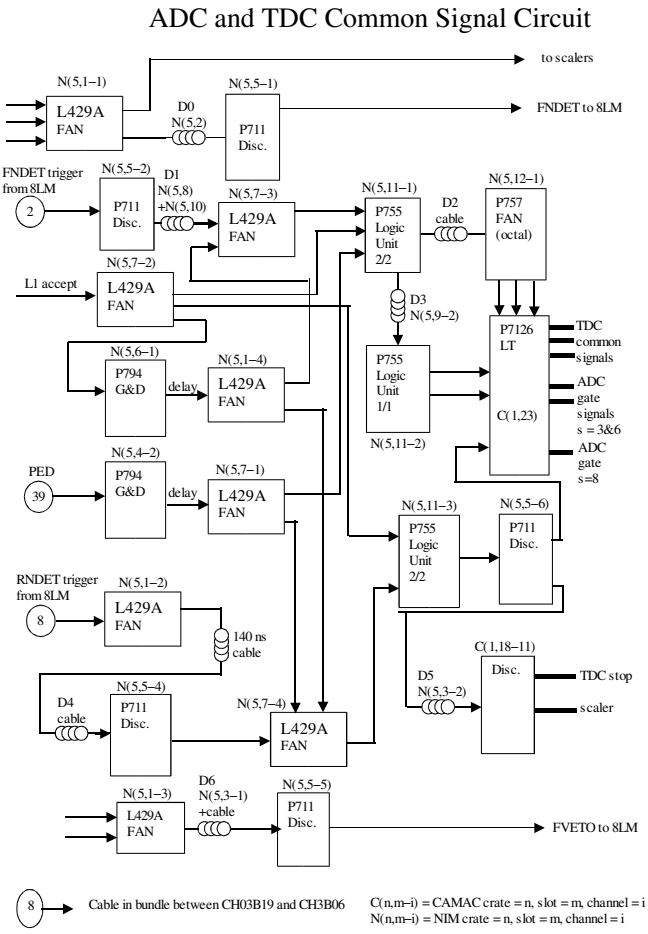

Figure 3.24: ADC and TDC common signal circuit

3.10 Data Acquisition

3.10.1 Overview of CODA

The ADCs and TDCs used in Hall C are fastbus modules made by the LeCroy corporation, and the scalers are VME modules made by the LeCroy corporation and by Struck Innovative Systems. All fastbus and VME crates were located in the Hall C counting house, and were controlled and read using the CEBAF on-line Data Acquisition (CODA) [Coda]. The main network components of the DAQ system are: (1) the readout controller (ROC), (2) the event builder (EB), (3) the event distributer (ET), and (4) the event recorder (ER). Each component communicates with the other components over a dedicated ethernet network. There are two types of ROCs in Hall C. One is Fastbus based and reads the digitizers (ADCs and TDCs). The other type is VME based; they are used to configure DAQ hardware and to read out scalers and trigger patterns. The Trigger Supervisor (TS) is the coordinator of trigger driven digitizers. It generates the trigger signals that are distributed to the VME and Fastbus Crates and tags each bundle of events from each crate with the event number. This event number tag is later used to associate data bundles from different crates as belonging to the same event trigger. Once a trigger is formed, data in Fastbus and VME crates are read out by the ROCs, which are CPUs in Fastbus and VME crates. For each event trigger, the Event Builder (EB) system receives the data fragments from the ROCs, bundles the fragments together into an event data bank, and writes event specific information in the header of the event bank. The event bank is then passed to the ET system, which is an event distribution system. The ET system passes the event bank to any client requesting it. For E93-038, the only client was the Event Recorder, which wrote the event banks to a disk data file.

Depending on the event type, an event contains digitized data from the HMS, NPOL, or both. The detailed descriptions on CODA are available at the CODA web site [Codb]

3.10.2 Triggers and Event Types for E93-038

In addition to coordinating the event fragments from the ROCs, the TS controls the status of data acquisition. The TS has three output control signals: GO, EN1, and BUSY. Whenever a new run is started or a run is resumed, a GO signal is generated. When a new data run is started, the first 1000 triggers are dedicated to pedestal calibration measurements for the HMS detectors. This event type is called PED. During this period, real physics triggers are blocked by the TS. After the PED events are finished, data accumulation for real physics triggers starts. When this happens, the following things must be satisfied. To form a *pretrigger*, data-taking has to be enabled (EN1) in the TS. In addition, the triggers must not come in the period of helicity transition (PHT). To form a *trigger*, it is further required that the DAQ is not busy (BUSY). In other words, trigger signals that arrive when the system is already processing a trigger are rejected. Definitions of E93-038 event pretriggers and triggers are given in Tables 3.1 and 3.2.

To form a three-fold coincident event, the following things must happen: (1) a trigger is generated by a hit in one of the NPOL front detectors, (2) there must be a hit in the NPOL rear detectors within a time window of $\sim$100 ns, and (3) a HMS trigger, which is independent of the NPOL trigger, must be generated within a time window of $\sim$40 ns. Figure 3.25 shows the relative coincidence timings of the pretriggers (HMS, front, rear, and veto) at the input to the LeCroy 8LM modules. Because of the importance of knowing the coincidence time between hits in the HMS

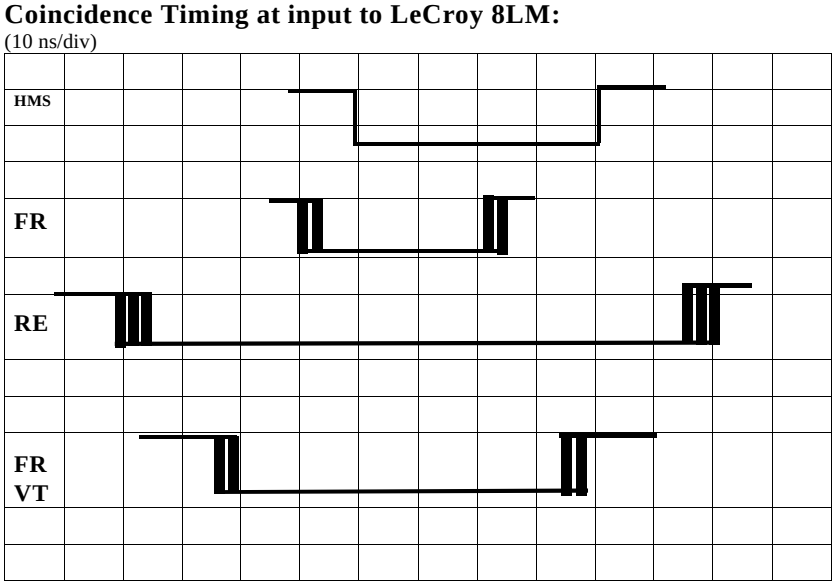

Figure 3.25: Coincidence timing

hodoscope and the NPOL front array, redundancy in this measurement was designed into the electronics. The trigger signal for the NPOL front and rear arrays were used as stop signals in a TDC in the HMS electronics; the HMS TDC start signals are defined from the HMS trigger signal. As discussed in Section 5.7, the NPOL-HMS coincidence timing was saved in the variable ph_start in our analyzing software. Table Table 3.3 gives the event types for JLab E93-038 that were used in the data acquisition and analysis. Each event type in fact corresponds to one of the trigger inputs.

3.10.3 EPICS and Scaler Events

A set of software tools called Experimental Physics and Industrial Control System (EPICS) [EPI] was used to control and monitor the status of the experimental

Output	Definition	Trigger
0	(HMS)&(EN1)&(not PHT)	HMS PreTrig
1	(SOS)&(EN1)&(not PHT)	SOS PreTrig
2	(HMS)&(FNDET)&(RNDET)&(EN1)&(not PHT)	G_E^n PreTrig
3	(PED)&(GO)&(not EN1)	PED PreTrig
4	(HMS)&(EN1)&(not PHT)&(not BUSY)	HMS Trig
5	(SOS)&(EN1)&(not PHT)&(not BUSY)	SOS Trig
6	(HMS)&(FNDET)&(RNDET)&(EN1)&(not PHT) &(not BUSY)	G_E^n Trig
7	(PED)&(GO)&(not EN1)&(not BUSY)	PED Trig

Table 3.1: 8LM #1 outputs for slot=17. (EN1: Data-taking enabled, PHT: Period of helicity transition, PED: Pedestal, FNDET: NPOL Front, RNDET: NPOL Rear.) SOS was not used in our experiment.

Output	Definition	Trigger
0	(HMS)&(FNDET)&(EN1)&(not PHT)	G_M^n PreTrig
1	(FNDET)&(RNDET)&(EN1)&(not PHT)	NPOL PreTrig
2	(RNDET)&(EN1)&(not PHT)&(not BUSY)	RNDET Trig
3	(HMS)&(FNDET)&(RNDET)&(not VT)&(EN1) &(not PHT)	Vetoed G_E^n PreTrig
4	(HMS)&(FNDET)&(EN1)&(not PHT)&(not BUSY)	G_M^nTrig
5	(FNDET)&(RNDET)&(EN1)&(not PHT)&(not BUSY)	NPOL Trig
6	(HGS)&(EN1)&(PHT)&(not BUSY)	HGS Trig
7	(FNDET)&(EN1)&(not PHT)&(not BUSY)	FNDET Trig

Table 3.2: 8LM #2 outputs for slot=16. (EN1: Data-taking enabled, PHT: Period of helicity transition, HGS: Helicity-gated scalers, FNDET: NPOL Front, RNDET: NPOL Rear.)

components. EPICS is the same system used to control the accelerator at JLab. Examples of the outputs from EPICS include the target temperature, the beam position, the current in the dipole magnet, and the high-voltages applied to the detectors. In general, the values of the EPICS outputs do not change significantly when data are taken unless something unaccepted happens to the system. One can monitor the status of the experimental components by reading the EPICS values (or so-called slow-control variables). Most of the EPICS outputs were read out from VME crate

Source	Trigger Input	Event Type	Comments
General Scalers	0	0	Not helicity-gated
HMS Singles	1	1	
SOS Singles	2	2	Not used during E93-038
NPOL Singles	3	6	
NPOL Cosmics	4	6	
HMS-NPOL Coin	5	3	G_E^n triggers
HMS-FrontNPOL Coin	6	3	G_M^n triggers
Helicity-Gated Scalers	7	5	
Pedestal	8	4	First 1000 physics events

Table 3.3: Trigger inputs and event types in E93-038 experiment. Event types for EPICS events (not given in this table) are 131 and 132.

every 30 seconds and were recorded on disk automatically. However, some EPICS outputs which needed to be frequently monitored were read out every 2 seconds.

To monitor the status of the entire experiment, many scaler variables were defined. Examples of the scaler outputs include the beam helicity, 1 MHz clock, counts from BCMs, and the counts for each detector. From the scaler counts, one can calculate, for instance, the elapsed time, beam current, and count rate for each detector. The scaler data are read out from VME crates every 2 seconds and were recorded on disk as a scaler event. The beam helicity information was recorded in each physics event bank.

Chapter 4

Methods for Extracting Asymmetry and the Ratio g

4.1 Cross Ratio and Scattering Asymmetry

The NPOL measures the scattering asymmetry of the neutron from the polarization component, $P_\perp$, which is *perpendicular* to the momentum of the neutron. If the spin of the neutron is precessed through an angle χ, $P_\perp$ is written as

$$P_\perp = P_S^{'} \cos\chi + P_L^{'} \sin\chi \tag{4.1}$$

$$= P_e(D_{LS'} \cos\chi + D_{LL'} \sin\chi), \tag{4.2}$$

where P_e is the polarization of the electron beam, P_S' and P_L' are the sideways and longitudinal polarization components, respectively, of the neutron emitted into the angular acceptance of NPOL, and $D_{LS'}$ and $D_{LL'}$ are the polarization transfer coefficients given in Equations 1.81 and 1.82, respectively. As will be discussed

below, we calculated the asymmetry from the the measured scattering yields using the *cross ratio* method. We outline in this section our application of the cross-ratio method to determine the asymmetries of neutron scattering from the front array of the scintillator bars.

We consider the number of particles detected in the top or bottom rear array which are scattered (or recoiled) from the front array. In this case, the front detector array serves as a *target*. The number of counts detected at the scattering angle θ and the azimuthal angle ϕ, $\mathcal{N}(\theta, \phi)$, in given in Equation 4.3.

$$\mathcal{N}(\theta, \phi) = n\, N_0\, \Delta\Omega\, \varepsilon\, \sigma(\theta, \phi), \tag{4.3}$$

where n is the number of neutrons incident on the *front* detector array, N_0 is the number of nuclei per square centimeter in the *front* array, $\Delta\Omega$ is the solid angle subtended by the *rear* detector array, ε is the efficiency of the *rear* detector array and $\sigma(\theta, \phi)$ is the cross section for scattering a *polarized* nucleon into the angles θ and ϕ. The scattering of a polarized nucleon is different from that of an unpolarized nucleon. The $\sigma(\theta, \phi)$ and the cross section for scattering an *unpolarized* particle, $\sigma_0(\theta)$, are related to each other:

$$\sigma(\theta, \phi) = \sigma_0(\theta)\, [\, 1 + \, P_\perp\, A_y(\theta)]. \tag{4.4}$$

Equation 4.4 is also as the *definition* of the analyzing power, $A_y(\theta)$, of the reaction. However, because our measurements integrate over the finite sizes of the front and rear detector arrays, Equation 4.3 must be written as an average over the acceptance of the rear array from *any* point inside the front array. Using Equations 4.3 and 4.4, the average of the total counts is expressed as

$$< \mathcal{N} > \cong n\, N_0\, < \Omega > < \varepsilon > < \sigma_0 > [\, 1 + \, P_\perp\, < A_y >]. \tag{4.5}$$

Here, <> means the variable is averaged over the acceptances of the experimental setup.

Let us now consider extracting the asymmetries using Equation 4.5. Definitions of several new variables used in this section are given in Table 4.1. Although the rear detectors were arranged in such a way that Ω^U and Ω^D were equal (see Appendix B for detector positions), we consider below the more general case in which those *were not identical* possibly due to a slight misalignment of the detectors. Similarly, n^+ and n^-, A_y^U and A_y^D, σ_0^U and σ_0^D should be nearly identical for our setup, but we allow for them to be different. We see below that the asymmetries computed using the *cross ratio* method [Ohl73] does not depend on most of these variables.

$N_U^+(N_D^-)$:	# of neutrons scattered **up (down)** when the beam helicity was **positive (negative)**
$N_U^-(N_D^+)$:	# of neutrons scattered **up (down)** when the beam helicity was **negative (positive)**
n^+ (n^-):	# of neutrons incident on the front detector array when the beam helicity was **positive** (**negative**)
Ω^U (Ω^D):	Solid angle from the front to the **upper** (**lower**) half of the rear array
ε^U (ε^D):	*Average* detector efficiency of the **upper** (**lower**) half of the rear array
A_y^U (A_y^D):	Analyzing power of the reaction in the front array averaged over the acceptance for a neutron being scattered from the front array into the **upper** (**lower**) half of the rear array
σ_0^U (σ_0^D):	Cross section of the *unpolarized* neutron in the front array averaged over the geometrical acceptance for a neutron being scattered from the front array into the **upper** (**lower**) half of the rear array

Table 4.1: Definition of the variables used in the computation of the scattering asymmetry.

Using the variables given in Table 4.1, the yields N_U^+, N_D^+, N_U^- and N_D^- are

written as follows:

$$N_U^+ = n^+ N_0 \Omega^U \varepsilon^U \sigma_0^U (1 + P_\perp A_y^U) \quad (4.6)$$

$$N_D^+ = n^+ N_0 \Omega^D \varepsilon^D \sigma_0^D (1 - P_\perp A_y^D) \quad (4.7)$$

$$N_U^- = n^- N_0 \Omega^U \varepsilon^U \sigma_0^U (1 - P_\perp A_y^U) \quad (4.8)$$

$$N_D^- = n^- N_0 \Omega^D \varepsilon^D \sigma_0^D (1 + P_\perp A_y^D) \quad (4.9)$$

Now, the geometrical mean of N_U^+ and N_D^- (Equations 4.6 and 4.9, respectively) gives us

$$\sqrt{N_U^+ N_D^-} = N_0 \sqrt{n^+ n^- \Omega^U \Omega^D \varepsilon^U \varepsilon^D \sigma_0^U \sigma_0^D (1 + P_\perp A_y^D)(1 + P_\perp A_y^U)}. \quad (4.10)$$

Similarly, the geometrical mean of N_D^+ and N_D^- (Equations 4.7 and 4.8, respectively) is

$$\sqrt{N_D^+ N_U^-} = N_0 \sqrt{n^+ n^- \Omega^U \Omega^D \varepsilon^U \varepsilon^D \sigma_0^U \sigma_0^D (1 - P_\perp A_y^D)(1 - P_\perp A_y^U)}. \quad (4.11)$$

Dividing Equation 4.10 by Equation 4.11 gives us the following:

$$r \equiv \left(\frac{N_U^+ N_D^-}{N_U^- N_D^+} \right)^{1/2} \quad (4.12)$$

$$= \sqrt{\frac{(1 + P_\perp A_y^D)(1 + P_\perp A_y^U)}{(1 - P_\perp A_y^D)(1 - P_\perp A_y^U)}}. \quad (4.13)$$

The quantity r in Equation 4.12 is the definition of *cross ratio*. Although we assumed the quantities for the *upper* rear array were different from those for the *lower* rear array, most of them *exactly* canceled out in Equation 4.13. Note that the detector efficiencies ε^U and ε^D were not necessarily the same because those depend on the performance of each rear detector. However, Equation 4.13 does not depend either on ε^U nor ε^D. Note also that in the E93-038 experiment the rear detectors were

arranged in such a way that Ω^U and Ω^D were equal unless detectors were misaligned. Therefore, we could claim that A_y^U and A_y^D were nearly identical. If $A_y^U = A_y^D$ $(= A_y)$, then Equation 4.13 becomes:

$$r = \frac{1 + P_\perp A_y}{1 - P_\perp A_y}. \tag{4.14}$$

From Equation 4.14, we have

$$\xi = P_\perp A_y = \frac{r-1}{r+1}, \tag{4.15}$$

where ξ is the *scattering asymmetry*. Equation 4.15 suggests that the asymmetry ξ is proportional to $P_\perp$, and ξ can be computed from the cross ratio r, which is defined in Equation 4.12. The measured value of the asymmetry contains the crucial information about the polarization component, $P_\perp$. We will discuss in Sections 4.4 and 4.5 the connection between the scattering asymmetry, which is given by Equation 4.15, and the electric form factors.

4.2 Uncertainties in Cross Ratio and Scattering Asymmetry

The uncertainty in r can be obtained easily by considering a log of both sides of Equation 4.12:

$$y \equiv \ln r = \frac{1}{2}\left(\ln N_U^+ + \ln N_D^- - \ln N_D^+ - \ln N_U^-\right). \tag{4.16}$$

Assuming that the uncertainties for N_U^+, N_D^-, N_D^+, and N_U^- are uncorrelated, the uncertainty in y can be calculated by applying Equation D.1 to Equation 4.16. Note that $\Delta y = \Delta r / r$.

$$\frac{\Delta r}{r} = \frac{1}{2}\sqrt{\left(\frac{\Delta N_U^+}{N_U^+}\right)^2 + \left(\frac{\Delta N_D^-}{N_D^-}\right)^2 + \left(\frac{\Delta N_D^+}{N_D^+}\right)^2 + \left(\frac{\Delta N_U^-}{N_U^-}\right)^2}, \tag{4.17}$$

where ΔN_U^+, ΔN_D^-, ΔN_D^+ and ΔN_U^- are the uncertainties in the yields N_U^+, N_D^-, N_D^+ and N_U^-, respectively. The detailed procedure for obtaining the yields N_U^+, N_D^+, N_U^- and N_D^- and their uncertainties ΔN_U^+, ΔN_D^+, ΔN_U^- and ΔN_D^- will be presented in Chapter 5.

Similarly, the uncertainty in ξ can be obtained from Equation 4.15 by applying Equation D.1:

$$\Delta\xi = \frac{2}{(r+1)^2}\Delta r. \tag{4.18}$$

4.3 Ratio of the Polarization Components of the Recoil Neutron

In E93-038, the ratio of the electric to magnetic form factor of the neutron, $g \equiv G_{En}/G_{Mn}$, was determined by measuring the ratio of the longitudinal component ($P_L^{'}$) to the sideways component ($P_S^{'}$) of the neutron polarization vector. The ratio of the neutron polarization components was determined by measuring the neutron scattering asymmetry in the polarimeter for two orientations of the polarization vector of the neutron incident on the front detector array. The neutron spin direction at the front detector array relative to the momentum direction of the neutron that was headed toward the polarimeter at the target was set with the current in the Charybdis magnet. That is, the magnetic field in the Charybdis caused the polarization vector of the neutrons to precess through an angle χ as the neutrons passed on their way from the target to the polarimeter.

The data for the ratio of the neutron polarization components were taken using two distinct types of spin-precession techniques, which will be referred to as *method-1*

and *method-2*. The first method is based on the principle of measuring each polarization component separately. While this method is an obvious choice and is relatively insensitive to errors in the precession angle, it does have the weakness that if one polarization component is small, the statistical uncertainty for that component will dominate the statistical uncertainty for the ratio. This weakness is avoided in the second method by always measuring a combination of the two polarization components. However, the compromise is that the measurement becomes more sensitive to errors in χ. The data at Q^2=1.14 $(GeV/c)^2$ were taken with precession angles $\chi = 0^\circ$ and $\chi = \pm 90^\circ$ (method-1). The data at Q^2=0.45 $(GeV/c)^2$ were taken with precession angles $\chi = \pm 40^\circ$ (method-2). Each method is described in detail below.

4.4 Method-1: Spin Precession by 0° and ±90°

The polarization vector of the neutron and its components are illustrated in Figure 4.1 for *no* precession (left figure) and for precession by $+90^\circ$ (right figure). With precession angle $\chi = 0^\circ$, the scattering asymmetry, ξ_S, from the *sideways* component (i.e, $P_\perp = P_S^{'}$) of the recoil neutron is obtained. On the other hand, with precession angle $\chi = +90^\circ$, the scattering asymmetry, ξ_L, from the *longitudinal* component of the recoil neutron is obtained because $P_L^{'}$ is now *perpendicular* to the momentum of the neutron (i.e, $P_\perp = P_L^{'}$). The data were also taken with precession angle $\chi = -90^\circ$ to check for systematic errors in the precession angle, i.e., the value for ξ_L should be the same for $\chi = -90^\circ$, and $\chi = +90^\circ$, except for the sign of the asymmetry. In addition, a similar consistency check was performed by inserting a half-wave plate between the laser and the photocathode at the electron source. The half-wave plate rotates the spin vector of the electron by 180° at the source.

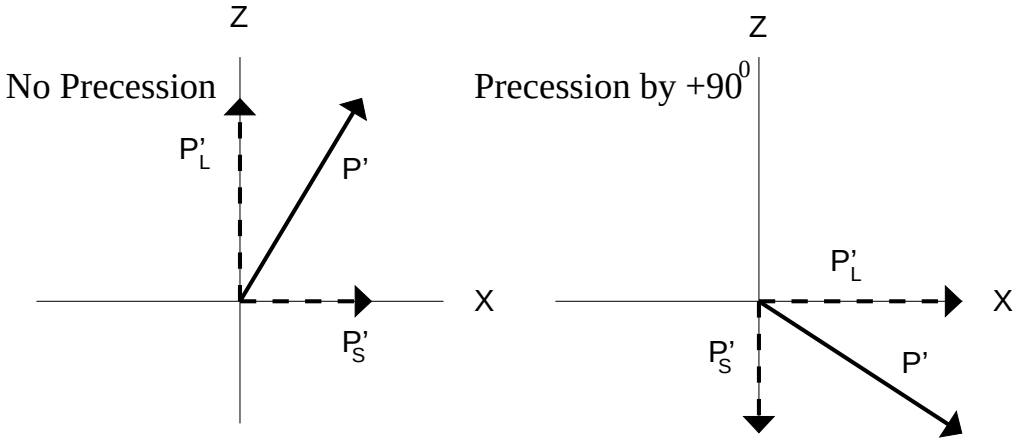

Figure 4.1: Spin precession by angles $\chi = 0°$ (no precession) and $\chi = +90°$. When the spin was not precessed (left figure), the neutron polarization vector with magnitude P$'$ (solid line) have longitudinal and sideways components P'_L and P'_S, respectively. The momentum vector of the neutron is along the $+z$ axis, and the neutron polarimeter only measures the spin component *perpendicular* to z, $p_\perp$, which is along the x axis. The P$'_L$ and P$'_S$ are parallel and transverse to the recoil neutron momentum, respectively (i.e, $P_\perp = P'_S$). After the spin vector was precessed by $+90°$ (right figure), P$'_L$ become *perpendicular* to the recoil neutron momentum (i.e, $P_\perp = P'_L$).

This rotation physically interchanges the + and − helicity of the electron beam and is effectively like rotating the entire polarimeter (including the Charybdis magnet) about the Z axis by 180°. The ratio g can be determined from the ratio of the measured two asymmetry values, because the asymmetry ratio η is equal to the ratio of P'_S to P'_L as will be shown below. Using Equation 4.15, the following two equations are obtained for ξ_S and ξ_L:

$$P'_S\, A_y = \xi_S \tag{4.19}$$

$$P'_L\, A_y = \xi_L \tag{4.20}$$

Therefore, dividing Equation 4.19 by Equation 4.20 gives us the following:

$$\eta \equiv \frac{\xi_S}{\xi_L} = \frac{P'_S}{P'_L}, \tag{4.21}$$

where η is the ratio of the asymmetries. Equation 4.21 indicates that the asymmetry ratio is equal to the ratio of the sideways to longitudinal component of the polarization vector. Therefore, using Equation 4.21 and the PWIA formula Equation 1.90, the value for g is given as follows:

$$g = -K_R \left(\frac{P'_S}{P'_L}\right) = -K_R\,\eta, \tag{4.22}$$

where K_R is a kinematic factor given in Equation 1.92. The advantage of this ratio method in Equations 4.21 and 4.22 is that the value for g does not depend on the analyzing power, A_y, nor on the beam polarization, P_e, as they canceled out in these equations. Therefore, the systematic uncertainty in g from this ratio technique is small as will be discussed in Chapter 8. It should be emphasized that Equation 4.22 is valid only for the PWIA. Because the neutron in a LD_2 target cannot be considered as a *free* nucleon, Equation 4.22 cannot be used to obtain our final result of g.

By applying Equation D.1 to Equations 4.21 and 4.22, respectively, the relative uncertainties in η and g can be calculated *assuming that the precession angle χ has no uncertainty* [1] :

$$\frac{\Delta\eta}{\eta} = \sqrt{\left(\frac{\Delta\xi_S}{\xi_S}\right)^2 + \left(\frac{\Delta\xi_L}{\xi_L}\right)^2} \tag{4.23}$$

$$\frac{\Delta g}{g} = \frac{\Delta\eta}{\eta}. \tag{4.24}$$

[1] We will discuss in Section 7.1 the systematic uncertainty in g due to the uncertainty in χ.

4.5 Method-2: Spin Precession by $\pm\chi$

The value for g can be determined from the ratio of the asymmetries which were obtained with precession angles $+\chi$ and $-\chi$. In this section, the expressions for η and P'_S/P'_L in terms of asymmetries are different from those given in the previous section. Figure 4.2 illustrates the polarization vector of the neutron before and after the precession by $+\chi$ (left figure) and $-\chi$ (right figure). The ratio of P'_S to P'_L, which is needed in the determination of g, can be written in terms of the angle δ, as shown in Figure 4.2.

$$\frac{P'_S}{P'_L} = \tan\delta \tag{4.25}$$

After the polarization vector is precessed by angle $+\chi$, the projection of the polar-

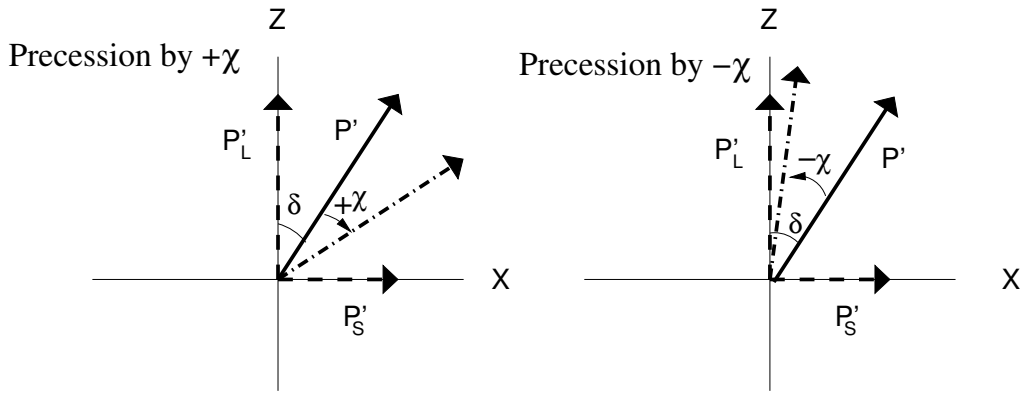

Figure 4.2: Spin precession by angles $\pm\chi$. The *unprecessed* neutron spin vector (solid line) had the magnitude P' and the longitudinal and sideways components (P'_L and P'_S, respectively). The angle δ is between the (unprecessed) spin vector and P'_L. The P'_L and P'_S were parallel and transverse to the momentum of the recoil neutron. After the spin vector was precessed by an angle $+\chi$ (left figure) or $-\chi$ (right figure), the vector with dash-dotted line was obtained. Therefore, the component along the x axis after the precession by $+\chi$ became $P'\sin(\delta+\chi)$. Similar to the precession by $-\chi$, the x component is $P'\sin(\delta-\chi)$.

ization vector onto the x-axis, P_x^+, is written in terms of δ, χ and the magnitude of

the polarization vector, $P^{'}$.

$$P_x^+ = P^{'} \sin(\delta + \chi). \tag{4.26}$$

Similarly to the polarization precession by angle $-\chi$, the projection of the polarization vector onto the x-axis, P_x^-, can be written as:

$$P_x^- = P^{'} \sin(\delta - \chi). \tag{4.27}$$

In method-2, the asymmetry ratio η is defined as the ratio of the asymmetry for $-\chi$ precession, ξ_-, to the asymmetry for $+\chi$ precession, ξ_+. From Equations 4.26 and 4.27, η can be evaluated in terms of δ and χ.

$$\eta \equiv \frac{\xi_-}{\xi_+} = \frac{P_x^-}{P_x^+} \tag{4.28}$$

$$= \frac{\sin(\delta - \chi)}{\sin(\delta + \chi)} = \frac{\sin\delta\cos\chi - \cos\delta\sin\chi}{\sin\delta\cos\chi + \cos\delta\sin\chi} = \frac{\tan\delta - \tan\chi}{\tan\delta + \tan\chi} \tag{4.29}$$

Therefore, from Equations 4.25 and 4.29, $\tan\delta$ is given by

$$\tan\delta \equiv \frac{P_S^{'}}{P_L^{'}} = \left(\frac{1+\eta}{1-\eta}\right)\tan\chi. \tag{4.30}$$

Finally, the g for the PWIA is given by

$$g = -K_R\left(\frac{P_S^{'}}{P_L^{'}}\right) = -K_R\left(\frac{1+\eta}{1-\eta}\right)\tan\chi. \tag{4.31}$$

Similarly for method-1, the value for g does not depend on A_y nor P_e as they cancel out in Equations 4.30 and 4.31. Therefore, the systematic uncertainty in g from this ratio technique is small as we will discuss in Chapter 8. As in method-1, it should be emphasized that Equation 4.31 is valid for the PWIA. Therefore, this equation cannot be used to obtain our final result of g.

By applying Equation D.1 to Equations 4.28 and 4.31, respectively, the relative uncertainties in η and g can be calculated *assuming that the precession angle χ has no uncertainty*:

$$\frac{\Delta\eta}{\eta} = \sqrt{\left(\frac{\Delta\xi_+}{\xi_+}\right)^2 + \left(\frac{\Delta\xi_-}{\xi_-}\right)^2} \tag{4.32}$$

$$\frac{\Delta g}{g} = 2\left(\frac{\Delta\eta}{\eta^2-1}\right). \tag{4.33}$$

As in method-1, a consistency check was performed by inserting a half-wave plate at the electron source which changed the sign of the measured asymmetry. The relative uncertainty in g due to the uncertainty in χ can be calculated from Equation 4.31, and it is given as follows:

$$\frac{\Delta g}{g} = \frac{2\,\Delta\chi}{\sin(2\chi)}. \tag{4.34}$$

From Equation 4.34, $\Delta g/g$ becomes minimum at $\chi = 45^\circ$ *if* $\Delta\chi$ *is the same for any angle* χ. However, because $\Delta\chi$ slightly depends on the choice of χ, we ran a simulation program with the realistic magnetic field to simulate the precession of the neutron polarization vector at Q^2=0.45 (GeV/c)^2. We chose the optimal value for χ to be 40° for which the value of $\Delta g/g$ became close to its minimum value.

4.6 Comment on Systematic Uncertainty in Analyzing Power

When Equation 4.14 was derived, we assumed that $A_y^U = A_y^D$. Although this assumption is quite fair (because detectors were assembled so that this condition would be satisfied), we consider below the case in which A_y^U and A_y^D are *slightly*

different from each other. If this happens, we introduce the average of the two analyzing powers for convenience:

$$\tilde{A}_y = \frac{A_y^U + A_y^D}{2}. \tag{4.35}$$

Using this $\tilde{A}_y$, A_y^U and A_y^D can be expressed as follows:

$$A_y^U = \tilde{A}_y + \Delta \tag{4.36}$$

$$A_y^D = \tilde{A}_y - \Delta \tag{4.37}$$

and

$$\Delta = \frac{A_y^U - A_y^D}{2}. \tag{4.38}$$

Let us assume the relation $\Delta \ll \tilde{A}_y$ holds. Plugging Equations 4.36 and 4.37 into Equation 4.13, the cross ratio r is written with $\tilde{A}_y$ and Δ. Then, r can be expanded in powers of Δ. It can be shown that the first-order term of Δ cancels in the ratio r:

$$r = \tilde{r}\,[1 - \mathcal{O}(\Delta^2)], \tag{4.39}$$

where $\mathcal{O}(\Delta^2)$ is a function of Δ^2 and $\tilde{r}$ is:

$$\tilde{r} = \frac{1 + P_\perp \tilde{A}_y}{1 - P_\perp \tilde{A}_y}. \tag{4.40}$$

Because the difference between $\tilde{r}$ and r is proportional to the second order in Δ, we consider below extracting the asymmetries from $\tilde{r}$, instead of using the true expression of r given in Equation 4.13. Because Equation 4.40 has the same form as Equation 4.15, we would obtain for method-1 the asymmetry $\tilde{\xi_S}$ from the sideways component and the asymmetry $\tilde{\xi_L}$ from the longitudinal component of the neutron polarization vector, respectively. From Equation 4.15, those asymmetries are given by:

$$P'_S \tilde{A}_y = \tilde{\xi_S} \tag{4.41}$$

$$P'_L \tilde{A}_y = \tilde{\xi_L} \tag{4.42}$$

Therefore, the asymmetry ratio $\tilde{\eta}$ is:

$$\tilde{\eta} \equiv \frac{\tilde{\xi_S}}{\tilde{\xi_L}} = \frac{P_S^{'}}{P_L^{'}} = \eta, \tag{4.43}$$

The analyzing power cancels out in the ratio as before and the asymmetry ratio $\tilde{\eta}$ becomes equal to η up to the second order in Δ. Similarly, the same result is obtained for method-2. Therefore, we conclude that if A_y^U and A_y^D satisfy the condition $\Delta \ll \tilde{A}_y$, the asymmetry ratio is not affected by this difference up to the second order in Δ. Because of this, we did not take into account the systematic uncertainty in A_y that contributes to the value for g, as this can be ignored in our methods.

Chapter 5

Data Analysis

5.1 Introduction

In the previous Chapter, it was shown that the ratio of the sideways to longitudinal components of the neutron polarization (P'_S/P'_L) can be computed from the cross ratio r which is defined in Equation 4.12. In this chapter, we discuss how to obtain the yields, N_U^-, N_D^-, N_U^+, and N_D^+ that are needed to calculate r. To do this, we have to identify 'good' quasielastic coincidence events by applying cuts on various physics quantities. In addition, the background counts must be subtracted.

In our analysis, TOF histograms are used to obtain the yields. As we discuss in this chapter, we use histograms of *front* TOF, which is the TOF from the interaction position in the 15-cm long target to the neutron detection point in the front array, and ΔTOF, which is the neutron TOF difference between the detection times in the front and rear arrays. These TOFs are corrected by taking into account the flight distance as described later.

In general, the background distribution on TOF histograms are flat because the background events are mostly particles detected in the NPOL that are not correlated with the particles detected in the HMS. Therefore, the subtraction of background events can be performed quite simply by using TOF histograms. Other histograms such as those for the neutron β and the neutron momentum are not suitable for obtaining yields because their background distributions are not flat.

At the beam energies used in our experiment, the following particles existed, and they may or may not hit the NPOL detectors:

- Neutral particles: neutron, gamma, and π^0
- Charged particles: electron, proton, and $\pi^{\pm}$

Therefore, we first need to find a way to identify the neutron events from other types of particle interaction in the NPOL detectors.

5.2 Procedure for Data Analysis

After data are taken, we ran Engine, a first-pass analysis software for our experiment, to create a binary data file called Data Summary Tape (DST). The DST contains the reconstructed electron momentum and interaction points, and the raw NPOL TDC and ADC numbers. The second-pass analyzer was used to perform the time-calibration for NPOL and to reconstruct the physics quantities. The results were stored in the HBOOK histogram for each run. Then, the program which integrates particular histograms to obtain the total yield from which the asymmetry value for particular polarization vector precession angle is calculated. This procedure is repeated to obtain an asymmetry for each run. After asymmetries for all good

runs are obtained, they are weighted-averaged to give the final asymmetry values for two different precession angles.

5.3 Criteria for Run Selection

There exist some runs which were taken when experimental components were malfunctioning. Those runs should not be included in the analysis. Table 5.1 lists the run-selection criteria which were applied to select 'good' runs for the analysis. To identify the problems listed in this Table, the following items were examined

1.	No problems with HMS and NPOL equipment
2.	No problems with MCC/beam delivery; no reports of unstable beam
3.	No problems with Data Acquisition (DAQ)
4.	No problems with target
5.	No runs with anomalously small or large yields [i.e., events/mC]
6.	No short runs (see text below)

Table 5.1: Run Selection Criteria

carefully: Hall-C electronic log book, E93-038 Run Sheets, Run Summary Tables, scaler and EPICS files, and various histograms created after the second-pass replay was finished. In addition, we removed all runs with fewer than 500k (250k) event triggers for Charybdis off (on) runs. However, runs were not excluded if there were not *serious* hardware problems (items 1 through 4 above). To determine the severity of the problem, relevant histograms for those runs were inspected.

5.4 E93-038 Engine – First-Pass Analysis Software

5.4.1 Standard Hall-C Engine

Standard Hall-C analysis software called Engine was designed to analyze raw data for the standard Hall-C detectors such as the HMS and the Short Orbit Spectrometers (SOS). It was developed by Hall-C staff members [Bea94, Woo94]. The Hall-C ENGINE software basically consists of initialization routines, main event loop, and end-of-run routines. Figure 5.1 shows a schematic flow chart for the E93-038 analysis Engine. Details of the standard Hall-C Engine can be found in Hall-C theses [Arr98, Dut99]. Upon running with CODA data as input, Hall-C ENGINE decodes raw event data, analyzes events, and outputs results in various output files, such as histograms, ntuples, DSTs, and ASCII data files. Engine output files are created according to the parameters a user defines in the REPLAY.PARM file. It is an Engine configuration file which defines many run parameters, file names and the file paths, etc. The Hall-C Engine can create histograms and ntuple (or DST) files for physics events, and scaler and pedestal output files written in ASCII for scaler and pedestal events.

5.4.2 Modifications to Hall-C Engine

To analyze events from the neutron detectors, changes were made to the standard Hall-C engine. In addition, all the calls to the the SOS subroutines were turned off because SOS was not used in our experiment. The E93-038 ENGINE was developed from the Hall-C ENGINE by adding the part which decodes raw TDC and ADC signals from the NPOL detectors. The decoded TDC and ADC channel numbers

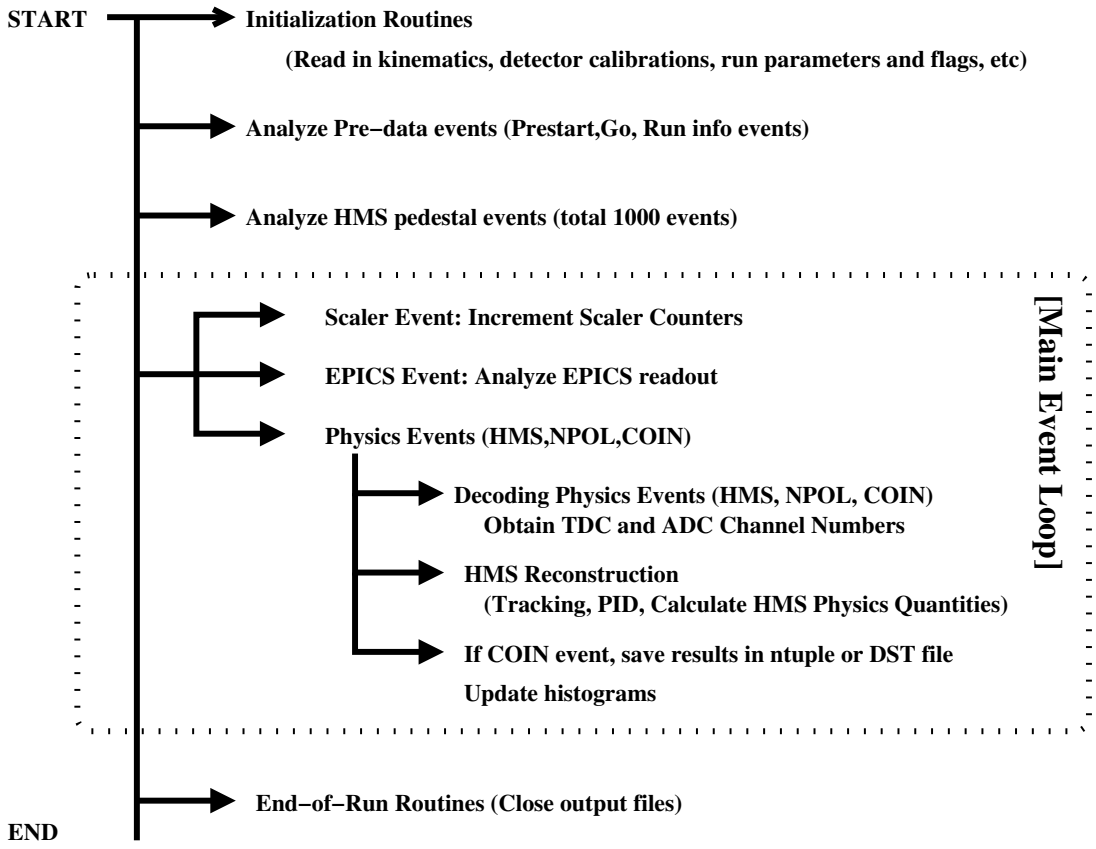

Figure 5.1: Flow chart for E93-038 Engine

from the NPOL detectors are saved in ntuple files (or DST files as we discuss for my analysis) for the npol-hms coincidence events. Those ntuple or DST files for E93-038 data were mainly used for the data analysis. A new scaler file, which we refer as NPOL scaler file, is created in E93-038 Engine for each run. The NPOL scaler file contains the trigger count rates from each of the 70 NPOL detectors. During the analysis, NPOL scaler files are used to obtain information such as the total charge and the average beam current for the run. In addition, it reports start date and time of the run, total charge accumulated, average beam current, HMS trigger counters,

number of events analyzed for each event type, etc. The E93-038 Engine also creates for each run an ASCII report file for EPICS events, which we refer as an EPICS file. The EPICS file contains output information from main EPICS variables for beam, Charybdis magnet, Moller polarimeter, target and HMS magnets. For data analysis, the current and polarity of the Charybdis magnet as well as the status of the half-wave-plane were obtained from the EPICS files. The first-pass analysis is performed by running E93-038 Engine.

In subsequent sections and chapters, 'Engine' refers to both Hall-C standard Engine and E93-038 Engine. However, we will refer to 'E93-038 Engine' if things described are applied to E93-038 Engine only.

5.4.3 The CEBAF Test Packages

The CEBAF Test Packages (CTP) is a set of analysis tools that are quite useful and convenient for on- and off-line data analysis. It has been developed by Wood [Woo95] and is based loosely on the LAMPF Q system [Lam78]. There are many CTP files, which are ASCII data files, that users can define. For example, one can define parameters such as run parameters, run flags, kinematics values, and calibration parameters for HMS detectors. They are loaded to ENGINE through CTP at the beginning of the Engine analysis. In addition to those parameters, one can list in CTP files histogram definitions and format of scaler files to be used when histogram and scaler files are created/updated. In the all-C Engine, histograms are created in a HBOOK file [Gee94]. In CTP, one can use the same variable names that are used in the Engine source code if those variables are registered in the Engine common block files (file extension is .cmn) and are called from a CTP initialization routine. After this is done, Engine variables can be accessible from CTP. Because

histograms are in general accumulated when some conditions are met, users set event test/cut definitions in CTP files. Users can change the cut/test definitions of histograms without recompiling the Engine software. That is quite convenient as users often need to modify cut definitions for histograms during data analysis.

5.4.4 Initialization Routines in E93-038 Engine

When the E93-038 Engine runs, it reads the main configuration file called REPLAY.PARM which defines the input and output file names and their paths, run flags, and run parameters. In the initialization routines of the E93-038 Engine, variables for physics quantities and input/output file names are registered which are to be used in the software and CTP. Next, parameter files (such as kinematic parameters, run parameters) and a map file which contains a table that maps hardware configuration to software definition are loaded. In addition, CERN routines are called. They create hbook and ntuple/DST files so that they can be updated while physics events are analyzed. Finally, pre-data events for CODA such as Prestart, Go, and Run events are analyzed before the Engine main event loop.

5.4.5 Main Event Loop in the E93-038 Engine

After the initialization routines, Engine proceeds to the main event loop in which events are decoded and analyzed. In the decoding routine, data are decoded according to the mapping information which maps hardware configuration with software definition. Events are then analyzed according to the event types used in E93-038. E93-038 triggers and event type are given in Table 3.3. For a scaler event type, E93-038 scaler variables are incremented. For an EPICS event type, EPICS event

is examined, and the updated values are saved in E93-038 EPICS variables. For all physics events, physics event types for this experiment are decoded. The first 1000 physics events in the CODA data are HMS pedestal events. They are used to calibrate the ADC pedestal values. Because a NPOL-HMS coincidence event consists of a NPOL and a HMS event, both of them must be analyzed. The E93-038 Engine used the original HMS routines from the standard Hall-C Engine. Therefore, the E93-038 Engine analyzes HMS events and does the tracking and physics reconstruction in HMS as in the standard Engine. However, the E93-038 Engine, which is the first-pass analyzer for this experiment, only decodes NPOL events. Physics reconstruction is not performed in the E93-038 Engine. It is performed in a second-pass analyzer and the time-calibration program for this experiment. For an NPOL event, the E93-038 Engine decodes raw NPOL data and obtains ADC and TDC channel numbers of a hit from each of the two phototubes attached to each of the 70 NPOL detector bars.

While in the main event loop, the E93-038 Engine updates three scaler files for GEN (it denotes *General*), HMS, and NPOL for each run. The GEN scaler file served as a summary of the general scalers for beam, target, and a brief summary of HMS scaler information. The HMS scaler file contains detailed scaler information on the HMS detector system. The NPOL scaler file contains not only NPOL detector count information but also has all the trigger information such as NPOL, HMS, and singles events. As mentioned earlier, the NPOL scaler file is our main scaler file. During on-line analysis, an EPICS report file was created at the beginning of each run. The file reports the status of the experimental components from which EPICS outputs were generated.

5.4.6 Data Summary Tape

For general purpose, the E93-038 Engine produced the ntuple files (the file extension is .rzdat) which contain all the reconstructed HMS physics quantities, beam and target information, NPOL TDC and ADC channel numbers and some miscellaneous items. Because each ntuple file for E93-038 data contains only 20,000 events, a lot of ntuple files were created for each run (a single run can contain up to 3 million events) after the first-pass analysis. Therefore, one had to deal with many ntuple files for data analysis. However, one can create in place of those many ntuple files a single Data Summary Tape (DST) for each run. The DST is a binary data file which contained basically the same items as those in ntuple files. However, because some of the items saved in ntuple files were not used nor useful for data analysis, we did not save those items in the DST. Advantages of the DST file is that a single data file is created for each run, and the data file size is smaller by nearly 30% than the total size of those ntuple files. In addition, DST contains EPICS and scaler events which were extracted from the original CODA data. Routines for generating the DSTs were developed by Churchwell [Chu01a], and were incorporated into the E93-038 Engine. For the data analyses performed for this dissertation, DST files were created at JLab by running a modified version of the E93-038 Engine. All the DST files were then transported to Duke where the analyses were performed and the files were saved on a local disk.

5.4.7 HMS Tracking and Reconstruction

We describe below how events in the HMS are analyzed in the Engine. As discussed in Section 3.5.1, timing information is obtained from the HMS hodoscopes

and position information from the drift chambers. The main purpose of the HMS analysis was the reconstruction of physics quantities for the scattered the electron such as TOF, momentum, scattering angle, and the interaction position in the focal plane and at the target. It will be explained how they are reconstructed from the signals obtained in the HMS. As we mentioned earlier, the HMS routines in the standard Hall-C Engine have been incorporated into the E93-038 Engine without modifications. Details on HMS tracking and reconstruction in the Engine can be found in early Hall-C theses [Arr98, Dut99].

Times and Energies in the HMS detectors

For each HMS event, TDC and ADC channel numbers from the scintillators are converted into times and energies deposited at the beginning of the HMS reconstruction routine in the Engine. Times are then corrected due to variations in pulse-heights, cable length offsets, and signal propagation through the scintillator bar. The scintillator time serves as the start time for the scintillator plane. All the drift chamber TDCs are then converted into times. In addition, the times when the charged particle passed through the drift chamber planes can be determined from this start time. The difference between the time measured from the drift chamber sense wire and the time the particle passes the drift chamber plane gives the drift time. The Engine calculates from the drift time the drift distance of the electron, assuming its drift velocity is known.

Similarly, the ADCs from the scintillators, Čerenkov, and calorimeter are converted for each event into energies from photo-multiplier tubes (PMTs). The total energy deposited in a scintillator bar is obtained by summing the energies from the PMTs attached to each end of the bar. In addition, the number of photoelectrons in

the Čerenkov detector and total energy deposited in the calorimeter are obtained.

Tracking

Once a charged particle passes through each drift chamber, which consists of six planes, position information from each plane is obtained as described above. The Engine then tries to reconstruct the track of the particle path from the position information of the hits. However, the location of the sense wire which detected the electron, and its drift distance do not uniquely determine where the charged particle passed through each drift chamber plane. The ambiguity is we do not know whether the particle passed left or right of the wire on the y and y' planes. Similarly for the other chamber planes; this is referred as a left-right ambiguity. A total of six planes yield a total of $2^6 = 64$ combinations as a result of this ambiguity. In the Engine, clusters of hits are identified and the space points of the hits are fitted with a straight line (due to no electric and magnetic fields in the chambers). The tracking routine loops over all the combinations in both chambers and a track for each chamber is found. A full track that consists of two tracks in both chambers is then fitted, and the track with the smallest χ^2 value gives the final track of the charged particle.

Event Reconstruction

After the final track has been identified, the Engine reconstructs track-related quantities in the focal plane. As mentioned in Section 3.5.2, the plane exactly halfway between the two wire chambers and perpendicular to the central trajectory is defined as the *focal plane* (but this plane is not exactly the same as the true focal plane as it is a curved surface). Figure 5.2 shows the true focal plane and the detector focal plane. Particles having the same momenta always converge in the focal plane.

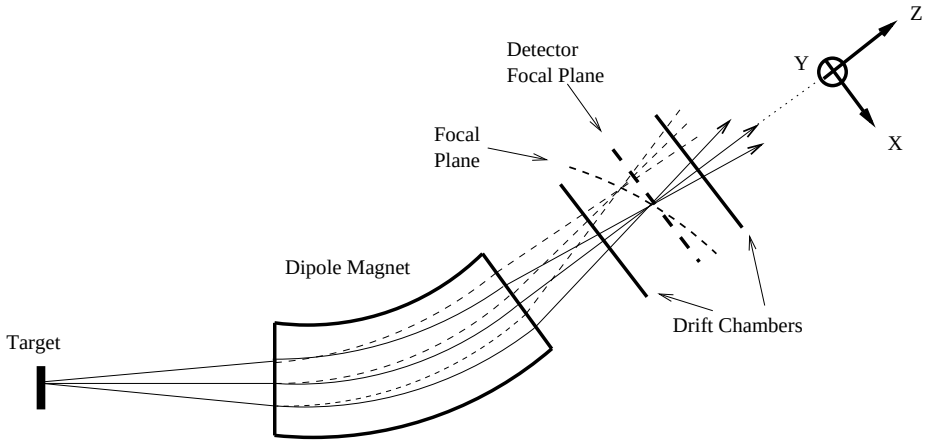

Figure 5.2: A schematic diagram of the focal plane (side view) and definition of the HMS transport coordinates. Solid and dashed curves drawn in the dipole indicate that the paths of charged particles having the same momenta converge on the same point in the focal plane. Particles for the solid curves have the central kinematic momentum, and therefore their paths converge both in the focal plane and in the detector focal plane. Particles for dashed curves have the momentum smaller than the central value, and their paths converge in the focal plane, but not in the detector focal plane.

The HMS quantities are evaluated in the transport coordinate system in Engine. In this system, $\hat{z}$ points along the central axis of HMS from the target toward the detector package, $\hat{x}$ points down (dispersive direction), and $\hat{y}$ is $\hat{y} = \hat{z} \times \hat{x}$ which points left (non-dispersive direction) when seen from the target to the spectrometer. The intersection of the HMS central axis and the focal plane gives the origin of this coordinate system. These coordinates are also drawn in Figure 5.2. The Engine calculates in this detector focal plane the following four quantities: the positions x_{fp} and y_{fp} as well as the vertical and horizontal slopes along the trajectory $x'_{fp} \equiv dx/dz|_{_{fp}}$ and $y'_{fp} \equiv dy/dz|_{_{fp}}$. Here, the subscript fp denotes the focal plane.

From the four quantities calculated in the focal plane, the following quantities are determined: (1) the interaction position at the target (x_{tar} and y_{tar}), (2) the

slope of the particle trajectory at the target (x'_{tar} and y'_{tar}), (3) the relative particle momentum $\delta_{\rm HMS} \equiv ((p_e - p_e^{cent})/p_e^{cent}) \times 100$, where p_e and p_e^{cent} are the measured electron momentum and the central kinematics value in the HMS, respectively. However, x_{tar} is not reconstructed, and we define $x_{tar} = 0$ because it's not possible to determine 5 unknowns from the four focal plane quantities. In summary, x'_{tar}, y_{tar}, y'_{tar} and $\delta_{\rm HMS}$ are reconstructed by the Engine software. Those target quantities can be expressed in terms of the focal plane variables using the matrix formalism of Penner [Pen61].

$$q^i_{tar} = \sum_{j,k,l,m} M^i_{jklm} \cdot (x_{fp})^j (x'_{fp})^k (y_{fp})^l (y'_{fp})^m, \tag{5.1}$$

where q^i_{tar} for $i = 1, 2, 3$, and 4 represents $x'_{tar}, y_{tar}, y'_{tar}$ and $\delta_{\rm HMS}$, respectively, and j, k, l, m are positive integers which satisfy $0 \leq j + k + l + m \leq N$, where N is the order of the expansion. M^i_{jklm} is a transport matrix element. which can be expressed as

$$M^i_{jklm} = \langle q^i_{tar} | x^j_{fp}\, x'^k_{fp}\, y^l_{fp}\, y'^m_{fp} \rangle, \tag{5.2}$$

The matrix elements are calculated for the HMS to 5th order in Engine.

Optimization of HMS Matrix Elements

Magnetic fields and the reconstruction of the matrix elements can be calculated by COSY Infinity program [Ber95] which was used to model the magnetic components of the spectrometer. Because it is not possible to provide the exact fields in the spectrometer, the matrix elements obtained from this program do not represent the optimal properties of the spectrometer. As suggested by Loffler *et. al.* [Löf73], the optical properties can be determined by means of an experimental ray tracing method in which rays of particles are traced over the acceptance of a spectrometer.

Matrix elements for this experiment were obtained from the measurement of the ^{12}C(e, e$'$)^{12}C reaction using a sieve slit [Mac02].

During E93-038, so-called δ-scan runs were taken with the beam energy of 884.25 MeV, and the scattering angle of 23.55°. Seven values of the HMS dipole magnetic field were chosen during the data taking while other kinematics parameters such as the beam energy, the scattering angle, and the momentum of the scattered electron, $p_s = 880.5$ MeV/c, were fixed. Because the *central* value of the momentum measured in the HMS, p_c, changed due to the seven values of the dipole fields applied, seven values of δ ($\delta = (p_s - p_c)/p_c$) were obtained. These data allowed us to study the optical properties of the HMS with the use of CMOP software for Hall-C [Ass97].

5.5 Pulse-Height Energy Calibration for NPOL

The ADC channel number for a particular PMT is proportional to the energy deposited in the scintillator viewed by the PMT. To set the low-level energy threshold on the neutron polarimeter, it was necessary to energy calibrate each PMT. The mean pulse-height energy in each scintillator bar was obtained by taking the average of the left and right light energies. The relationship between the light out of the scintillator and the energy deposited in the scintillator bar in units of MeV electron equivalent (MeVee) was obtained using a ^{228}Th γ-ray source. To take data for the NPOL energy calibration, a radioactive ^{228}Th source was placed at the center of each scintillator bar. The source emits 2.61 MeV gamma rays, which leads to a recoil electron energy in the range of 0.0 to 2.38 MeV. Because this electron energy is below the hardware threshold (4 MeVee for front detectors and 10 MeVee for rear detectors), the signal is amplified by a high linearity 10x amplifier so that it simulates a maximum energy

deposited of 23.8 MeV. A precision attenuator with four settings (0.1x, 0.2x, 0.5x, and 1.0x) was also used along with the linear amplifier. During the energy calibration runs, a trigger signal was generated whenever there was a coincidence between signals from left and right PMTs. Data were collected for each of the 44 scintillator bars with amplification settings of 1x, 2x, 5x, and 10x.

Scattering of photons by electrons, which is called Compton scattering, is a well-understood scattering phenomenon. If photons have much higher energy than the binding energy of the atomic electrons are considered as free. Suppose a photon with the frequency ν is scattered at angle θ by an electron. Then, the kinetic energy of the recoil electron, T, is given by

$$T = h\nu \frac{\gamma(1-\cos\theta)}{1+\gamma(1-\cos\theta)}, \tag{5.3}$$

where $\gamma = h\nu/m_e c^2$. In Equation 5.3, T has the maximum value of $T_{max} = h\nu\frac{2\gamma}{1+2\gamma}$ for a given photon energy, $h\nu$. This maximum recoil energy is known as the Compton edge. The energy distribution of the recoil electrons for Compton scattering is given by the Klein-Nishina formula [Leo94],

$$\frac{d\sigma}{dT} = \frac{\pi\, r_e^2}{m_e\, c^2\, \gamma^2}\left[2 + \frac{s^2}{\gamma^2(1-s)^2} + \frac{s}{1-s}\left(s - \frac{2}{\gamma}\right)\right], \tag{5.4}$$

where $s = T/h\nu$, σ is the cross section, $r_e = e^2/(4\pi\epsilon_0 m_e c^2) = 2.818$ (fm) is the classical electron radius [1], and ϵ_0 is the permittivity of free space.

We used a simple analysis program which is independent of the Hall-C Engine [How00] for the pulse height calibration. When the program runs, it decodes the raw NPOL CODA data banks and saves the results in a file for each calibration run. A histograms was created for each photomultiplier tube. The decoded

[1] This is a parameter introduced for convenience, and has nothing to do with the size of the electron.

ADC value for each event was saved in one of the histograms according to the ID of the phototube from which the signal was generated. In the end, all the histograms were saved in a HBOOK file for each run. After the file for the ADC histograms was created, we used the Physics Analysis Routine (PAW) which was developed at CERN [fPP] to analyze the ADC data. The ADC spectrum for each detector, however, does not resemble the distribution predicted by Equation 5.4. The reason for this difference is because the energy response of our detectors is not perfect in reality: it is Gaussian in shape. That is, a single value of energy deposition in the detector results in a Gaussian shaped distribution of ADC channels about a centroid channel. In addition, there is a contribution from background events in the ADC spectrum. Therefore, the ADC spectrum is fitted with a function that is a product of Equation 5.4 and a Gaussian function with three parameters. Assuming T scales linearly with the channel number, we have only two parameters (slope and offset) to determine for the energy calibration for each PMT. The spectrum is fitted with the five adjustable parameters (3 for the Gaussian resolution function and 2 for the line). The best fit with the minimum χ^2 value gives us the values for the five parameters. The fitting procedure is repeated for each of the 44 front and rear detectors, and the slope and offset for each detector PMT are obtained. The details of the pulse height calibrations for NPOL are described in [Tir01b]. The energy calibrations for the veto detectors were not performed because the energy information given by these detectors is not needed in our data analysis. The relative uncertainty in the slope and offset calibration parameters is estimated to be less than 10% [Tir01a].

We note that the detector energy calibration is based on the energy deposited by *electrons* from Compton scattering. Therefore, the calibrated energy is given in units of MeVee (MeV *electron equivalent*). However, when a neutron interacts in a NPOL

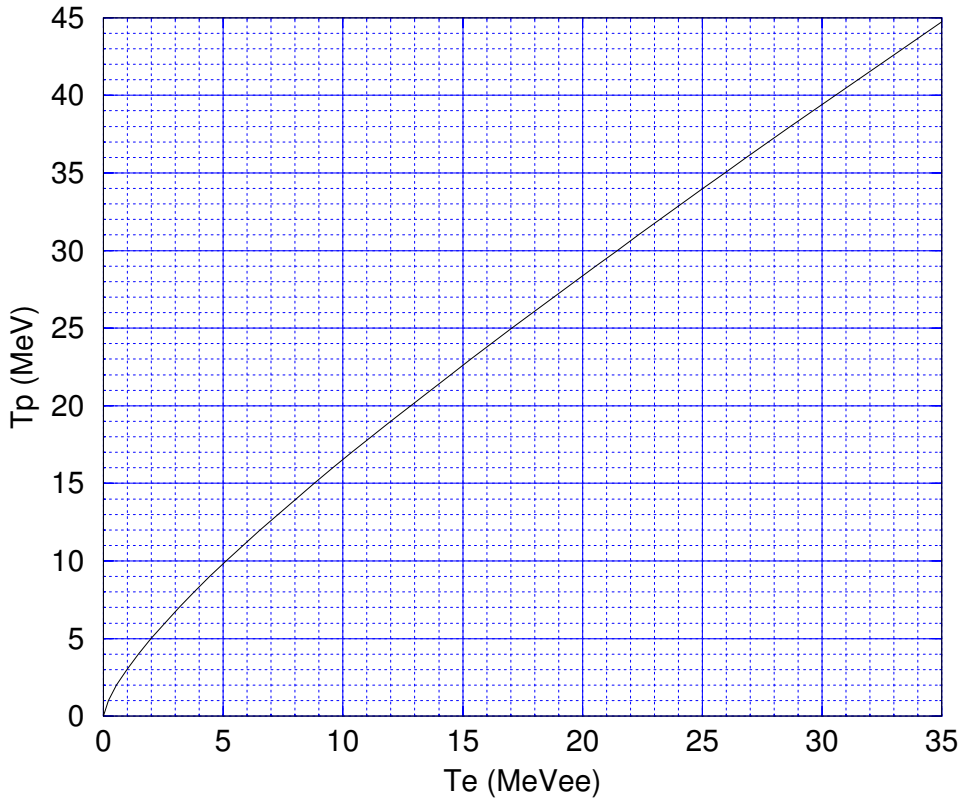

Figure 5.3: Light output of electrons vs protons. T_e (T_p) is the light energy of electrons (protons) deposited in a NE-102 scintillator bar. For large T_e, the relation between T_p and T_e is approximated by a linear function, $T_p = (T_e + 8.0)/0.95$.

scintillation detector, it is the recoil *proton* which produces the a light signal. Because the detector response to protons is different from that for electrons, the actual energy in MeV deposited by a proton cannot be obtained if the calibration constants for electrons are used. In other words, the reconstructed energy for a proton represents the energy in MeVee. However, a relationship between light output of electrons and that of protons for NE-102 scintillators has been measured [Mad78], and it is shown in Figure 5.3. The relation becomes linear at higher energy (above 20 MeVee). This relationship can be used to convert the energy obtained in MeVee to the actual energy in MeV deposited in a scintillator by a proton.

5.6 Second Pass Analyzer

A second pass analyzer was specifically developed for the data analysis presented in this dissertation. It consists of the time calibration program and physics reconstruction program. Both programs run with a DST file as input. The time calibration program performs time calibration for the NPOL detectors. They were calibrated from the raw TDC histograms, and the calibration constants were saved in a file. After the time calibrations were finished, production runs were analyzed with the analyzer for the NPOL physics reconstruction. This analyzer uses for each run a DST file and a time-calibration data file. The results were saved in an HBOOK file which has both an ntuple and histograms. Histograms were used to check the quality of data and the quality of the physics event reconstruction. In addition, they were used to obtain yields for the calculation of the scattering asymmetries. An ntuple file, which is a huge database, saves all the results (values) for *every* event. The analyzer also creates for each run a summary report, which is an ASCII file. It contains some general information about the run (run start time, the total charge and average beam current during the run, status of the Charybdis magnet and half-wave plate information, etc) as well as the yields and the value of the asymmetry for the run. The information and results saved in this output file are used later when the results are statistically weighted-averaged to give the final results a particular Q^2 value.

5.7 Timing Calibration for the NPOL

5.7.1 Introduction

The accurate time and position information were needed to select 'good' events. Therefore, the timing calibration for the NPOL needed to be performed as accurately as possible. The E93-038 trigger requires a three-fold coincidence: a hit in the HMS, at least one hit in the front array and at least one hit in the rear array of the polarimeter must occur within a time window of 70 (ns).

The timing-calibration method and routines for the Duke second-pass analyzer were developed by Churchwell [Chu01b]. The basic idea of the time-calibration method is to reference the time of a hit in the NPOL relative to the time in the HMS so that the NPOL trigger time is subtracted out. This will be explained in detail in the following subsections. We first introduce three time-calibration constants for *each* detector that are used to calculate the time and position of a hit in the polarimeter. Then, we discuss how to determine those constants. One might think that the calibration for the NPOL could be performed by measuring the gamma flush events from the target as the speed of the gamma is exactly c. However, we did not observe it because it was attenuated by the lead placed in front of the NPOL.

5.7.2 Time-of-Flight

Because the timing signal goes through, for example, cables and trigger circuits after a particle hit the detector, the time measured by the TDC is not the time-of-flight(TOF) that we need. Figure 5.4 illustrates how the signal propagates until it reaches the TDC. For the two scintillators shown in Figure 5.4, and the HMS trigger

signal, measured TDC times have the following relations,

$$T_L(1) = T(1) + T_L^S(1) + T_L^C(1) - T_s \quad (5.5)$$

$$T_R(1) = T(1) + T_R^S(1) + T_R^C(1) - T_s \quad (5.6)$$

$$T_L(2) = T(2) + T_L^S(2) + T_L^C(2) - T_s \quad (5.7)$$

$$T_R(2) = T(2) + T_R^S(2) + T_R^C(2) - T_s \quad (5.8)$$

$$T_{HMS} = TOF(HMS) + T_{HMS}^C - T_s. \quad (5.9)$$

All the time quantities given above have the units of TDC channel numbers (1

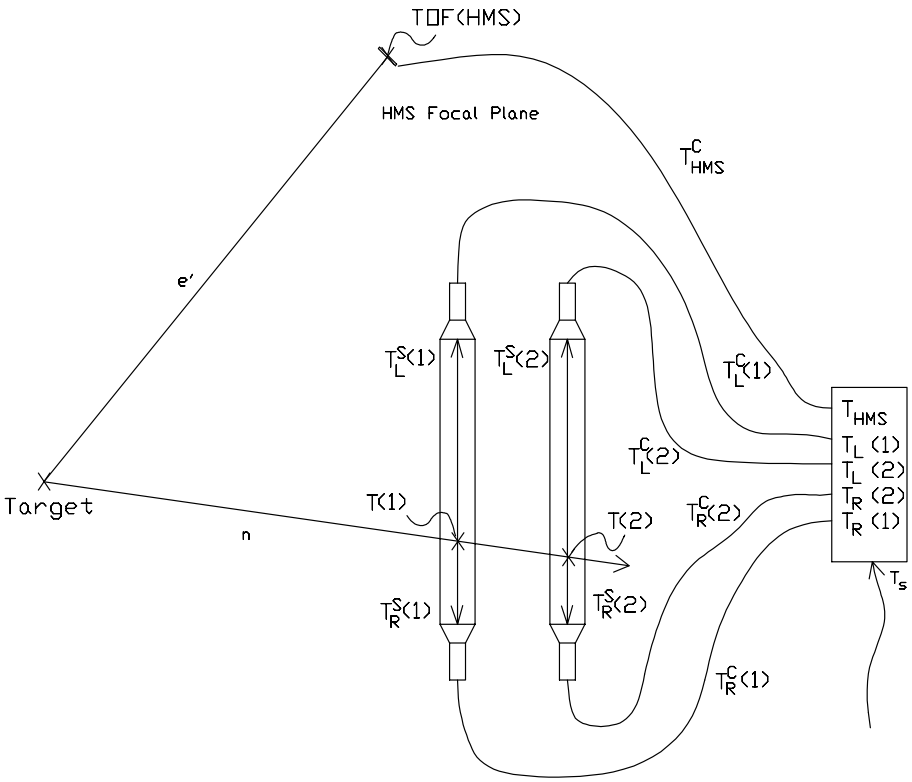

Figure 5.4: Timing delays

channel = 0.05 ns). The subscripts R and L refer to the right and left ends of the plastic scintillator bars, the superscript S refers to 'scintillator' propagation time,

the superscript C refers to the 'cable' delays, and the number identifies the detector. T_L, T_R and T_{HMS} (without a subscript) refer to the TDC signals stopped in the polarimeter. The actual TOF from the target to the interaction point in i^{th} detector is denoted by $T(i)$, while the corresponding electron TOF is denoted by $TOF(HMS)$. The TDC start signal in the polarimeter is given by T_s. In this notation, the T_s is relative to the time of interaction in the target. The scintillator propagation time, such as T_L^S and T_R^S, is defined to be the time required for the scintillation light generated by the recoil proton to travel from the interaction point to the left (or the right) end of the scintillator bar and is directly proportional to that distance, with the proportionality constant being the speed of light in the scintillator material. Therefore, The scintillator propagation time is different for every event. The cable delay times, such as T_L^C and T_R^C, include the propagation time through the light guides, phototubes, and any intervening electronics prior to the TDC, and they are expected to remain constant for every event.

We treat the NPOL trigger start time, T_s, to be completely unknown in the above equations. However, we do not need to know T_s because it can be eliminated by subtracting any of the equations (Equations 5.5 through 5.9) from another. In fact, time is always defined as the time referenced to another signal. Therefore, as we see below, time-calibrations can be performed without knowing T_s.

5.7.3 Calibrating λ and δ for All Detectors

Let us now consider how the position of the interaction in the i^{th} detector, x, can be expressed using the TOF quantities given previously. The x is the same as the x-position in the detector(DET) coordinate system defined in Appendix A. Using

$T_R^S(i)$ and $T_L^S(i)$, x is given by

$$x(i) = \frac{1}{2}\, v_s \, \left[T_R^S(i) - T_L^S(i)\right], \tag{5.10}$$

where $v_s \equiv c/n$ is the speed of light in the scintillator material, with n being the index of refraction of the scintillator.

Let us define the *differential time* for the i^{th} detector, $T_d(i)$, as

$$T_d(i) \;\equiv\; \frac{1}{2}\left[T_R(i) - T_L(i)\right]. \tag{5.11}$$

Then, $T_d(i)$ can then be written in terms of $T_k^S(i)$ and $T_k^C(i)$, where k is L or R,

$$T_d(i) = \frac{1}{2}\left[T_R^S(i) - T_L^S(i)\right] + \frac{1}{2}\left[T_R^C(i) - T_L^C(i)\right]. \tag{5.12}$$

Note that Equation 5.12 no longer depends on T_s as it is subtracted out. Because the second term in Equation 5.12 is a constant for each detector, let us define

$$\delta(i) \equiv \frac{1}{2}\left[T_R^C(i) - T_L^C(i)\right]. \tag{5.13}$$

Hence, from Equations 5.10, 5.12, and 5.13, the interaction position $x(i)$ can be written as

$$x(i) = v_s\left[T_d(i) - \delta(i)\right]. \tag{5.14}$$

Recall $T_d(i)$ is a measured quantity which depends on each event while $\delta(i)$ is an unknown constant, which needs to be calibrated.

The $\delta(i)$ for each detector can be calibrated from the histogram of $T_d(i)$. Figure 5.5 shows a typical histogram of $T_d(i)$ in units of channel numbers. Because the scintillator is irradiated uniformly, the left and right edge of this *timing* distribution in Figure 5.5 correspond, respectively, to the minimum and maximum x position of the detector in the DET coordinate system. In addition, the width of this distribution represents the total propagation time from one end of the detector to the other

end. Therefore, the sum of T_L^S and T_R^S is a constant for each detector. We define

$$T_L^S(i) + T_R^S(i) \equiv 2\lambda(i), \tag{5.15}$$

where the $\lambda(i)$ is the half-width of the distribution. The $\lambda(i)$, a constant which will be used in Section 5.7.4, can be determined from the histogram of $T_d(i)$. In addition, the center of this distribution corresponds to $x(i) = 0$ in DET coordinates. Therefore, the channel number which gives the center of this distribution is equal to $\delta(i)$ for this detector.

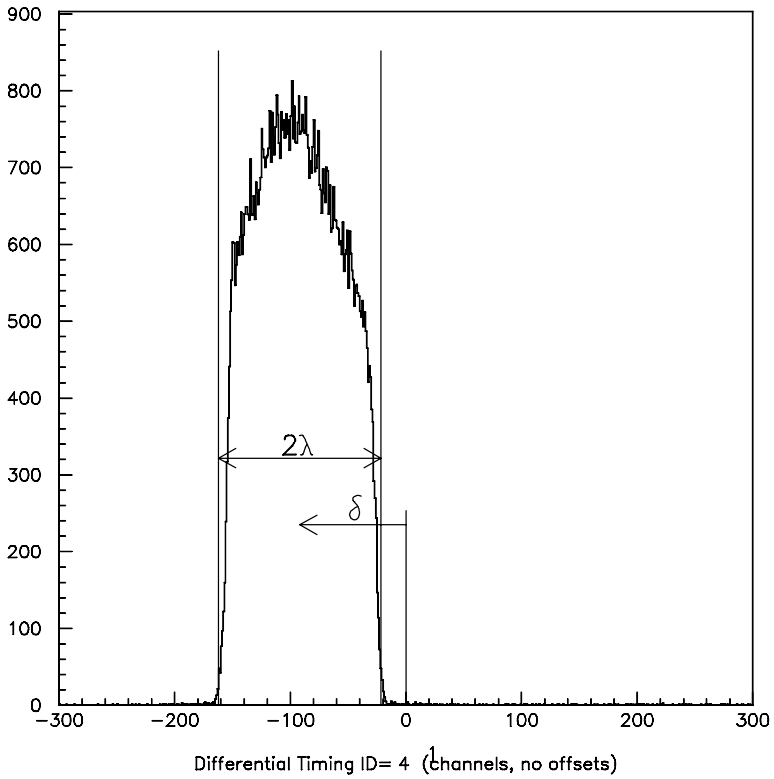

Figure 5.5: Differential timing spectrum. The calibration constants $\lambda(i)$ and $\delta(i)$ can be extracted from a histogram of $T_d(i)$.

To extract $\delta(i)$ and $\lambda(i)$, events with TDC values in both the left and right end of the detector are sampled to make a histogram of $T_d(i)$. The left and right edge

of this histogram are found by running a program. The left (right) edge is defined to be the first (last) channel number whose contents are greater than some fraction of the peak value. We chose the fraction to be 0.05. To improve the consistency, the raw histogram, which consists of 600 channels between the TDC values of -300 and $+300$, are first smoothed with a 3-channel boxcar algorithm. The difference in channel numbers between the right and left edges gives us the value of $2\,\lambda(i)$. Similarly, the average of the left and right channel numbers gives us the constant $\delta(i)$.

This procedure is repeated to determine the $\lambda(i)$ and $\delta(i)$ for all 70 detectors (the front, rear, and veto detectors). Then, the x position of an interaction for any detector can be found in DET coordinate system. However, we note that the y and z positions of any interaction point are still unknown. In fact, they cannot be determined. Because, an interaction of neutral particles can happen anywhere inside the plastic bar with equal probability, we always let the y and z positions of the interaction (in DET coordinates) be at the *center* of the plastic bar. That is, $y = z = 0$ in this coordinate system.

Once the 3-D position in DET coordinates is found, it can be converted into the position in POL coordinates.

5.7.4 Calibrating σ for the Front Detectors

Define the *mean time*, $T_m(i)$, for the i^{th} detector as

$$T_m(i) \;\equiv\; \frac{1}{2}\left[T_R(i) + T_L(i)\right]. \tag{5.16}$$

Similarly for $T_d(i)$, $T_m(i)$ can be expressed as

$$T_m(i) = T(i) - T_s + \frac{1}{2}\left[T_R^S(i) + T_L^S(i)\right] + \frac{1}{2}\left[T_R^C(i) + T_L^C(i)\right] \quad (5.17)$$

$$= T(i) - T_s + \lambda(i) + \sigma(i), \quad (5.18)$$

where the calibrated constant, $\lambda(i)$, is given in Equation 5.15. A new constant $\sigma(i)$ is defined as

$$\sigma(i) = \frac{1}{2}\left[T_R^C(i) + T_L^C(i)\right]. \quad (5.19)$$

If two scintillators ($\#i$ and $\#j$) fired, the difference between their *mean* times can be evaluated using Equation 5.18. It is the TOF from the first detector to the second.

$$\Delta TOF_{(i\to j)} \equiv T_m(j) - T_m(i) \quad (5.20)$$

$$= T(j) - T(i) + [\sigma(j) - \sigma(i)] + [\lambda(j) - \lambda(i)]. \quad (5.21)$$

Note that the trigger time T_s has been subtracted out. Equation 5.21 indicates that if a reaction with *known* particle velocity is used, the difference between $\sigma(j)$ and $\sigma(i)$ can be measured using this equation. As explained in Appendix C.2, the particle velocity, which depends on every event, can be estimated from the kinematics. This allows us to calculate $T(j) - T(i)$.

However, how can we determine the values of the two σ's from one measurement? Because we determine a difference between time intervals and not absolute times, one of the σ's, say, $\sigma(1)$ could be set to an arbitrary value like 0. In this way, one can determine the σ's relative to $\sigma(1)$. However, the TOF calculated using Equation 5.18 with those σ's then represents TOF relative to $\sigma(1)$, and it does not represent the actual TOF from the target. To solve this issue, we make use of *another* detector: we chose the HMS to be the *first* detector and set $\sigma(HMS)$ to 0. The σ's for the other detectors are then referenced against the HMS trigger time. The constant $\sigma(HMS)$

includes both T^C_{HMS} from Figure 5.4 and the TOF from the target to the HMS focal plane along the central axis, $TOF(HMS_{cent})$, which can be included because it is a *constant* for a fixed beam energy. The deviation of the TOF for each individual electron event is calculated separately by the HMS part of the analyzer and stored in the variable `hs_tof1`. Because the electron TOF from the target is measured in the HMS, time relative to HMS trigger time with $\sigma(HMS) = 0$ gives us the actual TOFs ($T(1)$ and $T(2)$ in Figure 5.4). Because the channel numbers are the normal units used in this section, a conversion factor, $C_{conv} = 20$ (channels/ns), needs to be multiplied to $TOF(HMS_{cent})$ and `hs_tof1`. The TOF of the electron to the HMS focal plane is given by

$$TOF(HMS) = TOF(HMS_{cent}) + \texttt{hs\_tof1}. \tag{5.22}$$

As shown in Figure 5.4 and Equation 5.9, the TDC value of the HMS trigger signal in the NPOL TDC consists of

$$T_{HMS} = C_{conv}\ [TOF(HMS_{cent}) + \texttt{hs\_tof1}] + T^C_{HMS} - T_s. \tag{5.23}$$

Using Equation 5.21 with the HMS as the second detector, we find

$$T_m(i) - T_{HMS} = T(i) + \sigma(i) + \lambda(i) - C_{conv}\ [TOF(HMS_{cent}) + \texttt{hs\_tof1}] - T^C_{HMS} \tag{5.24}$$

We combine all the *constants* from the HMS time together into

$$\sigma(HMS) \equiv T^C_{HMS} + C_{conv}\ TOF(HMS_{cent}), \tag{5.25}$$

and *define* it to be zero. Solving Equation 5.24 for $T(i)$, the TOF to detector $\#i$ is now

$$\begin{aligned} T(i) &= T_m(i) - \lambda(i) - \sigma(i) + \sigma(HMS) - T_{HMS} + C_{conv}\ \texttt{hs\_tof1} && (5.26)\\ &= T_m(i) - \lambda(i) - \sigma(i) - \texttt{ph\_start} + C_{conv}\ \texttt{hs\_tof1}, && (5.27) \end{aligned}$$

where the actual variable name used in the `engine.f` code, `ph_start` has been substituted for T_{HMS} in Equation 5.27.

Because every neutron entering the NPOL has a different velocity, the following is performed to estimate $T(i)$. We once again make use of the information already obtained in the HMS. Note that the electron momentum and the electron scattering angles as well as the 3-D interaction position at the target are measured in the HMS. In addition, from the 3-D location of the detected neutron in the polarimeter, the neutron recoil angles as well as the the flight distance $d(i)$ from the target can also be calculated. Therefore, the only unknowns from the $^2\mathrm{H}(\vec{e}, e'\vec{n})^1\mathrm{H}$ reaction are the magnitude of the neutron momentum and the three components of the *proton* momentum. These four quantities can be determined by solving the 3-body kinematics equations as discussed in Appendix C.2. From the estimated neutron momentum, the neutron velocity, β_{3body}, is easily calculated. Therefore, the actual neutron TOF, $T(i)$, is given by

$$T(i) = \frac{d(i)}{\beta_{3body}\, c} \equiv T_{3body}, \tag{5.28}$$

where we also call it T_{3body}.

We solve for $\sigma(i)$ in Equation 5.27 and use the value of $T(i)$ computed with 3-body kinematics to obtain

$$\sigma(i) = T_m(i) - \lambda(i) - \texttt{ph\_start} + C_{conv}\ \texttt{hs\_tof1} - T_{3body}. \tag{5.29}$$

To extract a front sigma, the value for $\sigma(i)$ in Equation 5.29 is histogrammed for events which have a *single* hit in the front and *no* hits in the front-veto array. The peak in the sigma distribution is fit with a Gaussian function to extract the constant $\sigma(i)$. An example of σ distribution for a front (#1) is shown in the left plot of Figure 5.6. Repeating the procedure described above for every front detector

gives us the constants σ's for the front array.

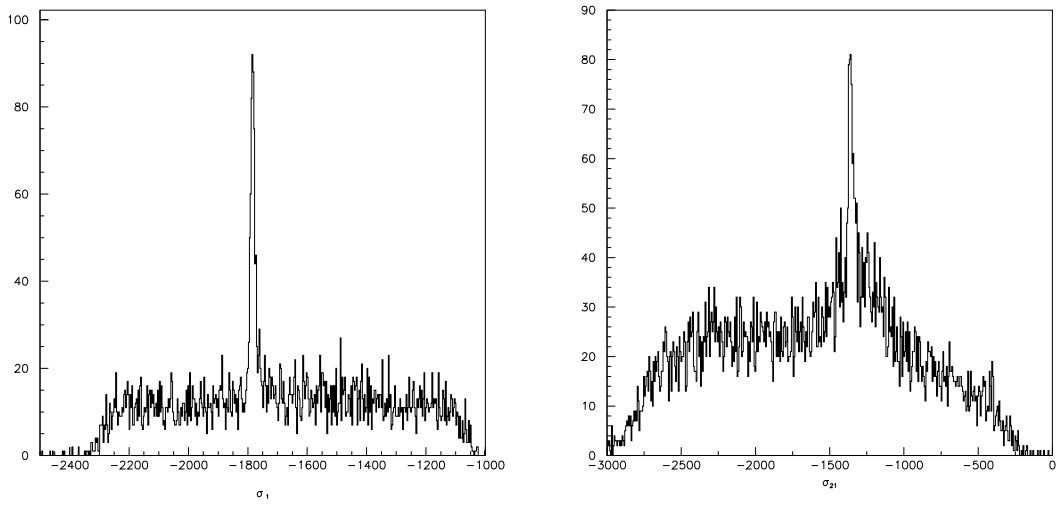

Figure 5.6: Distributions of sigma for a front detector (#1) on the left, and a rear detector (#21) on the right. The peak positions on these plots give us the calibration constants $\sigma(1)$ and $\sigma(21)$

5.7.5 Calibrating σ for the Veto Detectors

The veto detectors cannot be easily calibrated using neutron events, because their efficiency for neutron detection is very low. Therefore, we need to use charged particles, especially protons. We avoid using the pion events because the pion momentum cannot be determined kinematically due to a four-body final state.

We could perform using the proton events the same procedure described above to determine σ's for veto detectors. However, because the proton's momentum is reduced in the lead shielding, the T_{3body} obtained in Equation 5.28, will no longer represent the actual proton TOF. Therefore, this method will not work for calibrating the veto detectors. Instead, we make use of the fact that most charged particles hit

the veto detectors as well as the front detectors, which have been calibrated.

To calibrate the *front* veto detectors, we performed the following. Because each veto detector is so thin along z-axis (0.6 cm), the proton does not lose much momentum on the front-veto array. Thus, the TOF at the veto detector can be estimated from the time of the hit on the first layer of the front detector, assuming the TOF is proportional to the distance from the target along the z axis (in POL coordinates),

$$TOF_{(veto)} = TOF_{(Front)} \frac{dist_{(veto)}}{dist_{(front)}}. \tag{5.30}$$

Note that Equation 5.30 is not quite accurate as the proton velocity is slightly reduced due to the energy loss in the lead. However, Equation 5.30 is a good approximation.

To extract σ's for the front-veto detectors, proton events which have a hit in each of the two front-veto planes and a hit in the first layer of the front array are sampled. From the calibrated time of the front array, the time of hit in the front-veto is approximated by Equation 5.30. Then, the value for sigma is histogrammed and the peak position gives the constant σ for this detector.

A similar technique can be applied to the calibration of the *rear* veto array, Using proton events which go through all four front planes and two rear veto planes, the sigma can be calibrated. From the time of the hit in the fourth plane of the front array, the time of the hit on the veto layer is calculated from Equation 5.30. To extract σ for a rear veto detector, we sampled proton events which have a hit in every front plane and a hit in every rear-veto plane. The constant $\sigma(i)$ can be extracted from the sigma histogram for this detector.

5.7.6 Calibrating σ for the Rear Detectors

To calibrate the σ for the rear detectors, the TOF to the rear detector must be referenced to a front detector. In other words, take the i and j in Equation 5.21 to be the detector IDs in the front and the rear array, respectively. Then, $T(j)-T(i)$ in Equation 5.21 represents the TOF difference between these two detectors, which we call it *delta TOF*. Because of the collimator placed in front of the NPOL, the particles entering the front array *cannot* reach the rear array if they undergo no scattering in the front array. To find the *estimated* delta TOF, the following procedure is used: first, from the 3-D detection positions in a front and rear detector, the scattering angle is calculated. Second, assuming the interaction in the front is an *np* scattering, the magnitude of the momentum of the scattered particle is calculated by solving the 2-body kinematics equations with the known scattering angle and momentum of the incident particle. Finally, the delta TOF is calculated from the momentum of the scattered particle. Details are discussed in Appendix C.1.

We took the value of the incident neutron momentum to be the *estimated* neutron momentum obtained from the 3-body kinematics to calibrate σ for the rear detectors. (We also tested using the *measured* neutron momentum obtained from the calibrated front TOF to calibrate the σ, but we did not find any significant difference in the quality of the timing calibration.)

To extract a rear σ, single-hit events in front and rear array with no veto hits are sampled to make a histogram of sigma. An example of the σ distribution for a rear detector (#21) is shown in the plot on the right side of Figure 5.6.

5.7.7 How to Reconstruct TOF from TDCs

The system is calibrated once $\delta(i)$, $\sigma(i)$, and $\lambda(i)$ have been determined. To measure a neutron's longitudinal position within a single scintillator (the $\hat{x}$ direction in spectrometer coordinates), the differential timing and its calibration constant $\delta(i)$ are needed. For each detector the other two calibration constants are utilized along with the two HMS timing variables for the event, `hs_tof1` and `ph_start` to determine the TOF from the target to the detector.

$$TOF_{(ch)} = T(i) = T_m(i) - \lambda(i) - \sigma(i) - \texttt{ph\_start} + C_{conv}\ \texttt{hs\_tof1}. \tag{5.31}$$

Relative timing between detectors, such as from the front to the rear or from the veto to the front, is accomplished by taking the difference between these total TOF values.

Finally, because the TOF obtained in Equation 5.31 is in units of channel numbers, it needs to be converted into ns.

$$TOF_{(\mathrm{ns})} = \frac{TOF_(ch)}{C_{conv}} \tag{5.32}$$

5.7.8 Results of Timing Calibration

In the previous subsections, we discussed our timing calibration method for the NPOL detectors. We present below basic results for position and TOF spectra in NPOL using the single-hit events (one hit in the front, and one hit in the rear array) with no cuts applied. The detailed analysis on this is given in [Taj01].

The NPOL was designed in such a way that the particles must be scattered in the front array for them to be detected in the rear array because the rear array is shielded from the direct flux from the target as discussed in Section 3.8.1. Therefore,

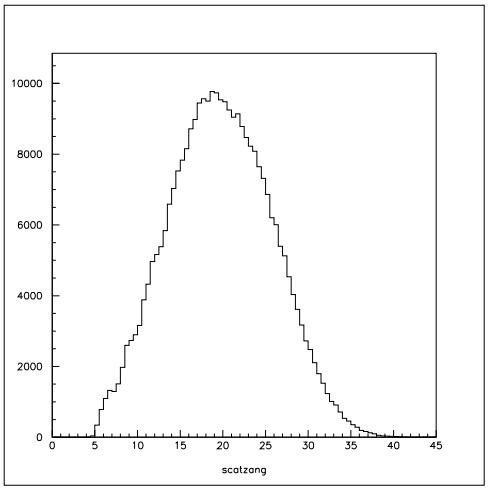

Figure 5.7: Reconstructed rear scattering angle for a Charybdis-off run at Q^2=1.14 $(GeV/c)^2$. Single-hit events in NPOL with no cuts applied.

the particle scattering angle from the front to the rear interaction points can be defined for each coincidence event. Figure 5.7 shows the distribution of the particle scattering angles. The minimum and maximum scattering angles are 5°and 38°, respectively, which can be verified from the positions of the front and rear detectors in Appendix B. The mean angle of this distribution is 19°.

Figure 5.8 shows the plots of the TOF spectra in ns for the front, rear, front-veto and rear-veto detector arrays. The micro-structure of the CEBAF beam with a period of 2 ns is clearly observed in the background regions of the front and veto TOF spectra. The structure in the front TOF histogram is less clear in this plot: the time structure was smeared out because the thickness of the front array along the NPOL Z-axis (see Appendix A for the polarimeter coordinates) is much larger (∼43 cm) than that of veto arrays (∼1cm). Figure 5.9 shows TOF histograms for each of the four planes in the front array. As you see, the micro-structures are clearly observed in these spectra. As in Figure 5.8, no cuts were applied. Because no cuts were applied

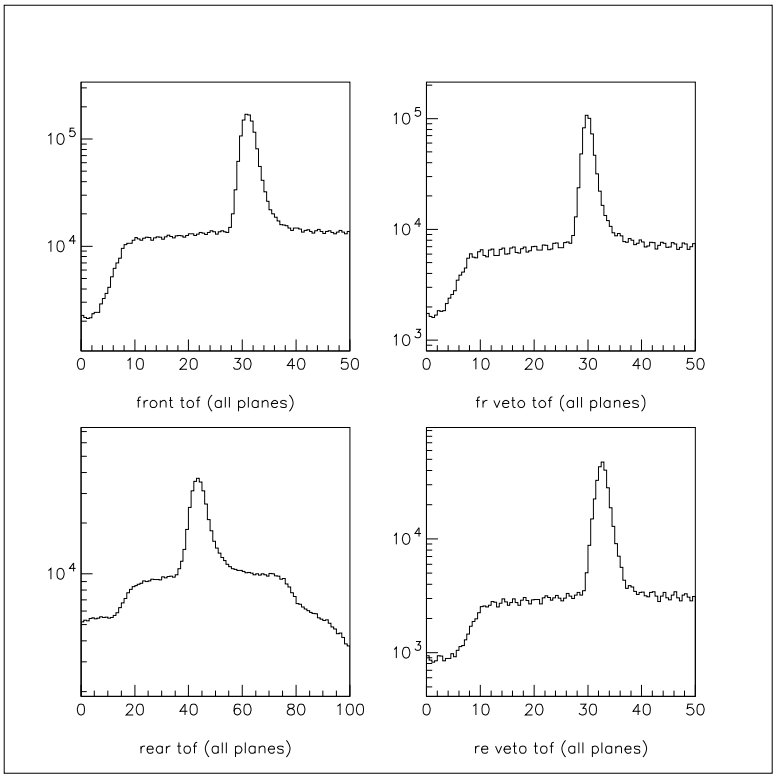

Figure 5.8: Reconstructed measured TOFs in ns from the target to the front, rear, front-veto, and rear-veto detectors for a Charybdis-off run at Q^2=1.14 $(GeV/c)^2$. Only single-hit events in NPOL were analyzed to make these plots. No cuts were applied.

in Figures 5.8 and 5.9, events due to both neutral particles (neutrons, gammas) and charged particles (electrons, protons, pions) contribute to these TOF spectra. We believe that the micro-structures seen in these plots were created mainly by the light particles (electrons and charged pions) which had high enough energies to penetrate the lead shielding in front of the NPOL. The reason for this is that the velocities of those light particles would be nearly constant, and are quite close to the speed of light. As we will see later, such a structure is not observed for events with neutrons because their velocities are not really constant and depend on each event. We do not give a detailed analysis of events which make this time-structure because events

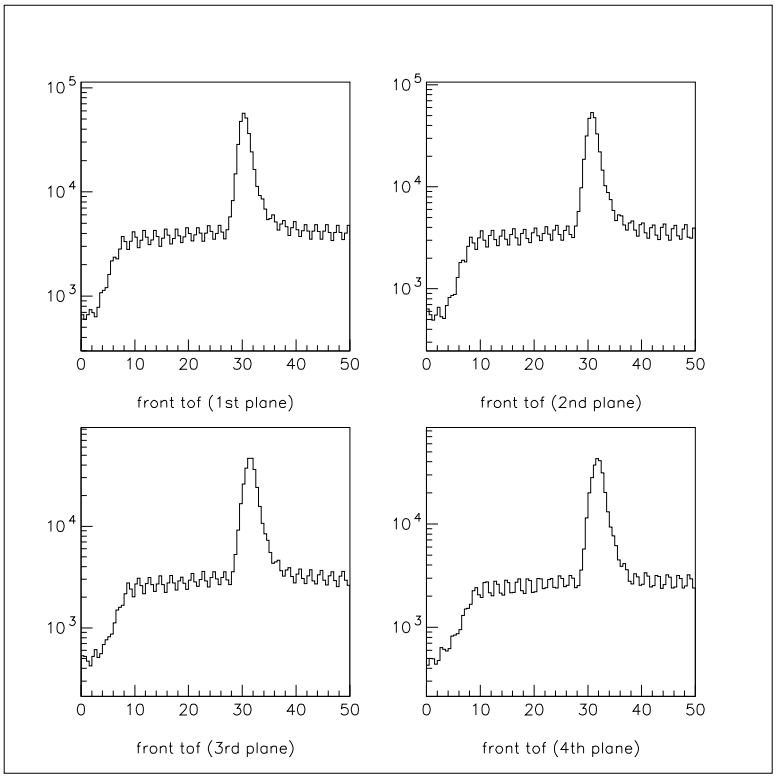

Figure 5.9: Reconstructed measured TOF for each front detector plane. for a Charybdis-off run at Q^2=1.14 (GeV/c)^2. Only single-hit events in NPOL were analyzed to make these plots. No cuts were applied. The micro-structure of CEBAF beam with period 2 ns is clearly shown these plots.

due to those *charged* particles are not needed for the neutron scattering asymmetry measurements.

We will discuss in the following sections how to identify good coincidence events to be used for the asymmetry calculations.

5.8 Event Selection for Calculating the Asymmetries

Data taken for this experiment are 3-fold coincidence events which consist of time-correlated hits in HMS, NPOL front and NPOL rear detectors: all of those hits must be detected within the time window of 70 (ns). In this section, we discuss how to obtain yields that will be used for the asymmetry calculations.

5.8.1 Overall Procedure for Event Selection

The following steps are taken for event selection. First, we must identify particles in the HMS and the NPOL front detectors and select the events with the right particles (the electrons in the HMS and the neutrons in the NPOL front). Next, we select *quasielastic* events from the $^2\mathrm{H}(\vec{e}, e'\vec{n})^1\mathrm{H}$ reaction. In our analysis, both of requirements were met by applying cuts to events for the HMS and the NPOL front. The events found at this point are *2-fold* coincidence events (HMS and NPOL front) from the quasielastic $^2\mathrm{H}(\vec{e}, e'\vec{n})^1\mathrm{H}$ reaction. Using these events, a histogram for *3-fold* coincidence events is created. The yield is obtained by integrating the peak region of the histogram. However, we also must estimate the background yield which exists under the peak region. To do this, we must identify *good background events* which lie in our case in the *flat* regions of coincidence histograms. The background yield under the peak region is then estimated under the assumption that the flat background also exists in the coincidence peak region. The final yield is then obtained by subtracting the estimated background yield from the peak yield. Because data taken for this experiment are 3-fold coincidence events (HMS, NPOL front, and NPOL rear), background subtraction has to be performed twice as discussed later.

As we discuss in Section 5.8.8, there exist two types of events detected in the rear array which we refer to (n,n) and (n,p) events. When the data were analyzed, we performed both *(n,n) event analysis* and *(n,p) event analysis* for each run to obtain the separate results for the yields and the asymmetry values for the two event types.

5.8.2 Particle Identification for the HMS

As discussed in Section 3.5.3, an HMS trigger was generated whenever 3 out of 4 HMS scintillator planes fired. Therefore, the electrons as well as the pions can generate an HMS trigger. To select good electron events, we used information from the Čerenkov detector and the shower counter in addition to the reconstructed physics quantities such as δ_{HMS} and the scattering angles for the HMS. We describe below the meaning of each cut for selecting electron events in the HMS.

Čerenkov and Shower Counter

Both the Čerenkov and the Shower Counter serve as detectors for particle-identification in the HMS arm as discussed in Section 3.5.1. The left plot in Figure 5.10 shows the number of photo-electrons detected in the Čerenkov detector. The left sharp peak near zero is due to the pions. Because the pions do not emit Čerenkov light in the gas Čerenkov detector, they made the left sharp peak near zero by minimal ionization in the gas. The counts which exist at near 1 photo-electron on the plot are due to the pions with single photo-electron noise [Arr98].

The right plot in Figure 5.10 shows the energy deposited in the shower counter. This energy is normalized by the electron energy measured for each event. The peak near 1 is clearly due to the electrons while the small left peak at near 0.1 is due to

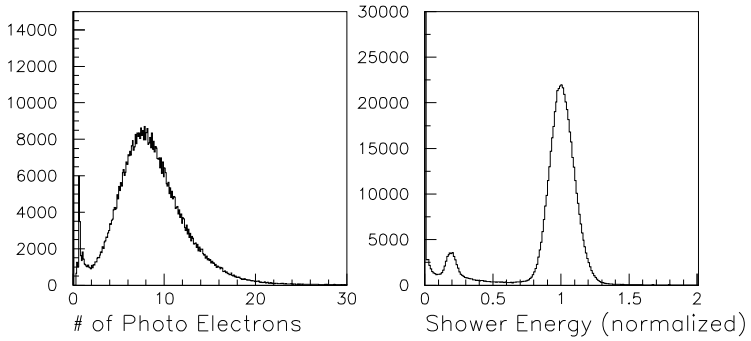

Figure 5.10: Number of photo-electrons in the Čerenkov Detector (left) and energy deposited in the calorimeter (right). These plots are for data at Q^2=1.14 $(GeV/c)^2$. No cuts were applied.

the low energy pions. The cut parameter values for the number of photo electrons in the Čerenkov and the normalized shower energy in the calorimeter are given in Table 5.2.

Reconstructed Physics Quantities

After the electron track is reconstructed, the track-related physics quantities are calculated in the Engine software as we saw in Section 5.4.7. Figure 5.11 shows

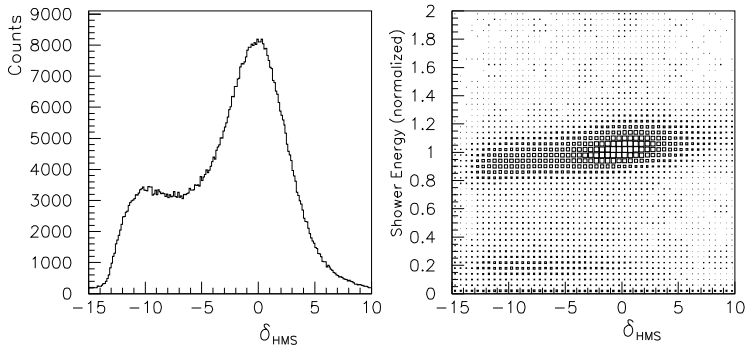

Figure 5.11: Deviation of the electron momentum in the HMS (δ_{HMS})

the reconstructed $\delta_{\rm HMS}$ and the 2-D plot of $\delta_{\rm HMS}$ and the shower energy for data at Q^2=1.14 $(GeV/c)^2$. The left shoulder on the plot of $\delta_{\rm HMS}$ is partially due to the pion events in HMS. In fact, as it is clear from the 2-D plot in Figure 5.11, the pion events are separated from the electron events (the pions have shower energy around 0.2). Therefore, this indicates that the cut on the shower energy will eliminate most of the pion events. The $\delta_{\rm HMS}$ histogram is rather used to identify the *quasi-elastic* events: after the pion events are eliminated, cuts on $\delta_{\rm HMS}$ around its peak region will be applied. Figure 5.12 gives histograms of other reconstructed physics quantities as well as the histogram of χ^2 which indicates the quality of the fit to the reconstructed track. The top two plots are vertical and horizontal scattering

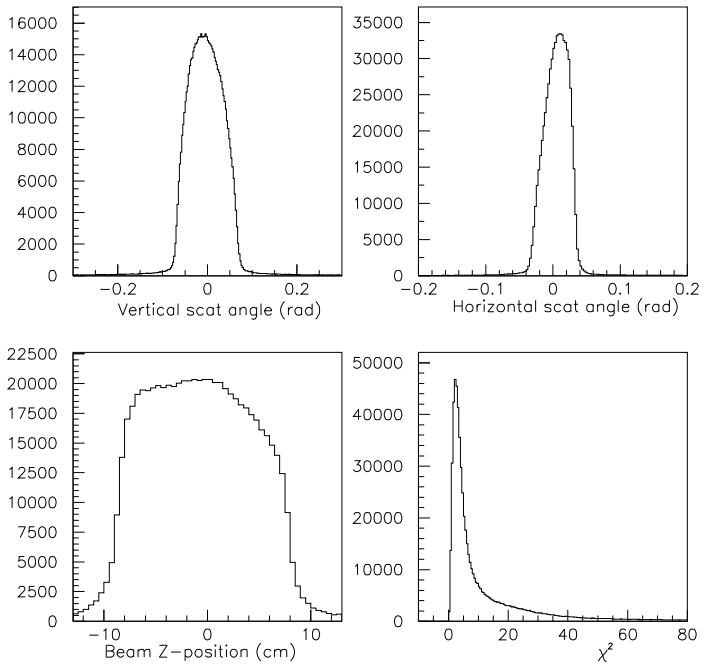

Figure 5.12: Other reconstructed quantities for the HMS

angles at the target. As discussed earlier, the vertical angle is the angle in the x direction (dispersive direction), and the horizontal angle is the angle in the y-direction (non-dispersive direction). From these histograms, the events with scattering angles

Variable	**Min**	**Max**
Shower Energy (normalized)	0.7	1.4
# of photoelectrons in Čerenkov	2.0	-
Beam z-position at the target (cm)	-7.0	7.0
Vertical scattering angle (rad)	-0.07	0.07
Horizontal scattering angle (rad)	-0.03	0.03
χ^2	0.	50.

Table 5.2: Cut parameters for HMS particle identification. The same cut values are applied for data at both Q^2=0.45 and 1.14 $(GeV/c)^2$. Cut values for δ_{HMS} are not given in this table as they are used for identifying quasi-elastic events. See text for detail.

outside of the HMS acceptances are not considered as good events because that indicates the reconstruction routine did not work properly for those events. The bottom-left plot in Figure 5.12 is the beam interaction position at the target along the Lab Z-direction. We require that the Z position at the target is within the target dimension. Although our target was 15-cm long, we accepted the events only if the beam position is in the range of $-7.0 < Z_{beam} < 7.0$. The bottom-right plot in Figure 5.12 is a histogram of χ^2. The quality of the HMS reconstruction is known from the χ^2 value. Very large χ^2 value indicates that the track reconstruction was not quite successful. Thus, events with $\chi^2 > 50.0$ were rejected in our analysis. The cut parameter values for the reconstructed quantities given in this subsection are given in Table 5.2.

5.8.3 Removing Bad Hits from the NPOL Events

At the beginning of the NPOL event analysis, some loose cuts on time, position and pulse height were applied to remove extremely bad hits in front, rear, and veto detectors. A NPOL hit was removed if any one of the following conditions was satisfied.

1. The position of a hit is located *outside* of the detector: if the measured position of a hit (that is, in the NPOL coordinates, the x position for the hit in the front and veto array and the z position for the hit in the rear array) is more than 10 cm away from the edge of the detector in which the hit occurred, that hit is removed.

2. The time of a hit is outside of the time window set for each detector: if the time of a hit in the front (rear) array is outside of the time window of 0 to 70 ns (-10 to 100 ns), the hit is removed. For the hit in the veto detectors, the range is from -100 to 100 ns. The same values were used for the data analysis at Q^2=0.45 and 1.14 $(GeV/c)^2$.

3. The particle energy calculated from the pulse height is negative.

After those bad hits were removed, the rest of the hits was examined to identify events that can be used for the scattering asymmetry calculations, as discussed below.

5.8.4 Identifying Neutral Particles in the NPOL Front Array

The charge status of the hits detected in the NPOL front array can be determined by examining the hits in the front-veto (FRVT) array which was located just in front of the front array. The FRVT consists of two planes with five thin detectors on

each plane. Because each FRVT detector has a thickness of 0.7 cm, the charged particles are likely to have an interaction with the detector material when they go through a FRVT detector. The probability that the neutrons fire in the FRVT array is quite small. Furthermore, when this happens, the charged particles go through both the FRVT and front detectors, and a strong time correlation between hits in the FRVT array and the front array is observed. Therefore, a hit in the front array due to a neutral particle can be identified by the lack of time-correlated hit in the FRVT array. Histograms of the time difference in ns between front hits and front-

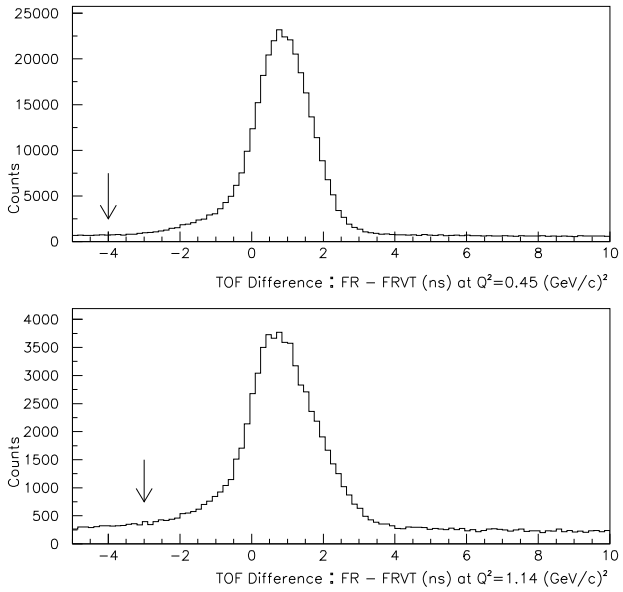

Figure 5.13: Time difference between hits in front and front-veto detectors. The top (bottom) plot is made for data at Q^2=0.45 (GeV/c)^2 (Q^2=1.14 (GeV/c)^2). The arrow on each plot shows the value of the cut parameter (low edge only) for identifying the time-correlated events. See text for detail.

veto hits are shown in Figure 5.13. A time difference was calculated whenever an event has at least one front-veto hit (any event *always* has at least one front hit).

If there are multiple hits in the front-veto and/or front detectors, the histogram counts were incremented for *every* pair of the front and front-veto hits. Because time-correlated events make a clear peak in this histogram, these events must be due to charged particles entering the NPOL. Therefore, the events under the peak region were excluded from further analysis. However, a veto paddle occasionally fired by an *early* accidental hit and later on the same paddle fired again by a charged particle which most likely fired front detectors as well. If this situation happens, we are not able to check the time correlation between the front-veto hit and the hits in the front array because our TDC channels do not have multiple-hit capability, i.e., for each event-trigger, we get only one TDC value for each PMT. If a bar fired twice during the time window for data acquisition of an event, only the time of the earlier hit is recorded in the TDC. Therefore, for these types of events, this limitation in the TDC can cause the time-correlation between hits in the front-veto and the front array to be lost, thereby resulting in a charged particle being misidentified as a neutral particle. This problem could happen when the time difference $T_{FR} - T_{FV}$ is positive and is outside of the peak region. Therefore, events from the flat region on the right side of the peak in Figure 5.13 were also removed from our analysis. The frequency of these types of events increases with increasing rate in the front-veto detector.

The criteria for identifying the neutral events in the NPOL front detector are as follows:

1. An Event has no front-veto hit.

2. The time-difference ($T_{FR} - T_{FV}$) is smaller than the threshold value (see Figure 5.13).

The threshold values are -4 (ns) for Q^2=0.45 (GeV/c)^2, and -3 (ns) for Q^2=1.14

$(\mathrm{GeV/c})^2$.

5.8.5 Multiple-Hit Analysis

In this experiment, about 50% (90%) of events taken with the Charybdis magnet *off* have only one front (rear) hit at Q^2=0.45 and 1.14 $(\mathrm{GeV/c})^2$. With the Charybdis magnet *on*, the trajectory of a charged particle was deflected when it passed through the magnetic field. Thus, many charged particles missed the NPOL and that reduced the background level in the data. With the magnet on, about 70% (90%) of events have only one front (rear) hit at Q^2=0.45 and 1.14 $(\mathrm{GeV/c})^2$. If only one front detector and one rear detector fired during the event time-window, which we refer to a *single-hit event*, identification of the vertex detector IDs for both arrays is trivial. On the other hand, if more than one detector in the front and/or rear array fired during the event time-window, which we refer to a *multiple hit event*, the vertex detector IDs for both arrays must be identified. We discuss below how to identify the vertex detector IDs when a multiple-hit event happens.

Multiple Hits in the Front Array

After interacting with the incident neutron, a recoil proton, knocked out from the material of a plastic scintillator, scintillates in a detector bar. The recoil proton loses energy due to the electromagnetic interaction with the detector material as it travels through the detector. If the recoil proton has sufficient energy, it can penetrate the detector bar in which the interaction occurred, and enter the next detector bar to cause a scintillation in that detector. If the pulse height energies in both detectors are larger than the hardware threshold, hits are generated in both detectors. If the recoil

proton still has enough energy left, it can similarly fire subsequent detectors located next to each other. When a multiple-hit event occurs, a *cluster* of hits are generated. They are easily identified in the analysis because time and position of those hits in the cluster are correlated. However, we rejected events which has more than one cluster in the front because it is difficult to identify the cluster which contains the true coincidence event. Therefore, we keep the events only if there exists only one cluster in the front detector array. We required that the time difference between one of the hits and the hit with the lowest detector ID is in the range of -1 to $+3$ (ns) and that the detectors are adjacent to each other in the yz plane in the NPOL coordinate system. If not all of the hits meet these criteria, that indicates there exists more than one cluster in the front array for the event, and therefore such an event is rejected. We then require that the difference between the maximum and minimum x positions for those pre-selected hits are within 15 cm. If this condition is met, those pre-selected hits indeed form a cluster. Otherwise, the event is rejected because it contains more than one cluster.

If the analysis program found only one cluster in the front array for an event, the ID of a detector for the interaction vertex is found. First, hits with the smallest z position are identified. (Because the z position of a hit is always assumed to be at the center of the detector, more than one hit can have the *smallest* z position in the cluster. In other words, they must be on the same front layer if this situation happens.) Next, the hit with the smallest TOF is identified. That gives the the detector ID for the interaction vertex. However, due to the uncertainty in our time measurement, this procedure still could cause a misidentification of the *first* hit. In addition, another kind of misidentification can happen due to the hardware threshold we applied. If the interaction point is located near the boundary of two adjacent

detectors, the pulse height signal might be *below* the hardware threshold. If this situation happens, a hit is not generated for the "true" detector for the interaction vertex. If the recoil proton then entered and fired the adjacent detector, the trigger is generated from the detector. There is no way to find the detector ID for the interaction vertex in this case because the information is lost due to the hardware threshold.

Multiple-Hits in the Rear Array

Almost the same criteria are applied to analyze multiple-hit events in the rear array. To identify a rear cluster, we imposed the same cut values for the time difference between hits. In addition, we required that the difference between the z positions of the hits are within 15 cm. As for the front, we kept events which have only one cluster. An event that has hits in both top and bottom rear detectors is rejected from our analysis (this event clearly contain at least two clusters). Because a misidentification of the true coincidence hit can cause a dilution of the measured scattering asymmetry in this case, it is important to reject such an event.

5.8.6 Miscellaneous Cuts

Front and Rear Pulse Height Thresholds

As discussed in Section 5.5, the pulse height energy, which is obtained from the ADC signals, gives the energy of the recoil proton (if the neutron interacted with the detector material). When the data were taken, we set the hardware pulse-height thresholds of 4 MeVee (10 MeVee) for the front (rear) detectors. These threshold cuts in the hardware served to reduce the accidental hits in the data and thereby the

overall counting rates. In our data analysis, the software threshold values were set to 8 MeVee (20 MeVee) for the front (rear) detectors to further remove the background particles. For a multiple-hit event, we require that at least one of the hits in the cluster has a pulse-height energy greater than the threshold. The software threshold value for the rear detectors is much larger than its hardware value. Because particles entering the rear array travel rather long distances inside a detector bar, low-energy background particles can produce pulse heights over the hardware threshold. We found the optimal value of the software threshold was 20 MeVee for the rear array.

Removing Events from a Malfunctioning Detector

During our experiment, one of the rear detectors, #22, was identified as a malfunctioning detector which counted much fewer events than the other rear detectors of the same dimensions. In addition, the spectrum of hit positions along the NPOL x axis obtained for this detector was found to be strange. Because of these observations, we removed events from our analysis if the interaction vertex for the rear was inside this detector.

Scattering Angles from the Front to the Rear

The distribution of the histogram for the scattering angle from the front to the rear with no cuts applied ranges from about 5° to about 38°due to the location of front and rear detectors. However, the value for the analyzing power A_y becomes small for angles greater than 30°, and it in fact changes sign at around 40°(35°) at Q^2=0.45 (GeV/c)^2 (Q^2=1.14 (GeV/c)^2) according to the SAID program [SAI]. Therefore, those events with small or negative A_y would cause a dilution of the measured scattering asymmetry. Because of these reasons, events with the scattering

angles smaller than 5°or larger than 30°were removed from our analysis.

5.8.7 Selecting Quasielastic Events

With all the cuts mentioned above applied, we were able to identify the electrons in the HMS, and the *neutral* particles in the NPOL front array. The next step is to identify the quasielastic events from the $^2\mathrm{H}(\vec{e}, e'\vec{n})^1\mathrm{H}$ reaction. To do this, we apply cuts on the relative electron momentum, missing momentum, invariant mass, and the front coincidence TOF.

Relative Electron Momentum, δ_{HMS}

As we saw in Section 5.8.2, a majority of the pion events which appeared in the δ_{HMS} spectrum is removed by the cut on the shower energy. We want to keep as many events as possible from this histogram in order to have enough statistics for the analysis. However, events with large value of δ_{HMS} will not be the quasielastic events, and therefore they must be removed. In addition, a pion contamination might still exist (even after the cuts were applied) on the left side of the δ_{HMS} histogram. Therefore, the minimum value of the cut must be limited by this. In our analysis, we kept the events if $-3 < \delta_{\mathrm{HMS}} < 5$ for Q^2=0.45 and 1.14 $(\mathrm{GeV/c})^2$.

Missing Momentum, p_{miss}

In the quasielastic limit, the recoil proton from the LD_2 target carries no momentum after the electron-deuteron interaction. However, in our experiment the recoil proton momentum was not zero in general, but it had a small value. A large proton momentum indicates that the reaction is not quasielastic. Therefore, a cut

on the proton momentum has to be applied. Because the proton is not detected in the $^2\mathrm{H}(\vec{e}, e'\vec{n})^1\mathrm{H}$ reaction, we refer the momentum of this recoil proton as *missing momentum*, p_{miss}. Knowing the initial and scattered electron momenta, the p_{miss} can be determined from the momentum of the detected neutron, which is calculated from the position and the TOF measurements in the NPOL front array. However, the uncertainty in the TOF measurement contributes to the uncertainty in p_{miss} in this calculation. Therefore, we calculated the p_{miss} for each event *without using the measured neutron TOF* [Chu00]. Consider the four-momentum equation for the electro-disintegration of the deuteron,

$$e^{\mu} + d^{\mu} = e^{'\mu} + n^{'\mu} + p^{'\mu}, \tag{5.33}$$

where the variables in Equation 5.33 are four-momenta of the incident electron, deuteron, scattered electron, recoil neutron, and recoil proton, respectively. The superscript μ is 0,1,2, or 3. Equation 5.33 represents one energy and three momentum conservation equations. In this experiment, components of e^{μ} and d^{μ} are known, assuming that the target is at rest in the lab frame. In addition, components of $e^{'\mu}$ and the scattering angles of the neutron in the NPOL front array are measured for each event. Therefore, there are four unknowns (magnitude of the neutron momentum and the three proton momentum components) in Equation 5.33. All of the unknowns can be determined by solving Equation 5.33, which consists of the four equations, which we refer to as the *three-body kinematics equations*.

Invariant Mass, W

Invariant mass of the interaction, W, also serves to identify the quasielastic events from the $^2\mathrm{H}(\vec{e}, e'\vec{n})^1\mathrm{H}$ reaction. It can be calculated from the four momentum of the target nucleon which is involved in the interaction and the incident and

scattered electron four momenta. Here, we assume a free neutron target which is at rest in the lab frame and consider the *elastic* electron-neutron reaction, which can be expressed as

$$q^\mu + n^\mu = n'^\mu, \tag{5.34}$$

where q^μ and n^μ are the four momentum transfer and the four momentum of the neutron before the interaction. The square of the left hand side of this equation defines the *invariant mass squared*, which is given by

$$W^2 \equiv (q^\mu + n^\mu)^2 = (\omega + m_n)^2 - |\vec{q}|^2 = q^2 + 2m_n\omega + m_n^2 \tag{5.35}$$

where $\omega \equiv E_e - E_{e'}$ is the energy transfered to the virtual photon, $\vec{q}$ is three momentum of the virtual photon, and q^2 is given in Equation 1.14. For *elastic* scattering, we have $\omega = -q^2/2m_n$ (see Equation 1.11). In our experiment, a deuterium target was used because of a lack of free neutron target. Because the deuteron has a binding energy, the above argument and the results (Equations 1.14 and 5.35) do not give an exact result of W. However, because the binding energy of the deuteron (2.2 MeV/c^2) is so small compared to the neutron mass (940 MeV/c^2), those equations can be used to calculate W. [2] For an inelastic reaction, the value for W becomes greater than m_n. Thus, we set the upper limit for W in order to select the quasielastic events that can be used in our analysis. We chose the upper limit to be 1.0 (GeV/c^2).

Front Coincidence TOF

Finally, the TOF of the neutron from the interaction point at the target to the detection point in an NPOL front detector is used to select the quasielastic events. The top plot of Figure 5.14 shows the measured coincidence TOF spectrum for the

[2] The relative error due to this approximation is in the order of $\sim 2.2/940 \times 100 \sim 0.2\%$.

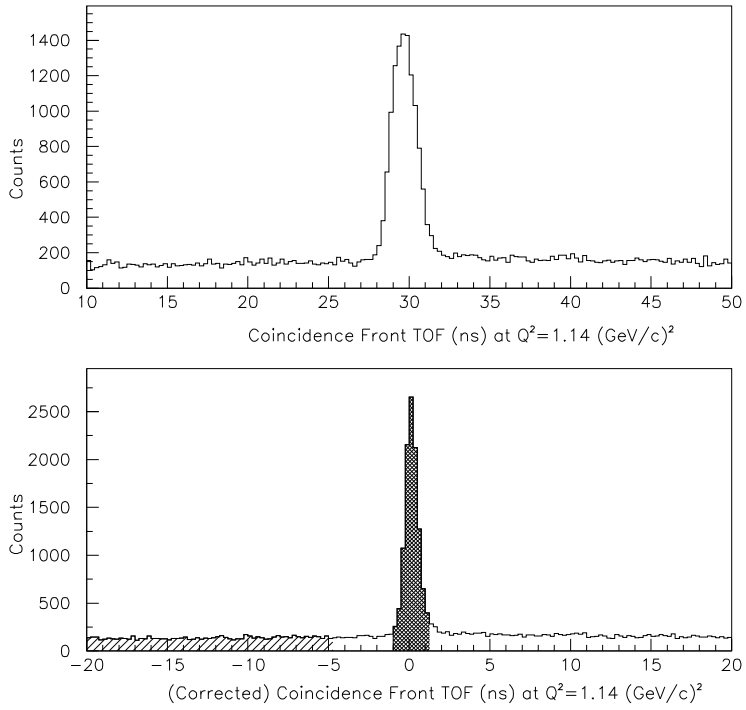

Figure 5.14: Coincidence front time-of-flight spectra at Q^2=1.14 $(GeV/c)^2$. The top plot is a histogram of the measured coincidence TOF from the target interaction point to the front detector where the trigger was generated. The bottom plot is a histogram of the *corrected* front TOF (CTOF), which is the difference between the measured TOF (shown on the top plot) and the estimated TOF obtained by solving the 3-body kinematics equations for the $^2H(\vec{e}, e'\vec{n})^1H$ reaction.

front at Q^2=1.14 $(GeV/c)^2$. All the cuts mentioned so far have been applied. At this Q^2 value the neutral particles to be considered were neutrons, neutral pions (decays to two gammas in 10^{-17} sec), and the gammas. A peak at around $TOF = 23$ (ns) (see the top plot of Figure 5.14) would be due to gammas coming from the target, considering that the speed of light is ∼30 cm/ns and the mean flight distance from the target to the NPOL front array is ∼700 (cm). The absence of the gamma peak indicates that the gamma rays from the target were absorbed by the lead sheets

placed in front of the NPOL and did not make it to the NPOL. Therefore, we expect that the peak shown on the top plot of Figure 5.14 is the quasielastic *neutron* peak. To confirm this expectation, we compared this TOF with the TOF calculated by solving the kinematics equation. As described in Section 5.7.4, we solved for each event the three-body kinematics equations for the ^{2}H$(\vec{e}, e'\vec{n})^1$H reaction to obtain the magnitude of the *estimated* neutron momentum, p_n^{est} and three components of the undetected proton momentum (see also Appendix C.2). The *estimated* neutron TOF is then easily obtained from the estimated velocity of the particle and the measured flight distance. The estimated neutron velocity, V_n^{est} is given by

$$V_n^{est} = c\frac{P_n^{est}}{E_n^{est}}, \tag{5.36}$$

where $E_n^{est} = \sqrt{(P_n^{est})^2 + m_n^2}$ is the estimated neutron energy. The estimated neutron TOF, TOF$_{est}$, is given by the measured flight distance to the front array divided by V_n^{est}. We obtained the *corrected* TOF (CTOF), which is the difference between the measured TOF and the estimated TOF. It is defined as

$$CTOF = TOF^{FR} - TOF_{est}^{FR}, \tag{5.37}$$

where TOF^{FR} and TOF_{est}^{FR} are measured and estimated front TOF from the target vertex, respectively. The CTOF spectrum is shown on the bottom plot of Figure 5.14. It has a clear peak centered about 0 (ns). As we stated earlier, we assumed that the neutral particle in the NPOL front is the *neutron* when the estimated momentum of the *neutral* particle was calculated. Therefore, the peak centered about 0 (ns) on the CTOF histogram confirms that the *neutrons* from the quasielastic ^{2}H$(\vec{e}, e'\vec{n})^1$H reaction indeed make this peak. The CTOF histogram serves to identify the quasielastic coincidence events. This plot was made after all the cuts described previously were applied.

The peak was more clearly resolved on the CTOF histogram than the front TOF as you see in Figure 5.14. Because the front array is ∼40 (cm) thick along the z direction, this causes a TOF spread of about $1.5 - 2.0$(ns) on the TOF histogram (top plot). This time smearing was corrected in the calculation of CTOF because the estimated TOF was obtained for each event taking into account the detection position in the front. The width of the CTOF peak defines our timing resolution for *neutron* events for the front detectors, and it is $\sim \pm 0.5$(ns) HWHM. [3]

Cuts for selecting the quasielastic coincidence events

Table 5.3 gives a list of cuts for selecting the quasielastic coincidence events. The yields of the quasielastic events are obtained by integrating the CTOF spectrum from -1.0 (ns) to $+1.0$ (ns), as shown on the bottom plot of Figure 5.14. The background events in the hatched region of Figure 5.14 will be used to estimate the background level of the 3-fold coincidence spectra as will be discussed later.

Variable	**Min**	**Max**
Relative particle momentum, δ_{HMS} (%)	-3.0	5.0
Missing Momentum, p_{miss} (GeV/c)	0.0	0.1
Invariant Mass, W_{inv} (GeV/c^2)	0.0	1.0
Coincidence TOF, CTOF (ns)	-1.0	1.0

Table 5.3: Cut parameters for identifying quasielastic events from the ^{2}H$(\vec{e}, e'\vec{n})^1$H reaction. The same cut values are applied for data at both Q^2=0.45 and 1.14 (GeV/c)^2.

[3] It stands for Half Width Half Maximum of the peak

5.8.8 Definition of (n,n) and (n,p) events

As discussed in Section 3.8.1, the polarimeter for this experiment is based on *np* scattering. The NPOL was designed in such a way that both the scattered neutron and the recoil proton from the same event in the front array cannot be detected in the rear detectors. Therefore, two types of *np* scattering events are detected in the rear.

1. The p(n, n)p reaction for which a neutron scattered in the front is detected in the rear. We define this type of event as an (n,n) event.

2. The charge-exchange reaction p(n, p)n for which a neutron is detected in the front, but the knock-on proton is detected in the rear. That is, the scattered neutron from the front missed the rear array. We define this type of event as an (n,p) event.

Note that both (n,n) and (n,p) events are due to *np* elastic scattering events in the front array. These two types of events give operational definitions of those *np* events. Because the *np* reaction is a two-body reaction, we can calculate for (n,p) events the momentum of the undetected neutron when the proton from the p(n, p)n reaction was detected in the rear. For example, if a proton was detected in the *upper* rear array, we know that the neutron must be scattered *down*. From the measured positions of the front and rear interaction vertices, the momentum vector of the undetected neutron can be calculated by solving the two-body kinematics equation for np scattering. Both (n,n) and (n,p) events can be used in the analysis. From the (n,n) events, the scattering asymmetry of the neutron is related to the polarization component(s) of the incident neutron as we saw in Chapter 4. From the (n,p) events, the scattering asymmetry of the *proton* is obtained. In this case, the direction of the scattered

neutron is opposite to that of the recoil proton if np scattering is assumed. In addition, the sign of the analyzing power for the undetected neutrons is opposite to that for the detected protons. Therefore, the sign of the scattering asymmetry for the (n,p) events is the same as that for the (n,n) events. To identify (n,n) events and (n,p) events, the time and position information from the front, rear, and the REVT detectors is used. We will discuss this analysis in the following sections.

5.8.9 Identifying the Charge Status of Particles in the NPOL Rear Arrays

The rear veto (REVT) detectors mainly served to identify the ID of the particle. As discussed in Section 3.8.1, any particles moving toward the rear arrays from the front must go through the REVT array located 5 (cm) behind the 4th plane of the front array. Because charged particles interact with the REVT detectors quite efficiently, the ID of a particle detected in the rear array can be determined by examining the time and position correlations between hits in the front, REVT, and rear hits. If an event contains no hit in the REVT detectors a *neutral* particle is detected in the rear array. (If this particle is a neutron, it is an (n,n) event by definition.) Therefore, we discuss below the events which contain at least one REVT hit.

Time Correlation between Front and REVT Hits

After the interaction of a neutron in the front, the recoil proton fires in front detector(s). The recoil proton, if it has sufficient energy, can penetrate the front detectors, and fire the REVT detectors as well. Therefore, if the REVT detectors

have hits, time and position of the front and REVT hits must be correlated. If such correlations are indeed found for an event, we know those REVT hits are due to the recoil proton generated in one of the front detectors. If an event has no REVT hit, or if any REVT hit is uncorrelated in time and position with front hits, we keep those events as the rear detectors must be fired by a neutral particle. If an event has a REVT hit, the TOF difference between the REVT hit and a front hit ($TOF_{REVT} - TOF_{Front}$) is made, and the histogram counts were incremented. If there are multiple hits in the front and/or REVT detectors, the counts were incremented for *every* pair of the front and REVT hits. If there are time and position correlations between front hits and REVT hit(s), both the front and REVT detectors must have been fired by the same charged particle (probably a recoil proton). (However, we still don't know yet if this charged particle has made it to the rear detectors.)

To find the time correlation between those hits, we defined the time-correlated region on the above-mentioned histogram to be in the range from -2.0 to 7.0 (ns) for Q^2=0.45 $(GeV/c)^2$ and -2.0 to 5.0 (ns) for Q^2=1.14 $(GeV/c)^2$.

Accidental Charged Particles with no Interaction in the Front Array

Due to the positions of the FRVT, front, and REVT detectors, charged particles can hit the *top-most (bottom-most)* part of the FRVT array, then hit the top (bottom) part of the REVT array, and finally hit the top (bottom) REAR array, *without passing through the front detectors*[Taj02a]. This situation is possible because the FRVT array is slightly longer in y-direction than the front detector array. The maximum y position (the top-most part) of the FRVT #49 (#54) is larger by 3.0 cm (2.0 cm) than that of the Front #5. (See Appendix B and Figure 3.17.) [Similarly for the bottom FRVT and front detectors.] Furthermore, because the first FRVT

plane was placed at a higher y position by 1 cm than the second FRVT plane, the charged particles can pass through only one of the FRVT planes and miss the other one if they hit the top-most part of FRVT #49 or the bottom-most part of #50. Because the trigger is generated by a hit in the front array, there is the possibility for a neutron to enter the NPOL (before or after a charged particle passes through the veto detectors) and fire one of the front detectors to make a trigger while within the trigger time window, a charged particle passes through the top-most (bottom-most) part of the veto detectors and misses the front detectors. For the type of event, no time correlation exists between the front hit and the REVT hit, but a time correlation exists between a (front and/or rear) veto hit and the rear hit. Consequently, the charge status for the particles detected in the rear array can be misidentified as *neutral* particle in our analysis if such events are not removed. To correctly identify the charge status of the particle detected in the rear array, we rejected an event if the TOF difference between a rear hit and a FRVT hit is in the range, $5(ns) < TOF_{Rear} - TOF_{FRVT} < 28(ns)$.

Tracking from the Front to the Rear

Our first task was to sort the events according to type, either (n,n) or (n,p). All events for which neither REVT plane fired were categorized as (n,n) events. Events in which a REVT plane fired could be either (n,p) or (n,n). All events with hits in the REVT detector but not in the 4th plane of the front array are rejected. While most of the events with REVT hits were of the (n,p) type, a significant fraction were (n,n) events. Because a misidentification of event type results in a dilution of the measured scattering asymmetry, it was important to accurately distinguish the two event types. To identify the charge status of the particle that fired the rear array,

we used the position information of the hits in the front, REVT, and rear detectors. Figure 5.15 shows typical tracks for an (n,n) and an (n,p) event and their track angles. Let us assume that we already found an event which contains front and REVT hits that are correlated in time. Meeting that requirement would indicate that the recoil proton from the front fired the REVT array. However, we need to impose additional conditions to confirm this expectation. For data analysis at Q^2=0.45 $(GeV/c)^2$, we required that *both* REVT planes have a hit. If one of the REVT planes does not have a hit, that certainly implies that the recoil proton doesn't have sufficient energy to go through the REVT detectors and consequently does not make it to the rear array. For data analysis at Q^2=1.14 $(GeV/c)^2$, we require a hit in only one REVT plane because only one REVT plane existed as mentioned in Section 3.8.1. If the recoil proton penetrated the front array and fired the REVT detectors, there must be a hit in the 4th plane of the front array. Therefore, an event is rejected if there is no hit in the front 4th plane. We further impose a correlation in the x positions of the REVT hits and the front hit in the 4th plane. An event is rejected if the x difference between these hits is larger than 20 cm. For events which satisfy the above criteria the track angle is calculated. The track angle is the angle between the REVT hit position in the 2nd REVT plane (1st REVT plane for Q^2=1.14 $(GeV/c)^2$ data), the front interaction vertex position, and the rear interaction vertex position.

As discussed in Section 3.8.1, the recoil proton [scattered neutron] from an (n,n) event [(n,p) event] always misses the rear detectors assuming the interaction in the front is *np* scattering. For (n,p) event for which the recoil proton is detected in the rear array, the path of the proton becomes close to a straight line. Thus a small track angle must be measured in this case. However, because the position resolution for the front, REVT, and rear detectors are limited, the *measured* track angle is not

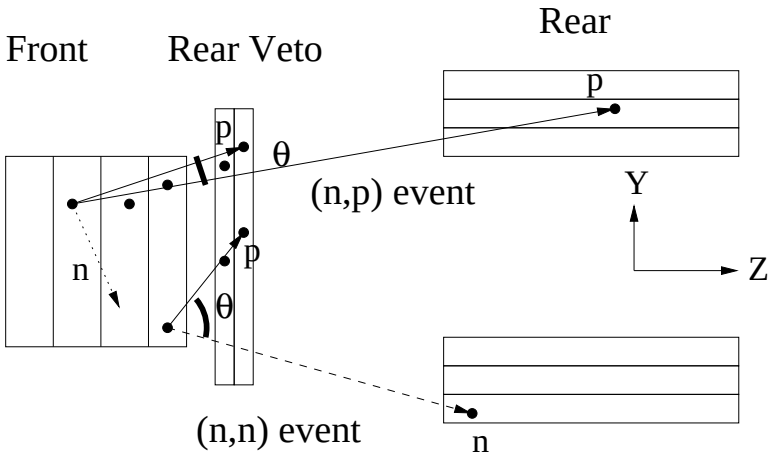

Figure 5.15: (n,n) and (n,p) events and their track angles. A side view of the front, REVT, and rear detectors (not drawn to scale), typical paths of the particles for (n,n) and (n,p) events, and their track angles are drawn. The block dots denote the detection points in the detectors. Track angle θ is the angle between the REVT hit position on the 2nd REVT plane, the front interaction vertex position, and the rear vertex position. For (n,n) event [(n,p) event], a large (small) track angle is measured.

necessarily close to zero. On the other hand, the track angle for (n,n) event, which is equal to the angle between the measured neutron and proton momentum vectors, must become large. (In the classical limit, this angle is 90° in the lab frame assuming the masses of the proton and neutron are identical.) Because the position resolutions for the veto and rear detectors were not very good, the distribution of the track angle is rather broad. We imposed the conditions on the track angle θ to distinguish (n,p) events from (n,n) events. The conditions are $\theta < 50°$ for (n,p) event analysis and $\theta > 60°$ for (n,n) event analysis for Q^2=0.45 and 1.14 $(GeV/c)^2$.

We have found so far the charge status of particles detected in the rear array. We now turn our attention to obtaining the yields for the asymmetry measurements.

5.8.10 3-Fold Coincidence Events

At this point, we found both neutral-particle and charged-particle events in the rear array from the quasielastic neutron events in the front array that formed a coincidence with the electrons in the HMS. These quasielastic events form *2-fold coincidences* between the HMS and the front array. In this section, we will find events that form coincidences between the HMS, front, and rear detectors, which we refer to *3-fold coincidence events*.

ΔTOF and Corrected ΔTOF

Events that form coincidences between the front and the rear array provide the data for the 3-fold coincidence events that can be used for the scattering asymmetry calculations. To obtain the yields for the asymmetry measurement, a histogram for the time difference between the rear and the front TOFs is made. We define the ΔTOF, which is a measured quantity, as

$$\Delta TOF = TOF^{RE} - TOF^{FR}, \tag{5.38}$$

where TOF^{RE} is the measured rear TOF from the target. The top plots of Figure 5.16 show the ΔTOF spectra at Q^2=0.45 and 1.14 $(GeV/c)^2$. Because all of the cuts mentioned preciously were applied to make these plots, these ΔTOF spectra were created for the *2-fold* coincidence neutron events. The background level at Q^2=0.45 $(GeV/c)^2$ is much higher than at Q^2=1.14 $(GeV/c)^2$ because beam currents were high ($\sim$ 70 [μA]) during data-taking at Q^2=0.45 $(GeV/c)^2$, while low beam currents ($\sim$ 40 [μA]) were used at Q^2=1.14 $(GeV/c)^2$. Also, neutron multiple scattering in the NPOL detector arrays is greater at Q^2=0.45 $(GeV/c)^2$. The ΔTOF spectra have a broad distribution. Because the rear detectors are so long ($\sim$ 100 [cm]) along the

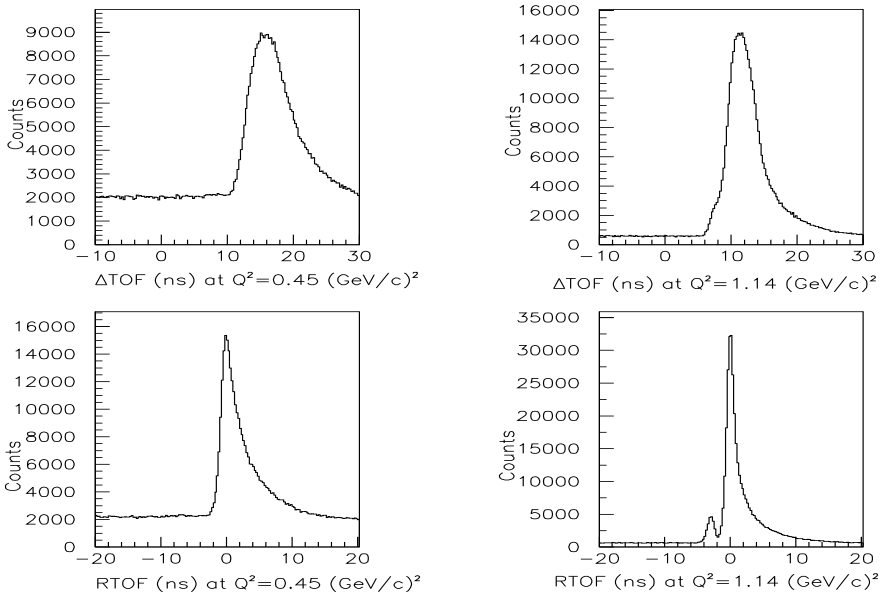

Figure 5.16: Histograms of ΔTOF and RTOF at Q^2=0.45 and 1.14 $(GeV/c)^2$. The left-upper and right-upper plots show the ΔTOF spectra at Q^2=0.45 and 1.14 $(GeV/c)^2$, respectively. The corresponding plots for the the *corrected* ΔTOF (RTOF) spectra are shown on the left-down and right-down plots. The area under the RTOF peak contains the *3-fold* coincidence events from which the scattering asymmetries are calculated. The plots at Q^2=0.45 $(GeV/c)^2$ (Q^2=1.14 $(GeV/c)^2$) shown here were made with (n,n) events, and runs with the spin precession angle of $+40°$ ($\pm 90°$) were used.

z-axis, the correction of the ΔTOF greatly depends on the determination of the z position of the detection point in a rear detector. As in the case for the front TOF, the ΔTOF can be corrected by taking into account the flight distance between the front and the rear detectors. The *corrected* ΔTOF, which we refer to RTOF, is the time difference between the *measured* ΔTOF given in Equation 5.38, and the *estimated* TOF from the front to the rear, ΔTOF_{est}.

$$RTOF = (\Delta TOF - \Delta TOF_{est}) \cdot \frac{250\,(cm)}{(Flight\ distance)}. \tag{5.39}$$

In Equation 5.39, the RTOF is normalized according to the nominal flight distance (from the front to the rear) of 250 cm. Similarly for the front, ΔTOF_{est} can be calculated from the *estimated* particle momentum obtained by solving the kinematic equations with the knowledge of the particle scattering angle and incident neutron momentum. Because we assumed the reaction in the front is *np* elastic scattering, the four-momentum equation for this reaction is given by

$$n^{\mu} + p^{\mu} = n^{'\mu} + p^{'\mu}, \tag{5.40}$$

where n^{μ}, p^{μ}, $n^{'\mu}$, and $p^{'\mu}$ are four momenta of the neutron incident on the front array, the proton in the scintillator material, the scattered neutron, and the recoil proton. We assume that the proton in the scintillator material is at rest in the lab frame. In addition, we know all the components of n^{μ} as they were measured. However, we take the values of n^{μ} for this kinematic calculation to be the *estimated* energy and momentum components of the neutron which were obtained when the CTOF was calculated. From the measurements of the interaction point at the target and the detection points in the front and rear arrays, the scattering angle of the particle from the front to the rear is calculated. (This angle is the neutron scattering angle [the proton recoil angle] for an (n,n) event [(n,p) event].) Thus, three unknowns (the magnitude of the scattered neutron momentum and the two components of the recoil proton momentum) can be determined by solving Equation 5.40 for each event. Details about the calculations of the estimated particle momentum for both (n,n) and (n,p) events are given in Appendix C.1. The estimated particle TOF, ΔTOF_{est}, is then easily obtained from the estimated particle velocity and the measured flight distance between the detection points in the front and rear. Because the RTOF has a peak centered about 0 (ns), this peak is certainly for the three-fold coincidence neutron events. Although the resolution of the TOF is greatly improved, the RTOF

spectrum still has a quite broad distribution compared to the CTOF spectrum. The events with large RTOF in the tail region of the histogram are due to *slow* neutrons, which are not from *np* scattering events [Taj02b]. One possible situation is that the neutron interacted with an organic material containing lots of protons and more than one proton is knocked out after the interaction in a front detector. That would explain why the slow neutrons are observed in the rear array. Even though they are not pure *np* scattering events, they can still be used for the scattering asymmetry calculation because they are indeed neutron events scattered from the front and the analyzing power for these processes is non-zero and have same sign as for *np* elastic scattering.

The γ Peak from the π^0 Creation Events in the Front

A small peak appeared at around $RTOF \sim -3$ (ns) on the plot of RTOF at Q^2=1.14 $(GeV/c)^2$ in Figure 5.16. The velocity of these particles were found to be close to the speed-of-light and that suggests those events must be due to light neutral particles created in the front array upon neutron interaction. We claim these events are due to the π^0 particles created in the front, which decays into two gammas immediately. At Q^2=1.14 $(GeV/c)^2$, a neutron incident on the front array has a nominal kinetic energy of 606 MeV as given in Table 1.2. Therefore, a neutral pion with the mass of about 135 MeV can be created in a neutron interaction, and one of the decay gammas can have high enough energy to fire a rear detector. Because the neutral pion decays into two gammas in 10^{-17} sec, the particles detected in the rear array are gammas. A pion created in the front array may or may not provide the scattering asymmetry information. As far as our determination of the scattering asymmetry of the *neutron* is concerned, it is not possible to determine the direction

(up or down) the neutron was scattered when a gamma is detected in the rear array. Therefore, gamma events were removed from our analysis. At Q^2=0.45 (GeV/c)^2, a gamma peak is not present on the RTOF plot in Figure 5.16.

Background Events

Figure 5.17 shows a 3-dim plot of CTOF vs RTOF at Q^2=1.14 (GeV/c)^2. All the cuts except for the CTOF and RTOF cuts were applied. A large peak in the middle around the origin represents the 3-fold coincidence events. A small peak right next to the large one is the gamma peak discussed above. This figure also shows background events that need to be subtracted from the 3-fold coincidence peak. A

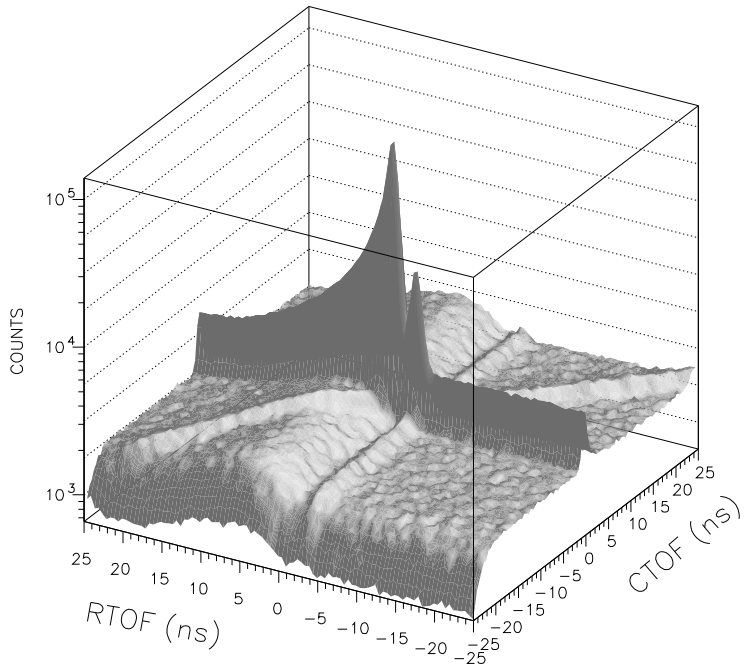

Figure 5.17: A 3-dim plot of CTOF vs RTOF at Q^2=1.14 (GeV/c)^2. Note that the counts are shown in log scale.

broad band parallel to the CTOF axis but outside of the 3-fold peak region is seen in an RTOF region from 0 to around 17 (ns). Events from this band did not make a coincidence with the HMS but they did make a coincidence between the front and the rear. They are called accidental coincidence events and will be discussed in detail below. Similarly, a band parallel to the RTOF axis at around CTOF=0 (ns) exists from RTOF = -25 to -4 (ns). This band is due to events which did not make a coincidence between the front and the rear. However, they did make a coincidence between the front array and the HMS. Figure 5.18 shows a density plot of Figure 5.17. Both types of background events mentioned above are clearly shown on this plot.

There is a diagonal band which goes through the origin (0,0) in Figures 5.17 and 5.18. This diagonal band is created due to events which form coincidence between the HMS and the rear array but are not time-correlated with the hit in the front array. The equation for this diagonal band can be expressed as $CTOF + RTOF \sim 0$. From Equations 5.37, 5.38, and 5.39, this relation is rewritten in terms of the measured rear TOF from the target to the rear, TOF^{RE},

$$TOF^{RE} \sim TOF^{FR}_{est} + \Delta TOF_{est}. \tag{5.41}$$

The accidental neutral events that cause the diagonal band can be understood as follows. As discussed in Section 3.8.1, the rear detectors are shielded from the direct flux from the target. Therefore, a particle must scatter in the front in order to reach the rear array. Suppose at some instant a neutron fires a front detector and causes a NPOL trigger but was not scattered into the rear array. After that occurs, a second neutron from the quasielastic reaction enters the NPOL and scatters from the front array and is detected in a rear detector. If these two random events happen within the 70 (ns) trigger coincidence time window, then a 3-fold coincidence is formed.

Another requirement is that either the second reaction did not fire a detector in the front array or it fired the same detector as the first neutron. Note that we cannot record more than one TDC value for the same PMT for each event. In this case, the measured front hit due to the *accidental* particle is not correlated with either the rear or the HMS. The situation described above would make the upper-left part ($CTOF < 0$)of the diagonal band. On the other hand, let us consider the situation when the second neutron that interacts in the front array is accidental (no time correlation with either the HMS or the rear array), and it causes the NPOL trigger. When a neutron scatters in both a front and a rear detector, it is possible that the pulse height signal in the front detector is *below* the hardware threshold of 4 MeVee. If this happens, no trigger is generated from this missing front hit. This could happen if the front interaction point is located close to the surface of the front array; the recoil protons cannot travel very far before they go out of the front array. After this happens, the trigger is generated if an accidental neutron fires a front detector at a later time. The situation would make the lower-right part ($CTOF > 0$) of the diagonal band. Finally, there is flat background that exists throughout the spectrum in Figures 5.17 and 5.18. These background counts are due to events with no time correlation between the HMS, front, and the rear detectors.

It is quite reasonable to assume these background events described above exist under the 3-fold peak region because these backgrounds happen randomly. Therefore, the yields for these background events must be subtracted from the yields for the 3-fold peak.

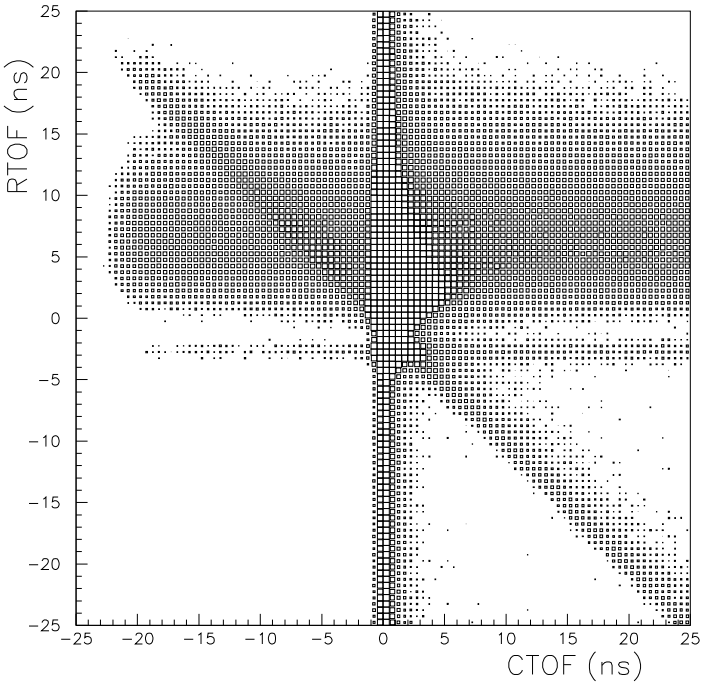

Figure 5.18: A density plot of CTOF vs RTOF at Q^2=1.14 $(GeV/c)^2$. To make this plot, the z-axis in Figure 5.17 is sliced between 2000 and 4000. That is, the bins with counts smaller than 2000 in Figure 5.17 are not shown, and the bins with counts larger than 4000 are treated the same as bins with 4000 counts on this plot.

CTOF Background Subtraction

As discussed in Section 5.8.7, events with the CTOF in the region of −1.0 (ns) and +1.0 (ns) (after other appropriate cuts were applied) were identified as the quasielastic events. The DTOF and RTOF histograms were made using events with CTOF in this region. However, events with the value of CTOF under the peak could still be accidental background events. Because of this possibility, the yields for such background events must be estimated, and they must be subtracted from the RTOF histogram. Those background neutrons which appeared in the CTOF histogram did

not form a coincidence with the HMS. However, many of those background neutrons have momenta comparable to (or smaller than) the nominal neutron momentum for the quasielastic reaction. Therefore, those neutrons could cause so called *accidental coincidences* between the front and the rear. That is, the distributions of the RTOF for those neutrons are not *flat*. These CTOF background events that contribute to

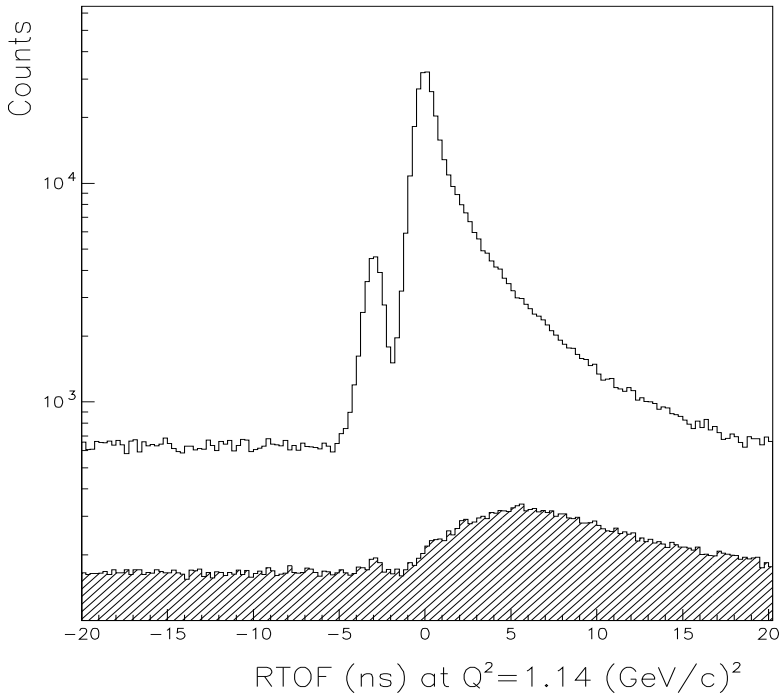

Figure 5.19: RTOFs for the real and accidental coincidence events at Q^2=1.14 $(GeV/c)^2$ plotted in log scale. The top plot is the RTOF spectrum for the neutron events in the HMS-front coincidence peak and the bottom plot is the RTOF spectrum created using the background events for CTOF from −20.0 (ns) to −5.0 (ns) as shown in Figure 5.14.

the RTOF histogram must be subtracted. To do this, we performed the following things. First, we chose a background region of −20.0 (ns) to −5.0 (ns) in the CTOF histogram as shown in Figure 5.14, and the RTOF was calculated for those events.

(Note that the *measured* neutron momentum incident on the front array was *not* used when ΔTOF_{est} was calculated from the kinematic equations. As we described earlier, an *estimated* incident neutron momentum was used so the values for RTOF for those events can still be calculable. Therefore, the RTOF can be calculable for those CTOF events in the background region.) Because the CTOF background region we chose is 7.5 times wider than the CTOF peak width of 2.0 (ns), the yields of the accidental coincidence need to be scaled by a factor 1/7.5 to correctly estimate the background yields on the RTOF histogram for real events. Figure 5.19 shows the RTOF histograms for real and *accidental coincidence* events. The latter (shown as a hatched region) has been scaled by a factor 1/7.5. (This distribution is in fact expected from Figure 5.18.) A peak at around RTOF=6 (ns) on this histogram indicates that those accidental neutrons incident on the front are much slower than the neutrons from the quasielastic reaction. A small gamma peak is also seen on this plot. The yields of those accidental coincidences must be subtracted from the real yields. In other words, the difference between the two histograms in Figure 5.19 is made, which will be shown next.

RTOF Background Subtraction and Obtaining the Yields

Figure 5.20 shows the RTOF histograms after the accidental coincidence events from the CTOF background region is subtracted out. As we saw in Chapter 4, To calculate the asymmetry, we must obtain the yields for the events with '-' helicity and particle scattered *up*, '+' helicity and particle scattered *up*, '-' helicity and particle scattered *down*, and '+' helicity and particle scattered *down*. Those yields can be obtained from the four histograms in Figure 5.20. Each of the four histograms is integrated from $RTOF = RTOF_{low}$ to $RTOF = RTOF_{high}$ as indicated by the two

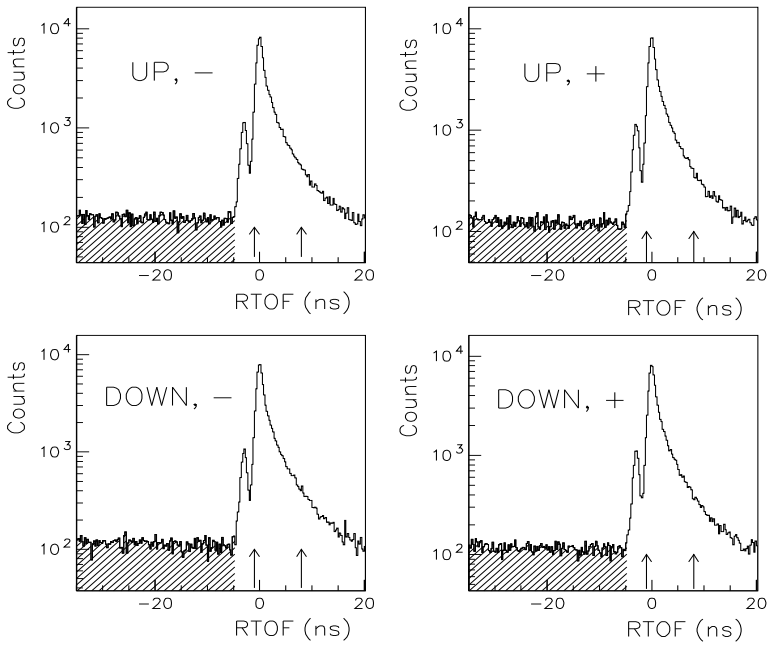

Figure 5.20: The final RTOF histograms used for the scattering asymmetry calculations. The accidental coincidence events from the CTOF background region have already been subtracted. Plots were made for (n,n) events at Q^2=1.14 $(GeV/c)^2$. The upper-left plot, labeled as 'UP, −', is created from events with '−' helicity and neutron scattered *up*. The bottom-right plot, labeled as 'DOWN, +', is created from events with '+' helicity and neutron scattered *down*. Similarly for the other plots. The two arrows on each histogram define the region of integration for obtaining yields.

arrows shown on each histogram. The optimal values for $RTOF_{low}$ and $RTOF_{high}$ are to be determined. Although the CTOF background events have been subtracted, the RTOF background events also need to be subtracted after the RTOF peak yields are obtained. A flat tail region from −35.0 (ns) to −5.0 (ns) (shown as a hatched region in Figure 5.20) is chosen as the RTOF background region. As for the CTOF background yields, the RTOF background yields must be scaled according to the width of the RTOF peak region. The scale factor for the background yields is given

by $(RTOF_{high} - RTOF_{low})/30.0$ (ns). The final yields are obtained by subtracting the (scaled) RTOF background yields using the peak yields. This procedure is repeated for each of the four histograms to obtain yields N_U^+, N_D^+, N_U^- and N_D^-.

Once those four yields are obtained for each run, the cross ratio r and then the scattering asymmetry ξ are calculated from Equation 4.12 and Equation 4.15, respectively. This procedure is repeated for all the good runs already selected in Section 5.3.

Collecting the Asymmetries

When the asymmetry values are averaged, the asymmetry for each run is weighted according to the uncertainty for the run. The following things were performed when the asymmetry results are averaged. First, because the asymmetry value for a run is proportional to the value of beam polarization during the period of data-taking, the value for polarization must be scaled accordingly. In our data analysis, it was scaled to a mean polarization of 80%.

Second, data at Q^2=0.45 $(GeV/c)^2$ ($\pm$40 method) were taken with the Charybdis currents of $\pm$170(A), and a half-wave plate was inserted for about half of the runs. Because the half-wave plate serves to flip the sign of the beam helicity when the electrons are injected to the hall-C arc from the linac, it changes the sign of the measured asymmetry value. Therefore, the asymmetry sign must be flipped in software for those runs taken with the half-wave plate in.

Third, data at Q^2=1.14 $(GeV/c)^2$ were taken with or without the half-wave plate, and with the Charybdis magnet off or on. For Charybdis-off runs, the asymmetry signs need to be flipped for the half-wave plate in when the results are averaged.

When the Charybdis was on, we used the magnet currents of +540 or −540(A). In our experiment, the negative Charybdis currents would precess the polarization of the neutron by +90°. Therefore, the measured asymmetry sign for a run taken with the Charybdis currents of −540(A) becomes opposite to the case with the currents of +540(A), assuming the status of the half-wave plate did not change for these runs. Because both the half-wave plate and the Charybdis currents could flip the asymmetry sign, we have the following cases. When collecting the asymmetries at Q^2=1.14 $(GeV/c)^2$, the sign for a run must be flipped if one of the following conditions is met.

1. Half-wave plate was not inserted *and* positive Charybdis currents were used to take data.

2. Half-wave plate was inserted *and* negative Charybdis currents were used to take data.

RTOF Bite Study

As we saw earlier, the RTOF histogram has a broad tail due to slow neutrons. If, for example, a neutron knocked out more than one proton from the front upon interaction, the analyzing power for such an event may or may not become small. If the analyzing power indeed becomes small for those events, those tail events will yield a small asymmetry value. To avoid a dilution of measured scattering asymmetry, we performed an optimization of the RTOF region of integration to obtain the yields, which we call an RTOF bite study [Taj02b]. The purpose of this study is to obtain the smallest statistical uncertainty in the value for g by optimizing the minimum and maximum RTOF values. To do this, the results were obtained by changing the

minimum and maximum $RTOF$ values, T_1 and T_2, respectively, which define the region of integration as shown in Figure 5.20. The value for g was calculated from the PWIA formulas (Equations 4.22 and 4.31). Although these formulas for g cannot be used to obtain the *final* result for g, they can be used to perform this study.

Tables 5.4 to 5.7 give the results for the asymmetries, the asymmetry ratio η, g, and G_E^n with the fixed value of $T_1 = -1.0$ (ns) and different values of T_2. Each table gives results for each Q^2 point and each event type [(n,n) or (n,p)]. These tables show that the values for the asymmetries become smaller as T_2 becomes larger. This trend indicates that the analyzing power of the tail region is small. The value for $T_1 = -1.0$ was used so that the events from the gamma peak are excluded from the analysis at Q^2=1.14 $(GeV/c)^2$.

The values for $|\Delta g/g|$ becomes minimum at small RTOF value. For example, the minimum is achieved at $T_2 = 4$(ns) for the Q^2=1.14 $(GeV/c)^2$ data with (n,p) events. However, the values for g are not stable at small RTOF values probably because the asymmetry values in this regime are susceptible to a slight change in timing calibration, and that would cause a fluctuation in the asymmetry ratio and g. Therefore, we decided to choose the T_2 value of 8.0 (ns).

Chapter 6

Acceptance Averaging and Corrections for Nuclear Physics Effects

The values of the scattering asymmetries of the neutron from the quasielastic $^2\mathrm{H}(\vec{e}, e'\vec{n})^1\mathrm{H}$ reaction were found as discussed in Chapter 5. We also obtained the results of g and G_E^n using the PWIA formula in the previous chapter. However, these results of g and G_E^n should not be quoted as the final results because the PWIA formula, which assumes a free neutron target, cannot be applied to our case. Because a LD_2 target was used in our experiment, we need to consider the electrodisintegration of the deuteron, and the nuclear physics effects such as FSI, IC, and MEC must be corrected for in our analysis. Because of the finite size of our detectors, the *acceptance averaging* must be considered in our analysis. As discussed in Chapter 4, the ratio of the polarization components, P'_S/P'_L can be written in terms

T_1 (ns)	T_2 (ns)	ξ_- (%)	ξ_+ (%)	η	g	$\lvert\Delta g/g\rvert$	G_E^n	$\frac{\Delta G_E^n}{G_E^n}$
-1.0	1.0	8.38 ± 0.27	-11.53 ± 0.39	-0.727 ± 0.034	-0.0533 ± 0.0077	0.1449	0.0383 ± 0.0059	0.1532
-1.0	2.0	7.02 ± 0.24	-9.66 ± 0.34	-0.726 ± 0.035	-0.0535 ± 0.0080	0.1495	0.0385 ± 0.0061	0.1577
-1.0	3.0	6.06 ± 0.22	-8.67 ± 0.32	-0.699 ± 0.036	-0.0597 ± 0.0084	0.1412	0.0429 ± 0.0064	0.1498
-1.0	4.0	5.35 ± 0.21	-7.90 ± 0.31	-0.677 ± 0.038	-0.0650 ± 0.0090	0.1388	0.0467 ± 0.0069	0.1476
-1.0	5.0	5.03 ± 0.21	-7.35 ± 0.30	-0.684 ± 0.040	-0.0632 ± 0.0095	0.1500	0.0455 ± 0.0072	0.1581
-1.0	6.0	4.79 ± 0.21	-7.02 ± 0.30	-0.682 ± 0.041	-0.0637 ± 0.0099	0.1549	0.0458 ± 0.0075	0.1628
-1.0	7.0	4.56 ± 0.21	-6.76 ± 0.30	-0.675 ± 0.043	-0.0654 ± 0.0103	0.1573	0.0471 ± 0.0078	0.1651
-1.0	8.0	4.41 ± 0.21	-6.47 ± 0.30	-0.681 ± 0.045	-0.0640 ± 0.0108	0.1685	0.0460 ± 0.0081	0.1758
-1.0	9.0	4.27 ± 0.21	-6.24 ± 0.30	-0.684 ± 0.047	-0.0632 ± 0.0113	0.1783	0.0455 ± 0.0084	0.1852
-1.0	10.0	4.18 ± 0.21	-6.12 ± 0.31	-0.683 ± 0.049	-0.0635 ± 0.0117	0.1838	0.0457 ± 0.0087	0.1905
-1.0	11.0	4.09 ± 0.22	-6.00 ± 0.31	-0.681 ± 0.051	-0.0639 ± 0.0121	0.1892	0.0460 ± 0.0090	0.1957
-1.0	12.0	4.00 ± 0.22	-5.89 ± 0.32	-0.680 ± 0.053	-0.0643 ± 0.0126	0.1953	0.0462 ± 0.0093	0.2016
-1.0	13.0	3.98 ± 0.22	-5.83 ± 0.33	-0.682 ± 0.054	-0.0638 ± 0.0129	0.2027	0.0459 ± 0.0096	0.2087
-1.0	14.0	3.86 ± 0.23	-5.82 ± 0.33	-0.664 ± 0.055	-0.0680 ± 0.0133	0.1960	0.0489 ± 0.0099	0.2023
-1.0	15.0	3.88 ± 0.23	-5.91 ± 0.34	-0.656 ± 0.055	-0.0701 ± 0.0134	0.1918	0.0504 ± 0.0100	0.1982

Table 5.4: Uncorrected results for (n,n) events at Q^2=0.45 $(GeV/c)^2$. The formula for ±40°method were used to calculate the asymmetries. The values for g and G_E^n were obtained from the PWIA formula.

T_1 (ns)	T_2 (ns)	ξ_- (%)	ξ_+ (%)	η	g	$\lvert\Delta g/g\rvert$	G_E^n	$\frac{\Delta G_E^n}{G_E^n}$
-1.0	1.0	4.29 ± 0.32	-6.13 ± 0.44	-0.699 ± 0.072	-0.0596 ± 0.0169	0.2831	0.0429 ± 0.0123	0.2875
-1.0	2.0	3.98 ± 0.24	-5.57 ± 0.34	-0.714 ± 0.061	-0.0563 ± 0.0141	0.2503	0.0405 ± 0.0103	0.2552
-1.0	3.0	3.59 ± 0.21	-5.48 ± 0.30	-0.654 ± 0.052	-0.0705 ± 0.0128	0.1817	0.0507 ± 0.0096	0.1885
-1.0	4.0	3.38 ± 0.19	-5.50 ± 0.27	-0.614 ± 0.046	-0.0807 ± 0.0120	0.1490	0.0580 ± 0.0091	0.1572
-1.0	5.0	3.30 ± 0.18	-5.45 ± 0.26	-0.606 ± 0.044	-0.0829 ± 0.0116	0.1401	0.0596 ± 0.0089	0.1487
-1.0	6.0	3.17 ± 0.18	-5.39 ± 0.25	-0.589 ± 0.043	-0.0871 ± 0.0115	0.1316	0.0627 ± 0.0088	0.1408
-1.0	7.0	3.09 ± 0.17	-5.37 ± 0.25	-0.575 ± 0.042	-0.0909 ± 0.0114	0.1251	0.0654 ± 0.0088	0.1347
-1.0	8.0	3.09 ± 0.17	-5.26 ± 0.24	-0.589 ± 0.043	-0.0873 ± 0.0114	0.1304	0.0628 ± 0.0088	0.1397
-1.0	9.0	3.03 ± 0.17	-5.22 ± 0.24	-0.580 ± 0.042	-0.0896 ± 0.0114	0.1275	0.0644 ± 0.0088	0.1370
-1.0	10.0	3.01 ± 0.17	-5.16 ± 0.24	-0.583 ± 0.043	-0.0888 ± 0.0115	0.1294	0.0639 ± 0.0089	0.1387
-1.0	11.0	2.98 ± 0.17	-5.10 ± 0.24	-0.582 ± 0.043	-0.0890 ± 0.0116	0.1302	0.0640 ± 0.0089	0.1395
-1.0	12.0	2.97 ± 0.17	-5.06 ± 0.24	-0.588 ± 0.043	-0.0876 ± 0.0116	0.1328	0.0630 ± 0.0089	0.1419
-1.0	13.0	2.97 ± 0.17	-5.03 ± 0.24	-0.590 ± 0.044	-0.0869 ± 0.0117	0.1346	0.0625 ± 0.0090	0.1436
-1.0	14.0	2.97 ± 0.17	-5.02 ± 0.24	-0.593 ± 0.044	-0.0862 ± 0.0117	0.1361	0.0620 ± 0.0090	0.1450
-1.0	15.0	2.97 ± 0.17	-5.00 ± 0.24	-0.592 ± 0.044	-0.0863 ± 0.0118	0.1367	0.0621 ± 0.0090	0.1455

Table 5.5: Uncorrected results for (n,p) events at Q^2=0.45 $(GeV/c)^2$. The formula for ±40°method were used to calculate the asymmetries. The values for g and G_E^n were obtained from the PWIA formula.

T_1 (ns)	T_2 (ns)	ξ_S (%)	ξ_L (%)	η	g	$\lvert\Delta g/g\rvert$	G_E^n	$\frac{\Delta G_E^n}{G_E^n}$
-1.0	1.0	-1.74 ± 0.18	-8.08 ± 0.28	0.215 ± 0.023	-0.1279 ± 0.0139	0.1084	0.0361 ± 0.0043	0.1194
-1.0	2.0	-1.64 ± 0.16	-7.19 ± 0.25	0.228 ± 0.024	-0.1357 ± 0.0142	0.1048	0.0384 ± 0.0045	0.1161
-1.0	3.0	-1.53 ± 0.15	-6.84 ± 0.24	0.224 ± 0.024	-0.1333 ± 0.0142	0.1064	0.0377 ± 0.0044	0.1175
-1.0	4.0	-1.41 ± 0.15	-6.53 ± 0.24	0.217 ± 0.024	-0.1290 ± 0.0144	0.1115	0.0364 ± 0.0045	0.1222
-1.0	5.0	-1.33 ± 0.15	-6.31 ± 0.23	0.211 ± 0.025	-0.1255 ± 0.0146	0.1162	0.0355 ± 0.0045	0.1265
-1.0	6.0	-1.27 ± 0.15	-6.05 ± 0.23	0.211 ± 0.025	-0.1254 ± 0.0151	0.1201	0.0354 ± 0.0046	0.1301
-1.0	7.0	-1.20 ± 0.14	-5.89 ± 0.23	0.204 ± 0.026	-0.1216 ± 0.0153	0.1259	0.0344 ± 0.0047	0.1355
-1.0	8.0	-1.22 ± 0.14	-5.79 ± 0.23	0.211 ± 0.026	-0.1257 ± 0.0156	0.1241	0.0355 ± 0.0047	0.1338
-1.0	9.0	-1.21 ± 0.14	-5.70 ± 0.23	0.211 ± 0.027	-0.1258 ± 0.0158	0.1259	0.0356 ± 0.0048	0.1354
-1.0	10.0	-1.17 ± 0.14	-5.54 ± 0.23	0.212 ± 0.027	-0.1262 ± 0.0163	0.1295	0.0357 ± 0.0050	0.1389
-1.0	11.0	-1.16 ± 0.14	-5.49 ± 0.23	0.211 ± 0.028	-0.1253 ± 0.0165	0.1317	0.0354 ± 0.0050	0.1409
-1.0	12.0	-1.15 ± 0.15	-5.48 ± 0.23	0.210 ± 0.028	-0.1249 ± 0.0166	0.1330	0.0353 ± 0.0050	0.1421
-1.0	13.0	-1.12 ± 0.15	-5.44 ± 0.23	0.206 ± 0.028	-0.1223 ± 0.0168	0.1371	0.0346 ± 0.0050	0.1459
-1.0	14.0	-1.09 ± 0.15	-5.40 ± 0.23	0.202 ± 0.028	-0.1204 ± 0.0170	0.1408	0.0340 ± 0.0051	0.1494
-1.0	15.0	-1.08 ± 0.15	-5.44 ± 0.23	0.199 ± 0.028	-0.1186 ± 0.0169	0.1429	0.0335 ± 0.0051	0.1514

Table 5.6: Uncorrected results for (n,n) events at Q^2=1.14 (GeV/c)^2

T_1 (ns)	T_2 (ns)	ξ_S (%)	ξ_L (%)	η	g	$\lvert\Delta g/g\rvert$	G_E^n	$\frac{\Delta G_E^n}{G_E^n}$
-1.0	1.0	-1.24 ± 0.19	-4.88 ± 0.30	0.254 ± 0.041	-0.1512 ± 0.0247	0.1633	0.0427 ± 0.0073	0.1708
-1.0	2.0	-1.07 ± 0.16	-4.70 ± 0.26	0.228 ± 0.037	-0.1355 ± 0.0221	0.1630	0.0383 ± 0.0065	0.1705
-1.0	3.0	-0.99 ± 0.15	-4.48 ± 0.24	0.222 ± 0.036	-0.1322 ± 0.0216	0.1632	0.0374 ± 0.0064	0.1707
-1.0	4.0	-0.91 ± 0.15	-4.26 ± 0.23	0.213 ± 0.036	-0.1271 ± 0.0217	0.1704	0.0359 ± 0.0064	0.1776
-1.0	5.0	-0.88 ± 0.14	-4.10 ± 0.23	0.213 ± 0.037	-0.1269 ± 0.0218	0.1721	0.0359 ± 0.0064	0.1792
-1.0	6.0	-0.78 ± 0.14	-3.88 ± 0.22	0.202 ± 0.038	-0.1203 ± 0.0225	0.1874	0.0340 ± 0.0066	0.1940
-1.0	7.0	-0.74 ± 0.14	-3.77 ± 0.22	0.197 ± 0.038	-0.1171 ± 0.0228	0.1950	0.0331 ± 0.0067	0.2013
-1.0	8.0	-0.71 ± 0.14	-3.62 ± 0.22	0.196 ± 0.040	-0.1164 ± 0.0236	0.2025	0.0329 ± 0.0069	0.2086
-1.0	9.0	-0.69 ± 0.14	-3.52 ± 0.22	0.196 ± 0.041	-0.1166 ± 0.0241	0.2067	0.0330 ± 0.0070	0.2127
-1.0	10.0	-0.68 ± 0.14	-3.47 ± 0.21	0.196 ± 0.041	-0.1164 ± 0.0244	0.2094	0.0329 ± 0.0071	0.2153
-1.0	11.0	-0.67 ± 0.14	-3.46 ± 0.21	0.194 ± 0.041	-0.1154 ± 0.0244	0.2112	0.0326 ± 0.0071	0.2170
-1.0	12.0	-0.67 ± 0.14	-3.42 ± 0.21	0.195 ± 0.041	-0.1159 ± 0.0246	0.2123	0.0327 ± 0.0071	0.2181
-1.0	13.0	-0.68 ± 0.14	-3.43 ± 0.21	0.198 ± 0.041	-0.1181 ± 0.0246	0.2084	0.0334 ± 0.0071	0.2143
-1.0	14.0	-0.69 ± 0.14	-3.44 ± 0.21	0.200 ± 0.041	-0.1192 ± 0.0245	0.2058	0.0337 ± 0.0071	0.2118
-1.0	15.0	-0.71 ± 0.14	-3.42 ± 0.21	0.208 ± 0.042	-0.1238 ± 0.0248	0.2003	0.0350 ± 0.0072	0.2065

Table 5.7: Uncorrected results for (n,p) events at Q^2=1.14 (GeV/c)^2

of the asymmetry ratio as shown in Equations 4.21 and 4.30. Therefore, P'_S/P'_L is *measured* from the ratio of the scattering asymmetries in our experiment. We developed a Monte-Carlo simulation program to average the theoretical predictions over the finite acceptance of our experimental setup to study the importance of nuclear physics effects in our data. The structure functions for the electrodisintegration of the deuteron ($e + d \rightarrow e' + n + p$) used in our simulation were calculated by Arenhövel *et. al.* [Are88, Lei91, Are95, Are02]. Their model takes into account the nuclear physics and relativistic effects. The final results were obtained by comparing the experimentally determined ratio of P'_S/P'_L to the simulated values.

6.1 The Lab and n-p CM Frame

Arenhövel *et. al.* calculated the five-fold differential cross section of $^2\mathrm{H}(\vec{e}, e'\vec{N})N$ and the recoil polarization observables from the $^2\vec{\mathrm{H}}(\vec{e}, e'n)\mathrm{p}$ reaction which involves not only the polarized electron beam but also the *target* polarization. Figure 6.1

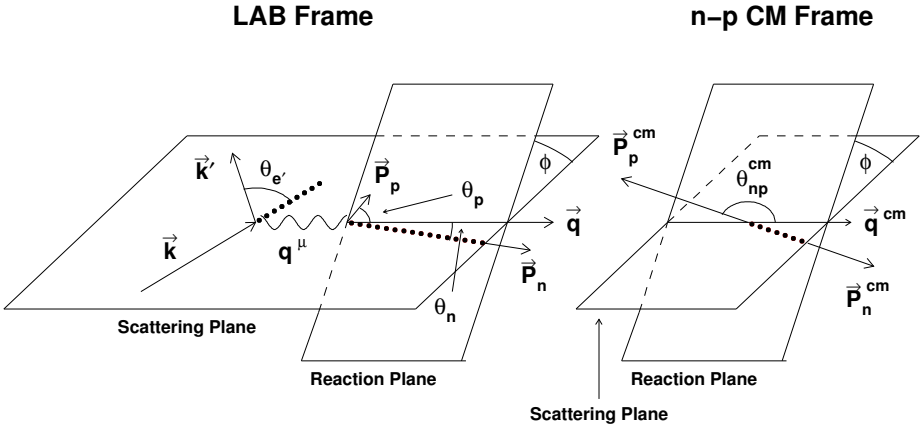

Figure 6.1: Coordinate systems for electrodisintegration of deuteron used by Arenhövel.

shows the LAB [1] and n-p center-of-momentum (CM) reference frames in which this model is based [Fab79]. A different coordinate system is defined for each of the planes drawn in Figure 6.1. The scattering plane is defined by $\vec{k}$ and $\vec{k'}$. In the LAB *scattering* basis, the z axis is along the $\vec{q}$. The y axis is perpendicular to the scattering plane and is along the direction of $\vec{k} \times \vec{k'}$. The direction of x axis is chosen so that the x, y, and z axes form a right-handed coordinate system.

The LAB reaction plane is defined by the recoil momentum vectors of the neutron and the proton, $\vec{p_n}$ and $\vec{p_p}$. In the Lab *reaction* basis, the $\hat{z}$ is along the $\vec{p_n}$, the $\hat{y}$ is along $\vec{q} \times \vec{p_n}$, and the $\hat{x}$ is $\hat{x} = \hat{y} \times \hat{z}$.

We denote $\hat{l}, \hat{m}, \hat{n}$ be the unit vectors along the x, y, and z axes, respectively, in the Lab reaction basis. They can be written as

$$\begin{aligned} \hat{l} &= \hat{m} \times \hat{n} \\ \hat{m} &= \frac{\vec{q} \times \vec{p_n}}{|\vec{q} \times \vec{p_n}|} \\ \hat{n} &= \frac{\vec{p_n}}{|\vec{p_n}|} \end{aligned} \tag{6.1}$$

The angle between the scattering and the reaction planes is labeled as ϕ, and the angle between $\vec{q}$ and $\vec{p_n}$ ($\vec{p_p}$) is called θ_n (θ_p). The angle between $\vec{q}$ and the *relative n-p motion*, $\vec{p_p} - \vec{p_n}$ is θ_{np} (not shown in the figure).

The n-p CM frame defined by Arenhövel *et. al.* is obtained by boosting the LAB frame along the LAB z axis so that the sum of the proton and neutron momentum vectors vanishes as shown in Figure 6.1. All the variables in the n-p CM frame are denoted by the superscripts 'cm' added to the LAB variables. In this reference frame, the vector of the relative n-p motion becomes parallel to $\vec{p_p}$. Thus, $\theta_p^{cm} = \theta_{np}^{cm}$ and

[1] Note that we already defined another Lab frame as discussed in Appendix A. The Lab frame in this chapter refers to the one defined by Arenhövel. When we refer to the other lab frame given in the Appendix, we refer to the *fixed* Lab frame.

in the quasielastic limit of $^2\mathrm{H}(\vec{e},e'\vec{n})^1\mathrm{H}$ reaction, the angle θ_{np}^{cm} is 180° because $\vec{p}_n^{cm}$ becomes parallel to $\vec{q}^{cm}$ in this case. Because of the small angular acceptances of our detectors, we only had to sample events with θ_{np}^{cm} close to 180° in our simulation. In addition, the electron scattering plane and the n-p reaction plane nearly coincide in our detector setup. Therefore, the events we sample from the simulation program must have ϕ angles close to either 0° or 180°.

We will discuss next the calculation of various physics quantities used in this formalism.

6.2 The Differential Cross Section for $^2\mathrm{H}(\vec{e},e'\vec{N})N$ Reaction

The differential cross section for the five-fold $^2\mathrm{H}(\vec{e},e'\vec{N})N$ reaction assuming the longitudinal electron beam polarization, $\sigma(h)$, is obtained by ignoring the terms which involve the target polarization. It is given by [Are88, Lei91, Are95],

$$\begin{aligned}\sigma(h) &\equiv \frac{\mathrm{d}^5\sigma}{\mathrm{d}E_{e'}^{Lab}\mathrm{d}\Omega_{e'}^{Lab}\mathrm{d}\Omega_{np}^{cm}} \\ &= C[\rho_L f_L + \rho_T f_T + \rho_{LT} f_{LT}\cos\phi + \rho_{TT} f_{TT}\cos 2\phi + h\rho'_{LT} f'_{LT}\sin\phi]. \quad (6.2)\end{aligned}$$

where h is the degree of the electron polarization, and the dynamic properties of the nucleon-nucleon system in the electrodisintegration of the deuteron are represented by the structure functions f_L, f_T, f_{LT}, f_{TT}, and f'_{LT}, which are functions of three quantities in the Lab frame (E_e, E'_e, and θ_e) and one quantity in the CM frame, θ_{np}^{cm}.

The five ρ quantities in Equation 6.2 are the virtual photon density matrix elements, $\rho_{\mu'\mu}$: here, $(\mu\mu') = (00), (11), (01), and(-11)$ correspond to the subscripts L, T, LT, and LT, respectively. These matrix elements are given in terms of the

boost velocity β from the Lab to the n-p CM frame, the four-momentum transfer squared, q_μ^2, and other kinematic quantities, ξ and η (defined below),

$$\rho_L = \beta^2 q_\mu^2 \frac{\xi^2}{2\eta}, \qquad \rho_{LT} = \beta q_\mu^2 \frac{\xi}{\eta}\sqrt{\frac{\xi+\eta}{8}}, \tag{6.3}$$

$$\rho_T = \frac{1}{2} q_\mu^2 \left(1 + \frac{\xi}{2\eta}\right), \qquad \rho_{TT} = -q_\mu^2 \frac{\xi}{4\eta}, \tag{6.4}$$

$$\rho'_{LT} = \frac{1}{2}\beta q_\mu^2 \frac{\xi}{\sqrt{2\eta}}, \qquad and \qquad \rho'_T = \frac{1}{2} q_\mu^2 \sqrt{\frac{\xi+\eta}{\eta}}, \tag{6.5}$$

where

$$\beta = \frac{|\vec{q}|}{|\vec{q}^{cm}|}, \qquad \xi = \frac{q_\mu^2}{|\vec{q}|^2}, \tag{6.6}$$

$$\eta = \tan^2(\theta_e/2), \qquad and \qquad \vec{q}^{cm} = \frac{m_d}{W_{np}}\vec{q}. \tag{6.7}$$

The W_{np} in Equation 6.7 is the invariant mass of the np final state,

$$W_{np} = \sqrt{(E_{np})^2 - |\vec{q}|^2} = \sqrt{(\omega + m_d)^2 - |\vec{q}|^2}, \tag{6.8}$$

where E_{np} is the energy of the Lab np system, $E_{np} = \omega + M_d$. From these relationships, the boost parameter γ, which gives the transformation from the Lab to the n-p CM frame and vice versa, is given by

$$\gamma = \frac{E_{np}}{W_{np}} = \frac{\omega + m_d}{W_{np}}, \tag{6.9}$$

and the boost velocity β is given as

$$\beta = \frac{\sqrt{\gamma^2 - 1}}{\gamma} \tag{6.10}$$

Once the boost velocity β along $\vec{q}$ from the Lab to the n-p CM frame (or vice versa) is determined, the components of the vectors, $\vec{q}^{cm}$, $\vec{p}_n^{cm}$, $\vec{p}_p^{cm}$, and the angle θ_{np}^{cm} in the n-p CM frame can be calculated from the lab momentum vectors $\vec{q}$, $\vec{p_n}$, and $\vec{p_p}$.

Note that the proton momentum vector in the Lab frame is known when an event is sampled in *simulation*.

The factor C in Equation 6.2 is given by

$$C = \frac{\alpha}{6\pi^2}\frac{|\vec{k}|}{|\vec{k'}|q_\mu^4}, \tag{6.11}$$

where α is the fine structure constant.

The contribution from the term which contains the electron helicity to the cross section can be clearly seen, by rewriting the five-fold cross section (Equation 6.2) in the following form,

$$\sigma(h) \;=\; \sigma_0(1 + hA_e), \tag{6.12}$$

where σ_0 and A_e are the unpolarized cross section which does not depend on h, and the electron asymmetry, respectively,

$$\sigma_0 \;=\; C[\rho_L f_L + \rho_T f_T + \rho_{LT} f_{LT}\cos\phi + \rho_{TT} f_{TT}\cos 2\phi] \tag{6.13}$$

$$A_e \;=\; \frac{C}{\sigma_0}\rho'_{LT} f'_{LT}\sin\phi. \tag{6.14}$$

In Equation 6.2, Ω_{np}^{cm} is the only differential evaluated in the CM frame. The theoretical data of the structure functions was calculated by Arenhövel [Are02], and the cross section for every event is calculated from Equation 6.2. However, the Lab cross section (that is, $\mathrm{d}\theta_{np}^{lab}$ is in the denominator) is needed to weight the events sampled in the simulation. The Jacobian factor J which transforms from Ω_{np}^{cm} to Ω_n, is given in terms of the quantities in the Lab frame [Chu99]

$$J \;\equiv\; \frac{\mathrm{d}\Omega_{np}^{cm}}{\mathrm{d}\Omega_n} \tag{6.15}$$

$$\;=\; \frac{1 - (\beta/\beta_n^{lab})\cos\theta_n^{lab}}{\gamma^2[(\cos\theta_n^{lab} - \beta/\beta_n^{lab})^2 + (1/\gamma^2)\sin^2\theta_n^{lab}]}, \tag{6.16}$$

where θ_n^{lab} is the angle between the $\vec{q}$ and $\vec{p_n}$ in the Lab frame.

6.3 The recoil Polarization Observables

From the structure functions calculated by Arenhövel *et. al.*, one can calculate not only the differential cross section but also the recoil polarization components from the $^2\mathrm{H}(\vec{e},e'\vec{n})^1\mathrm{H}$ reaction in the n-p CM frame. The polarization components of the recoil neutron from the $^2\mathrm{H}(\vec{e},e'\vec{n})^1\mathrm{H}$ reaction, are given by [Are95],

$$\begin{aligned}\frac{\mathrm{d}^5\sigma}{\mathrm{d}E^{Lab}_{e'}\mathrm{d}\Omega^{Lab}_{e'}\mathrm{d}\Omega^{cm}_{np}}P^{x/z}_{cm} &= -C[\rho_{LT}f^{x/z}_{LT}\sin\phi+\rho_{TT}f^{x/z}_{TT}\sin 2\phi \\ &\quad +h(\rho'_{LT}f^{'x/z}_{LT}\cos\phi+\rho'_{T}f^{'x/z}_{T})] \qquad (6.17)\\ \frac{\mathrm{d}^5\sigma}{\mathrm{d}E^{Lab}_{e'}\mathrm{d}\Omega^{Lab}_{e'}\mathrm{d}\Omega^{cm}_{np}}P^{y}_{cm} &= C[\rho_{L}f^{y}_{L}+\rho_{T}f^{y}_{T}+\rho_{LT}f^{y}_{LT}\cos\phi \\ &\quad +\rho_{TT}f^{y}_{TT}\cos 2\phi+h\rho'_{LT}f^{'y}_{LT}\sin\phi, \qquad (6.18)\end{aligned}$$

where P^{cm}_x, P^{cm}_y, and P^{cm}_z are the x, y, and z components of the recoil polarization, respectively. These components are evaluated in the *reaction basis* in the n-p CM frame. In this basis, the z axis is along $\vec{p}^{\,cm}_n$, the y axis is along $\vec{q}\times\vec{p}^{\,cm}_n$, and the x axis is chosen so that the x, y, and z axis form a right-handed coordinate system. Thus, this reaction basis depends on each event with respect to the Lab frame. There are thirteen structure functions which appeared in Equations 6.17 and 6.18. They are $f^{x/z}_{LT}$, $f^{x/z}_{TT}$, $f^{'x/z}_{LT}$, $f^{'x/z}_{T}$, f^{y}_{L}, f^{y}_{T}, f^{y}_{LT}, f^{y}_{TT}, and $f^{'y}_{LT}$. As before, they are functions of E_e, E'_e, and θ_e and θ^{cm}_{np}.

It is once again convenient to separate the terms which depend on the electron polarization,

$$\frac{\mathrm{d}^5\sigma}{\mathrm{d}E^{Lab}_{e'}\mathrm{d}\Omega^{Lab}_{e'}\mathrm{d}\Omega^{cm}_{np}}\mathbf{P} = \sigma_0(\mathbf{P^0}+h\mathbf{P'}), \qquad (6.19)$$

where the components of $\mathbf{P^0}$ and $\mathbf{P'}$ are given by

$$\mathbf{P^0_{x/z}} = \frac{-C}{\sigma_0}[\rho_{LT} f^{x/z}_{LT} \sin\phi + \rho_{TT} f^{x/z}_{TT} \sin 2\phi], \tag{6.20}$$

$$\mathbf{P^0_y} = \frac{C}{\sigma_0}[\rho_L f^y_L + \rho_T f^y_T + \rho_{LT} f^y_{LT} \cos\phi + \rho_{TT} f^y_{TT} \cos 2\phi], \tag{6.21}$$

$$\mathbf{P'_{x/z}} = \frac{-C}{\sigma_0}[(\rho'_{LT} f^{'x/z}_{LT} \cos\phi + \rho'_T f^{'x/z}_T)], \tag{6.22}$$

$$\mathbf{P'_y} = \frac{C}{\sigma_0}[\rho'_{LT} f^{'y}_{LT} \sin\phi]. \tag{6.23}$$

The polarization components computed from these equations show that the value for the P'_x and P'_z are quite insensitive to nuclear physics effects such as FSI, MEC, and IC.

The polarization components in Equations 6.17 and 6.18 are evaluated in the reaction basis in the n-p CM frame. However, they need to be converted into a Lab frame so that the experimental results of the scattering asymmetries, which are proportional to the transverse component of the neutron polarization vector in the Lab scattering basis can be compared to the polarization components obtained from the simulation. Therefore, we need to convert the polarization components obtained in the n-p CM reaction basis into the fixed NPOL reference frame, as given in Appendix A. To do this, we first convert them into the Lab *reaction* basis by applying a matrix to the CM polarization vector,

$$P^{lab}_k = R^W_{kl} P^{cm}_l, \tag{6.24}$$

where P^{lab} is the polarization vector evaluated in the Lab reaction basis, and the matrix R^W is known as the Wigner rotation matrix,

$$R^W = \begin{pmatrix} \cos\theta^W & 0 & \sin\theta^W \\ 0 & 1 & 0 \\ -\sin\theta^W & 0 & \cos\theta^W \end{pmatrix} \tag{6.25}$$

and the Wigner angle, θ^W, is given by [Are02]

$$\theta^W = \sin^{-1}\left[\frac{1+\gamma}{\gamma_n^{cm}+\gamma_n}\sin(\pi-\theta_{np}^{cm}-\theta_n).\right] \tag{6.26}$$

Next, we convert the polarization components in the Lab reaction basis into the *fixed* Lab coordinate system as defined in Appendix A. To do this, we consider the unit vectors for the Lab reaction basis, $\hat{l}, \hat{m}, \hat{n}$ defined in Equation 6.1. We define the components of these unit vectors evaluated in the *fixed Lab coordinates* as (l_1, l_2, l_3), (m_1, m_2, m_3), and (n_1, n_2, n_3), respectively. Therefore, we have

$$\begin{aligned}
\hat{l} &= l_1\hat{x_L} + l_2\hat{y_L} + l_3\hat{z_L} \\
\hat{m} &= m_1\hat{x_L} + m_2\hat{y_L} + m_3\hat{z_L} \\
\hat{n} &= n_1\hat{x_L} + n_2\hat{y_L} + n_3\hat{z_L},
\end{aligned} \tag{6.27}$$

where $\hat{x_L}$, $\hat{y_L}$, and $\hat{z_L}$ are the unit vectors along the x, y, and z axes in the fixed Lab coordinates, respectively. Consider any vector $\vec{A}$ which can be expressed in the Lab reaction basis as $\vec{A} = A_l\hat{l} + A_m\hat{m} + A_n\hat{n}$. The components of this vector in the fixed Lab basis can be found by plugging Equation 6.27 into this equation,

$$A_{x_L} = A_l l_1 + A_m m_1 + A_n n_1 \tag{6.28}$$

$$A_{y_L} = A_l l_2 + A_m m_2 + A_n n_2 \tag{6.29}$$

$$A_{z_L} = A_l l_3 + A_m m_3 + A_n n_3 \tag{6.30}$$

Therefore, the components of the polarization in the fixed Lab coordinates are found from the above formula. Finally, the polarization vector in the fixed NPOL frame is obtained by rotating the fixed Lab coordinates by 46°about the y axis in the counter-clockwise direction when looking along the $-y$ axis.

6.4 Simulation Program

A Monte-Carlo program which simulates the physics of the particles (the electrons, neutrons and protons) from the $^2\mathrm{H}(\vec{e}, e'\vec{n})^1\mathrm{H}$ reaction over our detector acceptances was developed by Tajima from a similar Monte-Carlo simulation program made by Churchwell [Chu01a]. The five-fold cross section transformed in the fixed Lab coordinates was used to weight the simulated events from this reaction. A subroutine for rotating the polarization vector was used to simulate the precession of the polarization vector in the Charybdis magnet field. The polarization components of the recoil neutrons averaged over the acceptances of the NPOL detectors were used for obtaining the ratio of the polarization components. The polarization ratio from the simulated events is then compared to the experimental data.

6.4.1 Theoretical Data of the Cross Section and the Polarization

The theoretical data of the 18 structure functions from which the cross sections and the polarization components were obtained were calculated by Arenhövel [Are02]. When these calculations were created, the Bonn r-space NN potential [Mac87] was used in them to model the nucleon-nucleon interactions. Two sets of the structure functions were calculated, and they are labeled as "PWBA" and "FULL" in our analysis. The "PWBA" denotes the calculations made with the plain-wave Born approximation. The "FULL" denotes the calculations which included FSI, MEC and IC. Leading order relativistic contributions were included in both PWBA and FULL calculations. The parameterization for G_E^n (or $g = G_E^n/G_M^n$) used by Arenhövel has

the following form,

$$G_E^n = -GSF\frac{a\,\tau}{1+b\,\tau}\,G_M^n, \tag{6.31}$$

$$g = -GSF\frac{a\,\tau}{1+b\,\tau}, \tag{6.32}$$

where a and b are parameters. The GSF in Equation 6.31 is called the Galster scale factor, and 5 sets of the structure functions were calculated which correspond to 5 values of GSF, $GSF \equiv G_E^n/G_{En}^{\rm Galster} = 0.5, 0.75, 1.0, 1.25$, and 1.50. In the first-pass analysis, we used the theoretical data made with the input G_E^n values that follow the Galster parameterization ($a = 1.0$ and $b = 5.6$). This is based on an assumption that the world data for G_E^n including our corrected data points follow the Galster parameterization. Lookup tables for the 18 structure functions for each GSF value and each calculation type (PWBA or FULL) were created for many sets of E'_e, θ_e, and θ_{np}^{cm} at each Q^2 point as summarized in Table 6.1. The ranges of E'_e and θ_e were chosen to cover the distributions of those quantities in our experimental data.

	E (MeV)	$E_e^{\prime(cent)}$ (MeV)	E'_e (Range) (MeV)	$\theta_e^{(cent)}$ (deg)	θ_e (Range) (deg)	θ_{np}^{cm} (Range) (deg)
kin1	884	643	611-688	52.65	50.65-54.65	0-180
kin2a	2326	1718	1632-1838	30.93	28.93-32.93	0-180

Table 6.1: The kinematic range of the structure functions. $E^{\prime(cent)}$ and $\theta_e^{(cent)}$ are the central values. There are total 25, 11, and 49 data points in the E'_e, θ_e, and θ_{np}^{cm} range, respectively.

6.4.2 Event Sampling

We used a uniform sampling method to sample events in simulation. The value for a kinematic quantity was chosen randomly within the experimental acceptance

so that the distribution of the quantity becomes flat. First, the 3-D position of the interaction vertex was selected randomly inside the target Next, the electron scattering angles (horizontal and vertical angles) were similarly selected within the HMS acceptances. The momentum of the scattered electron was selected within the range of the momentum acceptance which is from -7 to +7% from the central kinematic value. Similarly, the angles of the recoil neutron (horizontal and vertical) were chosen within the acceptances of the NPOL collimator. Given those quantities above, it is now possible to calculate the magnitude of the neutron momentum and the three components of the proton momentum vector using the kinematic equations that were discussed in Chapter 5. However, this procedure does not give the interaction point along the momentum direction in the front detector array, and therefore it had to be chosen randomly. Because the dimensions of each front detector bar are identical, we choose the ID of the front detector randomly and the 3-D position inside a detector in DET coordinates. Because there is a small gap between front detectors, we checked if the events sampled were indeed in one of the front detector bars. After the detection position in DET coordinates are found, it can be converted into the fixed LAB or the fixed NPOL coordinates.

The physics quantities for the rear were similarly sampled or calculated. Because of the orientation of the rear detectors seen from the front array, it is difficult to specify the acceptances for the rear array from the front. Therefore, the rear detection ID where the interaction occurred was chosen first. We recall that two types of rear detector bars are used in our experiment: the outer two detectors on each rear layer are wider by a factor 2 than the inner two detectors. Therefore, the ID of the rear array was selected in such a way that the outer detectors have twice as many events as the inner detectors. After that, the hit position in DET coordinates was

chosen randomly. The position was then converted into the LAB or POL coordinates. Because the neutron momentum incident on the front array is already known and the scattering angle from the front to the rear can be calculated, other physics quantities for the rear can be obtained from the 2-body kinematics equation as discussed in Chapter 5. For a (n,n) [(n,p)] event, where a neutron [proton] is detected in the rear array, the magnitude of the neutron [proton] momentum and the proton [neutron] momentum components can be computed.

6.4.3 Interpolating the Structure Functions

For each event sampled, the values of the 18 structure functions are interpolated from the lookup tables according to the values of the θ_e and E'_e and θ^{cm}_{np}. A 3-dim interpolation subroutine was developed for this purpose from the 2-dim polynomial interpolation routine polin2.f, which is available in the Numerical Recipes in Fortran [Pre92]. Essentially the same algorithms were used to create the 3-dim polynomial interpolation routine used in our simulation program. From the interpolated values of the structure functions, the five-fold cross section and the recoil polarization observables (P'_x and P'_z) were obtained from Equations 6.2 and 6.17, respectively.

6.4.4 Simulating the Precession of the Neutron Polarization Vector

The strength of the field in Charybdis is set for a nominal precession of the neutron polarization vector through an angle χ. However, the neutrons exit the Charybdis magnet with a distribution of precession angles about an average value, which can be different from the nominal setting. The dispersion in χ is due primarily

to three effects: (1) the velocity dispersion of the neutrons, (2) the path length difference in the neutron trajectories through the magnet, and (3) the non-uniform field strength in the magnet. In the simulations, the magnetic field at any location inside the Charybdis must be known to calculate the precession angle of a neutron because the angle is proportional to the integral of the magnetic field over a path length. Before our simulation was performed, a program called TOSCA was used to solve the Maxwell's equations in three dimensions. The calculations were performed for given currents and dimensions of the Charybdis magnet. The magnetic field was thus obtained at many 3-D grid points inside the Charybdis.

A subroutine which simulates the precession of the neutron polarization vector was developed by Taylor [Tay02, Tay01] and was incorporated into our simulation program. For simulation at
Q^2=0.45 (GeV/c)^2[Q^2=1.14 (GeV/c)^2], the input currents of 170.5 (A) [540 (A)] were used during the experiment while the TOSCA calculation was performed at 200 (A) [500 (A)] to obtain the magnetic field at each grid point in the space inside the Charybdis. Therefore, the magnetic field from the TOSCA calculation was scaled by a factor 0.85 [1.06] when our simulation program was run. The precession angle of the neutron entering the NPOL was calculated from the path and speed of the neutron and the scaled magnetic field from the TOSCA calculation inside the Charybdis.

6.4.5 Weighting Events

Because we used the uniform sampling method, the following three weights must be applied to obtain the correct distribution of the physical quantities in simulation.

Five-fold cross section

The five-fold cross section for the reaction $e+d \rightarrow e'+n+p$ was calculated from Arenhövel's formalism in the np CM frame. The cross section transformed into the fixed LAB coordinates must be used to weight the events sampled in simulation.

Polarized np cross section

In our experiment, neutrons (protons) were scattered (recoiled) in the front array. Assuming np scattering in the front array, we weighted the simulated events by the polarized np cross section in the Lab frame, σ_{lab}. In this frame, the z axis is along the incident neutron momentum, P_n, and the y axis is perpendicular to the scattering plane, which is defined by $\vec{P}_n$ and the scattered momentum vector, $\vec{P}_{n'}$: the unit vector $\hat{y}$ is given by $\hat{y} = \vec{P}_n \times \vec{P}_{n'}/|\vec{P}_n \times \vec{P}_{n'}|$. The σ_{lab} is given by

$$\sigma_{lab} = \sigma^0_{lab}(\theta)(1 + h\,\vec{P}' \cdot \hat{y}\,A^{lab}_y(\theta)), \tag{6.33}$$

where $\sigma^0_{lab}(\theta)$ is the unpolarized lab cross section, θ is the scattering angle, $\vec{P}'$ is the polarization vector of the neutron, h is the beam polarization, $A^{lab}_y(\theta)$ is the analyzing power. Before the simulation was performed, the lookup tables for the unpolarized np cross section in the CM frame σ^0_{cm} and the analyzing power (A^{lab}_y) for the np scattering were generated by the SAID program [SAI]. The program generated them for several values of the incident neutron momentum in the Lab frame (P_n) and many values of the scattering angle of the neutron in the CM frame (θ_{cm}). (Note that this CM frame is *not* Arenhövel's np CM frame where the Lab frame is boosted along the momentum transfer, $\vec{q}$.) The range of P_n values were chosen so that the entire experimental distribution of P_n was covered. The range of θ_{cm} was from 0° to 180°. For simulating (n,n) events, the following things were performed to obtain

the $(\vec{n}, n)$ cross section. For each simulated event, the values of σ^0_{cm} and A^{lab}_y are interpolated from the values of P_n and θ_{cm} for that event. A 2-D interpolation routine polin2.f [Pre92] was used to interpolate them. Those interpolated values are used to calculate the polarized np cross section in the CM frame. The cross section must be transformed into the Lab frame. To do this, the Jacobian factor which transforms from the CM solid angle Ω^{cm}_n to the Lab solid angle Ω_n must be calculated. The formula (Equation 6.16) can be in fact written in terms of the CM angle [Chu99].

$$J \equiv \frac{\mathrm{d}\Omega^{cm}_n}{\mathrm{d}\Omega_n} \tag{6.34}$$

$$= \left[\frac{1 + (\beta/\beta^{cm}_n)\cos\theta^{cm}_n}{\gamma^2[(\cos\theta^{cm}_n + \beta/\beta^{cm}_n)^2 + (1/\gamma^2)\sin^2\theta^{cm}_n]}\right]^{-1}, \tag{6.35}$$

where β is the velocity of the boost in units of c, γ is the same as Equation 6.10, and β^{cm}_n is the velocity of the neutron in units of c in the CM frame. This Jacobian factor must be multiplied to the σ^0_{cm} to obtain σ^0_{lab}. Finally, the polarized np cross section is obtained from Equation 6.33.

For simulating ^{1}H(n,p) events where recoil protons are detected, we did the following things. First, the angle of the recoil proton with respect to the incident neutron is found in the CM frame. The corresponding neutron angle in the CM frame is given by the supplement of the proton angle. Using this neutron angle, the values of the A^{lab}_y and σ^{cm}_0 are interpolated from the lookup tables as before. The Jacobian factor is similarly calculated and σ^{lab}_0 is also obtained.

Flight distance between the front and the rear

Finally, because the position in the rear detector was not chosen from the angle acceptances, events had to be weighted by the inverse-square of the flight distance

between the front and rear detection positions.

6.5 Results of Physics Quantities in the Simulation Program

Figure 6.2 shows the results of several kinematic quantities from the simulation program (shown in dashed lines). The results were compared to those from the experimental data (shown in solid lines). The simulation program basically reproduces the results from the experiment.

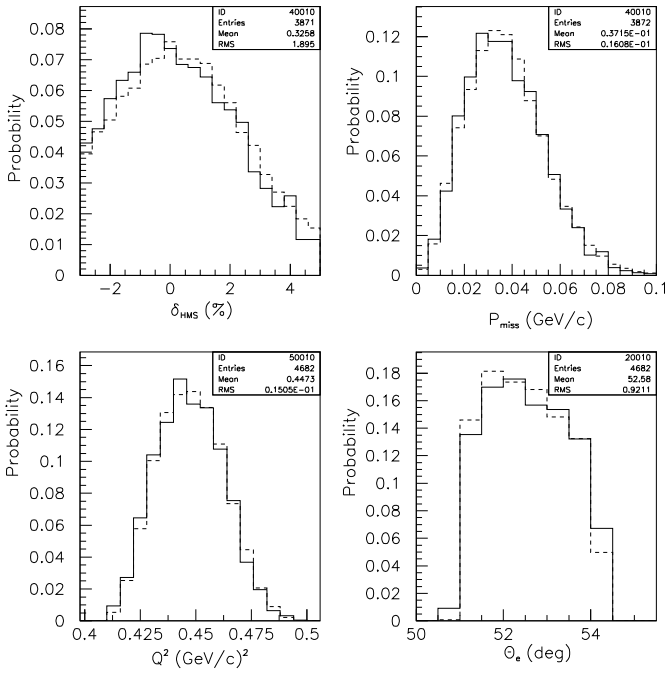

Figure 6.2: Comparison of histograms between experiment and simulation. The solid line is the experimental data and the dashed line is from the simulation. The plots were made at Q^2=0.45 (GeV/c)^2.

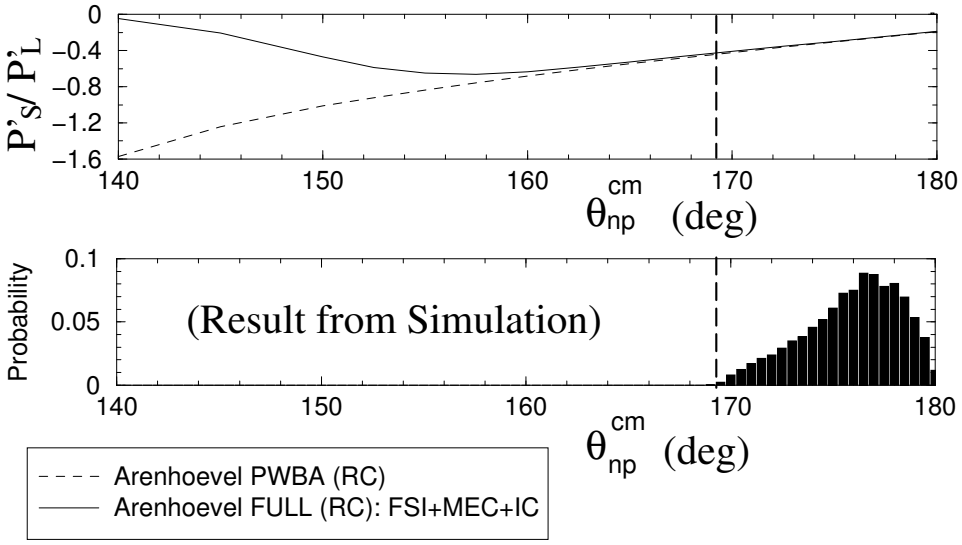

Figure 6.3: Ratio of P'_S/P'_L from Arenhövel's calculation and distribution of θ_{np}^{cm} from the simulation. The top plot shows how P'_S/P'_L changes with θ_{np}^{cm}. The dashed line is for the PWIA calculation while the solid line includes nuclear physics corrections. The bottom plot shows the simulated distribution of θ_{np}^{cm}. Both plots were made at Q^2=1.14 $(GeV/c)^2$.

The top plot in Figure 6.3 shows the ratio of P'_S/P'_L. The sideways (P'_S) and longitudinal (P'_L) polarization components were calculated by Arenhövel. The quasielastic limit corresponds to $\theta_{np}^{cm} = 180°$. This plot shows that the ratio P'_S/P'_L is *insensitive* to the nuclear effects such as MEC, FSI, and IC in the quasielastic region where θ_{np}^{cm} is close to 180°. The bottom plot shows the distribution of θ_{np}^{cm} obtained from our simulation program. Because our detectors were not *point* detectors, θ_{np}^{cm} has some finite distribution, but it lies in the quasielastic region as shown in the figure. The bottom plot also indicates that the value for P'_S/P'_L will be weighted by this θ_{np}^{cm} distribution when the acceptance-average is performed.

6.6 Acceptance Averaging

6.6.1 Analysis Procedure in Simulation

For the simulation at Q^2=0.45 (GeV/c)^2, the program was run with the positive electron beam helicity to sample 40,000 events. As discussed earlier, the precession of the neutron polarization vector simulated using the TOSCA field map corresponded to the actual magnetic field in the Charybdis. First, the polarization vector was precessed through the angle *close to* $+40^\circ$ using this field map. Note that not all neutrons have the same precession angle. Nonetheless, for convenience we refer to this run as a $+40^\circ$ *precession run*. For each event, the relevant physics quantities, including the kinematic quantities, the cross sections, and polarization components after precession of the neutron polarization vector, were saved in a PAW ntuple file for the run. After the run was finished, a histogram for P_x^+ was made after the cut parameters, which will be discussed shortly, and the weight factors discussed above were applied. The mean of P_x^+ distribution, $\bar{P}_x^+$, was found from the histogram. This procedure was repeated for a run with -40° precession, by changing the sign of the Charybdis current. The value for $\bar{P}_x^-$ was similarly determined. The simulated result for the ratio of the sideways to longitudinal polarization components, P'_S/P'_L was obtained from the ratio $\bar{P}_x^-/\bar{P}_x^+$. Because the precession through either $+40^\circ$ or -40° is performed for each neutron, it is not possible to make a plot of the ratio P_x^-/P_+^x for each simulation event. Therefore, the individual histograms must be made and the mean values of P_x^+ and P_x^- need to be determined to find the ratio. This is the identical situation for the experiment.

A quite similar procedure was employed for simulation at Q^2=1.14 (GeV/c)^2. We ran the simulation program with nominal polarization vector precession of $+90^\circ$and

-90°. In addition, we ran it with *zero* Charybdis current, which corresponds to the data with no precession of the neutron polarization vector. The mean values of the transverse component of the polarization with 0° and $+90^{\circ}$ precession are determined, and the ratio is computed. The result from the -90° precession simply changed the sign of the polarization component in the simulation.

6.6.2 Event Selection Criteria in Simulation

We did not include all observables in the simulations that were in the experimental data. Therefore, it was not possible for us to select events under the same condition. However, we applied the same cut parameters whenever the same physics quantities were available in our simulation. The following cut parameters have been applied to select 'good' simulated events. Note that the weight factors discussed earlier also need to be applied.

Variable	Min	Max
δ_{HMS} (%)	-3.0	5.0
p_{miss} (GeV/c)	0.0	0.1
z_{targ} (cm)	-7.0	7.0
W_{inv} (GeV/c^2)	0.0	1.0
$CTOF$ (ns)	-1.0	1.0
$RTOF$ (ns)	-1.5	5.0

Table 6.2: Cut Parameters applied to select 'good' simulation events. The z_{targ} is the z position of the interaction vertex in the LAB coordinates at the target. The definitions for the other variables are the same as in Chapter 5.

6.6.3 Precession of the Neutron Polarization

Figure 6.4 shows the transverse components of the polarization after precession by $\pm 40°$. The quantities P_x^+ and P_x^- are the transverse components of the polarization vector after $+40°$ and $-40°$, respectively. The ratio of the two polarizations, η, is determined from the mean values of P_x^+ and P_x^- for each value of GSF. In this precession method (Method-2), the ratio of the sideways to the longitudinal polarization component is given by Equation 4.30. In Method-1, the mean values of the transverse components P_x^0 and P_x^{90} for the precession angle 0°and 90°, respectively, are obtained from the simulation. In this method, the ratio of P_x^0/P_x^{90} becomes P'_S/P'_L [see Equation 4.21].

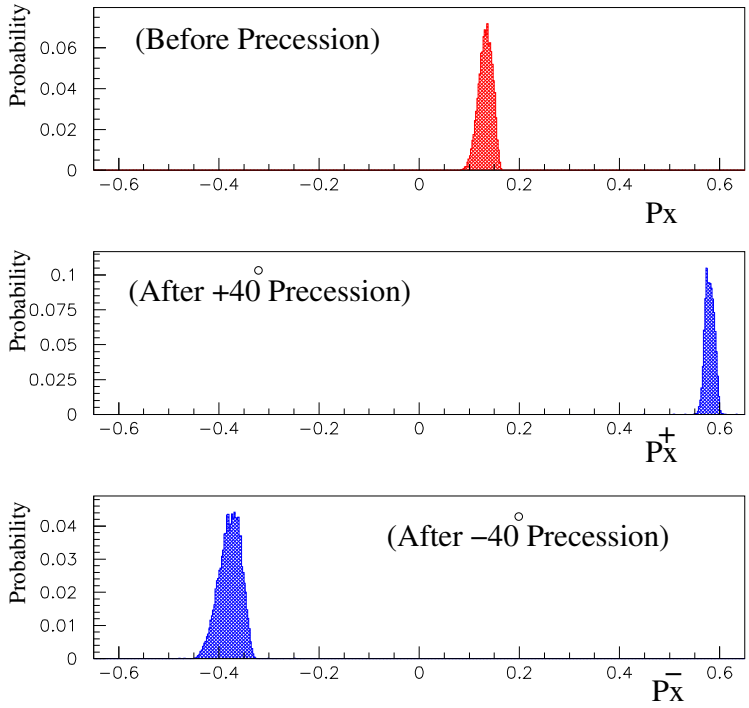

Figure 6.4: Simulated polarization vector precession by $\pm 40°$. The transverse component of the neutron polarization before and after the precession is shown. The plots were made for data at Q^2=0.45 $(GeV/c)^2$.

6.6.4 Acceptance-Averaged Q^2 Values

The acceptance-averaged Q^2 values, $\langle Q^2 \rangle$, were obtained in our simulation program. The value for $\langle Q^2 \rangle$ was determined from a mean of the Q^2 distribution after the cut parameters given in Table 6.2 were applied. For kin1, we found $\langle Q^2 \rangle = 0.45$ $(\mathrm{GeV/c})^2$, which is the same as the nominal Q^2 value. For kin2, $\langle Q^2 \rangle = 1.13$ $(\mathrm{GeV/c})^2$, which is slightly smaller than the nominal Q^2 value. In the subsequent chapters, these $\langle Q^2 \rangle$ values are used whenever our results are discussed.

Chapter 7

Systematic Uncertainties in G_E^n/G_M^n

In this chapter, we discuss systematic uncertainties from several sources that contribute to the error in the measurement of $g = G_E^n/G_M^n$. Because g depends on both χ and θ_e, the uncertainties in χ and θ_e both contribute to the uncertainty in g. In addition, the uncertainty in the measurement of the beam polarization contributes to the systematic uncertainty in g, although g doesn't depend on the beam polarization directly. We will also discuss the systematic uncertainties which arise due to the proton and neutron interactions in the lead sheets at the entrance to the polarimeter. The two main processes are the Pb$(\vec{p},\vec{n})$ charge-exchange reaction and the depolarization of the neutron in the lead. Other sources of systematic uncertainty are uncertainties in radiative corrections and time calibrations. As already discussed in Section 4.6, the uncertainty in A_y is negligible in our experiment, and therefore it is not included in the total systematic uncertainty in g.

The total systematic uncertainty $(\Delta g)_{syst}$ and the total relative uncertainty $(\Delta g/g)_{syst}$ can be written as follows,

$$(\Delta g)^2_{syst} = \sum_{i=1}^{N}[(\Delta g)_i]^2 \tag{7.1}$$

$$\left(\frac{\Delta g}{g}\right)^2_{syst} = \sum_{i=1}^{N}\left[\left(\frac{\Delta g}{g}\right)_i\right]^2, \tag{7.2}$$

where N is the total number of sources for the systematic uncertainty. The systematic uncertainty for each source (denoted by the subscript i) is added in quadrature to obtain the total systematic uncertainty assuming that all the sources are uncorrelated. We will discuss each of the uncertainties mentioned above in the following sections.

7.1 Uncertainty in the Precession Angle of the Neutron Polarization Vector

Because the polarization vector of the neutron was precessed in both Method-1 and Method-2, the uncertainty in the precession angle, $\Delta\chi$ contributes to the systematic uncertainty in g. To see the explicit dependence of g on χ for Method-1, one can obtain the formula for g with the precession angles 0°and $\pm\chi$.

$$g = -K_R\left(\frac{\eta\sin\chi}{1-\eta\cos\chi}\right) \qquad (\text{Method}\,1:0^\circ,\pm\chi). \tag{7.3}$$

For $\chi = 90°$, Equation 7.3 reduces to Equation 4.22. From Equation 7.3, the uncertainty and relative uncertainty in g due to the uncertainty in χ, are given by

$$(\Delta g)^2_\chi \equiv \left(\frac{\partial g}{\partial \chi}\right)^2 (\Delta\chi)^2, \tag{7.4}$$

$$\left(\frac{\Delta g}{g}\right)^2_\chi \equiv \frac{1}{g^2}\left(\frac{\partial g}{\partial \chi}\right)^2 (\Delta\chi)^2 \tag{7.5}$$

$$= \left(\frac{\cos\chi - \eta}{1 - \eta\cos\chi}\right)^2 \left(\frac{\Delta\chi}{\sin\chi}\right)^2 \qquad (\text{Method } 1 : 0°, \pm\chi). \tag{7.6}$$

Note that if χ is exactly 90°, we have $|dg/g|_\chi = |\eta\Delta\chi|$.

For Method-2, the relative uncertainty is similarly calculated from Equations 4.31 and 7.5,

$$\left(\frac{\Delta g}{g}\right)^2_\chi = \left(\frac{2}{\sin 2\chi}\right)^2 (\Delta\chi)^2 \qquad (\text{Method } 2 : \pm\chi). \tag{7.7}$$

7.1.1 Precession of the Neutron Polarization Vector in the Magnetic Field

To assess the uncertainty in χ, we consider the precession of the neutron polarization vector in the magnetic field of Charybdis. Assume the neutron with the velocity β_n travels through the magnetic field with magnitude B and direction perpendicular to the neutron momentum. The precession angle χ is given as [Hag63],

$$\chi = \int g\,\mu_{_N}\,B\,dt = \frac{ge}{2M_pc}\,\frac{\int Bdl}{\beta_n}, \tag{7.8}$$

where g is the gyromagnetic ratio with $g/2 = -1.913$ for the neutron. The $\mu_{_N} = e/(2M_p)$ is the nuclear magneton, and M_p is the proton mass. The integral $\int Bdl$ is performed over the path length of the particle in the region of the magnetic field using the map from TOSCA. Equation 7.8 shows that χ is proportional to $(1/\beta_n)$.

$\langle Q^2 \rangle$ (GeV/c)^2	Nominal χ(deg)	χ (deg)	$(\Delta g/g)_\chi$ (%)
0.45	± 40	40.17 ± 0.30	1.1
1.13	$0^\circ, \pm 90$	89.99 ± 0.22	0.27

Table 7.1: The uncertainty in χ and $\Delta g/g$ at $\langle Q^2 \rangle$ =0.45 and 1.13 (GeV/c)^2.

To determine the uncertainty in χ, a simulation program is used to sample events, and a histogram of χ vs $(1/\beta_n)$ was plotted. The distribution was fitted with a linear function, and the uncertainty in the precession angle χ was determined from the uncertainty in the fitting parameters. Table 7.1 shows the uncertainty in χ at $\langle Q^2 \rangle$ =0.45 and 1.13 (GeV/c)^2 and the resulting uncertainties in the measurement of g. The uncertainties are small at both $\langle Q^2 \rangle$ points.

7.2 Uncertainty in Electron Scattering Angle

The uncertainty in the measurement of the electron scattering angle θ_e also contributes to the systematic uncertainty in g. For convenience, let us give the expressions for g again (Equations 4.22 and 4.31).

$$g = -K_R\,\eta \qquad (\text{Method 1}: \chi = 0^\circ, \pm 90^\circ), \tag{7.9}$$

$$g = -K_R \left(\frac{1+\eta}{1-\eta}\right) \tan\chi \qquad (\text{Method 2}: \chi = \pm 40^\circ), \tag{7.10}$$

where η is the asymmetry ratio. The factor K_R and other related kinematic variables are also given below for convenience. The description of each variable is given

in Section 1.5.

$$K_R = \sqrt{\frac{\tau\left(1+\tau\sin^2\left(\frac{\theta_e}{2}\right)\right)}{\cos\left(\frac{\theta_e}{2}\right)}}, \tag{7.11}$$

$$\tau = \frac{Q^2}{4\,M_N^2}, \tag{7.12}$$

$$Q^2 = 4\,E_e\,E_e^{'}\,\sin^2(\theta_e/2), \tag{7.13}$$

$$E_e^{'} = \frac{E_e}{1+2(\frac{E_e}{M_N})\sin^2(\theta_e/2)}. \tag{7.14}$$

The uncertainty and relative uncertainty in g due to the uncertainty in θ_e are given by

$$(\Delta g)^2_{\theta_e} \equiv \left(\frac{\partial g}{\partial \theta_e}\right)^2 (\Delta\theta_e)^2, \tag{7.15}$$

$$\left(\frac{\Delta g}{g}\right)^2_{\theta_e} \equiv \frac{1}{g^2}\left(\frac{\partial g}{\partial \theta_e}\right)^2 (\Delta\theta_e)^2. \tag{7.16}$$

When the derivative $\frac{\partial g}{\partial \theta_e}$ is calculated, we consider that only K_R depends on θ_e in Equations 7.9 and 7.10. However, we note that χ and θ_e are kinematically related: if θ_e deviates from the quasi-elastic value, the electron, neutron and proton momenta will also change. That results in a change in the precession angle of the neutron polarization vector, χ, because χ depends on β_n (Equation 7.8). However, knowing the electron angle only is not enough to solve the three-body kinematic equations to determine both the neutron and proton momenta. Because of this, no correlation seems to exist between θ_e and θ_n. Therefore, we assume that χ does not depend on θ_e.

Under the assumption mentioned above, the relative uncertainty in g due to the uncertainty in θ_e becomes

$$\left(\frac{\Delta g}{g}\right)^2_{\theta_e} = \frac{1}{K_R^2}\left(\frac{\partial K_R}{\partial \theta_e}\right)^2 (\Delta\theta_e)^2. \tag{7.17}$$

Note that Equation 7.17 is valid for both Method-1 and Method-2. The derivative in Equation 7.17 can be evaluated using Equations 7.11 through 7.14. The systematic uncertainty in g in Equation 7.17 can be calculated once the value of θ_e is obtained. We note that there exist two different uncertainties in θ_e, which we refer to positioning and traceback uncertainties. The positioning uncertainty, $(\Delta\theta_e)_{\rm pos}$, is the offset in electron scattering angle from the nominal value and the traceback uncertainty, $(\Delta\theta_e)_{\rm tra}$, is the uncertainty in the reconstruction of the electron scattering angle from the focal plane to the target.

We calculate the systematic uncertainties due to $(\Delta\theta_e)_{\rm pos}$ and $(\Delta\theta_e)_{\rm tra}$ separately. Equation 7.17 with $\Delta\theta_e = \Delta\theta_{e,\rm pos}$ was used to obtain the systematic uncertainty, $(\Delta g/g)_{\theta_e,\rm pos}$, due to the positioning uncertainty. We used the value of $(\Delta\theta_e)_{\rm pos} = 1.2$ (mrad), which was reported by Christy [Chr00].

Similarly, Equation 7.17 with $\Delta\theta_e = \Delta\theta_{e,\rm tra}$ was used to obtain the systematic uncertainty, $(\Delta g/g)_{\theta_e,\rm tra}$, due to the traceback uncertainty. We used the value of $(\Delta\theta_e)_{\rm tra} = 1.3$ (mrad), which was obtained from the analysis of the HMS matrix elements [Jon01].

The uncertainties $(\Delta g/g)_{\theta_e,\rm pos}$ and $(\Delta g/g)_{\theta_e,\rm tra}$ are then added in quadrature to obtain the total systematic uncertainty in g, $(\Delta g/g)_{\theta_e,\rm tot}$ due to $\Delta\theta_e$. Note that $(\Delta g/g)_{\theta_e,\rm tot}$ gives the upper bound of the uncertainty because $\Delta\theta_{e,\rm pos}$ and $\Delta\theta_{e,\rm tra}$ are not independent from each other.

Table 7.2 gives the results of the systematic uncertainty in g at $\langle Q^2\rangle$ =0.45 and 1.13 (GeV/c)^2. The values of $(\Delta g/g)_{\theta_e,\rm tot}$ are small at both $\langle Q^2\rangle$ values.

$\langle Q^2 \rangle$ $(GeV/c)^2$	χ (deg)	$(\Delta\theta_e)_{pos}$ (mrad)	$(\Delta g/g)_{\theta_e,pos}$ (%)	$(\Delta\theta_e)_{tra}$ (mrad)	$(\Delta g/g)_{\theta_e,tra}$ (%)	$(\Delta g/g)_{\theta_e,tot}$ (%)
0.45	± 40	1.2	0.12	1.3	0.13	0.18
1.13	0, ± 90	1.2	0.19	1.3	0.20	0.27

Table 7.2: The systematic uncertainty in g due to uncertainty in θ_e. The 3rd and 4th (5th and 6th) columns contain the positioning (traceback) uncertainty. The last column contains the total systematic uncertainty in g due to the uncertainty in θ_e. See text for detail.

7.3 Uncertainty in Beam Polarization

Although the ratio g does not depend explicitly on the beam polarization P_e as has been discussed in Sections 4.4 and 4.5, the P_e had to be measured every few days during the data taking because the value of the beam polarization changed slightly with time. When the data were analyzed to extract asymmetries, the beam polarizations were normalized to 80%. However, the uncertainty in the measurements of the polarization contributes to the systematic uncertainty in g, and will be discussed next.

7.3.1 Method-1 (precessions by $0^\circ$and $\pm 90^\circ$)

Let the beam polarizations during the measurements of ξ_S and ξ_L be $P_e^S \pm \Delta P_e^S$ and $P_e^L \pm \Delta P_e^L$, respectively. Although the values for P_e^L and P_e^S became the same after they were normalized, we consider below the general situation that they can be different. Because asymmetry is proportional to beam polarization, the measured asymmetry ratio $\eta\,(\equiv \xi_S/\xi_L)$ for the case $P_e^L \neq P_e^S$ becomes (P_e^S/P_e^L) times the true asymmetry ratio which is obtained with $P_e^L = P_e^S$. Therefore, to extract g, the η in

Equation 4.22 needs to be scaled by a factor P_e^L/P_e^S.

$$\eta \longrightarrow \eta \left(\frac{P_e^L}{P_e^S}\right). \tag{7.18}$$

Then, Equation 4.22 becomes

$$g \;=\; -K_R\,\eta \left(\frac{P_e^L}{P_e^S}\right). \tag{7.19}$$

The systematic uncertainty in g due to the uncertainties in the polarization can be calculated from Equation 7.19,

$$\left(\frac{\Delta g}{g}\right)^2_{P_e} \;=\; \left(\frac{\Delta P_e^S}{P_e^S}\right)^2 + \left(\frac{\Delta P_e^L}{P_e^L}\right)^2. \tag{7.20}$$

For $P_e^S = P_e^L \equiv P_e$ and $\Delta P_e^S = \Delta P_e^L \equiv \Delta P_e$, Equation 7.20 becomes

$$\left(\frac{\Delta g}{g}\right)^2_{P_e} \;=\; 2\left(\frac{\Delta P_e}{P_e}\right)^2 \tag{7.21}$$

7.3.2 Method-2 (precessions by angles $\pm\chi$)

Similarly, let the beam polarizations during the measurements of ξ_+ and ξ_- be $P_e^+ \pm \Delta P_e^+$ and $P_e^- \pm \Delta P_e^-$, respectively. Using the same argument as in Method-1, the asymmetry ratio $\eta\,(\equiv \xi_-/\xi_+)$ in Equation 4.31 needs to be scaled as

$$\eta \longrightarrow \eta \left(\frac{P_e^+}{P_e^-}\right) \tag{7.22}$$

to extract g. Therefore, Equation 4.31 becomes

$$g \;=\; -K_R \left(\frac{1+\eta\,\frac{P_e^+}{P_e^-}}{1-\eta\,\frac{P_e^+}{P_e^-}}\right)\tan\chi. \tag{7.23}$$

The systematic uncertainty in g due to the uncertainties in the polarization is easily obtained from Equation D.4 in Appendix.

$$\left(\frac{\Delta g}{g}\right)^2_{P_e} \;=\; \left[\frac{2\eta P_e^- P_e^+}{(P_e^-)^2-(\eta P_e^+)^2}\right]^2 \left[\left(\frac{\Delta P_e^+}{P_e^+}\right)^2 + \left(\frac{\Delta P_e^-}{P_e^-}\right)^2\right] \tag{7.24}$$

Once again, for $P_e^- = P_e^+ \equiv P_e$ and $\Delta P_e^- = \Delta P_e^+ \equiv \Delta P_e$, Equation 7.24 reduces to

$$\left(\frac{\Delta g}{g}\right)^2_{P_e} = \frac{4\eta^2}{(1-\eta^2)^2}\left[2\left(\frac{\Delta P_e}{P_e}\right)^2\right]. \tag{7.25}$$

7.3.3 Systematic uncertainty in g due to the uncertainty in polarization

To obtain the uncertainty in the beam polarization that contributes to the systematic uncertainty in g, the value for each polarization was scaled to a mean polarization of 80%. In addition, the uncertainty in each polarization was scaled by a factor which is the ratio of the mean polarization of 80% to the measured polarization. Then, the statistical error was calculated for the entire set of measurements.

The relative uncertainty in the beam polarization $\Delta P_e/P_e$ was estimated to be

$$\frac{\Delta P_e}{P_e} = \frac{\delta\overline{P_e}}{\overline{P_e}}\sqrt{(\chi_{fit})^2}, \tag{7.26}$$

where $\overline{P_e}$ is the mean polarization, $\overline{\delta P_e}$ is the statistical uncertainty in $\overline{P_e}$, and the value of $(\chi_{fit})^2$ is obtained from the fit of each polarization measurement to the mean value. We assumed for Method-1 that $\overline{P_e^S} = \overline{P_e^L} \equiv \overline{P_e}$, $\overline{\delta P_e^S} = \overline{\delta P_e^L} \equiv \overline{\delta P_e}$, and $(\chi^S_{fit})^2 = (\chi^L_{fit})^2 \equiv (\chi_{fit})^2$, where the superscript, S (L), indicates the variable is for the measurement of sideways (longitudinal) asymmetry. Similarly, we assumed for Method-2 that $\overline{P_e^+} = \overline{P_e^-} \equiv \overline{P_e}$, $\overline{\delta P_e^+} = \overline{\delta P_e^-} \equiv \overline{\delta P_e}$, and $(\chi^+_{fit})^2 = (\chi^-_{fit})^2 \equiv (\chi_{fit})^2$, where the superscript: $+$ ($-$) indicates the variable is for the data with the precession angle of $+\chi$ ($-\chi$). Table 7.3 lists the results of this analysis. The last column in this table gives the relative systematic uncertainty in g at each $\langle \mathrm{Q}^2 \rangle$ due to the uncertainty in the beam polarization.

$\langle Q^2 \rangle$ (GeV/c)^2	χ (deg)	$\delta\overline{P_e}/\overline{P_e}$ (%)	$(\chi_{fit})^2$	$\Delta\overline{P_e}/\overline{P_e}$ (%)	$(\Delta g/g)_{P_e}$ (%)
0.45	$\pm$40	0.13	13.1	0.47	1.4
1.13	0, $\pm$90	0.13	5.5	0.30	0.42

Table 7.3: The systematic uncertainty in g due to the uncertainty in P_e. See text for detail.

7.4 Uncertainty in Timing Calibration

The data at each $\langle Q^2 \rangle$ were analyzed somewhat independently by two students. Both students who analyzed the same $\langle Q^2 \rangle$ data used the same cuts and the same run selection. However, each person obtained his own time-calibration parameters for the NPOL, and that was the main difference between the two analyses. We found that the results for g between the two analyses agree quite well, and the difference in $\Delta g/g$ between those independent results are at the level of about 2%. Therefore, we claim that the uncertainty in timing calibration that contributes to the $\Delta g/g$ is $\pm$2% at every $\langle Q^2 \rangle$ point.

7.5 Systematic Uncertainty from the False Asymmetry due to the Two-Step Process: $^2\mathrm{H}(\vec{e}, e'\vec{p}) + \mathrm{Pb}(\vec{p}, \vec{n})$

Because the mass of the neutron and the proton are almost identical, the protons from the quasielastic $^2\mathrm{H}(\vec{e}, e'\vec{p})$ reaction could cause coincidence between the HMS and the NPOL front array, and this could cause a three-fold coincidence event as well. Such a *proton* event in the NPOL was easily identified because of the veto detectors

as we discussed in Chapter 5, and therefore was rejected from our data analysis. However, there is a different issue that we need to consider. The protons from the quasielastic $^2\mathrm{H}(\vec{e}, e'\vec{p})$ reaction could cause the charge-exchange reaction, $\mathrm{Pb}(\vec{p}, \vec{n})$, in the lead shielding at the entrance collimator to the polarimeter. If the two-step process $^2\mathrm{H}(\vec{e}, e'\vec{p}) + \mathrm{Pb}(\vec{p}, \vec{n})$ occurs, the *neutrons* from this reaction can be detected in the NPOL. Because those neutrons are not from $^2\mathrm{H}(\vec{e}, e'\vec{n})^1\mathrm{H}$ reaction, these events must be removed from the data analysis or a correction must be made. Inclusion of these events could cause a dilution of the measured scattering asymmetry. However, it is difficult to tell on the event-by-event basis whether or not a neutron detected in the NPOL is from the two-step process. To estimate the contamination level due to this reaction, data were taken on a liquid hydrogen ($\mathrm{LH_2}$) target at each $\langle \mathrm{Q}^2 \rangle$ point during the experiment. The event rates from the $\mathrm{LH_2}$ data were compared with those from the $\mathrm{LD_2}$ data.

We write the measured asymmetry, ξ_m, in terms of the asymmetries from the real and background process, ξ_R and ξ_B, respectively. ξ_B represents the scattering asymmetry of the proton from this process.

$$\xi_m = f_R \xi_R + f_B \xi_B, \tag{7.27}$$

where f_R is the fraction from the $(e, e'n)$ reaction, and f_B from the two-step process $[^2\mathrm{H}(\vec{e}, e'\vec{p}) + \mathrm{Pb}(\vec{p}, \vec{n})]$. We have $f_R + f_B = 1$. We consider the case where all the lead sheets existed downstream of the Charybdis. In $^2\mathrm{H}(\vec{e}, e'\vec{p})$ reaction, the electron polarization was transfered to the proton. The polarization of the proton was then precessed in the Charybdis magnet before the proton reached the lead shielding. When the proton interacts with the lead to cause a charge-exchange reaction, the proton polarization can be transfered to the neutron as well. Considering all of this,

ξ_B can be written as

$$\xi_B = P_e(D^p_{LS}\cos\chi_p + D^p_{LL}\sin\chi_p)D^{Pb}_{SS'}A_y, \tag{7.28}$$

where P_e denotes the electron beam polarization, D^p_{LS} and D^p_{LL} are the proton polarization transfer coefficients for the $^2\mathrm{H}(\vec{e},e'\vec{p})$ reaction, χ_p is the precession angle for the proton, $D^{Pb}_{SS'}$ is the polarization transfer coefficient for the $\mathrm{Pb}(\vec{p},\vec{n})$ reaction, and A_y is the analyzing power of the polarimeter. From Equations 7.27 and 7.28, we have

$$\xi_R = \frac{\xi_m - f_B P_e(D^p_{LS}\cos\chi_p + D^p_{LL}\sin\chi_p)D^{Pb}_{SS'}A_y}{1-f_B}. \tag{7.29}$$

To estimate the contamination level from the two-step process, the LH_2 data were analyzed with the casym program (version 2.6) [Sem03], and the event rates from the LD_2 data were compared with those from the LH_2 data. The f_B is written as

$$f_B = C_\rho \frac{R_{LH2}}{R_{LD2}}, \tag{7.30}$$

where R_{LH2} and R_{LD2} are the event rates for the LD_2 and LH_2 targets, respectively. The correction factor C_ρ accounts for the difference in the LD_2 and LH_2 densities, and is given by

$$C_\rho = \frac{\rho_{LD2}/A_{LD2}}{\rho_{LH2}/A_{LH2}}, \tag{7.31}$$

where ρ_{LD2} [ρ_{LH2}] is the LD_2 [LH_2] density, and A_{LD2} [A_{LH2}] is the atomic number. We obtained $C_\rho = 1.1946$. From the calculations of f_B, the false-asymmetry contamination level is estimated to be less than 0.3% at $\langle Q^2\rangle$ =0.45 and 1.13 $(\mathrm{GeV/c})^2$.

The coefficients D^p_{LS} and D^p_{LL} can be written in the plain-wave approximation,

$$D^p_{LS} = -\frac{2\sqrt{\tau(1+\tau)}G^p_E G^p_M \tan(\theta_e/2)}{(G^p_E)^2 + (G^p_M)^2[1+2(1+\tau)\tan^2(\theta_e/2)]} \quad (7.32)$$

$$D^p_{LL} = \frac{2\tau\sqrt{(1+\tau)[1+\tau\sin^2(\theta_e/2)]}(G^p_M)^2 \sec(\theta_e/2)\tan(\theta_e/2)}{(G^p_E)^2 + (G^p_M)^2[1+2(1+\tau)\tan^2(\theta_e/2)]}, \quad (7.33)$$

where G^p_E and G^p_M are proton form factors, and $\tau = Q^2/4m_p^2$. To evaluate D^p_{LS} and D^p_{LL}, the parameterizations for G^p_E and G^p_M by Brash *et al.* [Bra02] were used.

Now let us estimate the amount of the proton precession angle. the proton and neutron precession angles χ_p and χ_n, respectively, are given by [Hag63],

$$\chi_p = \frac{(g_p - 2)\mu_N}{v_p} \int Bdl \quad (7.34)$$

$$\chi_n = \frac{g_n \mu_N}{v_n} \int Bdl, \quad (7.35)$$

where $g_p/2 = 2.79$, $g_n/2 = -1.91$, and μ_n is the nuclear magneton. v_p and v_n are the velocities of the proton and neutron, respectively. Let us compare χ_p from the two-step process to χ_n from the ^{2}H$(\vec{e}, e'\vec{n})^1$H reaction. In this case, we have $v_p \sim v_n$ if the charge-exchange reaction occurs at $\sim 0^\circ$ scattering angle. If we assume $v_p = v_n$, and the proton and neutron follow the identical path inside the magnetic field which is uniform in time, the ratio of the precession angles is given by

$$\frac{\chi_p}{\chi_n} = \frac{g_p - 2}{g_n} = -0.937. \quad (7.36)$$

Therefore, we estimate that the proton precession angle from the two step process is $\chi_p = \mp 37.5^\circ$ and $\chi_p = \mp 84.3^\circ$ for the magnetic field for $\chi_n = \pm 40^\circ$ and $\chi_n = \pm 90^\circ$ precessions, respectively. The analyzing power A_y for the NPOL was also extracted from the measured neutron scattering asymmetries [Pla03b]. Unfortunately, no data for $D^{Pb}_{SS'}$ is available for the kinetic energy of the proton at $T_p \sim 240$ (MeV) for $\langle Q^2 \rangle = 0.45$ (GeV/c)^2, and $T_p \sim 610$ (MeV) for $\langle Q^2 \rangle = 1.13$ (GeV/c)^2.

We employed the following procedure to estimate the systematic uncertainty due to the charge-exchange reaction. The corrected asymmetry ξ_R in Equation 7.29 was calculated for three values of $D_{SS'}^{Pb}$ ($D_{SS'}^{Pb} = -1, 0, +1$) at each $\langle Q^2 \rangle$ point. Using these values for ξ_R, the values for g were calculated. We calculated the estimation of the relative systematic uncertainty in g due to the charge-exchange reaction from the following expression,

$$\frac{\Delta g}{g} \sim \frac{1}{2} \left| \frac{g(D_{SS'}^{Pb} = 0) - g(D_{SS'}^{Pb} = -1)}{g(D_{SS'}^{Pb} = 0)} . \right| \tag{7.37}$$

The values for $\Delta g/g$ in Equation 7.37 are estimated to be less than 0.01% at $\langle Q^2 \rangle$ = 0.45 (GeV/c)^2, and 0.06% at $\langle Q^2 \rangle$ = 1.13 (GeV/c)^2.

In the above discussion, we treated the case where all the lead shielding was located downstream of the Charybdis, which was the case for the data taken at $\langle Q^2 \rangle$ = 0.45 (GeV/c)^2. However, for the data taken at Q^2=1.14 (GeV/c)^2 which was performed in year 2000, more than half of the lead sheets were placed *upstream* of the Charybdis as mentioned in Section 3.7. Because the uncertainty due to this two-step process that we found above is negligible, we believe that a similar result would be obtained for $\langle Q^2 \rangle$ = 1.13 (GeV/c)^2 if we estimated the uncertainty by taking into account the correct positions of the lead sheets.

7.6 Depolarization in the Lead

The polarized neutrons interacting with the lead cause depolarization. However it is difficult to tell from our real data if a neutron detected in the NPOL suffered from the depolarization in the lead. Therefore, this effect was studied in a simulation program called GENGEN [Kel03b], and the systematic uncertainty in g from this process was estimated.

Let us briefly summarize the procedure for estimating the depolarization in the lead. The details about this study and the algorithm are discussed in [Pla02, Pla03a]. Define three momentum of the neutron before it incidents on the lead as $\vec{P_1}$ in the fixed NPOL frame, and the three momentum of the target nucleon in the lead in the fixed NPOL frame as $\vec{P_2}$. The components of $\vec{P_1}$ and the neutron polarization vector $\vec{S_1}$ are already sampled by the event generator. The magnitude $|\vec{P_2}|$ is sampled according to a Fermi gas distribution, $|\vec{P_2}| = (rk_F^3/3)^{1/2}$. Here, r is a uniform random deviate, and k_F is the Fermi momentum with $k_F = 0.25$ (GeV/c). The direction of $\vec{P_2}$ is chosen randomly on a unit sphere. To evaluate the scattering of the neutron, the four momenta of the incident neutron and target nucleon as well as that of the neutron spin vector were transformed from the NPOL frame to the target nucleon's rest frame, which we refer to S_R frame. The direction of the boost is along $\vec{P_2}$. Because $\vec{P_1}$ is not parallel to $\vec{P_2}$ in general, the transformation of the spin involves a Wigner rotation discussed in Section 6.3. The direction of the scattering of the neutron in the target nucleon's rest frame is then chosen by sampling the polar and azimuthal angles. These angles are then evaluated in the CM frame of the incident nucleon and the target nucleon, which we refer to S_{CM} frame. Because the boost from S_R to S_{CM} is parallel to the incident neutron's momentum, the polarization vector is unchanged in both frames. The depolarization of the spin vector can be computed in the S_{CM} frame by evaluating the depolarization tensor and the cross section. Once the spin components after they are depolarized are found, those components are evaluated in the NPOL frame by applying the Lorentz transformation and the Wigner rotation. The estimated values for the systematic uncertainty that contributes to the measurement of g is small. It is < 0.1 % at $\langle \mathrm{Q}^2 \rangle = 0.45$ (GeV/c)^2, and is 0.2 % at $\langle \mathrm{Q}^2 \rangle = 1.13$ (GeV/c)^2.

7.7 Radiative Correction

Electrons interact with the electric field through the Coulomb interaction, and the electrons lose energy by emitting photons. This phenomenon is known as Bremsstrahlung radiation. Because radiative effects can cause depolarization of the electrons, recoil polarization components in our experiment became slightly smaller. To compensate this effect, the polarization components must be increased to some amount. However, this effect nearly cancels in the measured *ratio* of the polarization components. Therefore, this effect is expected to be small in the measured values for g.

Afanasev *et al.* calculated the model-independent radiative effect on *electron-proton* elastic scattering [Afa01]. They studied the ratio of the recoil polarization components of the proton. The exact calculations of the lowest-order model-independent correction were performed. The processes that they studied include the QED processes of radiation of an unobserved real photon, vacuum polarization, and lepton-photon vertex corrections. These processes give the largest contributions to the radiative corrections. The effects due to the radiative corrections on the ratio of the polarization components of the recoil neutron was calculated by Afanasev [Afa02] employing the same method. According to his results, both polarization transfer coefficients must be increased by ∼1.9% at $\langle Q^2 \rangle = 0.45$ (GeV/c)^2, and ∼3.7% at $\langle Q^2 \rangle = 1.13$ (GeV/c)^2. These effects nearly cancel in the polarization ratio. The relative systematic uncertainty in the measurement of g from the radiative correction is small (0.7%) at $\langle Q^2 \rangle = 0.45$ (GeV/c)^2, and is negligible (0.1%) at $\langle Q^2 \rangle = 1.13$ (GeV/c)^2.

7.8 Total Systematic Uncertainty in G_E^n/G_M^n

We have obtained the systematic uncertainty in $g = G_E^n/G_M^n$ due to the uncertainties in beam polarization, charge-exchange reaction in the lead, depolarization in the lead, electron scattering angle, precession angle, radiative corrections, and time calibrations. The total systematic uncertainty can be obtained from Equation 7.2 assuming all of these given above are uncorrelated. Table 7.4 summarizes the results for dg/g for each contribution to the systematic uncertainty. Total systematic uncertainty in g, $(\Delta g/g)_{syst}$ is obtained by adding each contribution in quadrature. $(\Delta g/g)_{syst}$ is small at each $\langle Q^2 \rangle$ point.

	$\langle Q^2 \rangle$ $[(GeV/c)^2]$	
Source	0.45	1.13
Beam polarization	1.4	0.4
Charge exchange in the lead	< 0.01	0.06
Depolarization in the lead	< 0.1	0.2
Electron scattering angle	0.1	0.3
Precession angle	1.1	0.1
Radiative corrections	0.7	0.1
Time calibration	2.0	2.0
Total of above sources	2.8	2.1

Table 7.4: The systematic uncertainty in $\Delta g/g$ [%] at $\langle Q^2 \rangle$ =0.45 and 1.13 (GeV/c)^2. The precession angles for the data at $\langle Q^2 \rangle$ = 0.45 (GeV/c)^2 [$\langle Q^2 \rangle$ = 1.13 (GeV/c)^2] are $\pm 40^\circ$ [0°,$\pm 90^\circ$].

Chapter 8

Results and Discussions

We discussed in Chapter 6 how the data are simulated in our Monte-Carlo program. Using the structure functions for the electrodisintegration of the deuteron calculated by Arenhövel *et. al.* [Are88, Lei91, Are95], the five-fold cross section and the polarization components of the neutron are computed. The theoretical predictions of the polarization components are averaged over the finite acceptance of our experimental setup. The polarization vector of the neutron was precessed in the simulation using the map of the magnetic field from TOSCA, and the transverse component of the polarization is obtained in the simulation for each field setting. The ratio of the polarization components is obtained for each GSF value, which is the input G_E^n value in Arenhövel's calculations in units of the Galster parameterization.

8.1 First-Pass Analysis

After the ratio of the average value of the polarization components for each of the 5 GSF values is obtained, the ratio is plotted against the GSF value. The plot is fitted with a linear function, and the slope and the intercept for the straight line are obtained. The measured value for P'_S/P'_L from the experiment is projected to this linear function to extract the corrected value for $g = G_E^n/G_M^n$ in units of the Galster parameterization (see Figure 8.1). The procedure is repeated to determine the uncertainty for the corrected g. The corrected value for g and its uncertainty are

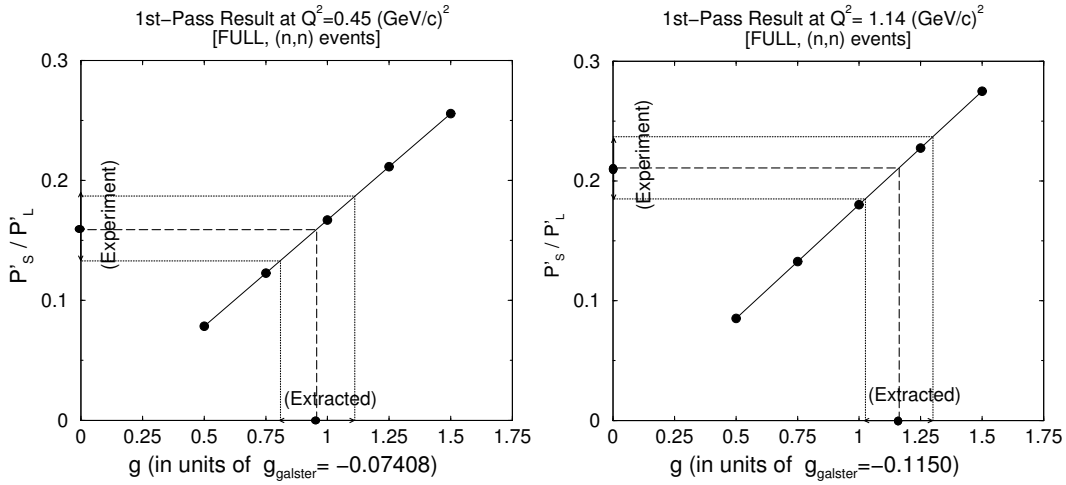

Figure 8.1: First-pass results for $\langle Q^2 \rangle = 0.45$ (GeV/c)^2 [left] and $\langle Q^2 \rangle = 1.13$ (GeV/c)^2 [right]. The plots shown were made for the (n,n) events with the FULL calculations. Each data point was obtained for one of the GSF values. The ratio of the polarization components as a result of the acceptance averaging and the nuclear corrections is plotted. The value and the uncertainties for P'_x/P'_z from the experiment data analysis are shown on the ordinate, and the corrected value for g and its uncertainty are extracted on the abscissa, as shown in the figure. Similar plots were made for the other three cases.

obtained for the following four cases at each $\langle Q^2 \rangle$ point,

1. PWBA calculation and (n,n) event type

2. PWBA calculation and (n,p) event type

3. FULL calculation and (n,n) event type

4. FULL calculation and (n,p) event type

Figure 8.1 shows the results of the first-pass analysis for (n,n) events with the FULL calculation at $\langle Q^2 \rangle$ =0.45 and 1.13 (GeV/c)^2. The measured ratio of P'_S/P'_L and its uncertainty are shown on the ordinate, and they are projected to the linear fit function. The extracted value for g and its uncertainty are shown on the abscissa. Tables 8.1 and 8.2 give the results of the first-pass analysis at $\langle Q^2 \rangle$ =0.45 and 1.13 (GeV/c)^2, respectively. The results for the PWIA calculations (2nd row) were computed from Equation 4.31 for $\langle Q^2 \rangle$ = 0.45 (GeV/c)^2, and Equation 4.22 for $\langle Q^2 \rangle$ = 1.13 (GeV/c)^2. These results from the experiment already reflect the effect of the acceptance averaging due to the finite acceptances of our detectors. The 3rd and 4th rows in the table were obtained from the simulation program using the measured values for P'_S/P'_L as inputs. The results for the PWBA calculations reflect the effect of the deuteron wave function and Fermi motion inside deuteron, and this effect leads to the increase in g by 3 to 4%. The results for the FULL calculations reflect the nuclear effects that include the FSI, MEC, and IC, in addition to the effects included in the PWBA calculations. These effects lead to the increase in g by 6 to 10%. Table 8.3 gives the values for g resulting from the weighted-average of the g values for the (n,n) and (n,p) event types. These g values are used to compute the values for G_E^n. As discussed in Section 1.4.6, we used the values for G_M^n from the fit to the world data to compute G_E^n from $g = G_E^n/G_M^n$. The values for $G_M^n/\mu_n G_D$ at the *acceptance-averaged* Q^2 values of $\langle Q^2 \rangle$ = 0.45 and 1.13 (GeV/c)^2 are 1.003 ± 0.006 and 1.057 ± 0.017, respectively [Kel02, Kel03a]. The values for G_E^n from the first-pass

	(n,n)	(n,p)
PWIA	-0.0640 ± 0.0108	-0.0873 ± 0.0114
PWBA	-0.0667 ± 0.0111 (4.2%)	-0.0903 ± 0.0119 (3.4%)
FULL	-0.0708 ± 0.0115 (10.6%)	-0.0950 ± 0.0123 (8.8%)

Table 8.1: Results for $g = G_E^n/G_M^n$ from the first-pass analyses at $\langle Q^2 \rangle = 0.45$ (GeV/c)^2. The second row gives the result for g from the experiment data analysis. The third and fourth rows give the extracted values for g for Arenhövel's PWBA and FULL calculations, respectively. The number in the parentheses indicates how much the corrected value increased from the experimental value (PWIA results).

	(n,n)	(n,p)
PWIA	-0.1257 ± 0.0156	-0.1164 ± 0.0236
PWBA	-0.1288 ± 0.0154 (2.5%)	-0.1213 ± 0.0238 (4.2%)
FULL	-0.1337 ± 0.0158 (6.4%)	-0.1260 ± 0.0242 (8.2%)

Table 8.2: Results for $g = G_E^n/G_M^n$ from the first-pass analyses at $\langle Q^2 \rangle = 1.13$ (GeV/c)^2. See the figure caption for Table 8.1.

analysis are extracted from the values of $g = G_E^n/G_M^n$ for the FULL calculations. We found $G_E^n = 0.0589 \pm 0.0060$ at $\langle Q^2 \rangle = 0.45$ (GeV/c)^2, and $G_E^n = 0.0395 \pm 0.0040$ at $\langle Q^2 \rangle = 1.13$ (GeV/c)^2.

We obtained a new set of fit parameters for G_E^n using the form of the equation given by Equation 6.31 with $GSF = 1.0$. The data used in the new fit included the G_E^n obtained in the E93-038 experiment at the acceptance-averaged Q^2 values of $\langle Q^2 \rangle = 0.45, 1.13$, and 1.45(GeV/c)^2 [Mad03] and the world data of G_E^n from the polarization experiments [Ede94, Her99, Pas99, Gol01, Ber03, Zhu01], the G_E^n data extracted by Schiavilla and Sick [Sch01], and the measured value of the slope of G_E^n at the origin [Kop97]. A *modified* Galster parameterization was obtained with the parameters $a = 0.894 \pm 0.023$ and $b = 3.55 \pm 0.37$ [Kel03a]

	$\langle Q^2 \rangle = 0.45$ (GeV/c)^2		$\langle Q^2 \rangle = 1.13$ (GeV/c)^2	
Experiment	-0.0750 ± 0.0078		-0.1229 ± 0.0130	
PWBA	-0.0777 ± 0.0081	(3.6%)	-0.1266 ± 0.0129	(3.0%)
FULL	-0.0821 ± 0.0084	(9.5%)	-0.1314 ± 0.0132	(6.9%)

Table 8.3: Results for $g = G_E^n/G_M^n$ (weighted-average) from the first-pass analysis. The results for g for (n,n) and (n,p) event types given in Tables 8.1 and 8.2 are averaged using statistical weighting. The number in the parentheses indicates how much the value increased from the experimental value.

8.2 Second-Pass Analysis

As we just discussed, the values for G_E^n from the first-pass analysis were obtained. The theoretical data for the first-pass analysis were made with the input G_E^n values that follow the Galster parameterization ($a = 1.0$ and $b = 5.6$). Because the new fit function deviates from the Galster parameterization, a second-pass analysis was made using new sets of theoretical data made with the input G_E^n values that follow the *modified Galster parameterization* ($a = 0.894$ and $b = 3.55$). The same procedure was repeated in the second-pass analysis, and the values for $g = G_E^n/G_M^n$, and G_E^n were similarly obtained.

Figure 8.2 shows how the values for $g = G_E^n/G_M^n$ were extracted. Tables 8.4 and 8.5 give the values of g at $\langle Q^2 \rangle$ =0.45 and 1.13 (GeV/c)^2, respectively, for each event type [(n,n) or (n,p)] and type of calculation [PWBA or FULL]. Table 8.6 gives the weighted-averaged results for g at $\langle Q^2 \rangle$ =0.45 and 1.13 (GeV/c)^2. The extracted values for G_E^n from the second-pass analysis are extracted from the values of $g = G_E^n/G_M^n$ from the FULL calculations. We found $G_E^n = 0.0589 \pm 0.0060$ at $\langle Q^2 \rangle$ = 0.45 (GeV/c)^2, and $G_E^n = 0.0395 \pm 0.0040$ at $\langle Q^2 \rangle$ = 1.13 (GeV/c)^2. Note that the results from the second-pass analysis are virtually the same as those from the first-pass analysis. Table 8.6 suggests that the measured value for g in the PWIA

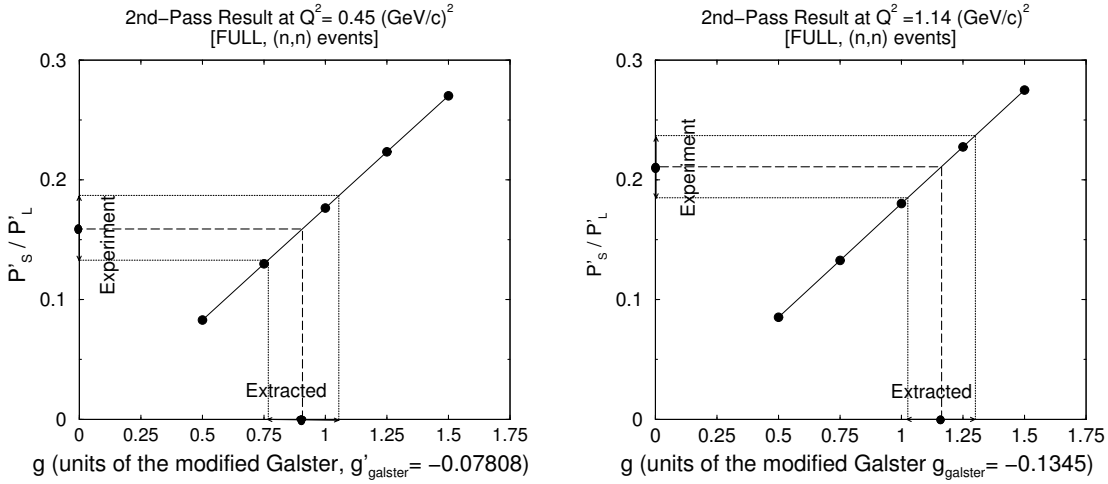

Figure 8.2: Second-pass results for $\langle Q^2 \rangle = 0.45$ (GeV/c)^2 [left] and $\langle Q^2 \rangle = 1.13$ (GeV/c)^2 [right]. The plots shown were made for the (n,n) events with the FULL calculations. As in Figure 8.1, the corrected value for g and its uncertainty are extracted on the abscissa from the experimental results. Note that the g is in units of the *modified* Galster value which is given by Equation 6.32 with $GSF = 1$, $a = 0.894$, and $b = 3.55$.

calculation (that assumes a *free* neutron in LD_2) differs by about 10% [7%] at $\langle Q^2 \rangle$ = 0.45 (GeV/c)^2 [$\langle Q^2 \rangle$ = 1.13 (GeV/c)^2] from the g in the FULL calculation.

	(n,n)	(n,p)
PWIA	-0.0640 ± 0.0108	-0.0873 ± 0.0114
PWBA	-0.0667 ± 0.0111 (4.2%)	-0.0902 ± 0.0119 (3.3%)
FULL	-0.0708 ± 0.0114 (10.6%)	-0.0950 ± 0.0122 (8.8%)

Table 8.4: Results for $g = G_E^n/G_M^n$ from the second-pass analyses at $\langle Q^2 \rangle = 0.45$ (GeV/c)^2. See the figure caption for Table 8.1.

8.3 Final Results for $g = G_E^n/G_M^n$ and G_E^n

We measured the values for $g = G_E^n/G_M^n$ at the acceptance-averaged Q^2 values of $\langle Q^2 \rangle = 0.45$, 1.13 and 1.45 (GeV/c)^2. In this thesis, we report the results for the lower

	(n,n)	(n,p)
PWIA	-0.1257 ± 0.0156	-0.1164 ± 0.0236
PWBA	-0.1289 ± 0.0156 (2.5%)	-0.1214 ± 0.0238 (4.3%)
FULL	-0.1337 ± 0.0157 (6.4%)	-0.1261 ± 0.0242 (8.3%)

Table 8.5: Results for $g = G_E^n/G_M^n$ from the second-pass analyses at $\langle Q^2 \rangle = 1.13$ (GeV/c)^2. See the figure caption for Table 8.1.

	$\langle Q^2 \rangle = 0.45$ (GeV/c)^2		$\langle Q^2 \rangle = 1.13$ (GeV/c)^2	
PWIA	-0.0750 ± 0.0078		-0.1229 ± 0.0130	
PWBA	-0.0776 ± 0.0081	(3.5%)	-0.1266 ± 0.0130	(3.0%)
FULL	-0.0821 ± 0.0083	(9.5%)	-0.1314 ± 0.0131	(6.9%)

Table 8.6: Results for $g = G_E^n/G_M^n$ (weighted-average) from the second-pass analysis. The results for g for (n,n) and (n,p) event types given in Tables 8.1 and 8.2 are averaged using statistical weighting. The number in the parentheses indicates how much the value increased from the experimental value.

two Q^2 measurements; in the previous section, we obtained the values for $g = G_E^n/G_M^n$ and the statistical uncertainties at $\langle Q^2 \rangle = 0.45$ and 1.13 (GeV/c)^2 using the FULL calculations by Arenhövel. The total systematic uncertainties in our measurements of g were about one-fourth of the statistical uncertainty. found in the previous chapter. The final values of g are $g = -0.0821 \pm 0.0084 \pm 0.0023$ at $\langle Q^2 \rangle = 0.45$ (GeV/c)^2, and $g = -0.1314 \pm 0.0132 \pm 0.0028$ at $\langle Q^2 \rangle = 1.13$ (GeV/c)^2. The first and second uncertainties are statistical and systematic uncertainties, respectively. The values for G_E^n were computed from our measurements of G_E^n/G_M^n using the G_M^n values of $G_M^n/(\mu_n G_D) = 1.003 \pm 0.006$ for $\langle Q^2 \rangle = 0.45$ (GeV/c)^2 and $G_M^n/(\mu_n G_D) = 1.057 \pm 0.017$ for $\langle Q^2 \rangle = 1.13$ (GeV/c)^2. We found $G_E^n = 0.0589 \pm 0.0060 \pm 0.0016$ at $\langle Q^2 \rangle = 0.45$ (GeV/c)^2, and $G_E^n = 0.0395 \pm 0.0040 \pm 0.0008$ at $\langle Q^2 \rangle = 1.13$ (GeV/c)^2. The first and second uncertainties are statistical and systematic uncertainties, respectively. Note that the uncertainty in our data is dominated by the statistical uncertainty.

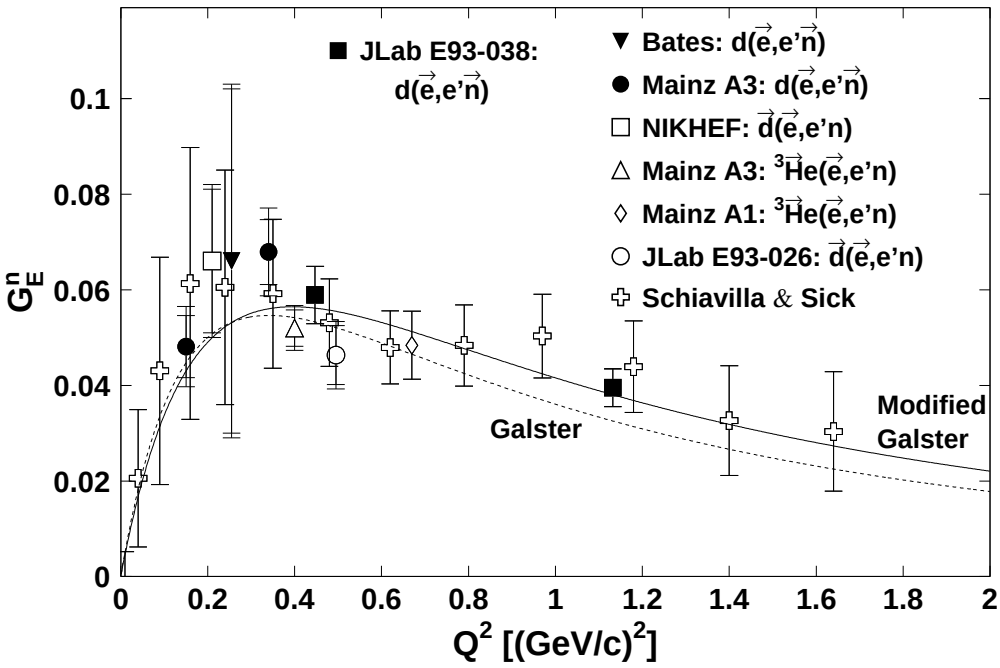

Figure 8.3: Our data in comparison with the world data and two empirical fits to the G_E^n data. The data points shown here are from the published results [Ede94, Her99, Pas99, Gol01, Ber03, Zhu01, Sch01] as well as our results for G_E^n at $\langle Q^2 \rangle$ =0.45 and 1.13 (GeV/c)^2 given at the beginning of this section. The solid line is the Galster parameterization, and the dashed line is the modified Galster parameterization that we obtained from those published results given above and the results from [Mad03]. The inner and outer error bars denote the statistical and total (statistical and systematic) uncertainties, respectively.

The implication here is that the uncertainty in these type of measurements can be reduced by simply counting longer or by increasing the efficiency and/or acceptance of the NPOL and HMS. Figure 8.3 shows the world data of G_E^n including the results from our measurements discussed in this thesis. The dashed line gives the standard Galster parameterization with $a = 1.0$ and $b = 5.6$, and the solid line gives the modified Galster parameterization with $a = 0.894$ and $b = 3.55$, which was discussed earlier. Our measurements are consistent with the world data.

As mentioned earlier, part of data were analyzed for this dissertation. The remaining set of data were analyzed by other individuals in our collaboration. Table 8.7 gives our published results for g and G_E^n from [Mad03]. Figure 8.4 shows the world

$\langle Q^2 \rangle$ [(GeV/c)^2]	$g = G_E^n/G_M^n$	$G_M^n/\mu_n G_D$	G_E^n
0.447	$-0.0761 \pm 0.0083 \pm 0.0021$	1.003 ± 0.006	$0.0550 \pm 0.0060 \pm 0.0016$
1.132	$-0.131 \pm 0.010 \pm 0.003$	1.057 ± 0.017	$0.0394 \pm 0.0029 \pm 0.0012$
1.450	$-0.190 \pm 0.016 \pm 0.004$	1.044 ± 0.024	$0.0411 \pm 0.0035 \pm 0.0013$

Table 8.7: Published results of g and G_E^n for E93-038.

data of G_E^n including our published results by Madey *et al.* [Mad03], and results for G_E^n at $Q^2 = 0.5$ and $1.0(GeV/c)^2$ by Warren *et al.* [War04], which are to be published. Our measurements of G_E^n at the two higher Q^2 values of 1.13 and 1.45 (GeV/c)^2 are more precise than prior measurements at lower Q^2. The G_E^n data at high Q^2($> 1.0(GeV/c)^2$) by Madey *et al.*, Warren *et al.*, and Schiavilla and Sick are consistent with each other, and all those data points in this Q^2 region are located slightly higher than the Galster parameterization.

8.4 Comparison of Data with Theoretical Model Calculations

Comparison of data for G_E^p/G_M^p and G_E^n/G_M^n *without our data points* were already discussed in Section 2.1.6. Our results of G_E^n/G_M^n at high Q^2 points allow us to eliminate some of the model calculations which are not consistent with our results. In Figure 8.5, polarization measurements of G_E^p/G_M^p (top panel) and G_E^n/G_M^n (bottom panel) are compared with predictions of selected models. The data points and

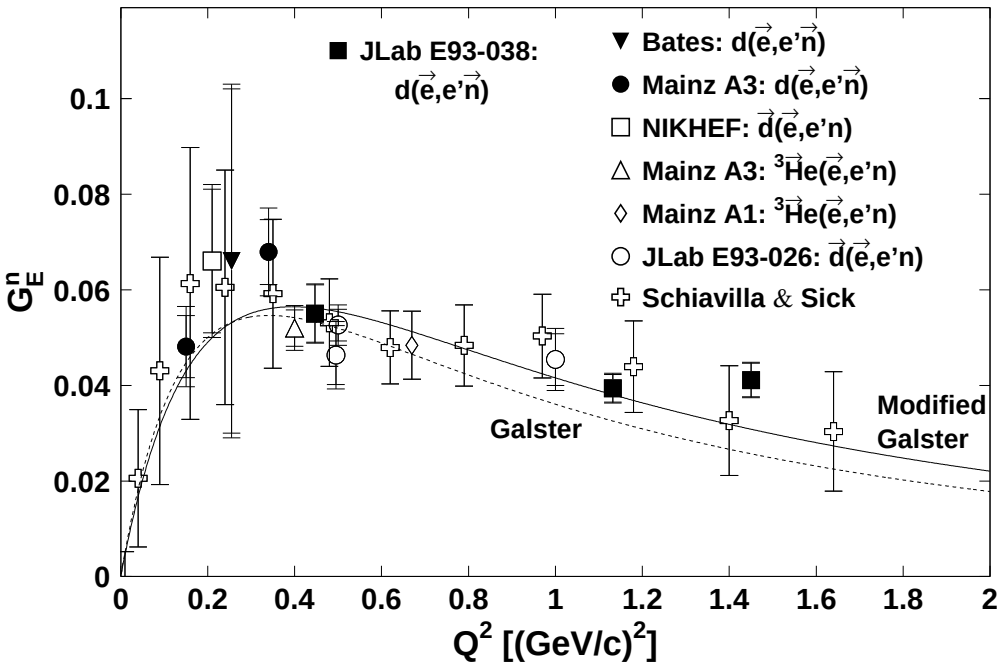

Figure 8.4: World data of G_E^n including the published results from the E93-038 experiment. In addition to the *published* data points shown in Figure 8.3, our published results by Madey *et al.* [Mad03], and results by Warren *et al.* [War04] are plotted. The solid and dashed lines are the same as those shown in Figure 8.3.

model calculations shown in this figure include those already appeared in Figure 2.3, our published results of G_E^n/G_M^n by Madey *et al.* [Mad03], and results of G_E^n/G_M^n by Warren *et al.* [War04], which are to be published. The chiral soliton model by Holzwarth, which reproduces the linear decrease of G_E^p/G_M^p quite well, fails to reproduce the data for G_E^n/G_M^n at large Q^2. The GBE CQM by Wagenbrunn *et al.* and Boffi *et al.*, which qualitatively agrees with the low Q^2 proton data, is not consistent with the neutron data at large Q^2. The model of VMD+pQCD by Lomon, which also achieves good agreement with the proton data, is consistent with the neutron data up to $Q^2 \sim 1.1(GeV/c)^2$, but it lies below the neutron data at larger Q^2. The

LFCBM by Miller achieves qualitative agreement with the neutron data. However, this model predicts smaller values for G_E^p/G_M^p at high Q^2. The OGE CQM also achieves qualitative agreement with the neutron data, but this model predicts larger G_E^p/G_M^p at high Q^2, Therefore, none of the models predict the behavior of both G_E^p/G_M^p and G_E^n/G_M^n.

8.5 Summary of the E93-038 Measurements

The Jefferson Laboratory E93-038 collaboration measured the ratio of the electric to the magnetic form factor of the neutron, $g = G_E^n/G_M^n$, from the $^2\mathrm{H}(\vec{e}, e'\vec{n})^1\mathrm{H}$ reaction via recoil polarimetry. In this thesis, we report the first measurements of G_E^n using polarization techniques at Q^2 greater than 1 $(\mathrm{GeV/c})^2$. The measurements were performed at three $\langle Q^2 \rangle$ values (0.45, 1.13, and 1.45 $(\mathrm{GeV/c})^2$). The values for g were obtained from the measured ratio of the polarization components of the recoil neutron which were determined from the measured scattering asymmetries of the neutron in the polarimeter. The correction of the data due to nuclear effects and acceptance averaging were performed using the formalism of the electrodisintegration of the deuteron by Arenhövel. The G_E^n at these $\langle Q^2 \rangle$ values are computed from the measured g using the G_M^n values obtained from the fit to the world data. The relative statistical uncertainty in the measurement of g is about 10% and the relative systematic uncertainty is small (2 to 3%). Our precise measurements of G_E^n [Mad03] combined with the proton form factor data are essential for scrutinizing and developing models of the nucleon.

In this dissertation, the data analyses at $\langle Q^2 \rangle$ =0.45 and 1.13 $(\mathrm{GeV/c})^2$ were performed, and the details about these measurements are discussed.

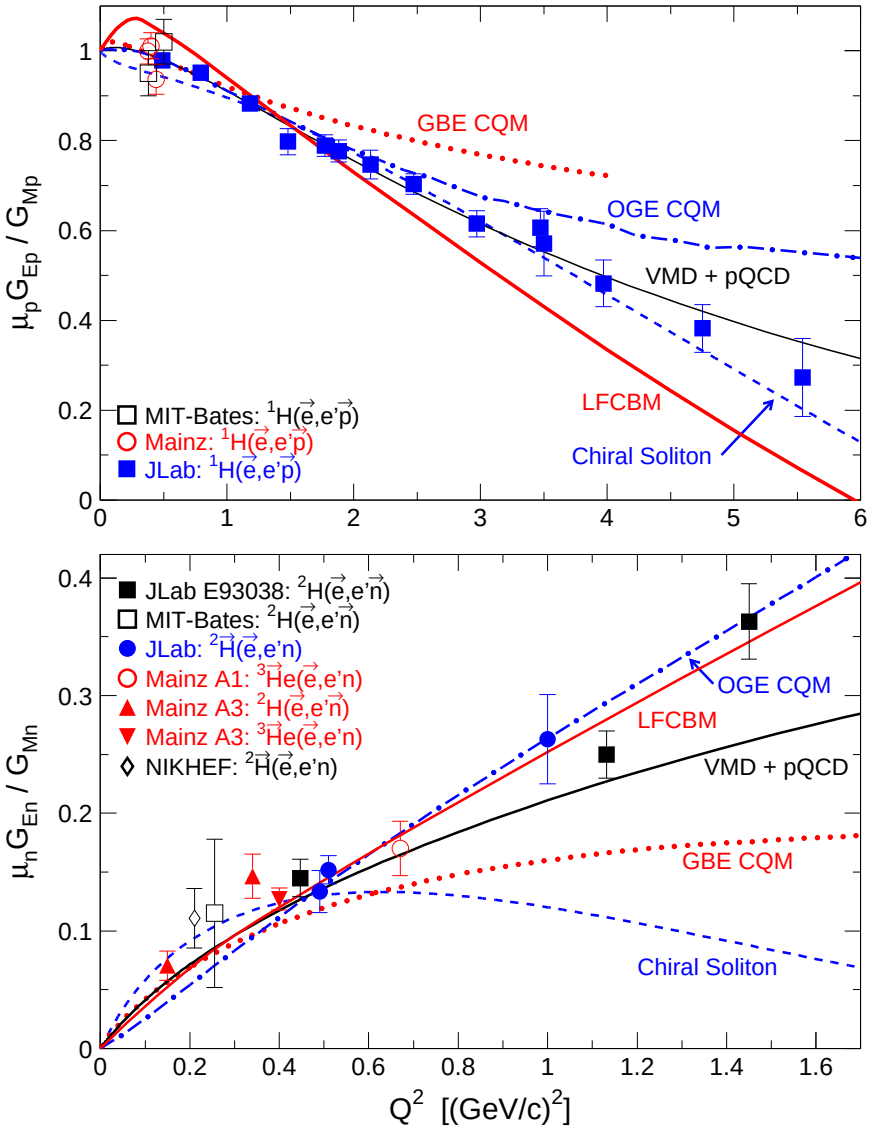

Figure 8.5: Comparison of data with Theoretical model calculations. The top (bottom) plot shows the data for G_E^p/G_M^p (G_E^n/G_M^n) and the theoretical model calculations. In addition to the data shown in Figure 2.3, the data for G_E^n/G_M^n by Madey *et al.* [Mad03] and by Warren *et al.* [War04] are added to the bottom plot. The labels for the theoretical models are the same as in Figure 2.3.

Appendix A

E93-038 Coordinate Systems

Figure A.1 illustrates the Laboratory (LAB) and Polarimeter (POL) coordinate systems. Z_{LAB} is along the incident electron beam and X_{LAB} is to the left on the horizontal plane. The Y axis in any coordinate system is along $\hat{Z} \times \hat{X}$. The POL coordinates are obtained by rotating the LAB coordinates by 46° c.c.w. about Y_{LAB}. The origin for both coordinate systems is located at the center of the target.

Figure A.2 illustrates the Detector (DET) coordinate system. It is defined for *each* of the 70 detectors and the origin is at the center of each detector bar. The X_{DET}, Y_{DET}, and Z_{DET} axes for the front and veto detectors are parallel to the axes in the POL coordinates. For upper (lower) rear detectors, X_{DET} points to the $-Z_{POL}$ ($-Z_{POL}$) axis while Z_{DET} points to the $+Y_{POL}$ ($-Y_{POL}$) axis.

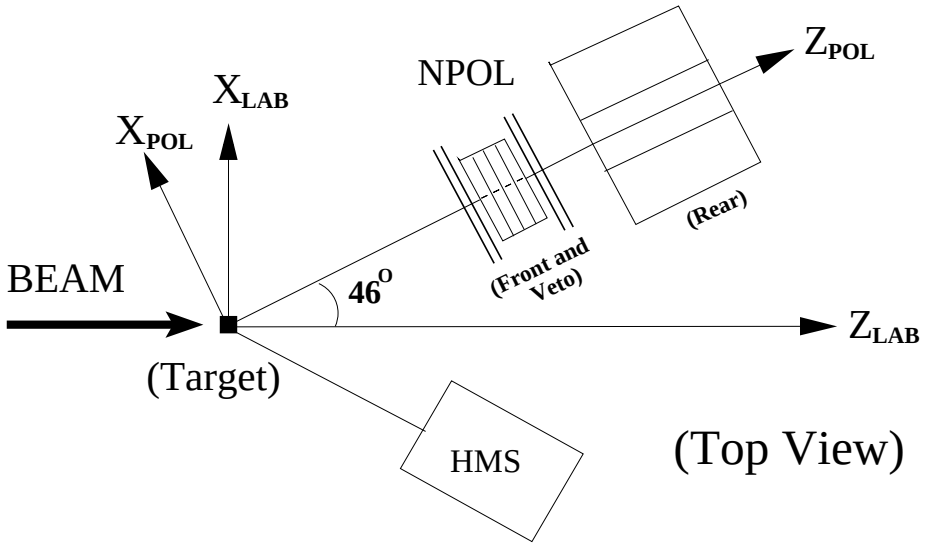

Figure A.1: Laboratory and Polarimeter coordinate systems. The subscript for each axis indicates the coordinate system in which it is defined. Y_{LAB} and Y_{POL} are out of the paper.

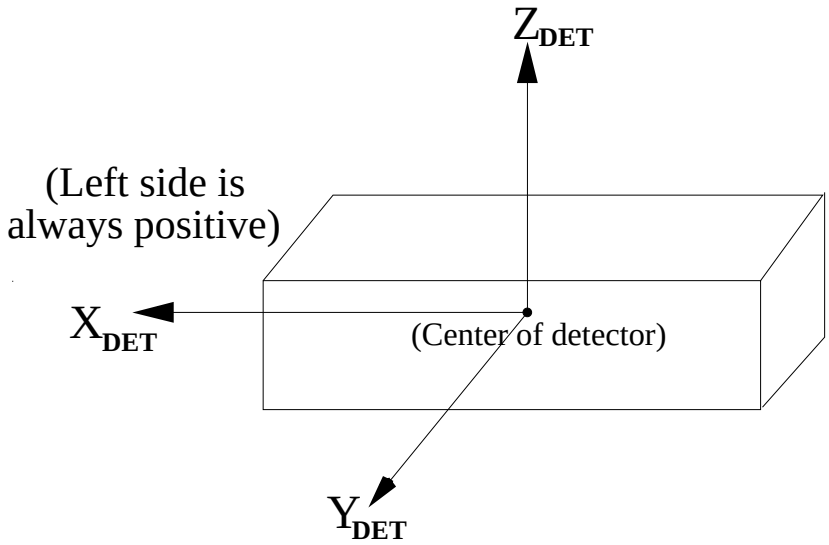

Figure A.2: Detector coordinate system. See text for detail.

Appendix B

Positions of the NPOL Detectors and the Collimator

Positions of the detectors and collimator for the NPOL used in this experiment are given below. Positions are in the POL Coordinates defined in Appendix A.

		Center Position (cm)			Size (cm)		
	Det. #	X	Y/3/	Z/1,2/	X	Y	Z
1st Layer	1	0.0	-20.2	683.7	100.0	10.0	10.0
	2	0.0	-10.1	683.7	100.0	10.0	10.0
	3	0.0	0.0	683.7	100.0	10.0	10.0
	4	0.0	10.1	683.7	100.0	10.0	10.0
	5	0.0	20.2	683.7	100.0	10.0	10.0
2nd Layer	6	0.0	-20.2	693.9	100.0	10.0	10.0
	7	0.0	-10.1	693.9	100.0	10.0	10.0
	8	0.0	0.0	693.9	100.0	10.0	10.0
	9	0.0	10.1	693.9	100.0	10.0	10.0
	10	0.0	20.2	693.9	100.0	10.0	10.0
3rd Layer	11	0.0	-20.2	706.1	100.0	10.0	10.0
	12	0.0	-10.1	706.1	100.0	10.0	10.0
	13	0.0	0.0	706.1	100.0	10.0	10.0
	14	0.0	10.1	706.1	100.0	10.0	10.0
	15	0.0	20.2	706.1	100.0	10.0	10.0
4th Layer	16	0.0	-20.2	716.3	100.0	10.0	10.0
	17	0.0	-10.1	716.3	100.0	10.0	10.0
	18	0.0	0.0	716.3	100.0	10.0	10.0
	19	0.0	10.1	716.3	100.0	10.0	10.0
	20	0.0	20.2	716.3	100.0	10.0	10.0

Table B.1: Position of the Front Detectors

		Center Position (cm)			Size (cm)		
	Det. #	X/3/	Y	Z/1/	X	Y	Z
1st Layer (Bottom, Outside)	21	-50.95	-89.74	952.0	50.8	10.16	101.6
	22	-12.75	-89.74	952.0	25.4	10.16	101.6
	23	12.75	-89.74	952.0	25.4	10.16	101.6
	24	50.95	-89.74	952.0	50.8	10.16	101.6
2nd Layer (Bottom, Midst)	25	-50.95	-73.23	957.0	50.8	10.16	101.6
	26	-12.75	-73.23	957.0	25.4	10.16	101.6
	27	12.75	-73.23	957.0	25.4	10.16	101.6
	28	50.95	-73.23	957.0	50.8	10.16	101.6
3rd Layer (Bottom, Inside)	29	-50.95	-56.72	952.0	50.8	10.16	101.6
	30	-12.75	-56.72	952.0	25.4	10.16	101.6
	31	12.75	-56.72	952.0	25.4	10.16	101.6
	32	50.95	-56.72	952.0	50.8	10.16	101.6
4th Layer (Top, Inside)	33	-50.95	56.72	952.0	50.8	10.16	101.6
	34	-12.75	56.72	952.0	25.4	10.16	101.6
	35	12.75	56.72	952.0	25.4	10.16	101.6
	36	50.95	56.72	952.0	50.8	10.16	101.6
5th Layer (Top, Midst)	37	-50.95	73.23	957.0	50.8	10.16	101.6
	38	-12.75	73.23	957.0	25.4	10.16	101.6
	39	12.75	73.23	957.0	25.4	10.16	101.6
	40	50.95	73.23	957.0	50.8	10.16	101.6
6th Layer (Top, Outside)	41	-50.95	89.74	952.0	50.8	10.16	101.6
	42	-12.75	89.74	952.0	25.4	10.16	101.6
	43	12.75	89.74	952.0	25.4	10.16	101.6
	44	50.95	89.74	952.0	50.8	10.16	101.6

Table B.2: Position of the Rear Detectors

		Center Position (cm)			Size (cm)		
	Det. #	X	Y[3]	Z[1]	X	Y	Z
1st Layer	45	0.0	-21.7	667.5	160.0	11.0	0.635
	46	0.0	-10.6	667.5	160.0	11.0	0.635
	47	0.0	0.5	667.5	160.0	11.0	0.635
	48	0.0	11.6	667.5	160.0	11.0	0.635
	49	0.0	22.7	667.5	160.0	11.0	0.635
2nd Layer	50	0.0	-22.7	673.3	160.0	11.0	0.635
	51	0.0	-11.6	673.3	160.0	11.0	0.635
	52	0.0	-0.5	673.3	160.0	11.0	0.635
	53	0.0	10.6	673.3	160.0	11.0	0.635
	54	0.0	21.7	673.3	160.0	11.0	0.635

Table B.3: Position of the Front-Veto Detectors

		Center Position (cm)			Size (cm)		
	Det. #	X	Y	Z	X	Y	Z
1st Layer	55	0.0	-38.85	726.7	160.0	11.0	0.635
	56	0.0	-27.75	726.7	160.0	11.0	0.635
	57	0.0	-16.65	726.7	160.0	11.0	0.635
	58	0.0	-5.55	726.7	160.0	11.0	0.635
	59	0.0	5.55	726.7	160.0	11.0	0.635
	60	0.0	16.65	726.7	160.0	11.0	0.635
	61	0.0	27.75	726.7	160.0	11.0	0.635
	62	0.0	38.85	726.7	160.0	11.0	0.635
2nd Layer	63[4]	0.0	-37.90	733.7	160.0	11.0	0.635
	64[4]	0.0	-26.80	733.7	160.0	11.0	0.635
	65[4]	0.0	-15.70	733.7	160.0	11.0	0.635
	66[4]	0.0	-4.60	733.7	160.0	11.0	0.635
	67[4]	0.0	6.50	733.7	160.0	11.0	0.635
	68[4]	0.0	17.60	733.7	160.0	11.0	0.635
	69[4]	0.0	28.70	733.7	160.0	11.0	0.635
	70[4]	0.0	39.80	733.7	160.0	11.0	0.635

Table B.4: Position of the Rear-Veto Detectors

	Center Position (cm)			Size (cm)	
	X	Y	Z	X	Y
Entrance	0.0	0.0	483.92	72.6	37.3
(Center Point)	0.0	0.0	549.96	–	–
Exit	0.0	0.0	616.0	92.4	47.5

Table B.5: Position of the Tapered Collimator

Notes

1. The mean flight path to the center of the front array is 7.0 m.
2. Spacing between layers is 2 mm.
3. Spacing between detectors in layer is 1 mm.
4. These detectors did not exist in year 2000 (for Q^2=1.14(GeV/c)^2 data).

Appendix C

Solutions to the 2- and 3-Body Kinematic Equations

We derive solutions to the 2-body kinematic equation for elastic np scattering, and the 3-body kinematic equation for the electrodisintegration of the deuteron, $ed \rightarrow e'np$ as presented in Chapter 5. We only give the solutions for the momentum magnitude of a particle from which the estimated TOF is calculated.

C.1 2-Body Kinematic Equation

When we consider the scattering from the Front to the Rear, we assumed the reaction is np elastic scattering.

$$n^{\mu} + p^{\mu} = n^{'\mu} + p^{'\mu}, \tag{C.1}$$

where n^{μ}, p^{μ}, $n^{'\mu}$, and $p^{'\mu}$ are four momenta of the incident neutron, the proton serving as a target, the scattered neutron, and the recoil proton, respectively. The

coordinates $\hat{x}, \hat{y}$, and $\hat{z}$ used in this section are as follows. We take $\hat{z}$ to be along the direction of the incident neutron. The $\hat{y}$ is perpendicular to the neutron scattering plane, $\hat{y} = (\vec{n} \times \vec{n'})/|\vec{n} \times \vec{n'}|$, and $\hat{x} = \hat{y} \times \hat{z}$. We note that one of the three momentum components can be set to zero without loss of generality. Because this is a two-body reaction, the equations can be described in the neutron scattering plane. Thus, Equation C.1 has a set of three equations: one equation for energy, and the other two for x and z momentum components. The y component of momentum is set to zero. We also note that all the components of $n^\mu = (E_n, \vec{p_n})$ were already known where E_n and $\vec{p_n}$ are energy and three-momentum of incident neutron. In addition, the proton is assumed to be at rest in lab frame, that is, $p^\mu = (m_p, \vec{0})$, Components of n'^μ and p'^μ are $n'^\mu = (E'_n, \vec{p'_n})$ and $n'^\mu = (E'_n, \vec{p'_n})$, respectively. For (n,n) event, the position of the detected neutron in the Rear is measured. Therefore, there remain three unknowns in Equation C.1 (the magnitude of the scattered neutron momentum, p_n, and the two momentum components of the recoil proton). To obtain p'_n from Equation C.1, we square the both sides of $n^\mu + p^\mu - n'^\mu = p'^\mu$. We have

$$n^\mu n_\mu + p^\mu p_\mu + n'^\mu n'_\mu + 2(n^\mu p_\mu - n^\mu n'_\mu - p^\mu n'_\mu) = p'^\mu p'_\mu \tag{C.2}$$

This equation can be simplified by using the following relations,

$$n^\mu n_\mu = n'^\mu n'_\mu = m_n^2 \tag{C.3}$$

$$p^\mu p_\mu = p'^\mu p'_\mu = m_p^2 \tag{C.4}$$

$$n^\mu p_\mu = E_n m_p \tag{C.5}$$

$$n^\mu n'_\mu = E_n E'_n - \vec{p_n}\vec{p'_n} \tag{C.6}$$

$$p^\mu n'_\mu = m_p E'_n, \tag{C.7}$$

where m_n and m_p are mass of the neutron and proton, respectively. Equation C.2 then becomes

$$m_n^2 + E_n m_p - (E_n E_n' - p_n p_n' \cos\theta_{nn}) - m_p E_n' = 0, \tag{C.8}$$

where $p_n = |\vec{p_n}|$, $p_n' = |\vec{p_n'}|$, and θ_{nn} is the angle between $\vec{p_n}$ and $\vec{p_n'}$, which can be calculated. Note that E_n' and p_n' are the only unknowns in Equation C.8 and they are related through $E_n' = \sqrt{m_n^2 + p_n'^2}$. From Equation C.8, E_n' is written in terms of p_n',

$$E_n' = A' + B' p_n' = \sqrt{m_n^2 + p_n'^2}, \tag{C.9}$$

where the coefficients A' and B', which are calculated for each event once E_n, p_n and θ_{nn} are determined,

$$A' = \frac{m_n^2 + E_n m_p}{E_n + m_p} \tag{C.10}$$

$$B' = \frac{p_n \cos\theta_{nn}}{E_n + m_p}. \tag{C.11}$$

By squaring both sides of Equation C.9, a quadratic equation for p_n' is obtained,

$$p_n'^2(1 - B'^2) - 2A'B'p_n' + (m_n^2 - A'^2) = 0 \tag{C.12}$$

Therefore, the solutions for p_n' are

$$p_n' = \frac{A'B' \pm \sqrt{A'^2B'^2 - (1 - B'^2)(m_n^2 - A'^2)}}{1 - B'^2} \tag{C.13}$$

$$= \frac{(m_p E_n + m_n^2) p_n \cos\theta_{nn} \pm p_n (E_n + m_p)\sqrt{m_p^2 - m_n^2 \sin^2\theta_{nn}}}{(E_n + m_p)^2 - p_n^2 \cos^2\theta_{nn}} \tag{C.14}$$

Since p_n' is the momentum magnitude, a solution with positive p_n' is an acceptable solution. However, both solutions in Equation C.13 turn out to be *positive*. (Because $m_n > m_p$, we have $1 - B'^2 > 0$ and $m_n^2 - A'^2 = p_n^2(m_n^2 - m_p^2)/(E_n + m_p)^2 > 0$.)

We take the larger solution to be the valid solution. To see this more clearly, let us assume $m_n = m_p (= m)$. In this case, Equation C.13 becomes

$$p'_n = 0 \tag{C.15}$$

$$p'_n = \frac{2m_n B'}{1 - B'^2} = \frac{2m_n \frac{p_n \cos\theta_{nn}}{E_n + m_n}}{1 - (\frac{p_n \cos\theta_{nn}}{E_n + m_n})^2} > 0 \tag{C.16}$$

One of the solutions, $p'_n = 0$, cannot be accepted because we cannot detect such events when this happens. Therefore, the acceptable solution is the one given in Equation C.16. Considering that $m_n \sim m_p$, the solution with *minus* sign in Equation C.13 must be quite small, and this implies that the recoil proton has a large momentum to conserve the total momentum. In our experiment, the momentum of an incident neutron is lost slightly for (n,n) event upon interaction, and therefore we expect that $p'_n > p'_p$ for (n,n) event, where p'_p is the momentum of the recoil proton. Therefore, we take the *larger* solution (the one with *plus* sign) in Equations C.13 and C.14, as the acceptable solution. [1]

From p'_n, which is the *estimated* particle momentum obtained from Equation C.1, the estimated neutron TOF is calculated from the estimated particle velocity and the measured flight distance between the detectors.

The other unknown variables, two components of the recoil proton momentum, can also be obtained from Equations C.1 and C.14. However, we do not give formula for these quantities as they were not used in our analysis.

For (n,p) event, we detect the recoil proton in the Rear instead of the neutron. Therefore, the proton recoil angle, θ_{np} can be determined from the directions of the incident neutron and recoil proton. For (n,p) event, the solutions for p'_p have the

[1] If the small solution for p'_n in Equation C.14 happens, the recoil angle of the proton is very small due to its large momentum. Therefore, the proton is likely to miss the Rear detectors.

same form as Equation C.13,

$$p'_p = \frac{A''B'' \pm \sqrt{A''^2B''^2 - (1-B''^2)(m_p^2 - A''^2)}}{1-B''^2}. \tag{C.17}$$

and the coefficients A'' and B'' are given by

$$A'' = \frac{m_p^2 + E_n m_p}{E_n + m_p} = m_p \tag{C.18}$$

$$B'' = \frac{p_n \cos\theta_{np}}{E_n + m_p}. \tag{C.19}$$

Because $A'' = m_p$, the solutions in Equation C.17 reduce to

$$p'_p = 0 \tag{C.20}$$

$$p'_p = \frac{2m_pB''}{1-B''^2} = \frac{2m_p\frac{p_n\cos\theta_{np}}{E_n+m_p}}{1-(\frac{p_n\cos\theta_{np}}{E_n+m_p})^2} > 0 \tag{C.21}$$

Because we cannot detect (n,p) events with $p'_p = 0$, we take Equation C.21 as the valid solution.

The results for p'_n for (n,n) event (Equation C.14), and p'_p for (n,p) event (Equation C.21) agree with the results given in [Kaj73].

C.2 3-Body Kinematic Equation

In Chapter 5, we used the *estimated* particle TOF to calibrate the time calibration constant σ for each Front detector and correct the measured Front TOF during the data analysis. We discuss in this section how to obtain the estimated TOF from the 3-body kinematic equation. We solved the conservation equation for the quasielastic $^2\mathrm{H}(\vec{e}, e'\vec{n})^1\mathrm{H}$ reaction for each event to obtain the estimated neutron momentum from which the estimated TOF is calculated.

The conservation equation for the electrodisintegration of the deuteron, $e\,d \rightarrow e'\,n\,p$, is given as

$$e^{\mu} + d^{\mu} \;=\; e^{'\mu} + n^{\mu} + p^{\mu}, \tag{C.22}$$

where $e^{\mu}, d^{\mu}, e^{'\mu}, n^{\mu}$, and p^{μ} are four momenta of the incident electron, target deuteron (assumed to be at rest in the lab frame), scattered electron, recoil neutron, and recoil proton, respectively. We wish to find the magnitude of the neutron momentum, p_n by solving Equation C.22. Note that all the components of e^{μ}, d^{μ}, and $e^{'\mu}$ are known and their energies and three-momentum vectors are given by $e^{\mu} = (E_e, \vec{p_e}), d^{\mu} = (m_d, \vec{0})$, $e^{'\mu} = (E'_e, \vec{p'_e})$ where E_e and $\vec{p_e}$ (E'_e and $\vec{p'_e}$) are energy and three-momentum of the incident (scattered) electron, and m_d is the mass of the deuteron. In addition, because the positions of the interaction at the target and the Front are known, we know the direction of the recoil neutron to the Front. That means the neutron four momentum, $n^{\mu} = (E_n, \vec{p_n})$, contains only one unknown where E_n, and $\vec{p_n}$ are energy and three-momentum of the neutron. To solve Equation C.22, we first simplify this equation by introducing a new four vector, z^{μ},

$$z^{\mu} \;=\; n^{\mu} + p^{\mu}, \tag{C.23}$$

where $z^{\mu} \equiv e^{\mu} + d^{\mu} - e^{'\mu} = q^{\mu} + d^{\mu}$. Here, $q^{\mu} = (\omega, \vec{q})$ is the four momentum for the momentum transfer, and ω is the energy lost by the electron. Note that all four components of $z^{\mu} = (\omega + m_d, \vec{q})$, are known. Scalar products, $z^{\mu}z_{\mu}$ and $z^{\mu}n_{\mu}$, which will be used later, are given by

$$z^2 \equiv z^{\mu}z_{\mu} \;=\; q^2 + m_d^2 + 2\omega m_d \tag{C.24}$$

$$z^{\mu}n_{\mu} \;=\; (\omega + md)E_n - \vec{q}\vec{p_n} = (\omega + md)E_n - |\vec{q}|p_n\cos\phi, \tag{C.25}$$

where ϕ is the angle between $\vec{q}$ and $\vec{p_n}$, which can be determined from the directions of these two vectors. We note the following three things on Equation C.23. First, all

the components on the LHS are completely known. Second, energy and momentum *magnitude* of the first term on the RHS are unknown. Third, all the components of the second term on the RHS are unknown. Notice that this situation is the same as that for Equation C.1 where the 2-body scattering reaction is considered. Because the form of Equation C.23 is in fact the same as that of Equation C.1, Equation C.23 can be solved quite similarly as before. By squaring both sides of $p^\mu = z^\mu - n^\mu$, we obtain

$$m_p^2 = z^2 + m_n^2 - 2z^\mu n_\mu = z^2 + m_n^2 - 2[(\omega + md)E_n - |\vec{q}|p_n \cos\phi], \tag{C.26}$$

where Equation C.25 has been used and z^2 is given by Equation C.24. As before, p_n and E_n are the only unknowns. This equation can be solved for E_n in terms of p_n,

$$E_n = A + Bp_n = \sqrt{m_n^2 + p_n^2} \tag{C.27}$$

$$A = \frac{z^2 + m_n^2 - m_p^2}{2(\omega + m_d)} = \frac{q^2 + 2m_d\omega + m_d^2 + m_n^2 - m_p^2}{2(\omega + m_d)} \tag{C.28}$$

$$B = \frac{|\vec{q}|\cos\phi}{(\omega + m_d)}, \tag{C.29}$$

where Equation C.24 has been used in Equation C.28. Because Equation C.27 has the same form as Equation C.9, the solutions for p_n are given by Equation C.13 with p_n', A', and B' replaced with p_n, A, and B, respectively,

$$p_n = \frac{AB \pm \sqrt{A^2B^2 - (1 - B^2)(m_n^2 - A^2)}}{1 - B^2}. \tag{C.30}$$

For the quasielastic $^2\mathrm{H}(\vec{e}, e'\vec{n})^1\mathrm{H}$ reaction, we expect that the the neutron momentum is much larger than the proton momentum. Therefore, we take the *larger* solution (the one with *plus* sign) in Equation C.30, as the acceptable solution.

The other unknowns, components of the proton four momentum, $p^\mu = (E_p, \vec{p_p})$, can also be determined by solving Equation C.22 with p_n in Equation C.30. However,

we do not give formula for these quantities as they were not important in our analysis. A procedure for determining the proton components are given in [Chu00].

Appendix D

Useful Formulas in Statistics

We present in this section a few useful formula used in this dissertation. For a detailed description on statistics and error analysis, we refer the reader to a book by Bevington [Bev69].

D.1 Uncertainty in a Function of Many Variables

Suppose that independent variables x_1, x_2,...,x_n are measured with uncertainties Δx_1, Δx_2,...,Δx_n. If these variables are used to calculate the function $Z(x_1, x_2, ..., x_n)$, the uncertainty in Z is given as follows, assuming that the uncertainties Δx_1, Δx_2 ... Δx_n are independent and random:

$$\Delta Z = \sqrt{\left(\frac{\partial Z}{\partial x_1}\right)^2 (\Delta x_1)^2 + \left(\frac{\partial Z}{\partial x_2}\right)^2 (\Delta x_2)^2 + ... + \left(\frac{\partial Z}{\partial x_n}\right)^2 (\Delta x_n)^2} \quad \text{(D.1)}$$

Example:

We often need to calculate in this thesis the uncertainty of a function of the following form:

$$Z(x,y) = \frac{ax-by}{ax+by}, \tag{D.2}$$

where a and b are constants. Let us calculate the uncertainty ΔZ assuming x and y have the uncertainty Δx and Δy, respectively. From Equation D.1, $(\Delta Z)^2$ and $(\Delta Z/Z)^2$ are given by the followings:

$$(\Delta Z)^2 = \frac{(2abxy)^2}{(ax+by)^4}\left[\left(\frac{\Delta x}{x}\right)^2+\left(\frac{\Delta y}{y}\right)^2\right] \tag{D.3}$$

$$\left(\frac{\Delta Z}{Z}\right)^2 = \left(\frac{2abxy}{(ax)^2-(by)^2}\right)^2\left[\left(\frac{\Delta x}{x}\right)^2+\left(\frac{\Delta y}{y}\right)^2\right]. \tag{D.4}$$

D.2 Weighted Average

Suppose there are N separate measurements of a quantity x. Their values and uncertainties are given by the followings:

$$x_1 \pm \Delta x_1, x_2 \pm \Delta x_2, ..., x_n \pm \Delta x_n.$$

Define a quantity w_i for the ith measurement of x, where i=1,2,..., N.

$$w_i = \frac{1}{\Delta x_i^2} \tag{D.5}$$

Let $x_{\rm wav}$ and $\Delta x_{\rm wav}$ be the statistically weighted average of the measurements x and Δx, respectively. Then, the results for $x_{\rm wav}$ and $\Delta x_{\rm wav}$ are given by the followings:

$$x_{\rm wav} = \frac{\sum_{i=1}^{N} w_i x_i}{\sum_{i=1}^{N} w_i} \tag{D.6}$$

$$\Delta x_{\rm wav} = \frac{1}{\sqrt{\sum_{i=1}^{N} w_i}} \tag{D.7}$$

The w_i can be interpreted as the *weight* factor. That is, the measurement of x with the smallest uncertainty contributes most in Equation D.6.

Appendix E

Jefferson Laboratory E93-038 Collaboration

Members of the collaboration are listed on the next page. The spokespersons are in **bold face**, and seven Ph.D. students are underlined.

Jefferson Laboratory E93-038 Collaboration

(The spokespersons are in **bold face**, and seven Ph.D. students are underlined.)

A. Aghalaryan[19], A. Ahmidouch[11], B. D. Anderson[6], H. Arenhövel[5], R. Asaturyan[19], O. Baker[4], A. R. Baldwin[6], D. Barkhuff[9], H. Breuer[17], R. Carlini[16], E. Christy[4], S. Churchwell[2], L. Cole[4], E. Crouse[1], S. Danagoulian[11,16], D. Day[18], T. Eden[4,6], M. Elaasar[15], R. Ent[16], M. Farkhondeh[9], H. Fenker[16], J. M. Finn[1], L. Gan[4], K. Garrow[16], A. Gasparian[4,11], P. Gueye[4], C. R. Howell[2], B. Hu[4], M. K. Jones[16], J. J. Kelly[17], C. Keppel[4], M. Khandaker[10], W.-Y. Kim[7], **S. Kowalski**[9], A. Lai[6], A. Lung[16], D. Mack[16], G. MacLachlan[12], **R. Madey**[6,16], D. M. Manley[6], P. Markowitz[3], J. Mitchell[16], H. Mkrtchyan[19], A. K. Opper[12], C. Perdrisat[1], B. Plaster[9], V. Punjabi[10], B. Raue[3], T. Reichelt[14], J. Reinhold[3], J. Roche[1], Y. Sato[4], N. Savvinov[17], A. Yu. Semenov[6], I. A. Semenova[6], W. Seo[7], N. Simicevic[8], G. Smith[16], S. Stepanyan[7,19], V. Tadevosyan[19], S. Tajima[2], L. Tang[4], S. Taylor[9], W. Tireman[6], P. Ulmer[13], W. Vulcan[16], J. W. Watson[6], S. Wells[8], F. Wesselmann[18], S. Wood[16], Chen Yan[16], Chenyu Yan[6], S. Yang[7], L. Yuan[4], W.-M. Zhang[6], H. Zhu[18], and X. Zhu[4]

[1] *The College of William and Mary, Williamsburg, Virginia 23187*
[2] *Duke University, Durham, North Carolina 27708*
[3] *Florida International University, Miami, Florida 33199*
[4] *Hampton University, Hampton, Virginia, 23668*
[5] *Johannes Gutenberg-Universität, D-55099 Mainz, Germany*
[6] *Kent State University, Kent, Ohio 44242*
[7] *Kyungpook National University, Taegu 702-701, Korea*
[8] *Louisiana Tech University, Ruston, Louisiana 71272*
[9] *Massachusetts Institute of Technology, Cambridge, Massachusetts 02139*
[10] *Norfolk State University, Norfolk, Virginia 23504*
[11] *North Carolina A&T State University, Greensboro, North Carolina 27411*
[12] *Ohio University, Athens, Ohio 45701*
[13] *Old Dominion University, Norfolk, Virginia 23508*
[14] *Rheinische Friedrich-Wilhelms-Universität, D-53115 Bonn, Germany*
[15] *Southern University at New Orleans, New Orleans, Louisiana 70126*
[16] *Thomas Jefferson National Accelerator Facility, Newport News, Virginia 23606*
[17] *University of Maryland, College Park, Maryland 20742*
[18] *University of Virginia, Charlottesville, Virginia 22904*
[19] *Yerevan Physics Institute, Yerevan 375036, Armenia*

Bibliography

[Afa01] A. Afanasev, I. Akushevich, and N. Merenkov. *Model independent radiative corrections in processes of polarized electron nucleon elastic scattering.* Phys. Rev., **D64**(2001) 113009.

[Afa02] A. Afanasev. *(private communication).* (2002).

[Akh74] A. I. Akhiezer and M. P. Rekalo. Sov. J. Part. Nucl., **4**(1974) 277.

[Ank94] H. Anklin et al. *Precision measurement of the neutron magnetic formfactor.* Phys. Lett., **B336**(1994) 313–318.

[Ank98] H. Anklin et al. *Precise measurements of the neutron magnetic form factor.* Phys. Lett., **B428**(1998) 248–253.

[Are87] H. Arenhövel. *On the determination of the electric neutron form-factor in* $\mathrm{d}(\tilde{\mathrm{e}},\mathrm{e}'\tilde{\mathrm{n}})\mathrm{p}$. Phys. Lett., **B199**(1987) 13–16.

[Are88] H. Arenhövel, W. Leidemann, and E. L. Tomusiak. *The role of the neutron electric form-factor in* $\mathrm{d}(\mathrm{e},\mathrm{e}'\mathrm{N})\mathrm{N}$ *including polarization observables.* Z. Phys., **A331**(1988) 123–138.

[Are95] H. Arenhövel, W. Leidemann, and E. L. Tomusiak. *Nucleon polarization in exclusive deuteron electrodisintegration with polarized electrons and a polarized target.* Phys. Rev., **C52**(1995) 1232–1253.

[Are02] H. Arenhövel. *(private communication).* (2002).

[Arn81] R. G. Arnold, Carl E. Carlson, and Franz Gross. *Polarization transfer in elastic electron scattering from nucleons and deuterons.* Phys. Rev., **C23**(1981) 363.

[Arr98] J. Arrington. Ph.D. Thesis, California Institute of Technology, (1998).

[Ass97] K. Assamagan, D. Dutta, and P. Welch. *Hall C Matrix Element Optimization.* Hall-C Internal Report (unpublished), (1997).

[Bak95] O. K. Baker et al. *The High Momentum Spectrometer drift chambers in Hall C at CEBAF.* Nucl. Instrum. Meth., **A367**(1995) 92–95.

[Bar69] W. Bartel et al. *Neutron form-factors from quasielastic ed scattering.* Phys. Lett., **B30**(1969) 285–288.

[Bar72] W. Bartel et al. *Electromagnetic form factors of the neutron at squared four-momentum transfers of 1.0 and 1.5 (GeV/c)*^{2}. Phys. Lett., **B39**(1972) 407–410.

[Bar73] W. Bartel et al. *Measurement of proton and neutron electromagnetic form-factors at squared four momentum transfers up to 3 (GeV/c)*^{2}. Nucl. Phys., **B58**(1973) 429–475.

[Bea94] K. B. Beard and S. A. Wood. *Engine 1.1.2: Hall-C analysis engine.* Hall-C Internal Report: Csoft-NOTE-94-007 (unpublished), (1994).

[Bec99] J. Becker et al. *Determination of the neutron electric form factor from the reaction* ^{3}**He***(***e***,e' n) at medium momentum transfer.* Eur. Phys. J., **A6**(1999) 329–344.

[Ber95] M. Berz. *COSY Infinity Version 7 Reference Manual, NSCL Technical Report MSUCL-977, Michigan State University.* (1995).

[Ber03] J. Bermuth et al. *The neutron charge form factor and target analyzing powers from* $^3\vec{\mathrm{He}}(\vec{e},e'n)p$ *scattering.* Phys. Lett., **B564**(2003) 199–204.

[Bev69] P.R. Bevington. *Data Reduction and Error Analysis for the Physical Sciences.* McGraw-Hill, 1969.

[Blo69] E. D. Bloom et al. *High-energy inelastic e-p scattering at 6° and 10°.* Phys. Rev. Lett., **23**(1969) 930–934.

[Boc99] C. Bochna. Ph.D. Thesis, University of Illinois, (1999).

[Bof02] S. Boffi et al. *Covariant electroweak nucleon form factors in a chiral constituent quark model.* Eur. Phys. J., **A14**(2002) 17–21.

[Bos92] P. Bosted et al. *Measurements of the electric and magnetic form-factors of the proton from Q**2 = 1.75-GeV/c**2 to 8.83-GeV/c**2.* Phys. Rev. Lett., **68**(1992) 3841–3844.

[Bra02] E. J. Brash, A. Kozlov, S. Li, and G. M. Huber. *New empirical fits to the proton electromagnetic form factors.* Phys. Rev., **C65**(2002) 051001.

[Bre69] Martin Breidenbach et al. *Observed behavior of highly inelastic electron-proton scattering.* Phys. Rev. Lett., **23**(1969) 935–939.

[Bru95] E. E. W. Bruins et al. *Measurement of the neutron magnetic form-factor.* Phys. Rev. Lett., **75**(1995) 21–24.

[Cap86] Simon Capstick and Nathan Isgur. *Baryons in a relativized quark model with chromodynamics.* Phys. Rev., **D34**(1986) 2809.

[Car99] Fabio Cardarelli and Silvano Simula. *Relativistic effects on the neutron charge form factor in the constituent quark model.* Phys. Lett., **B467**(1999) 1–7.

[Car00] Fabio Cardarelli and Silvano Simula. *SU(6) breaking effects in the nucleon elastic electromagnetic form factors.* Phys. Rev., **C62**(2000) 065201.

[Cha32] J. Chadwick. *The existence of a neutron.* Proc. Roy. Soc. A, **136**(1932) 692–708.

[Cha56] E. E. Chambers and R. Hofstadter. *Structure of the proton.* Phys. Rev., **103**(1956) 1454–1463.

[Chr00] M. E. Christy. *(unpublished).* (2000).

[Chu91] P. L. Chung and F. Coester. *Relativistic constituent quark model of nucleon form- factors.* Phys. Rev., **D44**(1991) 229–241.

[Chu99] S. Churchwell. *Relativistic Kinematics.* JLab E93-038 internal report, (1999).

[Chu00] S. T. Churchwell. *Three body kinematics.* JLab E93-038 Internal Report (unpublished): http://www.jlab.org/~semenov/reports/, (2000).

[Chu01a] S. Churchwell. *(private communication).* (2001).

[Chu01b] S. T. Churchwell. *Timing calibration for the E93038 polarimeter - The Duke method.* JLab E93-038 Internal Report (unpublished): http://www.jlab.org/~semenov/reports/, (2001).

[Coda] *CEBAF On-line Data Aquisition User's Manual.* CEBAF Internal Report.

[Codb] *CODA Home Page at CEBAF.* http://coda.jlab.org/.

[Dom69] N. Dombey. *Scattering of polarized leptons at high energy.* Rev. Mod. Phys., **41**(1969) 236–246.

[Don86] T. W. Donnelly and A. S. Raskin. *Considerations of polarization in inclusive electron scattering from nuclei.* Annals Phys., **169**(1986) 247–351.

[Dun97] F. Duncan. *Hall-C cryogenic target user manual.* CEBAF Internal Report (unpublished), (1997).

[Dut99] D. Dutta. Ph.D. Thesis, Northwestern University, (1999).

[Ede94] T. Eden et al. *Electric form-factor of the neutron from the* $^2\mathrm{H}(\vec{e}, e'\vec{n})^1\mathrm{H}$ *reaction at* $Q^2 = 0.255\ (GeV/c)^2$. Phys. Rev., **C50**(1994) 1749–1753.

[EPI] *Experimental Physics and Industrial Control System.* http://www.aps.anl.gov/epics/.

[Fab79] W. Fabian and H. Arenhovel. *Electrodisintegration of deuterium including nucleon detection in coincidence.* Nucl. Phys., **A314**(1979) 253–286.

[fPP] CERN European Laboratory for Particle Physics. *Physics Analysis Workstation.* http://wwwinfo.cern.ch/asd/paw/.

[Gal71] S. Galster et al. *Elastic electron - deuteron scattering and the electric neutron form-factor at four momentum transfers 5* $fm^{-2} < q^2 < 14\ fm^{-2}$. Nucl. Phys., **B32**(1971) 221–237.

[Gao94] H. Gao et al. *Measurement of the neutron magnetic form-factor from inclusive quasielastic scattering of polarized electrons from polarized* ^3He. Phys. Rev., **C50**(1994) 546–549.

[Gao03] H. Gao. *Nuclear electromagnetic form factors.* Int. J. Mod. Phys, **E12**(2003) 1–40.

[Gar85] Manfred Gari and W. Krümpelmann. *Semiphenomenological synthesis of meson and quark dynamics and the electromagnetic structure of the nucleon.* Z. Phys., **A322**(1985) 689–693.

[Gar86] Manfred Gari and W. Krümpelmann. *The electromagnetic form-factor of the neutron.* Phys. Lett., **B173**(1986) 10–14.

[Gar92] M. F. Gari and W. Krümpelmann. *The Electric neutron form-factor and the strange quark content of the nucleon.* Phys. Lett., **B274**(1992) 159–162.

[Gay02] O. Gayou et al. *Measurement of G_{Ep}/G_{Mp} in $\vec{e}p \rightarrow e\vec{p}$ to $Q^2 = 5.6$ $(GeV)^2$.* Phys. Rev. Lett., **88**(2002) 092301.

[Gee94] D. F. Geesaman. *Example: Adding a histogramming routine to the Hall C analysis software.* Hall-C Internal Report Csoft-NOTE-94-014 (unpublished), (1994).

[Glo98] L. Ya. Glozman, W. Plessas, K. Varga, and R. F. Wagenbrunn. *Unified description of light- and strange-baryon spectra.* Phys. Rev., **D58**(1998) 094030.

[Gol01] J. Golak, G. Ziemer, H. Kamada, H. Witala, and W. Glockle. *Extraction of electromagnetic neutron form factors through inclusive and exclusive polarized electron scattering on polarized ^{3}He target.* Phys. Rev., **C63**(2001) 034006.

[Gro00] D. E. Groom et al. *Review of Particle Physics. Particle Data Group.* European Physical Journal, **C15**(2000).

[Guea] P. Gueye. *Status of the actual beam position monitors in the Hall C beamline.* CEBAF Internal Report (unpublished).

[Gueb] P Gueye, M. Tiefenback, and C. Yan. *Hall C Beam Energy Measurment.* CEBAF Internal Report (unpublished).

[Hag63] R. Hagedorn. *Relativistic Kinematics.* W.A. Benjamin, Inc, 1963.

[Hal84] F. Halzen and A. Martin. *Quarks & Lepton.* John Wiley & Sons, 1984.

[Hau01] M. Hauger et al. *A high-precision polarimeter.* Nucl. Instrum. Meth., **A462**(2001) 382–392.

[Her99] C. Herberg et al. *Determination of the neutron electric form factor in the D(**e**,e' **n**)p reaction and the influence of nuclear binding.* Eur. Phys. J., **A5**(1999) 131–135.

[Hof53] R. Hofstadter, H. R. Fechter, and J. A. McIntyre. *Scattering of high-energy electrons and the method of nuclei recoil.* Phys. Rev., **91**(1953) 422–423.

[Hof55] R. Hofstadter and R. W. McAllister. *Electron scattering from the proton.* Phys. Rev., **98**(1955) 217–218.

[Hoh76] G. Hohler et al. *ANALYSIS OF ELECTROMAGNETIC NUCLEON FORM-FACTORS.* Nucl. Phys., **B114**(1976) 505.

[Hol96] G. Holzwarth. *Electro-magnetic nucleon form factors and their spectral functions in soliton models.* Z. Phys., **A356**(1996) 339–350.

[Hol02] G. Holzwarth. *Electromagnetic form factors of the nucleon in the chiral soliton model.* arXiv:hep-ph/0201138, (2002).

[How00] C. R. Howell. *(private communication).* (2000).

[Iac73] F. Iachello, A. D. Jackson, and A. Lande. *Semiphenomenological fits to nucleon electromagnetic form- factors.* Phys. Lett., **B43**(1973) 191–196.

[Jon00] M. K. Jones et al. *G_{Ep}/G_{Mp} ratio by polarization transfer in $\vec{e}p \rightarrow e\vec{p}$.* Phys. Rev. Lett., **84**(2000) 1398–1402.

[Jon01] M. K. Jones and A Aghalaryan. *(private communication).* (2001).

[Kaj73] B. Kajantie. *Particle Kinematics.* John Wiley & Sons, Inc, 1973.

[Kel02] James J. Kelly. *Nucleon charge and magnetization densities from Sachs form factors.* Phys. Rev., **C66**(2002) 065203.

[Kel03a] J. J. Kelly. *(private communication).* (2003).

[Kel03b] J. J. Kelly and B. Plaster. *JLab E93-038 Simulation Program,* GENGEN *ver. 2.9.* (2003).

[Kir73] Paul N. Kirk et al. *Elastic electron - proton scattering at large four momentum transfer.* Phys. Rev., **D8**(1973) 63–91.

[Kop97] S. Kopecky et al. *Neutron charge radius determined from the energy dependence of the neutron transmission of liquid ^{208}Pb and ^{209}Bi.* Phys. Rev., **C56**(1997) 2229–2237.

[Kub02] G. Kubon et al. *Precise neutron magnetic form factors.* Phys. Lett., **B524**(2002) 26–32.

[Lam78] *Introduction to Q.* LAMPF internal report LA-7001-M, (1978).

[Lei91] W. Leidemann, E. L. Tomusiak, and H. Arenhovel. *Inclusive deuteron electrodisintegration with polarized electrons and a polarized target.* Phys. Rev., **C43**(1991) 1022–1037.

[Leo94] W.R. Leo. *Techniques for Nuclear and Particle Physics Experiments.* Springer-Verlag, 1994.

[Löf73] K. Löffler, H. J. Scheerer, and H Vonach. *The ion optical properties of the Munich Q3D-spectrograph investigated by means of a special experimental raytracing method.* Nucl. Instr. Meth, **111**(1973) 1–12.

[Lom67] E. Lomon and H. Feshbach. *A nucleon-nucleon interaction consistent with theory and experiment.* Rev. Mod. Phys., **39**(1967) 611–621.

[Lom01] Earle L. Lomon. *Extended Gari-Krümpelmann model fits to nucleon electromagnetic form factors.* Phys. Rev., **C64**(2001) 035204.

[Lom02] Earle L. Lomon. *Effect of recent R_p and R_n measurements on extended Gari-Krümpelmann model fits to nucleon electromagnetic form factors.* Phys. Rev., **C66**(2002) 045501.

[Lun93] A. Lung et al. *Measurements of the electric and magnetic form-factors of the neutron from Q^2= 1.75 (GeV/c)^2 to 4 (GeV/c)^2.* Phys. Rev. Lett., **70**(1993) 718–721.

[Mac87] R. Machleidt, K. Holinde, and C. Elster. *The Bonn meson exchange model for the nucleon nucleon interaction.* Phys. Rept., **149**(1987) 1–89.

[Mac02] G. Maclachlan. *Delta M. E. optimization.* JLab E93-038 Internal Report (unpublished): http://www.jlab.org/~semenov/reports/, (2002).

[Mad78] R. Madey, F.M. Waterman, A. R. Baldwin, and J. N. Knudson. *The response of NE-228A, NE-228, NE-224, and NE-102 scintillators to protons from* 2.43 *to* 19.55 *MeV.* Nuc. Inst. & Meth., **151**(1978) 445–450.

[Mad93] R. Madey. *JLab E93-038 Proposal: The electric form factor of the neutron from the* ^{2}H$(\vec{e}, e'\vec{n})^1$H*reaction.* CEBAF Internal Report, (1993).

[Mad95] R. Madey, A. Lai, and T. Eden. *Polarization phenomena in nuclear physics, edited by E. J. Stephenson and P. E. Vigdor.* AIP Conf. Proc., **339**(1995) 47–54.

[Mad99] R. Madey and T. Eden. *The electric form-factor of the neutron by recoil polarimetry.* Fizika, **B8**(1999) 35–40.

[Mad03] R. Madey et al. *Measurements of $G_E^n/G_M^n$from the* ^{2}H$(\vec{e}, e'\vec{n})^1$H *reaction to Q^2*= 1.45 *(GeV/c)^2.* Phys. Rev. Lett., **91**(2003) 122002.

[Mar93] P. Markowitz et al. *Measurement of the magnetic form-factor of the neutron.* Phys. Rev., **C48**(1993) 5–9.

[Mey94] M. Meyerhoff et al. *First measurement of the electric form-factor of the neutron in the exclusive quasielastic scattering of polarized electrons from polarized ^3He.* Phys. Lett., **B327**(1994) 201–207.

[Mil98] B. D. Milbrath et al. *A comparison of polarization observables in electron scattering from the proton and deuteron.* Phys. Rev. Lett., **80**(1998) 452–455.

[Mil02] Gerald A. Miller. *Light front cloudy bag model: Nucleon electromagnetic form factors.* Phys. Rev., **C66**(2002) 032201.

[Mus94] M. J. Musolf et al. *Intermediate-energy semileptonic probes of the hadronic neutral current.* Phys. Rept., **239**(1994) 1–178.

[Ohl73] G. G. Ohlsen and P. W. Keaton, Jr. *Techniques for measurement of spin-$\frac{1}{2}$ and spin-$\frac{1}{2}$ polarization analyzing tensors.* Nuc. Instr. Meth., **109**(1973) 41–59.

[Ost99] M. Ostrick et al. *Measurement of the neutron electric form factor $G_{E,n}$ in the quasifree ^{2}H$(\vec{e}, e'\vec{n})^1$H reaction.* Phys. Rev. Lett., **83**(1999) 276–279.

[Pas99] I. Passchier et al. *The charge form factor of the neutron from the reaction $^2\vec{\mathrm{H}}(\vec{e}, e'n)$p.* Phys. Rev. Lett., **82**(1999) 4988–4991.

[Pen61] S. Penner. *Calculations of properties of magnetic deflection systems.* Rev. Sci. Instr., **32, nr2**(1961) 150–160.

[Pla90] S. Platchkov et al. *Deuteron $A(Q^2)$ structure function and the neutron electric form-factor.* Nucl. Phys., **A510**(1990) 740–758.

[Pla02] B. Plaster. *Neutron Scattering in the Lead Curtain.* JLab E93-038 Internal Report (unpublished): http://www.jlab.org/~semenov/reports/, (2002).

[Pla03a] B. Plaster. Ph.D. Thesis, Massachusetts Institute of Technology, (2003).

[Pla03b] B. Plaster. *An Estimation of the Charge-Exchange Systematic Uncertainty: Version III.* JLab E93-038 Internal Report (unpublished): http://www.jlab.org/~semenov/reports/, (2003).

[Pos01] T. Pospischil et al. *Measurement of G_E^p/G_M^p via polarization transfer at Q^2= 0.4 (GeV/c)^2.* Eur. Phys. J., **A12**(2001) 125–127.

[Pre92] W.H. Press, S.A. Teukolsky, W.T. Vetterling, and B.P. Flannery. *Numerical Recipes in FORTRAN: The Art of Scientific Computing.* Cambridge University Press, 1992.

[Roc82] Stephen Rock et al. *Measurement of elastic electron-neutron cross-sections up to Q^2 = 10 (GeV/c)^2.* Phys. Rev. Lett., **49**(1982) 1139.

[Roh99] D. Rohe et al. *Measurement of the neutron electric form factor G(en) at 0.67 (GeV/c)^2 via $^3\vec{\mathrm{He}}(\vec{e},e'n)$.* Phys. Rev. Lett., **83**(1999) 4257–4260.

[Ros50] M. N. Rosenbluth. *High energy elastic scattering of electrons on protons.* Phys. Rev., **79**(1950) 615–619.

[Sac62] R. G. Sachs. *High-energy behavior of nucleon electromagnetic form factors.* Phys. Rev., **126**(1962) 2256–2260.

[SAI] *Partial-Wave Analysis Facility (SAID program).* **http://gwdac.phys.gwu.edu**.

[Sak67] J. J. Sakurai. *Advanced quantum mechanics.* Addison-Wesley Pub. Co., 1967.

[Sak69] J. J. Sakurai. *Currents and Mesons.* The University of Chicago Press, 1969.

[Sch01] R. Schiavilla and I. Sick. *Neutron charge form factor at large q^2.* Phys. Rev., **C64**(2001) 041002.

[Sem00] A. Yu Semenov. *(private communication).* (2000).

[Sem03] A. Yu Semenov. casym *program for E93-038 analysis, version. 2.6.* (2003).

[Sim01] Silvano Simula. *Relativistic quark models.* arXiv:nucl-th/0105024, (2001).

[Sky61] T. H. R. Skyrme. *A Nonlinear field theory.* Proc. Roy. Soc. Lond., **A260**(1961) 127–138.

[Taj01] S. Tajima and C. R. Howell. *Physics quantity reconstruction for E93038.* JLab E93-038 Internal Report (unpublished): http://www.jlab.org/~semenov/reports/, (2001).

[Taj02a] S. Tajima and C. R. Howell. *Investigation of the origin of the diagonal band in CTOF vs ΔTOF histogram.* JLab E93-038 Internal Report (unpublished): http://www.jlab.org/~semenov/reports/, (2002).

[Taj02b] S. Tajima and C. R. Howell. *Optimization of bite in ΔTOF histogram.* JLab E93-038 Internal Report (unpublished): http://www.jlab.org/~semenov/reports/, (2002).

[Tay01] S. Taylor. *Field integrals and precession angles for GeN.* E93-038 Internal report (unpublished): http://www.jlab.org/~semenov/reports/, (2001).

[Tay02] S. Taylor. *More on spin precession.* E93-038 Internal report (unpublished): http://www.jlab.org/~semenov/reports/, (2002).

[Tho01] Anthony W. Thomas and Wolfram Weise. *The Structure of the Nucleon.* Wiley-VCH, 2001.

[Tir01a] W. Tireman. *Comparison between pulse height calibrations for NPOL during E93-038.* JLab E93-038 Internal Report (unpublished): http://www.jlab.org/~semenov/reports/, (2001).

[Tir01b] W. Tireman. *Pulse height calibration of the E93-038 neutron polarimeter with a ^{228}Th source.* JLab E93-038 Internal Report (unpublished): http://www.jlab.org/~semenov/reports/, (2001).

[Wag01] R. F. Wagenbrunn, S. Boffi, W. Klink, W. Plessas, and M. Radici. *Covariant nucleon electromagnetic form factors from the Goldstone-boson exchange quark model.* Phys. Lett., **B511**(2001) 33–39.

[War04] G. Warren et al. *Measurement of the electric form factor of the neutron at Q^2=0.5 and 1.0 (GeV/c)^2.* arXiv:nucl-ex/0308021; To be published in Phys. Rev. Lett., (2004).

[Woo94] Stephen A. Wood. *Event decoding.* Hall-C Internal Report: Csoft-NOTE-94-008 (unpublished), (1994).

[Woo95] Stephen A. Wood. *The CEBAF test package: A symbolic and dynamic test, histogram, and parameter package for on- and off-line particle physics data analysis.* CEBAF Internal Report (unpublished), (1995).

[Xu00] W. Xu et al. *The transverse asymmetry A(T') from quasielastic polarized $^3\vec{\mathrm{He}}(\vec{e},e')$ process and the neutron magnetic form factor.* Phys. Rev. Lett., **85**(2000) 2900–2904.

[Xu03] W. Xu et al. *PWIA extraction of the neutron magnetic form factor from quasi-elastic $^3\vec{\mathrm{He}}(\vec{e},e')$ at Q^2 = 0.3 (GeV/c)^2 to 0.6 (GeV/c)^2.* Phys. Rev., **C67**(2003) 012201.

[Zhu01] H. Zhu et al. *A measurement of the electric form-factor of the neutron through $\vec{\mathrm{d}}(\vec{e},e'n)$p at Q^2= 0.5 (GeV/c)^2.* Phys. Rev. Lett., **87**(2001) 081801.